ATOMISTIC SIMULATION STUDIES OF Li^+, Na^+ and Mg^{2+} INSERTED NANO-ARCHITECTURED TiO_2 FOR METAL ION BATTERIES.

by

BLESSING NKATEKO RIKHOTSO

RESEARCH THESIS

Submitted in fulfilment of the requirements for the degree of

Doctor of Philosophy

in

CHEMISTRY

in the

FACULTY OF SCIENCE AND AGRICULTURE

(School of Physical and Mineral Sciences)

at the

UNIVERSITY OF LIMPOPO

SUPERVISOR: Prof. P. E. Ngoepe

2023

DECLARATION

I declare that the thesis hereby submitted to the University of Limpopo, for the degree of Doctor of Philosophy in Chemistry has not previously been submitted by me for a degree at this or any other University; that it is my work in design and in execution, and that all material contained herein has been duly acknowledged.

30 March 2023

Rikhotso B. N

Date

DEDICATION

To my parents Father Laurence (Late) and Mother Mervis Rikhotso, my four brothers, two sisters, Nieces, nephew, cousins and extended families most of all my son Ndzalo Mboweni.

ACKNOWLEDGEMENTS

There are many I must be grateful for I must say that I could not have done it without their great support and love. I would like to express my heartfelt words of gratitude to Prof P.E Ngoepe for allowing me to continue expanding the study topic in material sciences with my chemistry background. Your guides and patience have helped a lot over these years. It was a great honour for me to work with you and gained some of your deep knowledge in discussions and meetings. Your advice, inspiration and encouragement enabled me to enjoy all the scientific seminars, workshops and talks that were held in and out of Material Modelling Centre. I would also like to thank Dr. K.M Kgatwane and Dr. M.G. Matshaba for their extensive guides throughout the study.

To all my colleagues at Material Modelling Centre (MMC), where all my work was done. Your discussions have helped me a lot to achieve this degree. All thanks to the University of Limpopo community for providing a good working environment throughout my research study. All conferences that I have attended throughout my study have helped me a lot in contribution to my research work.

The Centre for High Performance Computing (CHPC) in Cape Town, I would like to say thank you for allowing me to use your systems throughout my research. All calculations of this work were done using their cluster systems, I really appreciate their help. I would like to acknowledge partial and full financial assistance from the National Research Foundation (NRF) and CSIR-Merseta Bursary respectively. Most of all, I thank Jesus Christ the son of God for giving me strength and guidance all these years. Not forgetting my family for being there for me when I needed them most. Your presence and support helped me a lot to achieve this degree.

ABSTRACT

Since the rechargeable battery performance involving TiO_2 anode strongly depends on its structural, transport and electrochemical properties, it is important to explore different TiO_2 nanostructures in order to improve its operation through its ability of hosting mono and multivalent ions. Consequently, the current study involves synthesizing M_xTiO_2 (M = Li^+, Na^+, and Mg^{2+}) (x= 0.11, 0.15, 0.19 and 0.23) nanospheres, nanoporous and nanosheets using the molecular dynamics based amorphization and recrystallization technique, employing a DL_POLY code. This is followed by predicting structural and mobile ion transport properties for future rechargeable batteries. Li^+, Na^+ and Mg^{2+} were inserted into the amorphous TiO_2 nanosphere, nanoporous and nanosheet architectures in order to produce Li_xTiO_2, Na_xTiO_2 and Mg_xTiO_2 (x= 0.11, 0.15 ,0.19 and 0.23) for each nano-architecture. The amorphous nano-architectures were recrystallized by simulations at 2000 K and resultant structures were cooled from 1500 K to 0 K at intervals of 500 K. Finally all cooled nano-architectures at 0 K were analysed and subsequently heated to 2000 K at 100 K intervals. The TiO_2 nanospheres with 0.11, 0.15, 0.23 Li^+ and Na^+ concentrations had similar microstructural defects, present in pure TiO_2 and before Li insertion, characterised by dominant zigzag (brookite) and straight (rutile) tunnels with empty vacancies and Li^+ and Na^+ filled vacancies with few Li^+ and Na^+ located on the surface. On the other hand, the TiO_2 nanospheres with 0,19 Li^+ and Na^+ concentrations remained amorphous after recrystallization, cooling and heating; hence their structural and microstructural features were not constructed. Surprisingly, the $Mg_{0.19}TiO_2$ nanosphere recrystallised successfully together with those of 0.11, 0.15, and 0.23 Mg^{2+} concentrations and their microstructures had zigzag (brookite), straight (rutile), tunnels with empty vacancies, Mg^{2+} filled vacancies and few Mg^{2+} were situated on the surfaces. The microstructures of the TiO_2 nanoporous structures, with 0.11, 0.15, 0.19 and 0.23 Li^+, Na^+ and Mg^{2+} concentrations, showed crystalline patterns of zigzag tunnels (brookite), straight (rutile) tunnels with empty vacancies and Li^+, Na^+ and Mg^{2+} filled vacancies after being recrystallised and cooled, except for the 0.23 Mg^{2+} concentration which showed highly disordered patterns. The microstructures of TiO_2 nanosheets, with 0.11, 0.15, 0.19 and 0.23 Li^+, Na^+ and Mg^{2+} concentrations, had a mixture of disordered and crystalline (ordered) patterns of zigzag (brookite) and straight (rutile) tunnels with few empty vacancies, and some were filled with Li^+, Na^+ and Mg^{2+} where most Li^+ and Na^+ ions were situated around the surface of the microstructure except for TiO_2 nanosheets with 0.23 Mg^{2+} concentration which was amorphous, similar to that of $Mg_{0.23}TiO_2$ nanoporous architecture. All resulting TiO_2 nanostructures and microstructures were further characterised and analyzed by their respective radial distribution functions (RDFs), simulated X-ray diffraction (XRD) patterns, diffusion coefficients and activation energies to study the effects of increased lithiation, sodiation, and magnesiation at various temperatures. The simulated Ti-O radial distribution functions were utilised to confirm the extent of crystallinity of nano-architectures after recrystallisation, cooling, and heating. In addition, simulated X-ray diffraction (XRD) patterns were employed to determine and compare crystallinity at low and elevated temperatures. Furthermore, they depicted rutile and brookite polymorphs in Li_xTiO_2, Na_xTiO_2 and Mg_xTiO_2, shown by our simulated microstructures, and observed in previous experimental and

simulated studies of Li_xTiO_2; which suggests possibility of easy and fast Li^+, Na^+ and Mg^{2+} ion passage in the current study. In the case of Li transport, for different nano-architectures, diffusion coefficients (DCs) for most Li concentrations were predominantly near zero at low temperatures and increased gradually above 500 K and significantly at higher temperatures beyond 1000 K. DCs of higher Li concentration nano-architectures tend to be highest. On the contrary, the diffusion coefficient of the amorphous $Li_{0.19}TiO_2$ nanosphere is elevated at low temperatures, however, it is exceeded by those of other concentrations at higher temperatures. On the whole the activation energies of Li in TiO_2 nanosphere, nanoporous and nanosheet structures, in appropriate temperature range, were consistent with observed transport properties. In particular, the lowest activation energy for the amorphous $Li_{0.19}TiO_2$ nanosphere concurs with non-zero DC at lower temperatures. On Na transport in various TiO_2 nano-architectures, DCs for most Na concentrations were predominantly near zero at low temperatures, except for the $Na_{0.23}TiO_2$ (associated explanation for such deviant behaviour is not yet available). Diffusion coefficients subsequently increased gradually above 500 K to substantial at higher temperatures, with DCs of higher Na concentrations in different nano-architectures tending to be highest; in particular the DC of the amorphous $Na_{0.19}TiO_2$ which was slightly higher than other crystalline Na_xTiO_2. The activation energy of the nanosphere with the highest Na concentration ($Na_{0.23}TiO_2$) was low, consistent with the trend of non-zero diffusion coefficients at low temperatures. The AEs of nanoporous structures at different Na contents were equivalent and related DCs almost overlap in the 500 to 1000 K range. In the case of nanosheets AEs are also almost equal for all Na_xTiO_2 with that of the $Na_{0.23}TiO_2$ (highest Na concentration) being highest resulting in a slightly lower diffusivity, except at very high temperatures. These results provide insights and an understanding on how much such TiO_2 nano-architectures can enable operations of sodium ion batteries. Non-zero diffusion coefficients of Mg^{2+} commenced at lower temperatures in nanospheres, especially those with lower Mg concentrations. Related activation energies were also relatively low and increased with Mg^{2+} concentrations. However, in the nanoporous and nanosheet architectures, the Mg^{2+} DCs were almost zero below 1000 K and increased significantly above 1200 K with DC being highest in the heavily intercalated nanostructures. The activation energies for the latter two nano-architectures were in the range of 0.400 eV which is higher than in nanospheres, but comparable to those of the nanoporous Li-MnO_2. Generally, on matching maximum diffusion coefficients of Li, Na and Mg mobile ions in TiO_2 nano-architectures, it is apparent that they are all highest in nanospheres with $DC_{Li} > DC_{Na} > DC_{Mg}$. On comparing magnitudes of DCs in different nano-architectures the following trend emerges; for the monovalent Li and Na mobile ions $DC_{Sphere} \sim 5DC_{Porous} \sim 3DC_{Sheet}$ and for the divalent Mg mobile ion $DC_{Sphere} \sim 2.5DC_{Porous} \sim 2.5DC_{Sheet}$. Such comparisons provide insights and an understanding on how much such TiO_2 nano-architectures can enable performance of various mobile ion rechargeable batteries.

Table of Contents

List of Figures

List of Tables

Chapter 1

1. Introduction and Background

The use of intermittent renewable energy sources such as solar, wind, tidal, and geothermal, as well as the electrification of transportation systems, requires the use of high-performance electrical energy storage (EES) systems; therefore, research into material systems that can be used for EES are in high demand. The EES system must meet the following characteristics: [1] portable power supply for electric vehicles (EVs); [2] smart grid stations that provide affordable, secure, stationary storage of electrical energy generated from renewable but variable energy sources such as solar and wind [3] [4] [5]. Alkaline-ion batteries (AIBs), i.e., lithium-ion batteries (LIBs), sodium-ion batteries (SIBs), and magnesium-ion batteries, are considered the most promising approaches to address both challenges [6] [7] [8]. However, in order to be compatible with internal combustion engines and to be used in large-scale smart grid applications, the energy density and performance of metal ion batteries (MIBs) need to be improved to achieve the following goals 1. Acceptable range; 2. Shorter charging time for electric vehicles; 3. Rapid response to solar and wind energy fluctuations; and 4.Further reduction in cost [9].

In this context, the energy density and performance of commercial LIBs, research-based SIBs, and MIBs need to be improved to advance the search for alternative composite anode materials with high working voltage (potential difference between cathode and anode), high specific capacity, high performance, and, in particular, stability and capacity retention under extreme charging conditions, as has been suggested recently [10] [11] [12] to complement the current commercially available batteries. In this thesis, the research study focus is on simulation synthesis of Li_xTiO_2, Na_xTiO_2, Mg_xTiO_2 nanosphere, nanoporous and nanosheets architectured materials simulated using molecular dynamics technique at atomistic scale to be considered one of the excellent anode electrode materials utilised in LIBs, SIBs and MIBs for energy storage applications. In this chapter introduction and background discussion of TiO_2 ion-intercalated nano-architectured structures in lithium-ion batteries, sodium ion batteries and magnesium ion batteries applications along with the description of the operating principle of rechargeable batteries then followed by literature review of TiO_2 nano-architectured materials and the research problem of this study, lastly the outline of the entire thesis will be summarized.

1.1. Overview

Nanostructured TiO_2 is a promising material for large-scale Li^+ intercalated energy storage systems and has been investigated as an anode electrode material in lithium-ion batteries using other experimental techniques but has not been fully explored using atomistic modelling techniques [13]. The storage capacity and stability of these anodes strongly depend on the structural morphology (microstructure), crystalline phases, and rapid Li^+ transport within TiO_2 nanostructures [14]. The mechanism for the incorporation of Li into TiO_2 has been investigated, and the crystalline phases of Li_xTiO_2 have been identified but not fully explored [15]. Although further work to improve Li storage capacity and long-term thermal stability through charging and recharging processes is critical, the physiochemistry of lithium intercalation in TiO_2 has

been fairly well explored and implemented [16] [24].The widely commercialized Li-ion batteries are slowly becoming costly due to their demanding requirements and economic fluctuations, hence countless safety challenges of Li-ion batteries have led the studies for other rechargeable batteries with similar chemistries. Na-ion and Mg-ion batteries are two of the promising alternatives in this regard, as they are generally safer and less expensive compared to Li-ion batteries [17] [18]. Many electrode materials used in Li-ion batteries are also promising for Na-ion and Mg-ion batteries [19], and TiO_2 structures with nanostructure have great potential in this field [20] [21] [22]. There are several stable or metastable polymorphs of TiO_2; two of particular interest are rutile and the brookite phase (TiO_2 (B)). The rutile structure has straight channels, while brookite has zigzag channels, both of which should facilitate ion intercalation [13]; frameworks with open pores and channels generally confirms to be excellent host lattices for Na and Mg, as has been shown for Ti and other transition metal-based polyionic materials [23] [24]. TiO_2 (B) has a lower density than rutile and therefore may have a greater capacity for Na^+ and Mg^{2+}. Furthermore, anatase is more stable thermodynamically [14], and therefore can withstand repeated cycling better. Crystal structure alone is not sufficient to determine battery performance; morphology, i.e., microstructures, and rapid ion transport, i.e., electrode diffusion coefficients and activation energies, also play important roles [24]. TiO_2 nanostructures can undergo different phase transformations depending on the simulation temperature and pressure.

1.2. Lithium-ion Batteries

Titanium dioxide (TiO_2) has been studied in different research filed, mostly in energy related devices [25] [26]. Its unique physical-chemical properties are appropriate for utilisation in energy harvesting systems such as photo catalysts, water splitting devices, and dye-sensitized solar cells [27]. Outstanding research as anode material for lithium-ion batteries has also been focused on its application, due to its abundance, low cost and excellent structural ability when lithiated [28] [29]. Moreover, it has a high working voltage of more than 1.5 V vs. Li which allows stable operation without forming any solid electrolyte interface during decomposition of liquid electrolyte at low potential and extremely high-rate operation to prevent lithium plating on the electrode [30]. The TiO_2 nanostructure is a typical Li^+, Na^+ and Mg^{2+} intercalation compound. The M=Li^+, Na^+ and Mg^{2+} ion intercalation–deintercalation reaction in TiO_2 nanostructures can be described as follows:

$$TiO_2 + MLi^+ + Xe^{-1} = M_XTiO_2, (0 \leq X \leq 1) \quad 1.1$$

where X is the mole fraction of M = Li^+, Na^+ and Mg^{2+} in TiO_2. The theoretical capacity of Li was found to be 335 mA h g^{-1} at X =1, but the maximum value of the mole fraction of Li insertion is limited to X = 0.5, which is equivalent to the theoretical capacity of 167.5 mA h g^{-1} [31] [32]. Li^+ has low specific capacity when compared to the commercially adopted graphite but is still a potential material for large scale storage systems due to its safe operation. However, its slow kinetics and intrinsically poor electronic conductivity restrain its practical use [33] [30]. Sustainable research has been devoted to improve the electrochemical properties of TiO_2 nanostructures-based electrode materials by enhancing lithium-ion kinetics and its electronic conductivity. There three main properties dominating the rate capability of TiO_2 anode materials are (1) the electrode electronic conductivity (film), (2) Li-ion kinetics (transportation) and

(3) the electronic contact between the active material and metallic current collector. The electronic conductivity in the electrode (film) can be improved by engineering its microstructure via intrinsic defects. The improvement of intrinsic electronic conductivity of TiO_2 and (or) the introduction of highly conducting materials [33] is of fundamental.

Zero-dimensional (0D), One-dimensional (1D), two-dimensional (2D) and three-dimensional (3D) TiO_2 nanostructures are intensively explored to upgrade the rate performance [24] [26] [34] of rechargeable batteries. However, these dimensional structures allow smooth electron diffusion through dimensional networks, while the performance is mostly affected by electrical conductivity of TiO_2 [35]. Therefore, improving electronic conductivity of TiO_2 without introducing heavy metals or Li in active functional materials become highly critical for its practical use. TiO_2 nanostructures has the capability to improve the Li ion kinetics by reducing its diffusion length and increasing its flux at the interface connecting the active TiO_2 material and the electrolyte.

Since TiO_2 nanostructures allows better Li-ion kinetics along other possibilities to function better TiO_2 nanostructures electrode electrochemically, the tap density will sufficiently reduce [36]. Low tap density is important in the practical use of TiO_2 based electrodes because of its low specific capacity and high operating voltage over 1 V [31]. The energy barrier at the interface between the active material and the electrolyte must be higher than that for the bulk diffusion, to enabling Li insertion on the surface which can then improve the battery rate performance [24][37]. The specific plane In TiO_2 nanomaterials allow fast interfacial charge transfer. Hence, the Li ion kinetics could be improved by engineering the crystallinity patterns of the material through crystallisation, cooling, and heating synthesis on the systems. TiO_2 nanostructures could significantly reduce the Li ion diffusion length and increase the Li ion flux at the interface [35][37]. Specifically, the nanosized TiO_2 material enables the improvement in Li ion kinetics without significant loss in tap density . The demand of improving Li_xTiO_2 nanostructured anode electrode materials with highly crystalline polymorphs to direct very fast Li ion transportation at low and high exposed temperatures conditions without structural deformations are highly required hence nanospheres, nanoporous and nanosheets structures are proposed.

1.3. Sodium-ion batteries

The sodium-ion battery (NIB) is a type of rechargeable battery analogous to the lithium-ion battery but using sodium ions (Na^+) as the charge carriers. Its working principle and cell construction are almost identical with those of commercially widespread lithium-ion battery types, but sodium compounds are used instead of lithium compounds. Sodium-ion batteries have received much academic and commercial interest in the 2010s and 2020s as a possible complementary technology to lithium-ion batteries, largely due to the uneven geographic distribution, high environmental impact, and high cost of many of the elements required for lithium-ion batteries. Chief among these are lithium, cobalt, copper, and nickel, which are not strictly required for many types of sodium-ion batteries [36]. The largest advantage of sodium-ion batteries is the high natural abundance of sodium. This would make commercial production of sodium-ion batteries less costly than lithium-ion batteries [37]. NIBs have attracted increasing attention for large-scale energy storage applications because of the natural abundance and low cost of sodium resources [38]

[39] [40]. Na has a larger ionic radius (0.97Å) and higher redox potential (-2.71 V vs. SHE) than Li, and the interactions between Na ions and the host crystal structures can vary greatly from those of their Li analogues [41], which is why Na-intercalation in compounds is often very different from the behaviour of the Li-analogues [38] [39] [40]. The anode material most applied in Li-ion batteries is graphite, for which Na-ion intercalation is not thermodynamically favourable [39]. Currently, reports on applicable anode materials for Na-ion batteries are limited in the literature [38] [40] [41], as summarized in Fig. 1. Hard carbon exhibits a reversible capacity of 240 mA h g^{-1} with stable cycle performance in a $NaClO_4$/ EC: DEC electrolyte [42]. However, its density is very low, and most of the usable capacity is located near the sodium plating voltage, leading to potential safety concerns. Alloys such as Sn and Sb have been shown to exhibit very high storage capacities (~600 mA h g-1); however, undesired large volume changes during sodium insertion and extraction make it challenging to attain satisfactory cyclability without the use of special binders and electrolyte additives, and to achieve effective energy density [43].

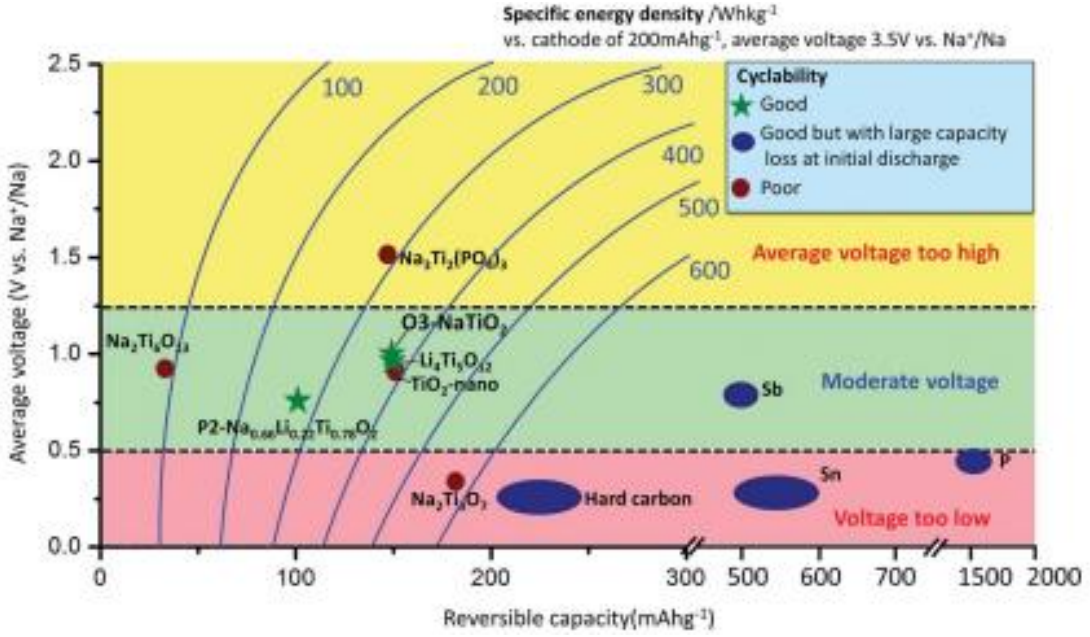

Figure 1.1: Illustrates the average voltage versus the reversible capacity for different anode materials for Na-ion batteries. Specific energy densities of constant lines are also indicated, suggesting a cathode of 200 mA h g^{-1} at 3.5 V average voltage. The specific energy density calculated from full cells within balanced weight of anode and cathode [44].

Furthermore, alloy anodes were found to suffer from large capacity losses (150–500 $mAhg^{-}1$) during initial sodiation while oxides have also been explored as potential electrode candidates for Na ion batteries [44]. The initial capacity of $Na_2Ti_3O_7$ is more than 200 $mAhg^{-1}$; however, its cycling performance is not that sufficient [45] [46]. Whereas the $Li_4Ti_5O_{12}$ can deliver a reversible capacity of 155 $mAhg^{-1}$ in a displacement reaction with Na and shows good cyclability using carboxymethyl-cellulose as the binder [47]. On the other hand a new anode material of P_2-$Na_{0.66}$-$[Li_{0.22}Ti_{0.78}]O_2$, exhibits excellent cyclability partly due to its negligible volume change (0.77%) during sodium insertion and extraction; even though, the usable capacity is limited to 100 $mAhg^{-1}$ which corresponds to 1/3 Na per formula unit [48]. Research

on layered $NaMO_2$-type oxides (M ¼ 3d transition metal, such as Ti, V, Cr, Mn, Fe, Co, Ni) as intercalation electrode materials was initially commenced in 1980s but has received renewed interest recently [49].

The use of advanced electrolytes has demonstrated reinvestigation of $NaMnO_2$ and $NaNiO_2$ compounds indicating reversibly exchange approximately of 0.8 Na and 0.5 Na [50] [51], respectively. Noticeably these are larger than the previous results reported in the 1980s [52] [53]. Consequently, Mazzaz et al examined electrochemical performance of $NaTiO_2$ [52] as a potential anode intercalation material same year when the $NaMnO_2$ and $NaNiO_2$ was restudied. Even though limited cyclable capacity corresponding to z0.3 Na was reported. Recent DFT calculation hinted at an unusually high barrier of 0.75 eV for Na migration in $NaTiO_2$, [48] which could prevent intercalation at any reasonable rate. In 2020, sodium ion batteries had a small share within the battery market hence this technology was not mentioned in report by South Africa and the United States Energy Information Administration on battery storage technologies [54]. Hence, no electric vehicles use sodium ion batteries. The challenges to adoption include low energy density and a limited number of charge-discharge cycles [55] .

1.4. Magnesium-ion batteries

Magnesium batteries are an alternative to those using lithium ion and sodium chemistry, are attractive for portable applications, potentially offering comparative or improved specific capacities to current Li-ion technology, and significant advances in volumetric capacity [56] [57] [58]. Lithium metal anodes grow dendrites upon cycling, which ultimately lead to battery short circuiting [59]. To avoid this issue, graphite is used as an intercalation host at the anode for Li-ion batteries, but this limits the volumetric capacity to 800 mA h cm^{-3}. Magnesium metal anodes plate more uniformly upon cycling [60] , and thus the intercalation host can be avoided at the anode end, enabling a volumetric capacity of 3833 mA h cm^{-3} for Mg metal. Mg is heavier and less electropositive than Li and Na, but these deficits are compensated by its divalency and the reduced weight of a battery design that avoids the anode intercalation host, indicating that a specific capacities of Mg battery systems can approach or exceed those of Li-ion batteries using a graphite anode [57].

Magnesium is also inherently safer than lithium-ion battery systems, and is far more abundant and cheaper than lithium, making it a more scalable technology for future energy storage solutions. Issues finding Mg battery electrolytes compatible with both electrodes remain [58], however a key bottleneck in the development of Mg batteries is the search for a suitable cathode material [56]. The intercalation of divalent ions presents several challenges compared to those of monovalent ions. Multivalent cathode materials are more prone to conversion reactions, and this is a particular issue for Mg due to the high thermodynamic stability of MgO [61]. Divalent Mg ions also experience a stronger electrostatic interaction with the anionic framework of the cathode host than Li ions, so despite their similar size, Mg ions typically experience significantly higher activation barriers for movement, leading to poor kinetics [62]. Therefore, the options available for suitable cathode materials are limited. The pioneering work of Aurbach first demonstrated that Mg battery chemistry was possible,

yet the Chevrel phase Mo_6S_8 cathode used offered a limited voltage [63]. Since this work, extensive experimental and computational work has investigated materials that may be suitable for Mg intercalation cathodes, often motivated by their known performance as Li-ion intercalation hosts [57] . One of the materials that has been the subject of numerous studies as Li intercalation host is TiO_2 [64] [65] [66]. Although they do not offer high operating voltages, the titania anatase [67] and TiO_2 (B) [68] polymorphs show good rate performance for Li intercalation, making them attractive for high power applications. Anatase TiO_2 has also been explored as a possible cathode material for Na-ion batteries [69]. As an Mg-battery cathode, intercalation to $Mg_{0.5}TiO_2$ provides a high theoretical capacity of 294.5 mA h g^{-1}. Furthermore, the anatase TiO_2 displays excellent stability, low toxicity, and high abundance hence an attractive sustainable battery material .

1.5. Applications

The large oxidizing power of photogenerated holes in TiO_2 together with the low cost and good physical and chemical stability of the material render it the semiconducting material of choice for many applications. Many promising technologies in the field of energy generation accumulation and saving as well as environmental decontaminations as illustrated in Figure 1.2, are based on TiO_2 nanoarchitectured materials, hence the discussions in this thesis will be based on these fields.

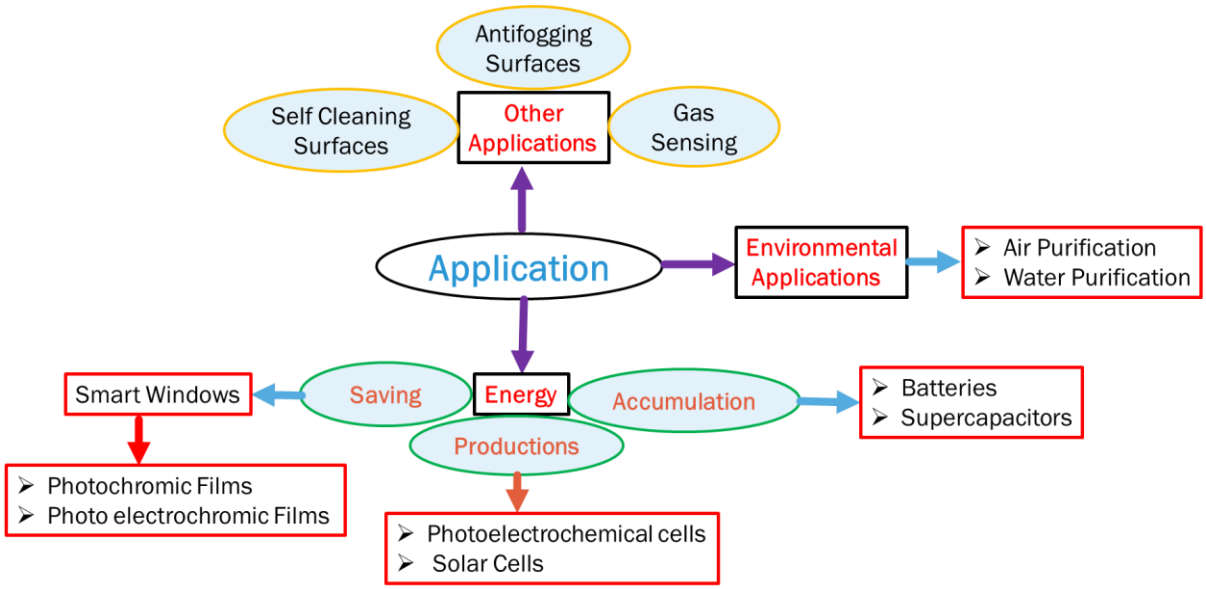

Figure 1.2: Field of applications of TiO_2 nanomaterials directly and indirectly related to their electrochemical properties.

1.5.1. Energy Accumulation

The high specific energy and power available from commercialized Li-ion batteries to research-based Na-ion and Mg-ion batteries with the ability to charge/discharge them many times are of key importance in electronic portable devices, the current and future developments of hybrid electric vehicles [70] [100]. Metal ion batteries are composed of cells that employ cation intercalation compounds as positive and negative electrode (Figure 1.3) [71] . Most commercial batteries i.e., lithium-ion batteries use graphite as

the anode materials (negative electrode), despite its utilisation graphite electrodes have some disadvantages, such as the loss of its initial capacity due to it structural deformation. To avoid these imperfections, in the past decades there has been increasing interest in developing new anode electrode materials with enhanced kinetics [72]. All crystalline phases of TiO_2 (anatase, rutile, brookite, and TiO_2 (B)) can accommodate Li^+, Na^+, Mg^{2+} in their structures to some extent. The accommodation capacity depends on the size of the particles [73] [74]. Kinetic limitations are responsible for the differences between micro- and nanosized TiO_2 [75] [76]. The latter materials are beneficial for these applications because they provide a large electrode/electrolyte interface, which favours fast insertion/extraction [77] [78] [79].

Another crucial characteristic of TiO_2 for applications in Metal-ion batteries in addition to particle size is its interstitial defects through microstructural properties. In our previous study we have studied and explored lithiation into bulk, nanosphere, nanoporous, and nanosheets TiO_2 systems to find more structural and microstructural stability insights influenced by Li-ion concentration and simulation temperature between 0 K and 500 K [24]. Their improved performance in comparisons with other nanoarchitectures can be ascribed to shorter diffusion lengths for the electrons and metal ions.

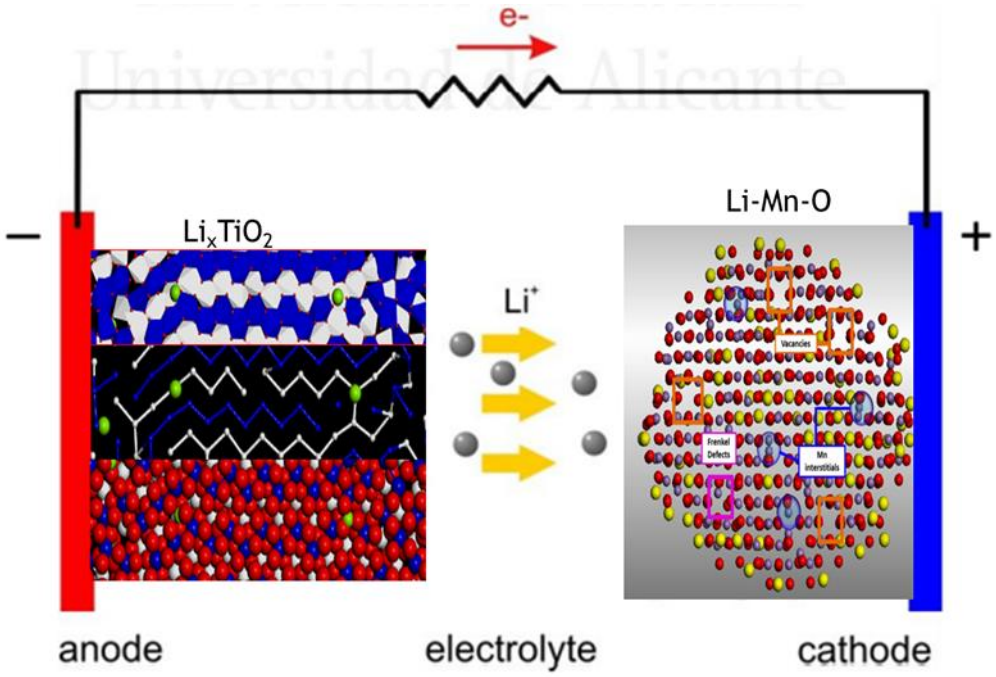

Figure 1.3: Illustrate lithium-ion cell during discharge.

1.5.2. Saving Energy

The use of TiO_2 nanomaterials in the development of electrochromic and photochromic layers with fast responses and high coloration efficiency has been explored in the literature [80] [110]. Electrochromic can be defined as the ability of a material to undergo a colour change upon oxidation or reduction. Almost all transition metal oxides are electrochromic [81]. These materials have been extensively investigated due to their potential application in practical devices [80] [82]. The

mechanism of electrochromic as in the case of the intercalation batteries, is the double injection of electrons and ions into the oxide matrix (Eq.1.2) [83]:

$$TiO_2 + x(M^+ + e^-) \leftrightarrow M_xTiO_2 \qquad 1.2$$

Where M^+ can be either Li^+ or Na^+ (x is the insertion coefficient, whose effective value depends on the micro- and nanostructure of the electrode). During charge injection, electrons are localised at the titanium sites, thereby changing the valence of Ti ions from 4 to 3. The Ti^{3+} ions formed lead to additional electronic states in the TiO_2 located at 0.75-1.18eV below the edge position of the conduction band edge position on the electrode potential scale, triggering light absorption in the visible range. Reaction 1.2 is reversible, that is upon applying anodic potential to the TiO_2 electrode in the inserted ions are expelled and Ti^{3+} ions are oxidized again to Ti^{4+}.The insertion/extraction of M^+ during reduction/oxidation the associated coloration/bleaching of the thin film is depicted in Figure 1.4.

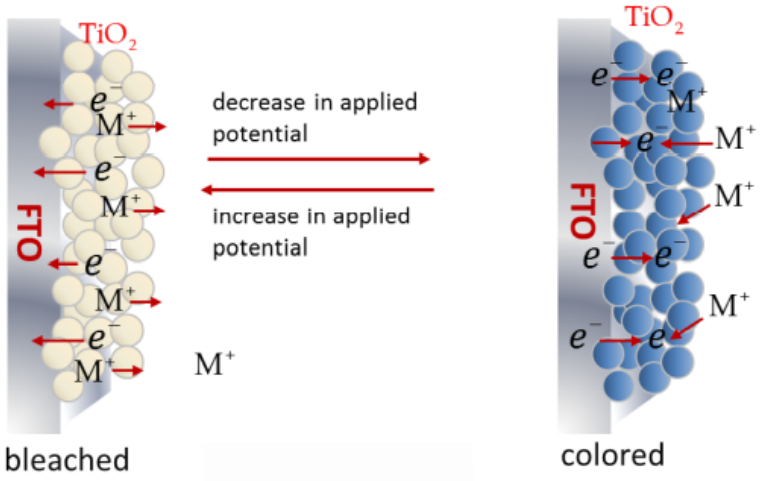

Figure 1.4: Illustrates the working principle scheme of electrochromic TiO_2 nanoporous thin films. M^+ can either be Li^+ or Na^+ [82][84].

The electrochromic properties of different nanomaterials can be compared by performing spectroelectrochemical measurements. Electrochromic parameters such as the counter electrode, cyclic durability and the kinetics of the coloration and bleaching processes strongly depend on structural, morphological and composition characteristics and therefore on the technique employed for the preparation of the electrode [84]. As reversible ion intercalation is typically limited to a very thin metal oxide layer, to achieve a substantial contrast, a high surface area is required [85] [86].

1.6. Battery Operations

The battery lifespan can be influenced by knowing what factors can be improved to mitigate the battery capacity loss through achieving optimal battery efficiency. During discharge, ions (Li^+, Na^+, Mg^{2+}) carry the current within the battery from the negative to the positive electrode, through the non-aqueous electrolyte and separator diaphragm [87]. During charging, an external electrical power source (the charging circuit) applies an over-voltage (a higher voltage than the battery produces, of the

same polarity), forcing a charging current to flow within the battery from the positive to the negative electrode, i.e., in the reverse direction of a discharge current under normal conditions. The ions then migrate from the positive to the negative electrode, where they become embedded in the porous electrode material in a process known as intercalation. Energy losses arising from electrical contact resistance at interfaces between electrode layers and in contacts with current collectors can be up to 20% of the entire energy flow of batteries under typical operating conditions [88].
The charging procedures for single Metal-ion cells, and complete Metal-ion batteries, are slightly different:

- A single metal-ion cells is charged in two stages [89] [90]:
  1. Constant current (CC).
  2. Constant voltage (CV).
- A metal-ion battery (a set of metal-ion cells in series) is charged in three stages:
  1. Constant current.
  2. Balance (not required once a battery is balanced).
  3. Constant voltage.

During the constant current phase, the charger applies a constant current to the battery at a steadily increasing voltage until the voltage limit per cell is reached. During the balance phase, the charger reduces the charging current (or cycles the charging on and off to reduce the average current), while the state of charge of individual cells is brought to the same level by a balancing circuit, until the battery is balanced. Some fast chargers skip this stage. Some chargers accomplish the balance by charging each cell independently. During the constant voltage phase, the charger applies a voltage equal to the maximum cell voltage times the number of cells in series to the battery, as the current gradually declines towards 0, until the current is below a set threshold of about 3% of initial constant charge current. Periodic topping charge about once per 500 hours. Top charging is recommended to be initiated when voltage goes below 4.05 V/cell.

Failure to follow current and voltage limitations can result in an explosion [91] [92]. Charging temperature limits for Li-ion are stricter than the operating limits. Lithium-ion chemistry performs well at elevated temperatures but prolonged exposure to heat reduces battery life. Metal-ion batteries mostly commercialised Li-ion batteries offer good charging performance at cooler temperatures and may even allow 'fast-charging' within a temperature range of 5 to 45 °C (278.15 K to 318.15 K) [124]. Charging should be performed within this temperature range. At temperatures from 0 to 5 °C charging is possible, but the charge current should be reduced. During a low-temperature charge, the slight temperature rise above ambient due to the internal cell resistance is beneficial. High temperatures during charging may lead to battery degradation and charging at temperatures above 45 °C will degrade battery performance, whereas at lower temperatures the internal resistance of the battery may increase, resulting in slower charging and thus longer charging times [93].Consumer-grade lithium-ion batteries should not be charged at temperatures below 0 °C (273.15 K). Although a

battery pack [94] may appear to be charging normally, electroplating of metallic lithium can occur at the negative electrode during a subfreezing charge, and may not be removable even by repeated cycling. Most devices equipped with Li-ion batteries do not allow charging outside of 0-45 °C for safety reasons, except for mobile phones that may allow some degree of charging when they detect an emergency call in progress [95].

Batteries gradually self-discharge even if not connected and delivering current. Li-ion rechargeable batteries have a self-discharge rate typically stated by manufacturers to be 1.5–2% per month [96] [97]. The rate increases with temperature and state of charge. A 2004 study found that for most cycling conditions self-discharge was primarily time-dependent; however, after several months of stand on open circuit or float charge, state-of-charge dependent losses became significant. The self-discharge rate did not increase monotonically with state-of-charge but dropped somewhat at intermediate states of charge [98]. Self-discharge rates may increase as batteries age [99]. In 1999, self-discharge per month was measured at 8% at 21 °C, 15% at 40 °C, 31% at 60 °C [100] . By 2007, the monthly self-discharge rate was estimated at 2% to 3% [101], and 2-3% by 2016 [102].

Different Conditions including battery age, temperature, state of charge (SOC), and Depth of discharge (DOD) all have different effects on a battery's lifespan as the result of battery calendar-life loss and cycle-life loss through charging and discharging processes [103]. Different environmental factors which affect battery life during battery storage, as well as cycling conditions during usage, are discussed below.

1.6.1. During storage

1) Temperature

Temperature is one of the major contributions of battery capacity loss during storage. High temperatures cause thermal decomposition of the electrodes and electrolyte. Decomposition of the electrolyte increases the solid electrolyte interface (SEI) film thickness on the anode consuming ions which then increases the cell internal resistance (IR) and reduces battery capacity. In addition, gases are formed during the decomposition, which increases the internal pressure in the cell and poses safety issues. Table 1 shows percentage of Li-ion batteries' capacity lost in one year when stored at different temperatures [104]. The Li-ion batteries were stored under the same SOC (40%). The higher the temperature, the more the batteries degrade. In addition, Table 1 also shows that extreme temperature significantly accelerates the capacity loss. The 25 degrees increase from 273.15 K to 298.15 K only caused 2% more capacity loss, while the 20 K increase from 313.15 K to 333.15K caused 10% more capacity loss.

Temperature (K)	40% charge	100% charge
273.15 (0 ^{o}C)	98% (after 1 year)	94% (after 1 year)
298.15 (25 ^{o}C)	96 (after 1 year)	80 % (after 1 year)
313.15 (40 ^{o}C)	85% (after 1 year)	65% (after 1 year)
333.15 (60 ^{o}C)	75% (after 1 year)	60% (after 3 months)

Table 1: Estimated recoverable capacity when storing Li-ion batteries at various temperatures and SOC [135]

For metal-ion batteries, temperatures above 303.15 K are considered stressful environments and can cause significant battery calendar-life loss [104]. It is recommended to store Li-ion batteries at temperatures between 278.15 K and 293.15 K to prolong battery life [104].

2) State of Charge (SOC

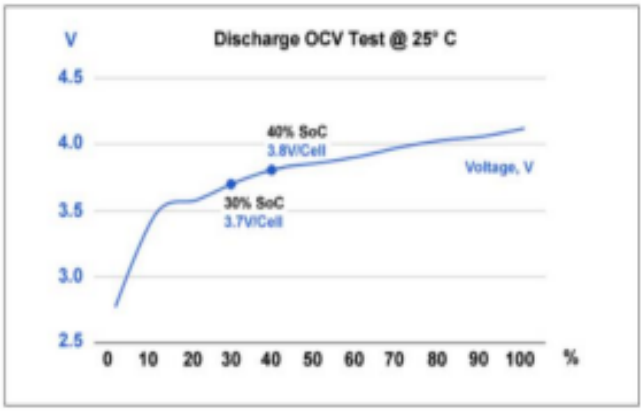

Figure 1.5: illustrates discharge voltage as a function of SOC [135]

For Li-ion batteries, open circuit voltage (OCV) increases with SOC, as shown in Figure 1.5. During storage, the higher battery SOC, the higher the battery OCV. However, high OCV can increase SEI growth and initiate electrolyte oxidation inside Li-ion batteries, which causes capacity loss and increase of IR. Figure 1.6 shows different Li-ion battery degradation rates at various SOCs during a ten-year period of storage. The remaining capacity of Li-ion batteries decreases faster as the SOC level increases [105].

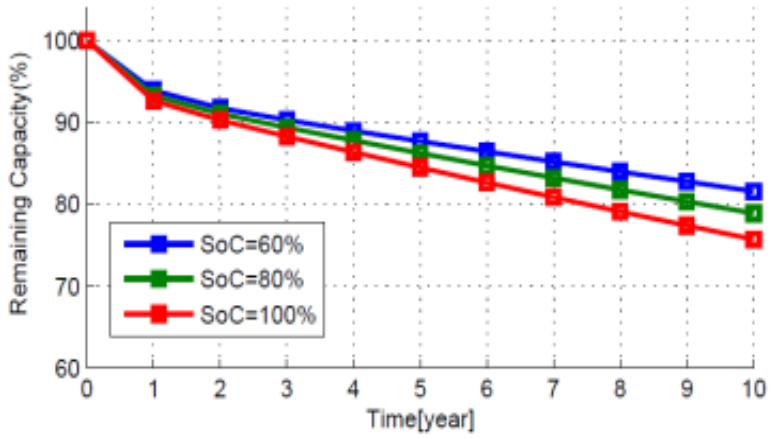

Figure 1.6: Calendar aging with varying SOC at 25 Celsius [105]

Table 1 also includes SOC as a variable, which shows that the Li-ion batteries that were stored at 100% SOC retained significantly less capacity than the ones stored at 40% SOC. However, a SOC lower than a certain level increases the battery IR and capacity fading [106]. Extremely low OCV (< 2V/cell) results in slow degradation of $LiCoO_2$ and $LiMn_2O_4$ batteries, oxygen release and irreversible capacity loss [107]. Thus, maintaining Li-ion batteries at an intermediate SOC level can reduce battery degradation and prolong battery life. Li-ion batteries are recommended to charge or discharge them to approximately 50% SOC before storage [103].

1.6.2. During cycling

1). Temperature

Increased temperature during battery operation can improve battery performance. For example, warming a dying battery in a smartphone in one's pocket might provide additional runtime due to improved electrochemical reaction. Manufacturers specify the nominal temperature at 300.15 K to prolong the battery runtime while prolonged cycling under high temperature shortens battery life. A battery operated at 303.15 K has a 36 reduced cycle life by 20%. At 318.15 K, the battery only has half of its optimal lifetime, which can be achieved when operating at 293.15 K [108]. Extremely low temperatures increase the battery IR and decrease significant amount of discharge capacity. A battery that provides 100 % capacity at 300.15 K will typically deliver only 50% capacity at 255.15 K [108]. Figure 1.7 shows the variations of the discharge capacity of a lithium polymer cell when discharged from 4.2 V to 3.0 V at different temperatures [109].

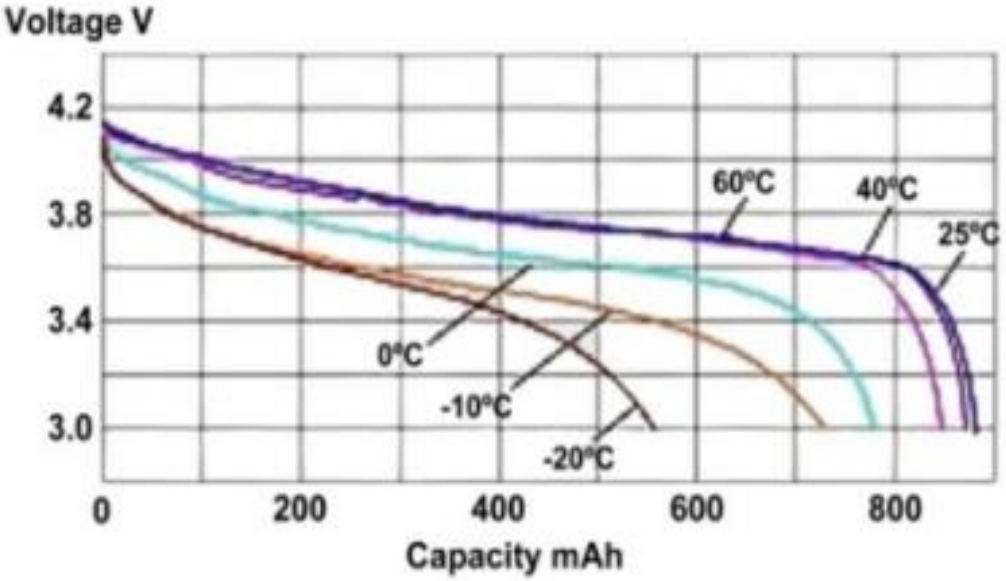

Figure 1.7: Battery discharge capacity at various temperatures [140]

The batteries' capacity at low temperatures (0°C, - 10°C, -20°C) are lower than the ones at higher temperature (25°C, 40°C, 60°C). In addition, charging Li-ion batteries at low temperatures (below 15°C) leads to lithium plating due to the slow-down of the intercalation of lithium ions. This process accelerates the degradation of Li-ion batteries by increasing the internal resistance (IR) and decreasing battery discharge capacity of the battery [108]. Thus, moderate operating temperatures are recommended to improve Li-ion battery performance and useful life. A temperature of 20° C or slightly below is recommended for Li-ion batteries to achieve optimum service life. However, manufacturers recommended a temperature of 27°C, for maximum battery runtime [108].

2. Depth of discharge (DOD)

DOD has a dominant effect on the cycle life of metal-ion batteries. Deep discharges cause pressure in battery cells and damage negative electrode cites, which accelerates capacity loss and possible cell damage. As shown in Figure 1.8, the higher the cycling DOD, the shorter the battery cycle life.

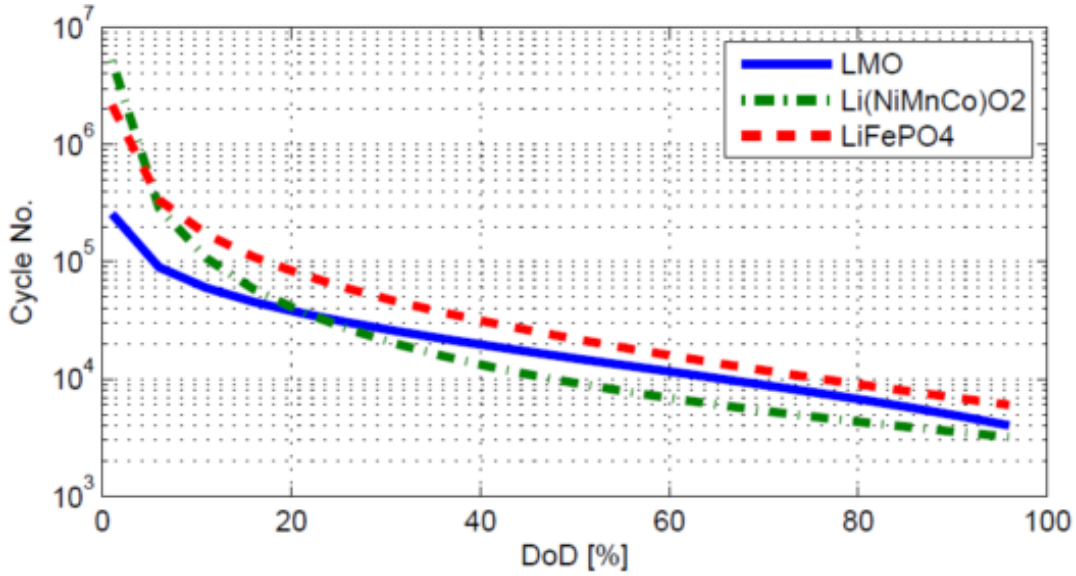

Figure 1.8: Li-ion battery cycle number vs. DOD [105].

DODs greater than 50% are considered deep discharge. When a Li-ion battery is discharged from 4.2V to 3.0 V, roughly 95% of its energy is spent, and continued cycling will result in the shortest battery life. Full discharge should be avoided during Lithium-ion battery cycling to reduce capacity loss. Partially discharging and charging Li-ion batteries is recommended to prolong battery life. Manufacturers often use the 80% DOD formula to rate a battery, which means that only 80% of the input energy is delivered during battery use and another 20% is reserved to achieve a longer battery service life. However, even though decreasing DOD can prolong Li-ion battery cycle life, too low a DOD can lead to insufficient battery runtime and then ability to finish certain tasks. Around 50% DOD is recommended during usage of Li-ion batteries to achieve maximum lifespan, as well as to provide optimal battery service time; hence the same must apply on both sodium ion batteries and magnesium ion batteries.

3) Charge voltage

High charge voltage gives metal-ion batteries high capacity and enables prolonged battery runtime. However, it is not recommended to fully charge metal-ion batteries. Charging Li-ion batteries above 4.1V/cell leads to lithium plating, which increases the loss of lithium ions as they form metallic lithium on the anode. This process not only decreases battery capacity, but also might lead to internal short circuits and cause fires. Figure 1.9 shows metal-ion batteries capacity degradation under high charge voltages (> 4.2 V/cell). The higher the charge voltage, the faster the capacity degrades and the shorter the cycle life.

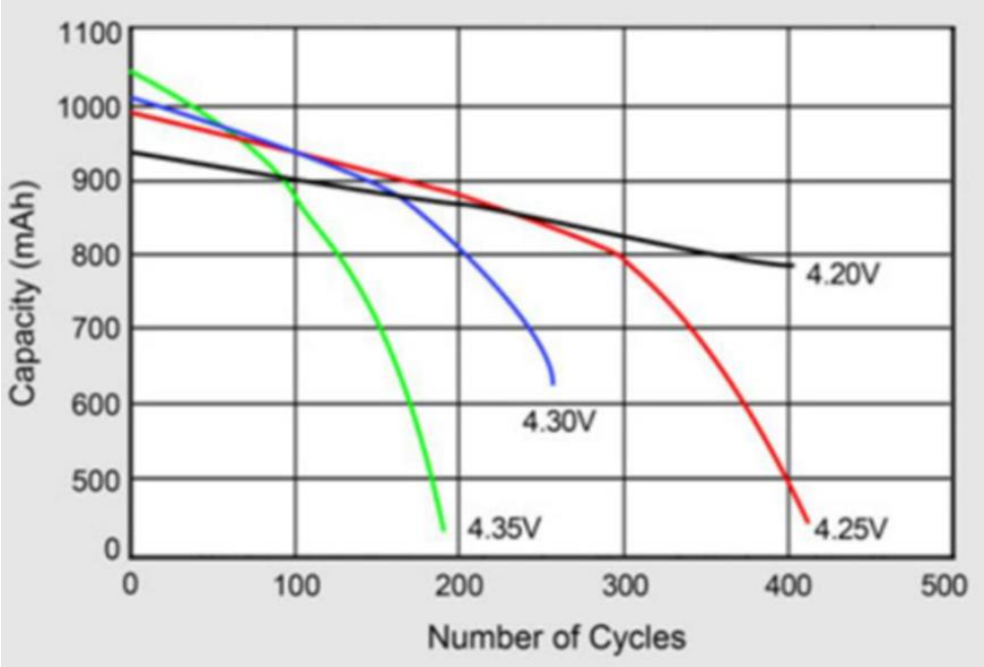

Figure 1.9: Effects on cycle life at elevated charge voltages [109].

Table 2 shows that among charge levels from 3.70V- 4.30V, 4.20 V is the charge voltage level at which batteries gain the most capacity (100%) under Li-ion battery safety specifications. Every 70 mV reduction in charge voltage lowers the overall capacity by approximately 10% [104]. Table 2 also shows the shortened cycle life because of the high charge voltage. The cycle life at the charge voltage of 3.90 V is the longest (2400-4000) among charge levels from 3.90V- 4.30V and is reduced to half with every increase of 0.10V in charge voltage.

Charge Level (V/cell)	Discharge cycles	Available Stored Energy
[4.30]	[150-250]	[110-115%]
4.25	200-350	105-110%
4.20	**300-500**	**100%**
4.15	400-700	90-95
4.10	600-1000	85-90%
4.05	850-1500	80-85%
4.00	1200-2000	70-75%
3.90	2400-4000	60-65%
3.80	See note	34-40%
3.70	See note	30% and less

Table 2: Discharge cycles and capacity as a function of charge voltage limit [104].

For most Li-ion batteries, a voltage above 4.10V is considered a high voltage and significantly accelerates battery degradation. Lower charge voltage prolongs battery life but provides less runtime for the user. Moreover, Li-ion batteries should avoid

discharge below 2.5V/cell. Optimal charge voltage is 3.92V, which allows the batteries to achieve longest cycle life [104]. Electronic products such as laptops and cell phones usually have a high voltage threshold to achieve maximum battery runtime. Large energy storage systems for more expensive applications such as EV or satellites, on the other hand, set the voltage threshold lower to prolong battery life. However in both cases, it is important not to overcharge Li-ion batteries, which will damage them, significantly shorten battery life, and potentially cause fires or explosions.

1.7. Literature Review

Electric motors are now used as an alternative power source for combustion engines with a fuel tank; (plug-in hybrid) electric vehicles equipped with large-scale LIBs as power sources have been introduced to the automotive market, which could reduce the energy dependence on fossil fuels for a transportation system in the future. The energy of a battery module is increased to 5000−20 000 Wh for (plug-in hybrid) electric vehicles (EVs). To reduce the battery cost, high-energy cobalt-based materials as positive electrodes cannot be used for large-scale application. In addition, recently, the demand for advanced energy storage technology is rapidly emerging throughout the world. A large-scale energy storage system for the grid is necessary to utilize high efficiency electrical energy with and for peak shift operation [110].1 Indeed, some battery companies have already developed LIBs with megawatt hour (MWh) scale and plan to begin a demonstration test for electrical energy storage (EES). Such MWh-class batteries are also probably used to store electricity generated from solar cells and wind turbines as green and renewable energy resources. Lithium is widely distributed in the Earth's crust but is not considered as an abundant element [111]. The relative abundance of lithium in the Earth's crust is limited to be only 20 ppm as shown in Figure 1.10 [112]

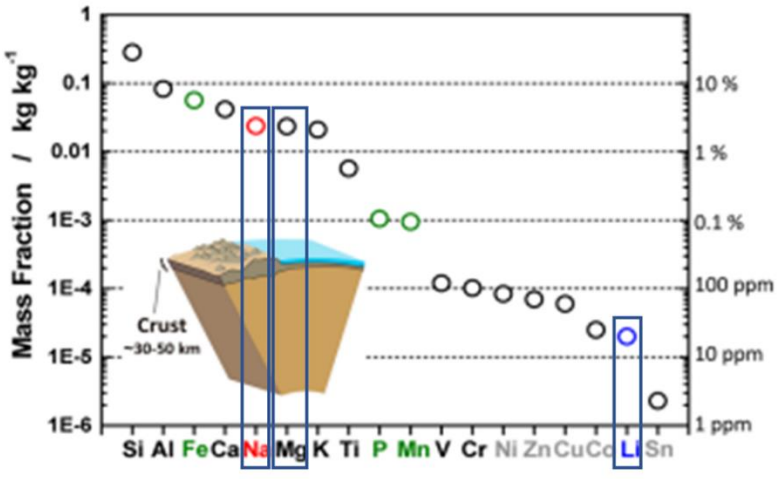

Figure 1.10: Elemental abundance in the Earth's crust [112].

Indeed, the materials cost (the price of Li_2CO_3) was steeply increased during the first decade of this century.4 Moreover, lithium resources are unevenly distributed in most countries; therefore, production of LIBs depends on the import of lithium from other countries. In contrast to lithium, sodium and magnesium resources are unlimited

everywhere, and they are one of the most abundant elements in the Earth's crust. Table 3. Based on material abundance and standard electrode potential, rechargeable sodium batteries and magnesium ion batteries are the ideal alternative to LIBs [113] [114] [38]. NIBs are operable at ambient temperature and metallic sodium is not used as the negative electrode, which is different from commercialized high temperature sodium-based technology, for example, Na/S batteries and $Na/NiCl_2$ batteries [115] [116].

	Li^+	Na^+	Mg^{2+}
Relative atomic Mass	6.94	23.00	24.31
Mass to electron ratio	6.94	23.00	12.16
Shannon's Ionic radii/Å	0.76	1.02	0.72
E^o (vs SHE)/V	-3.04	-2.71	-1.55
Melting Point/^{o}C	180.5	97.7	650.0
Theoretical Capacity of metal electrodes/$mAhg^{-1}$	3861	1166	2205
Theoretical Capacity of metal electrodes/$mAh\ cm^{-1}$	2062	1131	3837
Theoretical Capacity of ACoOH/$mAhg^{-1}$	274	235	260 as $Mg_{0.5}CoO_2$
Theoretical Capacity of ACoOH/$mAhcm^{-1}$	1378	1193	
Molar conductivity in $AClO_4$/PC/S/$cm^2\ mol^{-1}$	6.54	7.16	
Disolvation energy in PC/kJ mol^{-1}	218.0	157.3	572.3
Coordination preference	Octahedral and tetrahedral	Octahedral and prismatic	Octahedral and tetrahedral

Table 3: Illustrates physical properties of Li^+, Na^+, Mg^{2+} comparison as chargers for rechargeable batteries [117] [118] [119].

1.7.1. Structural Properties of TiO_2

Titanium dioxide (TiO_2) it is an important and widely used band gap (3.0-3.2 eV) oxide semiconductor, that presents unique physical and chemical properties that can satisfy the criteria of providing clean energy based on advanced nanomaterials [7] [28]. TiO_2 is an excellent candidate for anode electrode materials for lithium-ion batteries, sodium ion batteries, and magnesium-ion batteries [120], due to its ability to host higher concentrations of single valent (Li^+ and Na^+) and divalent cations (Mg^{2+}) and maintained its structural stability framework when exposed to lower (0 K) and higher (2000 K) temperature conditions. At least 11 reported bulk or nanocrystalline phases of TiO_2 have been reported. In nature, TiO_2 forms three main phases: rutile (tetragonal), anatase (tetragonal) and brookite (orthorhombic) [121]. All these TiO_2 phases can be seen as constructed by Ti-O octahedral units and the basic building block of the structures of a titanium atom surrounded by six oxygen atoms in a distorted TiO_6 octahedral configuration. The crystal models of the three polymorphs are illustrated Figure 1.11 [122]. The main structural differences are the connecting ways of the basic

Ti-O octahedral repetitive units; for instance, octahedral shares two, three, and four edges in rutile, brookite, and anatase polymorphs respectively. Under the conditions of normal temperature and atmospheric pressure, the relative stability of bulk polymorphs is rutile>brookite>anatase>TiO_2 (B) [123]. However, this stability order can be affected by ambient conditions and samples properties (particle size, morphology, surface state, etc). These TiO_2 polymorphs are distinguished by running X-ray diffraction analysis, microstructural view snapshots or electrochemical techniques where each phases have their specific applications. Therefore, this study was conducted to find more insights into phase transformation in TiO_2 nanosphere, nanoporous, and nanosheets architectures to improve phase stability throughout the atomistic simulation technique.

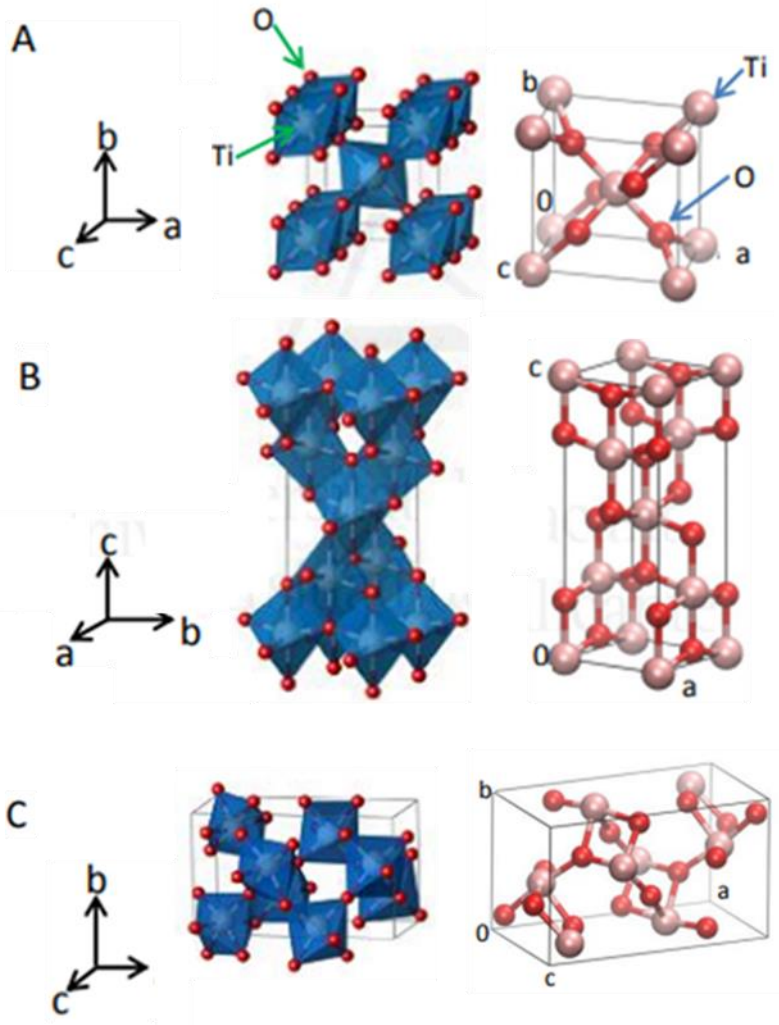

Figure 1.11: Indicates TiO_6 polyhedral of a (A) rutile, (B) anatase and (C) brookite. Right: a unit cell of the natural TiO_2 crystal phases. Adapted from ref [122] and [123]. The light red and dark red spheres are Ti^{4+} and O^{2-} ions, respectively.

Rutile is the most common mineral form of TiO_2 in nature. Its unit cell is tetragonal with one axis 30% shorter than the other two (a= 4.593Å, c= 2.959Å). The structure is constituted by distorted octahedral TiO_6 units with oxygen ions shared with other adjacent Ti ions. Every Ti ion is surrounded by six O ions and every O ion is surrounded by 3 Ti ions in a trigonal planar arrangement. Anatase presents a more

distorted structure, where every octahedral share 4 edges with the adjacent ones [121]. The size of the unit cell is given by a = 3.785 Å and c = 9.514 Å. The difference between anatase and rutile properties arises from structural differences between them that is the local structure of rutile is more regular with shorter metal-metal bond distances, thus being denser than anatase [124].

In recent years the interest in brookite has increased. Its structure is also composed of distorted octahedra that's share edges and corners among them. The size of this unit cell (orthorhombic) is given by a = 9.174Å, b = 5.449Å and c = 5.138Å. Because of differences in their lattice structure, rutile and anatase are characterised by different electronic band structures. In both cases, the VB states are derived from O 2p atomic orbitals, while the covalent bond mostly derived from Ti 3d orbitals [125]. Moreover, TiO_2 under normal conditions is thermodynamically stable as a non-stoichiometric compound, with anion (oxygen) deficiencies. Therefore, It can be denoted as TiO_{2-x}. Generally, the vacancies can introduce localised ionised states. In the case of TiO_2 oxygen vacancies are formally compensated by the adoption of +3 oxidation states by an equivalent number of titanium atoms. These Ti^{3+} ions behave as electron donors, introducing localised levels next to the CB, providing an n-type character to TiO_2.

The electronic structure of anatase is shown in Figure 1.12, and that of rutile in Figure 1.13. The relevant states of TiO_2 results from the combination of Ti e_g, Ti t_{2g}, O P_σ and O 2p z. The VB can be decomposed into three-main regions that resulting from Ti 3d – O 2p σ (P_σ orbitals) bonding states (low energy region), that resulting from Ti 3d-O 2p π bonding in the middle energy region and resulting of O Px orbitals in the higher energy region due to O Px nonbonding orbitals at the top of the valence band. For both anatase and rutile, the VB is around 6eV wide. The CB for both structures is composed of the Ti e_g and t_{2g} bands. The d_{xy} states in the case of anatase are located at the bottom of the CB, while in the case of rutile, the bottom of the CB is composed of π antibonding MO.

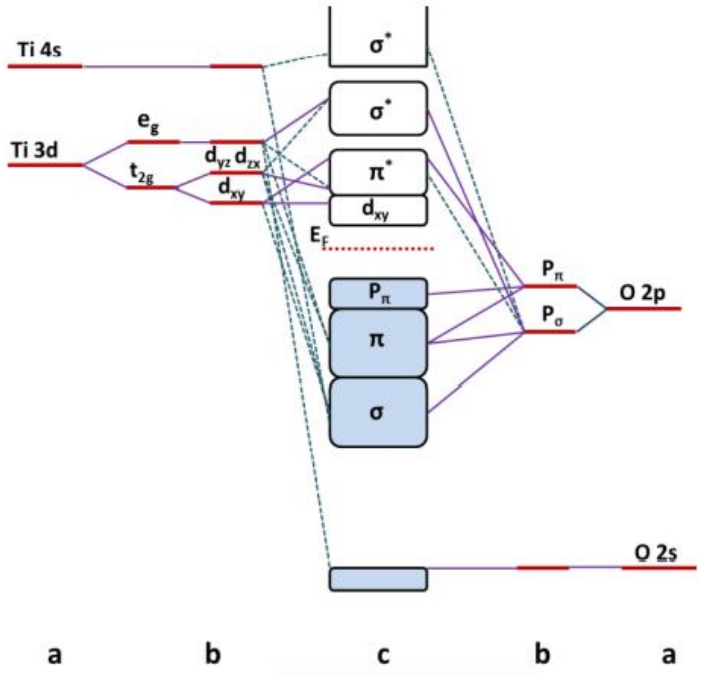

Figure 1.12: Molecular orbital for anatase TiO_2: a) Atomic levels, b) crystal-filed split levels, c) final interaction states. The solid and dashed lines represent large and small contributions, respectively [125].

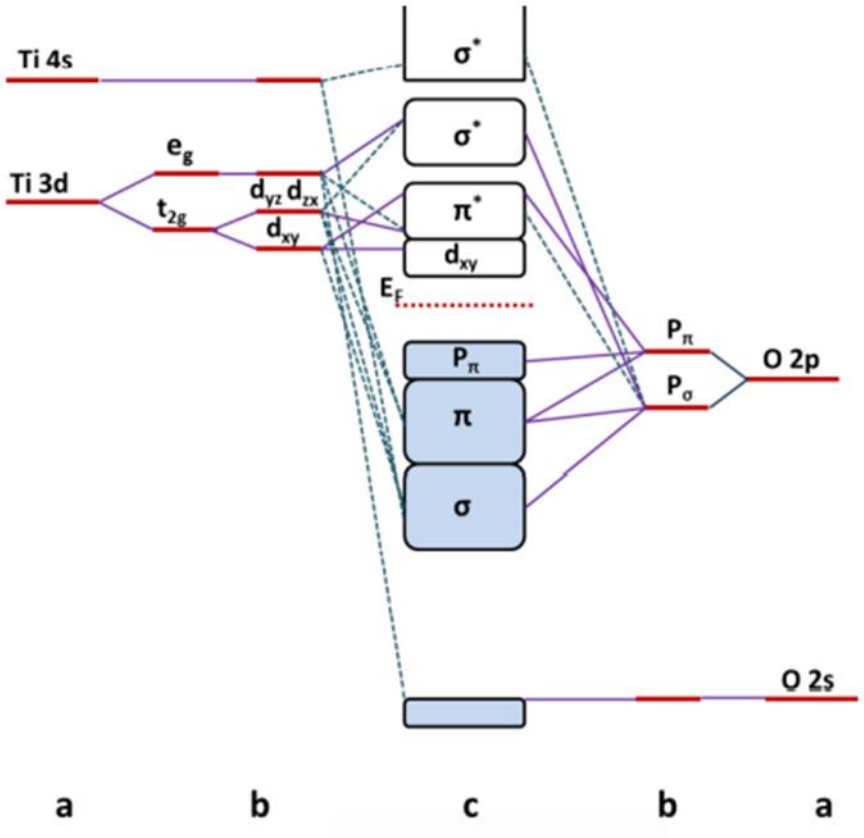

Figure 1.13: Molecular orbital for rutile TiO_2: a) Atomic levels, b) crystal-filed split levels, c) final interaction states. The solid and dashed lines represent large and small contributions, respectively [124].

The bond distances of Ti-O and O-O in rutile, anatase, and brookite are shown in Table 4. Generally, the orbital intersection within a bond decrease as the bond distance increases. The Ti-O and O-O bond distances are longer in the brookite and shorter in rutile phase. Therefore, a stronger orbital interaction is expected for rutile than for brookite, which in turn results in a lower band gap in the case of rutile [126]. The band gap of brookite (3.14 eV) is intermediate between those of anatase (3.2 eV) and rutile (3eV).

	Ti-O (Å)	O-O (Å)	E_g/eV
Rutile	1.91-1.94	2.43	3
Anatase	1.92-1.95	2.43	3.2
Brookite	1.87-2.04	2.49	3.14

Table 4: Bond distances of Ti-O and O-O and energy band gap for rutile, anatase, and brookite.

Thermodynamically, rutile is stable and anatase is metastable at ambient pressure and temperature. Thermodynamics indices that the phase stability is also dependent on particle size and was found that anatase is more stable than rutile when particle size is smaller than 14nm [127]. Anatase has been reported to be thermodynamically

stable for nanostructure sizes < 11nm [122] [127]. This may explain why anatase is 11 and 35 nm and rutile are stable for nanostructures >35nm. This may explain why anatase is the main phase in the synthesis of nanocrystalline of TiO_2. These observations have been attributed to two main effects: surface energy and precursor chemistry. For very small particle dimensions, the surface energy is an important part of the total energy, and surface anatase has been found to be lower than that of rutile and brookite [122] [128]. X-ray diffraction patterns characterisation is one of the best tools to instantly differentiate these three major polymorphs as seen from Figure 1.11 for the three polymorphs was also explored by various researchers for their respective applications, where an almost similar characteristics of that of pure structure have always been observed through different experimental techniques.

1.7.2. TiO_2 Nanostructures

The nanostructures of TiO_2 have created a lot of interest in various applications due to their different forms and surface energy, applications such as biosafety, health [129], rechargeable ion batteries (RIB) and supercapacitor [130] [131]. Recently, TiO_2 nanostructures such as nanosphere [132], nanorods [133], nanowires [134], nano whiskers [135], nanoporous [136], nanosheets [137] and nanosizing [138] have been studied for different applications with different methods. Nanoparticle TiO_2 is more effective as a photocatalyst compared to the bulk parent material [139]. When the diameter of the crystallites of a semiconductor particle falls below a critical radius of about 10 nm, each charge carrier behaves quantum mechanically [140]. Lithium insertion into nanoparticles of other TiO_2 common polymorphs, such as rutile and brookite, was not well known until very recently, when a high Li electroactivity was reported in nanometre sized rutile and brookite TiO_2 at room temperature [141] [142]. It was noticed that crystalline size of brookite TiO_2 has effect on lithium intercalation [143]. The bulk rutile TiO_2 and its (110) surface have been investigated with a computationally efficient semi-empirical tight binding method [130]. However, the study has not reported on the interatomic parameters of this system or its bulk. The anatase phase of bulk structure of TiO_2 has been preferred for lithium intercalation than the brookite [142]. More structural features must be studied so that we can have a clear understanding of which polymorphs can accommodate more lithium atoms. Various authors for different applications have studied nanoporous structure [144] [145]. It has reported that nanoporous structure has a good electrochemical performance due to its large surface area [136]. Nanoporous structure has been studied with an ordered structure and it shows enhanced photocatalytic activity [146]. Large-scale preparation of nanoporous structure have shown the anatase TiO_2 porous morphology with the diameter of 20 nm.

Nanosheets in an anatase phase have improved photoelectric conversion efficiency [147]. They also reported nanosheets with facet and their applications for solar cells [146]. The energy storage, conversion, and catalytic activities of TiO_2 nanosheets are a more recent area of study compared to nanoparticulate and nanoporous TiO_2 because the exposure of highly reactive surfaces renders the nanosheets unstable during crystal growth [148]. Nanosheets of TiO_2 comprising mixed polymorphic phases (brookite with anatase and rutile) are easier to synthesise than pure brookite and were

found to be photoactive, particularly for photo-oxidation reactions in solid-liquid and gas-solid systems [148]. TiO_2 nanoparticles have being studied for high-pressure crystallisation where they generated full atomistic model of a TiO_2 nanocrystal [149]. Their simulation technique has been used to study various nanostructures of TiO_2 [150].

1.7.3. Simulated TiO_2 Nanostructures

To study chemical and physical properties of TiO_2 nanostructures through atomistic simulation synthesis, realistic models of TiO_2 containing interstitial microstructural defects, X-ray diffraction patterns, and Ti-O bond distances observed in experiments are crucially required for fast Li^+, Na^+ and mg^{2+} diffusion during charging and discharging. Utilisation of the previously generated TiO_2 nanosphere, nanoporous and nanosheets models through amorphisation and recrystallisation simulation synthesis allows natural evolution for most structural feature frameworks that exist in genuine systems. Structural evolution is dependent only on interatomic potentials and lattice misfit rather on the instinct of the simulator [151]. In summary the synthesis of generating TiO_2 nanosphere, nanoporous, and nanosheets includes cutting a cube of about 15972 atoms (5324 titanium and 10648 oxygen atoms) from the crystalline bulk TiO_2 composite followed by placing it at the basis position within the cell, then amorphising it by increasing the lattice parameter by a specific percentage to induce strain, and finally running a molecular dynamics simulations synthesis at exactly 2000 K. The nanosheet was generated by reducing the three cell dimensions whereas the nanoporous was generated by reducing three cell dimensions. Finally, a constant volume molecular dynamics simulation calculation was performed for each TiO_2 nano-architectures until recrystallisation was complete [24]. The external view of the previously generated TiO_2 a) nanospheres, b) nanoporous and c) nanosheets architectures to be undergone through lithiation, sodiation and magnesiation synthesis in this current study along with their corresponding SEM structures obtained through experimental research are shown in 1.14, Figure 1.15, Figure 1.16 below.

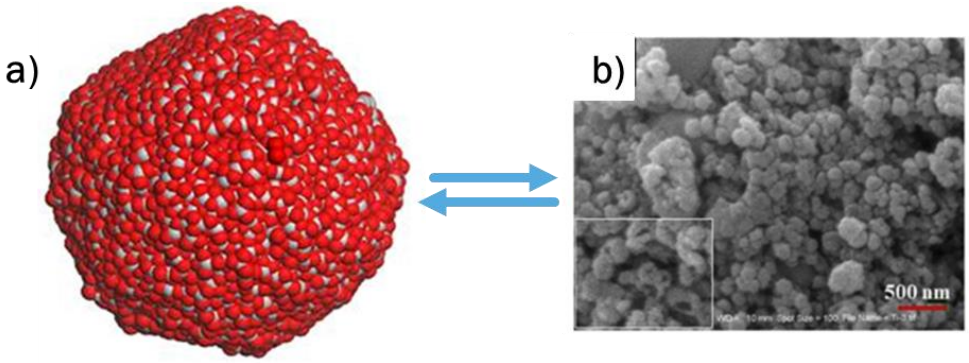

Figure 1.14: Illustrates structural view of a) simulated TiO_2 nanosphere and b) SEM image of pure TiO_2 of Pradubkorn et al [152]

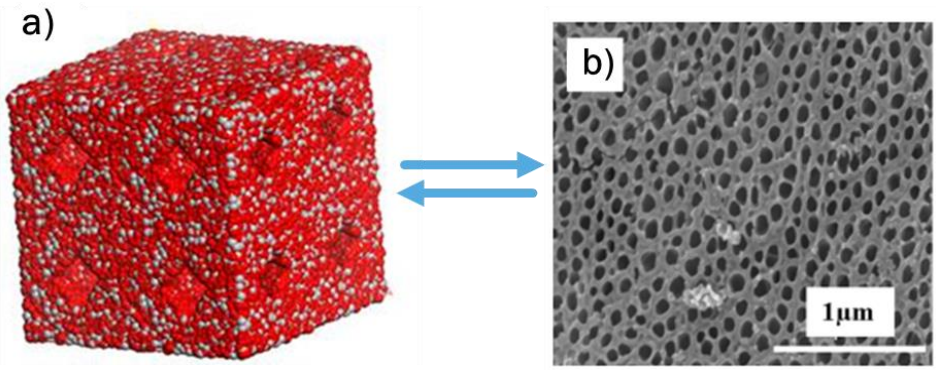

Figure 1.15: Illustrates structural view of a) simulated TiO_2 nanoporous and b) SEM image of nanoporous TiO_2 film Sajad et al [153]

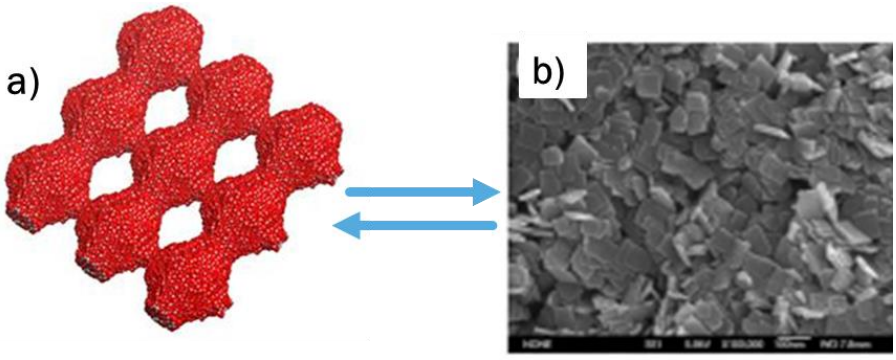

Figure 1.16: Illustrates structural view of a) simulated TiO_2 nanosheets and b) SEM image of TiO_2 nanosheets song et al [154].

1.8. Research Problem

The safety problems associated with commercially available rechargeable metal-ion batteries can occur under abnormal abuse conditions, namely mechanical abuse (e.g., crushing, nail penetration, dropping, shock, etc.), electrochemical abuse (e.g., overcharging, over discharging, short-circuiting fully charged batteries, gas generation, etc.), and thermal abuse (e.g., external heating, scorching with flames, hot combustion gases from fire, etc.). Electrochemical abuse in most cases leads to the formation of dendrites at the anode, where dissolution of the current collector, exothermic decomposition of the electrolyte, gas evolution, and heat generation eventually lead to a thermal discharge reaction of the entire battery. In addition, batteries exposed to external heating are directly damaged by the heat effect and quickly suffer thermal discharge. These incidents have become a critical problem for most metal ion batteries, which cannot withstand very harsh conditions.

1.8.1. Problem statement

Lithium (Li) ion batteries have been widely used in portable electronic devices and regarded as promising devices in the application of electric vehicles [4]. The energy density and performance of Li-ion batteries are largely dependent on the physical and chemical properties of the cathode and anode materials [111]. Typically, both electrodes in a Li-ion battery are intercalation compounds which, as their name

implies, store Li^+ by inserting them into their crystal structure in a top tactic manner [6]. Graphite is the state-of-the-art commercial anode material widely used for Li batteries because of its high Coulombic efficiency and better cycle performance [155]. However, this graphite suffers from one or more of these problems: limited Li storage capacity, large irreversible capacity loss, low charge/discharge rate capacity and poor capacity retention upon the charge/discharge cycling, etc [77].

Therefore, the anode used in most Li-ion batteries is based on graphite carbon, which stores up to one Li^+ for every six carbon atoms between its graphene layers [156]. As a results of the capacity limit of graphite, the energy density of the Li-ion battery cannot satisfy the requirements of portable electronic devices. Traditional intercalation-type graphite materials show low Li storage capacity (372 $mAhg^{-1}$, LiC_6) due to limited Li ion storage sites within a hexagonal carbon structure [110]. To meet the increasing demand for high-energy density, much effort has been made to explore new anode materials [8]. Therefore, Titanium dioxides (TiO_2) nano-architecture materials are possible alternative anode materials with excellent capacity to host Li^+, Na^+ and Mg^{2+} and solve most graphite challenges.

The recent findings of computationally generated bulk, nanosheets, nanoporous and nanosphere TiO_2 can reversibly insert lithium ions [9]. These nano-architecture materials have attracted a lot of attention due to their ability to store/host higher Li contents (concentrations) that undergo through recrystallisation simulations synthesis, along with their high temperature resistant. Thus, these have led us to quench more interest in scientific investigations on replacing Li^+ ions with Na^+ and Mg^{2+} ions in the specified TiO_2 nanostructures to compare their structural, thermodynamic, and transport properties. The TiO_2 precursor materials are environmentally friendly, exhibits excellent thermal/chemical stability and are commercially available in South Africa.

1.8.2. Significance of the study

TiO_2 nano-architectured structures provide high surface area, chemical stability, semiconducting properties, and low cost [157]. TiO_2 have been widely investigated as anode materials for Li^+ ion batteries because they allow safer operating conditions compared to the graphite electrodes due to higher working potential that does not give rise to Li electroplating (Li^+ reduction) [158]. The size effects of TiO_2 polymorphs yield electrochemical performance by improving their ionic or electronic transportation, or both are of significance [159]. Polymorphic Li_xTiO_2 shows good cycle characteristics with little capacity loss due to no noticeable lattice dimension change during lithium insertion and de-insertion processes [160] and is already in practical use in commercially available lithium-ion batteries [161].

The intercalation technique using structured electrodes can be a suitable path to rapidly delivering high capacity required for Li^+, Na^+ and Mg^+ ion driven electric vehicles [162]. The electrode materials of TiO_2 nanoporous, nanosheet and

nanospheres architectures have been found to contribute to the superior electronic performance, their highly crystallized facets enhance lithium-ion transportation properties [151]. This is due to their fast diffusion kinetics and high-rate capability which contribute to the structural stability of electrode materials [24]. In the proposed study, Li_xTiO_2, Na_xTiO_2, and Mg_xTiO_2 systems will be investigated using the amorphisation and recrystallisation simulation synthesis technique. Such techniques have the capability for enabling spontaneous nucleation and crystal growth of nanomaterials as demonstrated in binary systems i.e., MnO_2 [163], TiO_2 [151] ternary systems i.e., Li_xTiO_2 nanosheets [24] electrode materials for rechargeable batteries.

1.8.3. Aim of the study

The aim of this study is to synthesize $MTiO_2$ (M = Li^+, Na^+ and Mg^{2+}) nano-architectures using amorphisation and recrystallisation technique to predict their electrochemical properties as anodes for rechargeable batteries.

i. evaluate the effect of Li^+, Na^+ and Mg^{2+} intercalation in TiO_2 nano-architectures with different ion contents/concentrations,
ii. employ amorphisation and recrystallization technique to atomistically synthesize the Li_xTiO_2, Na_xTiO_2, and Mg_xTiO_2 nano-architectures (i.e., nanosheet, nanosphere, and nanoporous),
iii. cool all Li_xTiO_2, Na_xTiO_2 and Mg_xTiO_2 nano-architectures from 1500 K to 0 K after recrystallisation,
iv. heat all cooled (0 K) from 100 K to 2000 K,
v. characterize structural properties using the radial distribution functions (RDFs), simulated X-ray diffraction (XRD) patterns and microstructural defects,
vi. analyse the high temperatures effect on Li_xTiO_2, Na_xTiO_2 and Mg_xTiO_2 nano-architectures after heating from 100 K to 2000 K,
vii. by investigating the host capability and ion transport i.e. (M= Li^+ Na^+ and Mg^{2+}) in TiO_2 nano-architectures through diffusion coefficients and activation energies calculations,

1.9. Outline of the study

Chapter 1: Describes the fundamental differences and similarities involved with lithium-ion batteries, sodium-ion batteries and magnesium-ion batteries during technical and practical aspects influencing its performance and lifespans through different applications and battery operation when simulated TiO_2 nanostructured is used as a host material for ion insertion reviewed in the literature. Finally, the current problems, significance, and intentions of this research study were discussed.

Chapter 2: Molecular simulation methods and all the theoretical methodologies necessary to understand this research are presented in detail. A description of the program code that intercalates the ion into simulated TiO_2 nanostructures along with characterisation techniques used on all simulated structures was discussed.

Chapter 3: Present all the results of Li_xTiO_2 nanoporous, nanosphere, and nanosheets obtained after being recrystallised, cooled to 0 K and then heated to 2000 K through structural and microstructural snapshots, RDFs and XRD patterns, diffusion coefficients and activated energies.

Chapter 4: Present all results of Na_xTiO_2 nanoporous, nanosphere and nanosheets obtained after being recrystallised, cooled to 0 K and then heated to 2000 K through structural and microstructural snapshots, RDFs and XRD patterns, diffusion coefficients and activated energies.

Chapter 5: Present all the results of Mg_xTiO_2 nanoporous, nanosphere and nanosheets obtained after being recrystallised, cooled to 0 K and then heated to 2000 K through structural and microstructural snapshots, RDFs and XRD patterns, diffusion coefficients and activated energies.

Chapter 6: Describes the conclusions and discussions based on chapter 3, chapter 4 and chapter 5 in summary.

Chapter 2

Research Methodology

2.1. Computational Modelling of Materials

Computational modelling of materials is a tool designed to model new properties similar to those of real systems. Its functions are to investigate the effects of change on different systems as well as further predict of their properties. The first and most important factor is the validity of the model, and this may include simulating the model under known input conditions and comparing the model output with the actual output e.g., if melting temperature is reported at 150 ºC in experiments, the computational model should be comparable to that [85]. Computational techniques can undertake accurate and predictive simulations of the crystal structures and properties. As such, it should be acknowledged that computer models can contribute to the design and improvement of materials with different properties under extreme conditions such as high temperatures, high pressure, and high ion concentration [137]. Figure 2.1 below is a summary illustrating the steps involved in developing a simulation model, designing a simulation experiment, and performing simulation statistical analysis. Atomistic modelling techniques use modern advanced supercomputing power to carry out studies on how atoms interact at a nanoscale level to lay fundamental foundation of all 27 materials science. This technique provides endless possibilities for studies of current and future complex systems and geometries, such as full quantum simulations. It further enables studies based on effects of environmental conditions on crystallographic properties ranging from defects in semiconductors to transport/diffusion mechanisms in high power lithium, sodium, and magnesium-ion batteries [31].

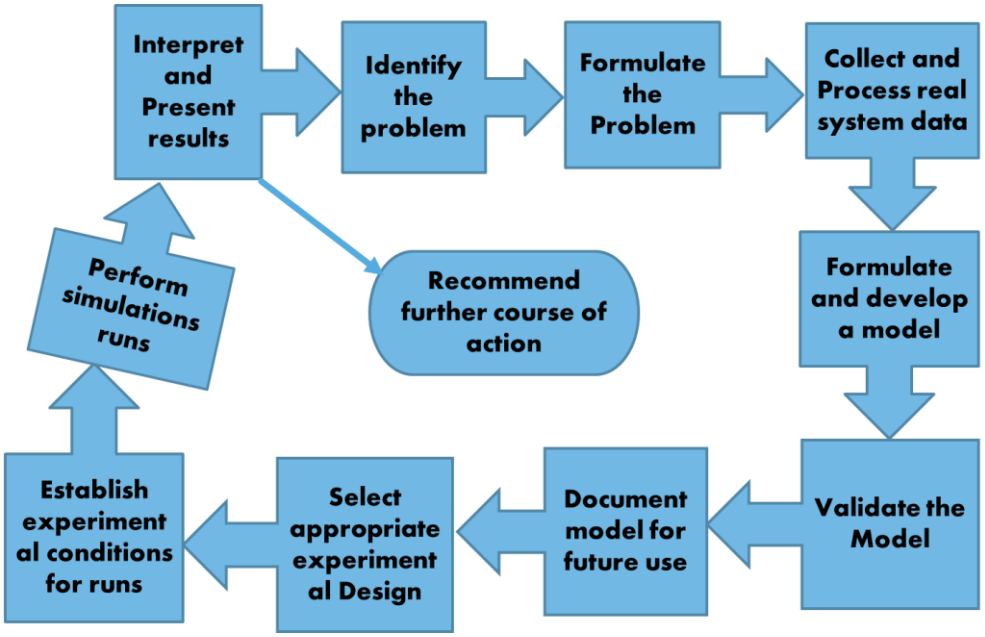

Figure 2.1: Illustrates steps involved in developing a simulation model, designing a simulation experiment, and performing simulation analysis.

There are different scales in modelling, as shown in Figure 2.2 below. The current work will be based on molecular dynamic simulations of nanomaterials. These materials were mentioned in chapter 1, where it was highlighted that they possess beneficial properties which can be exploited for a variety of applications. The theoretical modelling will add significant understanding to the design and synthesis of nanomaterials, hence the use of atomistic simulations.

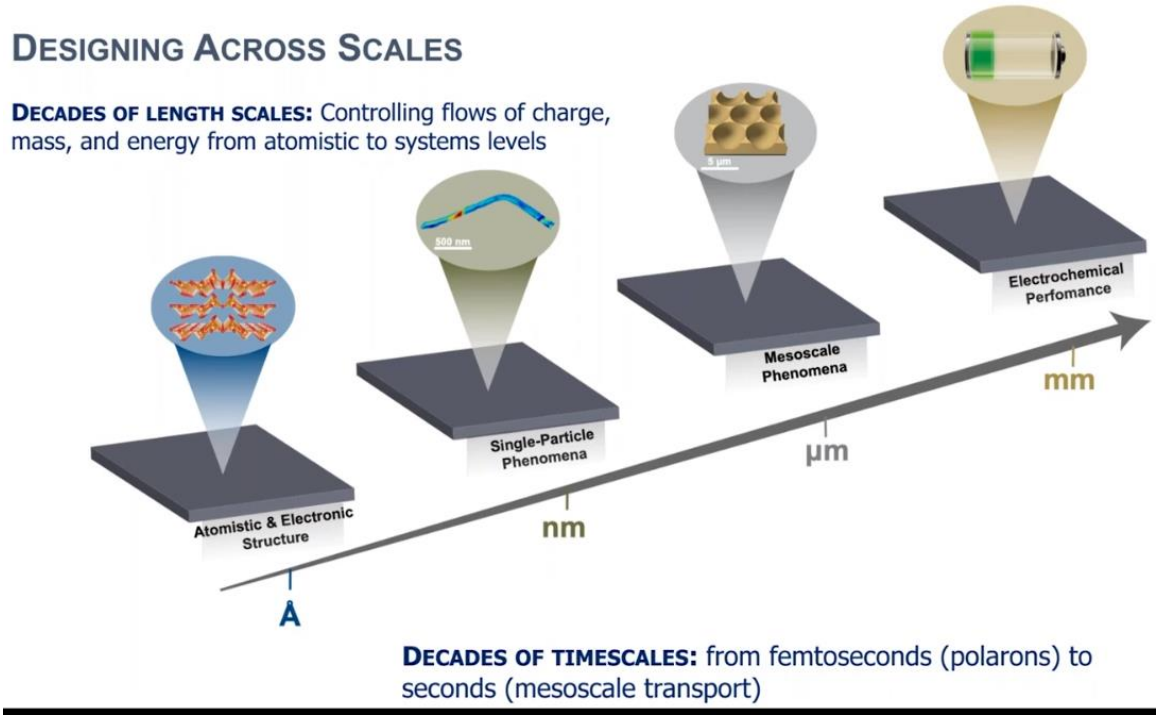

Figure 2.2: Illustrate hierarchal modelling showing the multiscale modelling levels.

2.2. Molecular Dynamics (MD)

Molecular dynamics simulation is a computational technique used to study the motions of atoms in each system (e.g., a solid material or a solid solution could equally be liquids and gases) to understand and predict the structural, dynamic, kinetic, and /or equilibrium properties under a chosen condition (e.g., compositions, temperatures, and pressures) [164]. MD is a powerful method to explore the structure of solids, liquids, and gases. It is a modern method, which requires electronic computers and recently supercomputers. Molecular dynamics simulations are in many respects very similar to real experiments. When we perform a real experiment, we proceed as follows. We prepare a sample of the material that we wish to study. We connect this sample to a measuring instrument (e.g., a thermometer, manometer, or viscometer), and we measure the property of interest during a certain time interval. If our measurements are subject to statistical noise (as most measurements are), then the longer we average, the more accurate our measurement becomes. In molecular dynamics simulation, we follow the same approach. First, we prepare a sample: we select a model system consisting of N particles and solve Newton's equations of motion for this system until the properties of the system no longer change over time (we equilibrate the system). After equilibration, we perform the actual measurement.

In fact, some of the most common mistakes that can be made when performing a computer experiment are very similar to the mistakes that can be made in real experiments (e.g., the sample is not prepared correctly, the measurement is too short, the system undergoes an irreversible change during the experiment, or we do not measure what we think) [165].

2.2.1. Approach

We call molecular dynamics (MD) a computer simulation technique in which the time evolution of a set of interacting atoms is followed by integrating their equations of motion. The molecular dynamics can be used to investigate the detailed atomistic mechanisms. With the MD technique, it is possible to simulate the dynamic thermal behavior of atoms in solids. By performing simulations at different temperatures and studying the displacements of the ions as a function of time we can predict diffusion coefficients. The molecular dynamics technique involves solving Newton's laws of motion over a finite period for all the particles of a system. The main difference with the energy minimization method discussed in the previous section, is those molecular dynamics simulation gives the effect of temperature by assigning kinetic energy to the atoms in the simulation cell and thus allows us to follow the trajectory of the atoms and molecules with time. Hence, unlike in energy minimization calculations, atoms and molecules can potentially jump over energy barriers to reach a global minimum; however, due to the very short 'real time' accessible to molecular dynamics simulations, this only applies to small energy barriers, i.e., of the order of few $k_B T$.
All molecular dynamics simulations in this work were performed using the computer code DL_POLY [166].In molecular dynamics simulation, the particles are initially assigned random velocities, such that the system starts with the required temperature and that the simulation cell has no translational momentum, i.e.,

$$\sum_{i=1}^{N} m_i . v_i^2 = 3Nk_B T \qquad 2.1$$

and

$$\sum_{i=1}^{N} m_i . v_i = 0 \qquad 2.2$$

where N is the number of particles, k_B is the Boltzmann constant, T is the temperature, m_i is the mass of ion i, and v_i its velocity.

The second step of a molecular dynamics simulation is to calculate the force acting on each particle. Once the forces, F_i are obtained the accelerations, a_i can be calculated and the velocities, v_i and positions F_i, are updated, for an infinitely small-time step, according to

$$a_i(t) = \frac{F_i(t)}{m_i} \quad 2.3$$

$$v_i(t+\delta t) = v_i(t) + a_i(t).\delta t \quad 2.4$$

$$r_i(t+\delta t) = r_i(t) + v_i(t).\delta t \quad 2.5$$

These are the Newton's equations of motion and can only be applied strictly for an infinitesimal time step. In practice, computer codes use integration algorithms such as the Verlet algorithm [167] to solve Newton's laws of motion, as explained in the next section. The choice of the time step δt, in these equations is very important. Indeed, it δt is too large; molecular vibrations will occur within the time step, giving rise to large errors. However, if δt is too small, the particles will take too long to move a significant distance. In addition, another factor needs to be considered to choose the time factor. After each step, run time properties such as the potential energy, the temperature, or the pressure of the system are calculated. Then the process is repeated several thousand or million times to reach the required simulation time. In the first few tens of thousands of steps, the particles' velocities are scaled to meet the desired temperature. This period is the equilibrium period, and it allows the system to come to equilibrium at a given temperature and pressure before data are collected. The simulation runs, if possible, without scaling the velocities of the particles, to obtain converged averages of the properties of interest and reduce statistical noise.

In molecular dynamics, we follow the laws of classical mechanics, and most notably Newton's law of motion:

$$\vec{F}_i = m_i \vec{a}_i \quad 2.6$$

for each atom *i* in a system constituted by *N* atoms. Here, m_i is the atom mass, $\vec{a}_i = \frac{d^2\vec{r}_i}{dt^2}$ its acceleration, and $\vec{F}_i$ the force acting on it, because of interactions with other atoms.

2.2.2. Ensemble

Integrating Newton's equations of motion allows you to explore the constant energy surface of a system. However, most natural phenomena occur under conditions where the system is exposed to external pressure and/or exchanges heat with the environment. Under these conditions, the total energy of the system is no longer conserved and extended forms of MD are required. Several methods are available to control temperature. Depending on which state variables the energy, E, enthalpy, H (i.e., E + PV), number of particles, N, pressure, P, stress, S, temperature, T, and

volume, V – are kept fixed, different statistical ensembles can be generated. A variety of structural, energetic, and dynamic properties can be calculated from the averages or fluctuations of these quantities over the ensemble generated. There are three most common ensembles that are often used in MD simulations of NVT, NVE, and NPT ensembles.

NVT ensemble is also known as canonical ensemble where temperature and volume are kept constant. NVT ensemble in statistical mechanics is a statistical ensemble that represents a probability distribution of microscopic states of the system. For a system taking only discrete values of energy, the probability distribution is characterized by the probability of finding the system in a particular microscopic state with energy level, conditioned on the prior knowledge that the total energy of the system and reservoir combined remains constant.

The NVE ensemble is also known as micro-canonical ensemble where energy and volume are kept constant. NVE ensemble is obtained by solving the standard Newton equation without any temperature and pressure control. Energy is conserved when this (adiabatic) ensemble is generated. However, because of rounding and truncation errors during the integration process, there is always a slight fluctuation, or drift, in energy.

NPT ensemble is also known as isothermal-isobaric ensemble. This ensemble plays an important role in chemistry as chemical reactions are usually carried out under constant pressure condition. In the NPT ensemble, pressure and temperature are kept constant. The NPT ensemble is used for comparison of MD simulations with experiments. The temperature in the NPT ensemble is controlled using Langevin method. The partition function can be written as the weighted sum of the partition function of canonical ensemble, Z (N, V and T).

$$\rho(N,P,T) = \int Z(N,V,T)e^{(-\beta PV)CdV} \quad 2.7$$

Where

$$\beta = \frac{1}{k_B T} \quad 2.8$$

k_B is the Boltzmann constant and V is the volume of the system.

2.2.3. Amorphisation and Recrystallisation

The amorphization and recrystallization simulation synthesis technique [168] is the strategy used in atomistic simulation when complex structures evolve during a pseudo-recrystallization from an amorphous starting point. Amorphisation and recrystallisation is an evolutionary simulation technique which compression or tension is applied to the system to displace atoms from equilibrium positions. When pressure is released, atoms are accelerated to equilibrium positions having high ionic mobility as molten systems. To generate realistic models of supported oxide thin films one must consider various factors including the epitaxial relationships, defects and reduced interfacial ion densities. The defects, which evolve in responds to misfit accommodation, may include dislocations arrays, vacancies, substitutions, and interstitials including clustering of such defects. These structural features must be achieved to generate a realistic model, even though some are challenging. To overcome the problems associated with the starting structure, the supported thin film is forced to undergo an

amorphous transition before recrystallising to a final structure. Such a procedure eliminates any possibility of the final structure reflecting artificially the starting structure. Essentially, the system loses all memory of the preparatory configuration and dynamical simulation, as applied to an amorphous structure, allows a more comprehensive exploration of the configurationally space, which is likely to result in an energetically more favourable, and hence more realistic, final interface structure. This method allows interfacial structures to evolve while the simulation is solely influenced by substrate material and associated lattice misfit.

Various mechanisms for inducing amorphisation have been explored for supported metal-oxide thin films associated with both positive and negative lattice misfits. These include performing dynamical simulation at very high temperatures to melt the thin film and constraining the thin film under conditions of compression or tension: under dynamical simulation, the considerable strain within the thin film results in an amorphous structure. The latter can be achieved either by modifying artificially the potential parameters during the amorphisation step or by constructing an interface system with a particular associated lattice misfit (positive or negative) based upon, for example, some particular near coincidence site lattice [169] [150].

The amorphisation is induced by the thin film bending of the support under high compression. The application of high-temperature dynamical simulation to this strained system results in the amorphisation of the thin film over the layer. Prolonged dynamical simulation is required to allow the system to recrystallise under the influence of the support. This methodology is purely a simulation technique to derive low energy structures, and the structural evolution of the system bears no physical significance. The main driving force to the amorphisation is the strain under which the thin film is constrained, whereas the temperature at which the dynamical simulation is run is secondary to inducing amorphisation. For example, the procedure can be performed equally well at 20 K as at 200 K. However, the recrystallisation process at 20 K is much slower. In essence, the optimal temperature is one that allows the structure to evolve but that falls of melting the thin film.

This would be detrimental, as it would prevent recrystallisation and require an additional quenching step [170]. An important feature of the methodology is that the amorphous transition enables all memory of the preparatory configuration to be lost (radial distribution functions for the amorphous thin film are broad, indicating no long-range ordering) and therefore the final structures cannot artificially reflect on the starting structure [170]. The recrystallisation is deemed complete when the system is no longer evolving structurally or energetically, the duration of which is system dependent. Furthermore, dynamical simulation, as applied to an amorphous structure, allows a more comprehensive exploration of the configurational space, which is likely to result in an energetically more favourable, and hence more realistic final interface structure [171].This technique has been implemented on various materials such as thin films and nanoparticles [172], generate models for CeO_2 nanocrystallites [173],

microstructure in MnO_2 [174], shape of CeO_2 nanoparticles [175], MgO cluster supported on BaO (100) [168] and lithium insertion into MnO_2 [176]. In this work, we will employ this technique in the Lithiated, sodiated, and magnesiated nanostructures of TiO_2. The lithium, sodium and magnesium were randomly inserted into an amorphous nanosphere, nanoporous and nanosheets TiO_2 architectures with chosen coordinates to ensure that Metal ions are not positioned on top of other atoms in the simulation cell. To facilitate charge neutrality, an equivalent number of Ti^{4+} species were reduced to Ti^{3+}. The method was previously used successfully in bulk MnO_2 [176]. We will also present the radial distribution functions of the systems to verify the process of amorphisation and recrystallisation.

2.3. Potential Model

The potential model describes the variation in the energy of the molecule or solid as a function of atomic coordinates [108]. The reliability of the calculation depends on the quality and accuracy of the potential model. The potential model describes the interactions between two or more species. The different Coulombic summation schemes that have been employed are described.

2.3.1. Born model of an Ionic Solid

All calculations are based on the Born model [177] of ionic solids, where ions interact through long-range Coulomb and short-range interactions. Rigid ion potentials with partial charges were used and Matsui developed these for isostructural rutile TiO_2. In this section, we are going to describe the potential models. Usage of appropriate potential model to describe the interaction of atoms within the crystal is essential to ensure that the surface and interface calculations reflect the system under study. The types of potential model can be divided into two main categories. The first are molecular mechanical force fields in which the energy is given as a function of 53 bond lengths, angles, torsional planes, and other cross terms, which are described explicitly for the system with different potential forms existing for each system. The second approach focuses on atoms or ions rather than bonds and is particularly useful for extended solids where bonds are not defined specifically, although the potential contains two-body and if is necessary three-body terms. One such example of the latter category is the Born model potential for ionic solids [109]. In the Born model of solids, it is assumed that the energy and its derivatives can be defined as the simulation of all interactions between the atoms in the system, which give rise to the total interaction and total net force acting on each atom due to others [110]. In this model, the atoms of a system are represented as point charge particles that interact via long-range electrostatic forces and short-range interactions. Hence the interaction energy between them is obtained by:

$$\boldsymbol{U_{ij} = \frac{1}{4\pi\varepsilon_0}\frac{q_i q_j}{r_{ij}} + \Phi(r_{ij})} \qquad 2.9$$

where term one represents long-range Coulombic interactions, ϵ_0 is the permittivity of vacuum, q_i and q_j are the ionic charges and r_{ij} is the interatomic distance. The second

term, $\Phi(r_{ij})$ describes short-range interactions between ions, including the repulsion between the electron charge clouds and the van Der Waals attraction forces.

2.3.2. Rigid Ion Model

The simplest form of potential is one in which the electronic polarizability is neglected, the rigid ion model. This model is good in reproducing structural parameters for static systems. However, lattice vibrations are poorly modelled because they are strongly coupled to polarisation. Also, once a defect is introduced, polarisation will be expected to occur around a defect to stabilise it. The problem of defect energies in static conditions can be handled by revamping short-range potential parameters to model the static dielectric constants overestimating the polarization due to lattice relaxation to compensate for the shortfall to the neglect of electronic polarizability and thus obtain correct defect energies.

2.3.3. Long-Range Interaction

The long-range interaction energy is the sum of the interaction energies between the charges of a central unit cell and all the charges of the lattice. In an ionic system, if a pair of ions i and j are separated by a distance r_{ij}, there is a Coulombic interaction energy between them. The long-range interaction energy of two ions (ion *i* and ion *j*) with charges q_i and q_j is given by:

$$\boldsymbol{\Phi_{LR}(r_{ij}) = \sum \frac{q_i q_j}{4\pi\varepsilon_o (r_{ij}+l)}} \qquad 2.10$$

Where r_{ij} is the displacement separating the two ions, ε_o is the permittivity of free cell and *l* is the set of lattice vectors representing the periodicity of the crystal lattice. Long-range interactions describe the Coulombic summation. In non-ionic systems this interaction will not be present and only short-range interactions need to be considered.

Ewald Summation

The Ewald method calculates the electrostatic potential acting on an object ion in a lattice. The lattice is made up of ions acting as an array of positive and negative charge points. The total potential, φ, acting on the object ion by the array of point charges is separated into two components. One part in real space, φ1, and the other in reciprocal space, φ2, such that:

$$\boldsymbol{\varphi = \varphi_1 - \varphi_2} \qquad 2.11$$

The real part, φ_1, comprised of the array of point charges, is countered by an array of Gaussian charge distributions equivalent in magnitude but opposite in charges. Thus, each ion is effectively neutralised, and neighbouring ions no longer interact. The reciprocal part, φ_2, comprises an array of Gaussian charge distributions, φ, with equivalent charge and magnitude as the original point charge array.

2.3.4. Short Range Interaction

The short-range two body potentials are an interaction between two charge clouds and

is more complex than long-range interaction. At small distances, the electron cloud overlap leads to strong short-range repulsive forces due to electron density and therefore nuclear shielding is reduced. This in turn increases the columbic repulsion between the positively charged nuclei. It is this partly force, which prevents a crystal lattice from collapsing on itself. However, before the nuclear repulsion becomes significant there is also a quantum mechanical effect due to the electrons which are forced to occupy a smaller portion of space. Since the electrons must maintain orthogonal orbitals, [55] the energy states increase in energy. This is known as the orthogonalization or Pauli repulsion. There is a contrasting longer-range attractive interaction at larger interatomic distances arising from the formation of instantaneous dipoles between adjacent electron clouds. This effect (Van Der Waals interaction) is also quantum-mechanical in origin. By adjusting only the much smaller short-range contribution the whole spectrum of crystal structures can be reproduced. The most basic form would be a simple harmonic interaction given by:

$$\boldsymbol{\Phi_{SR}(r_{ij}) = \frac{1}{2}K(r_{ij} - r_0)^2} \qquad 2.12$$

Where rij is the distance between two atoms i and j, r_0 is the distance equilibrium bond and K is the harmonic force constant. This model is quite sufficient for systems that only deviate slightly from r0 and for which interactions can realistically be confined to adjacent pairs of ions. That is, the short-range attractive and repulsive interactions of the ions. Attractive interaction contains van der Waals. The short-range interaction energies are described well by simple parameterised analytical functions. Below we give descriptions of short-range interactions potentials.

2.3.4.1 Buckingham Potentials

The Buckingham potential describes the exchange repulsion, which originates from the Pauli Exclusion Principle, by a more realistic exponential function of distance. However, since the Buckingham potential remains finite even at very small distances, it runs the risk of an un-physical "Buckingham catastrophe" at short range when used in simulations of charged systems. Buckingham potential is a formula that describes the van der Waals energy Φ (r_{ij}) for the interaction of two atoms that are indirectly bonded as a function of the interatomic distance (r). It is used to model two body non-bonded interactions in ionic solids. The general form of Buckingham potential is given by

$$\boldsymbol{\Phi_{ij}(r) = A_{ij}\exp^{\frac{-r_{ij}}{\rho_{ij}}} - \frac{C_{ij}}{r_{ij}^6}} \qquad 2.13$$

Where A_{ij} is the size of the ions, ρ_{ij} is the hardness, and C_{ij} is the dispersion parameter. The repulsive interaction between the ions is represented by the first term while the second term is the van der Waals attractive interaction of the ions. For the cation-anion interactions, the attractive term is often ignored because of its small contribution to the short-range potential.

2.3.4.2. Three-body potentials

A further component of the interactions of covalent species is the bond-bending term,

which is added to consider the energy penalty for deviations from the equilibrium value. This potential describes the directionality of the bonds and has a simple harmonic form by:

$$\mathbf{U(\theta_{ijk}) = \frac{1}{2} k_{ijk}(\theta_{ijk} - \theta_o)^2} \quad 2.14$$

where $\mathbf{k_{ijk}}$ is the three-body force constant and θ_0 is the equilibrium angle

2.4. Properties of Molecular Dynamics

2.4.1. Temperature

The temperature depends on a certain kind of ensemble for a particular simulation. In a canonical ensemble, the total temperature is constant whereas in the micro canonical ensemble the temperature is fluctuating. The temperature is directly related to the kinetic energy of the system as follows:

$$\mathbf{K = \sum_{i=1}^{N} \frac{|\acute{p}_i|}{2m_i} = \frac{k_B T}{2}(3N - N_c)} \quad 2.15$$

Where p_i is the total momentum of particle i, mi is its mass and N_c is the number of constraints on the system. Each degree of freedom contributes $k_BT/2$ this is according to the equipartition of energy. If there are N particles, each with three degrees of freedom, then the kinetic energy should be equal to $3Nk_BT/2$. The total linear momentum of the system is often constrained to a value of zero in a molecular dynamics simulation, which has the effect of removing three degrees of freedom from the system, and N_c would be equal to 3.

2.4.1.1. Melting Temperature

The melting temperature is defined as the temperature at which, under a specific pressure, the liquid and solid phases of a substance co-exist in equilibrium. At melting the systems appear disordered, molecular diffusion can occur, and it is a high-pressure case. At low temperatures, systems are ordered with little molecular motion and that occurs at low pressures. The melting temperature of most substances is the same as their freezing temperature because the substance melts at a temperature similar to that at which it freezes. The example is that of the most interesting liquid, water, which melts very close to 0 °C (273.15 K). Co-existence is easily achievable in larger systems in two dimensions. Unlike the boiling point, the melting temperature is relatively insensitive to pressure. Meting points are often used to characterise organic compounds and ascertain the purity. The melting point of a pure substance is always higher and has a smaller range than the melting point of an impure substance.

The higher the impurity, the lower the melting point and the broader the range. The chemical element with the highest melting point is tungsten which melts at 3695 K (3422 °C) making it excellent for use in light bulbs. Platinum, with the melting point of 1772 °C (2045.15 K), has the highest melting point amongst the precious metals while metallic gold melts at 1064 °C (1337 K). Computationally, we can keep the pressure

and temperature constant while allowing the energy to fluctuate until a stable value is reached. Not only is heat required to raise the temperature of the solid to the melting point, but also the melting itself requires heat called the heat of fusion. From thermodynamics, at the melting point the change in Gibbs free energy (ΔG) of the material is zero, because the enthalpy (*H*) and the entropy (*S*) of the material are increasing (Δ*H*, Δ*S* > 0).

Melting occurs when the Gibbs free energy of the liquid becomes lower than the solid energy for that material. Carnelley's rule established in 1882 by Thomas Carnelley states that high molecular symmetry is associated with high melting point. A good example is that of three structural isomers with molecular formula C_5H_{12} where the melting point increases in the series: isopentane 113 K, n-pentane 143 K and nenopentane 255 K. Pyridine has a lower symmetry than benzene, hence it's lower melting point. A high melting point results from a high heat fusion, a low entropy of fusion, or a combination. In highly symmetrical molecules, the crystal phase is densely packed with many efficient intermolecular interactions, resulting in a higher enthalpy change on melting.

2.4.1.2. Annealing process

Annealing is a heat treatment in which a material is exposed to an elevated temperature for an extended period of time and then slowly cooled down. It is regarded as the toughening process and prevents the creation of defects on the atomic scale such as defects like vacancies; misplacement, etc. The strength of material can really hurt. In the glass factory, it is extremely important to anneal, the glass before it is ready or else it will be very fragile and even removing it from its mould will be impossible. Glasses, which are not properly annealed will contain stress, which may result in breakage before or at any time after their removal from the kiln. Annealing is critical to the longevity of glass.

Annealing is also used as an optimisation tool in finding the global minima. Another important application is to relieve internal stress, refine the structure, and improve the cold working properties. There are three stages in the annealing process, with the first being the recovery phase, which results in softening of the metal through removal of crystal defects and the internal stresses that they cause. The second phase is recrystallization, where new grains nucleate and grow to replace those deformed by internal stresses. If annealing can continue once recrystallization has been completed, grain growth will occur, in which the microstructure starts to coarsen and may cause the metal to have less than satisfactory mechanical properties. The high temperature of annealing may result in oxidation of the surface of the metal, resulting in scale. If scale is to be avoided, annealing is carried out in an oxygen, carbon, and nitrogen free atmosphere. In thermodynamics, annealing occurs by diffusion of atoms within a solid material, so that the material progresses towards its equilibrium state.

2.4.2. Radial Distribution Functions

The RDF is defined as the probability of finding an atom at a distance r from another atom compared to a homogeneous distribution [178] [179] and is given by

$$g(r) = \frac{V}{N_1 N_2} \frac{1}{4\pi r^2 \delta r} \left\langle \sum_i \sum_{j>i} \delta\left(r - r_{ij}\right) \right\rangle \qquad 2.16$$

where V is the volume, N_1 and N_2 are the atom types of the RDF, the delta function must give rise to a value of one for a range of $r(\delta r)$. The RDF tends to one at long distances with sharp peaks indicating a regular lattice structure. For amorphous or liquid systems, the RDF shows characteristically show a small number of broad peaks at short distances, indicating short-range order, superimposed on an oscillating trace to one, indicating loss of long-range order [180]. The structural properties of our system were investigated by analysing the partial radial distribution functions (RDFs), $g_{CoS}(r), g_{SS}(r)$. The partial RDFs $g_{\alpha\beta}(r)$ are defined in such a way that, considering an atom of the species α, the probability of finding an atom of the species β in a spherical shell $(r, r+dr)$ is:

$$\rho_\beta 4\pi r^2 g_{\alpha\beta}(r) dr \qquad 2.17$$

where $\rho_\beta = {}^{x_\beta}\!/_{V}$, is the number density of species β with mole fraction x_β, and V is the volume per atom.

RDFs give the probability of finding the centre of a particle or atom at a given distance from the centre of another particle. We calculated the partial distribution functions obtaining the nearest-neighbour interatomic distances of Ti -O. The light atom at the centre is the reference atom in Figure 2.3, and the circles around it represent the other atoms. A ring centred on the reference is drawn with radius r and thickness dr .The radial distribution function can be an effective way to describe the structure of a system at different temperatures.

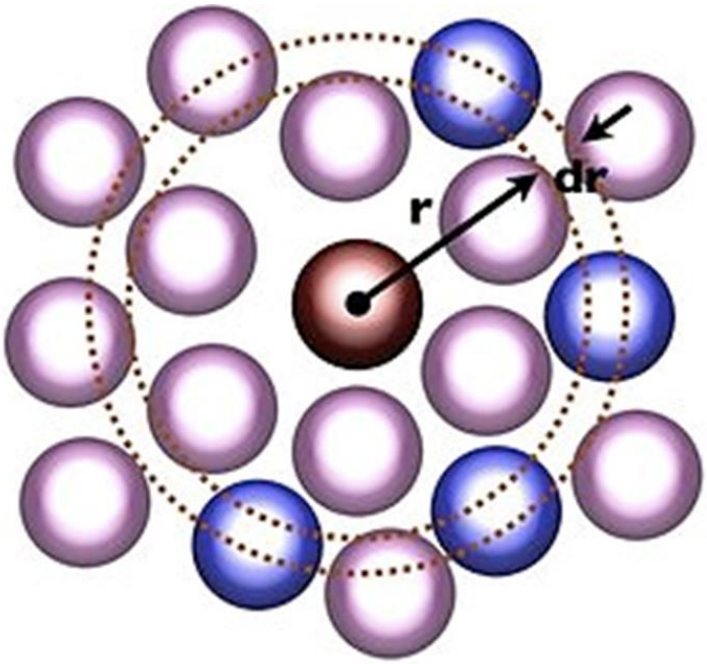

Figure 2.3: Illustrates radial distribution function (RDFs) of an atom.

The light atom at the centre is the reference atom, and the circles around it represent the other atoms. A ring centred on the reference is drawn with radius **r** and thickness **dr**. The radial distribution function can be an effective way to describe the structure of a system at different temperatures.

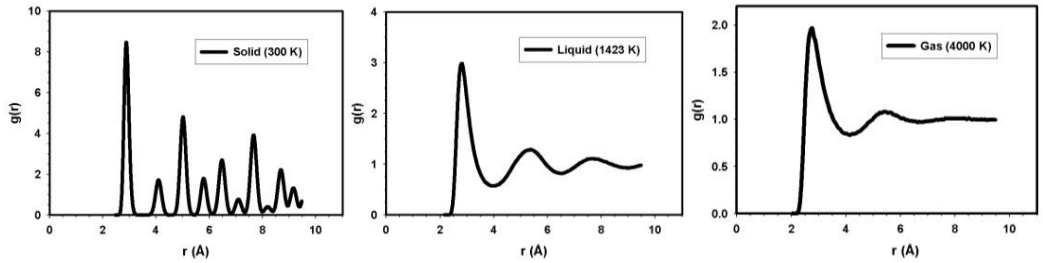

Figure 2.4: Illustrates RDFs of TiO_2 bulk for solid, liquid, and gas phases.

The RDFs for TiO_2 bulk, starting from a solid crystal on the left, the system reaches melting in the central Figure and on the right, the gaseous system is shown in Figure 2.4. The number of peaks decreases, and the broadening of the peaks is quite noticeable**.** Differentiation between a solid and a liquid is detected using the RDFs by the number of peaks appearing in a particular RDF plot. In a crystal or solid, the radial distribution functions have a multiple number of sharp peaks, and heights are characteristic of the lattice structure. The radial distribution function of a liquid has a small number of peaks at short distances, and the height of the peaks decreases. For the crystalline solid, the peaks are sharp and thin and show long-range order. In case of a liquid phase, the peaks are broad, and the radial distribution function rapidly converges to one as observed in the gaseous phase.

2.4.3. X-Ray Diffraction Patterns

X-ray diffraction (XRD) is a powerful tool for materials characterization as well as for detailed structural elucidation. As the physical properties of solid (e.g., electrical, optical, magnetic etc.) depend on atomic arrangements of materials, determination of the crystal structure is an indispensable part of the structural and chemical characterization of materials. X-ray patterns are used to establish the atomic arrangements of the materials because the lattice parameter, d (spacing between different planes) is of the order of x-ray wavelength. Furthermore, the XRD method can be used to distinguish crystalline materials from nanocrystalline (amorphous) materials. From the X-ray diffraction pattern, we can obtain the following information:

i. to judge formation of a particular material system.
ii. Unit cell structure, lattice parameters, miller indices.
iii. Types of phases present in the material
iv. Estimation of crystalline/amorphous content in the sample.
v. Evaluation of the average crystalline size from the width of the peak in a particular phase pattern.
vi. The large crystal size gives rise to sharp peaks, whereas the peak width increases with decreasing crystal size.
vii. An analysis of structural distortion arising because of variation in d spacing caused by the strain, thermal distortion.

2.4.3.1. Determination of Crystal Size:

XRD analysis has been the most popular method for the estimation of crystallite size in nanomaterials and therefore has been extensively used in the present work. The evaluation of crystallite sizes in the nanometre range warrants careful analytical skills. The broadening of the Bragg peaks is ascribed to the development of crystallite refinement and internal stain. To size-broadening and stain-broadening, the full width at half-maximum (FWHM) of the Brag peaks as a function of the diffraction angle is analysed. The X-ray diffraction (XRD) peak broadening calculates the crystallite size of the deposits. Diffraction patterns are obtained using Cu Kα radiation at a scan rate of 10/min. The full-width half maxima (FWHM) of the diffraction peaks were estimated by fitting the pseudo-Voigt curve. After subtracting the instrumental line broadening, which was estimated using quartz and silicon standards, the grain size can be estimated the Scherer equation

$$\frac{0.9\lambda}{\beta\cos\theta} = \mathrm{D} \qquad 2.18$$

Where λ is the wavelength of X-ray, β is the FWHM in radian, θ is peak angle. As for single-crystal diffraction, an essential ingredient for the simulation of a powder diffraction experiment is the calculation of the structure factors F_{hkl}, which are related to the atomic positions and atomic scattering factors via equation below.

$$\boldsymbol{F_{hkl}} = \sum_1^N \boldsymbol{f_n} \boldsymbol{e^{2\pi i(hu_n + kv_n + lw_n)}} \qquad 2.19$$

The powder diffraction intensity observed at the diffraction angle 2θ is then given as:

$$I(\theta) = \sum_{hkl} p_{hkl}(2\theta - 2\theta_{hkl})I_{hkl} \quad 2.20$$

Where the Integrated Bragg Intensity I_{hkl} is related to the structure factors F_{hkl} via:

$$I_{hkl} = M_{hkl}P_{hkl}L_{hkl}|F_{hkl}|^2 \quad 2.21$$

Here

M_{hkl} is the multiplicity of reflection *hkl.*

P_{hkl} is the preferred orientation correction for the reflection *hkl.*

$L_{hkl\ is}$ the Lorentz and polarization corrections for reflection *hkl*.

$P_{hkl}\ (2\theta - 2\theta_{hkl})$ is an appropriate profile function.

The profile function may include an asymmetry correction and its width depend on instrument resolution and sample broadening effects. In the framework of these thesis, XRD was employed to perform structural characterisation of Li_xTiO_2, Na_xTiO_2 and Mg_xTiO_2 (where x = 0.11, 0.15, 0.19 and 0.23) nanosphere, nanoporous and nanosheets electrode at Low (0) and High (2000 K) temperatures

2.4.4. Diffusion Coefficients

Diffusion coefficients is another measure to estimate relative mobilities of individual Li^+, Na^+ and Mg^{2+} in TiO_2 atoms at varied temperature conditions. It is known that diffusion coefficient can be estimated from the slope of MSD plots using the Einstein relation as follows:

$$D = \frac{1}{6}\frac{d}{dt} <| r_i(t) - r_i(0) |> \quad 2.22$$

The integral Equation 2.28 is the velocity autocorrelation function (VAF), which is related to the diffusion coefficient. The VAF decays to zero at long time; the function is integrated mathematically to calculate the diffusion coefficient as in Equation 2.29.

$$D = \frac{1}{3}\int_0^\infty < v_i(t).v_i(0) > dt \quad 2.23$$

The melting point of the simulated system can be located by increasing the temperature of a crystalline system until diffusion appears. Diffusion is also the phenomenon of random motion causing a system to decay towards uniform conditions. For example, diffusion of particles causes a net movement of particles from areas of high concentration to areas of lower concentration until equilibrium is reached.

Diffusion is a spontaneous process more familiarly known as a passive form of transport, rather than being active and affects a variety of different quantities. Spontaneous processes are not reversible.

Examples of diffusion include diffusion of concentration, heat, or momentum. Diffusion increases entropy, decreasing Gibbs free energy, and therefore is thermodynamically favourable. In all cases of diffusion, the flux of the transported quantity (atoms, energy, or electrons) is equal to a physical property (diffusivity, thermal conductivity, electrical conductivity) multiplied by a gradient (a concentration, thermal, electrical field gradient). Diffusion in this type of molecular dynamics simulations is calculated as the slope of the graph of mean square displacement as a function of time.

2.4.5. Activation Energies

As temperature increases, gas molecule velocity also increases (according to the kinetic theory of gas). This is also true for liquid and solid substances. The (translational) kinetic energy of a molecule is proportional to the velocity of the molecules (KE = 1/2 mv^2). Therefore, when temperature increases, KE also increases; as temperature increases, more molecules have higher KE, and thus the fraction of molecules that have high enough KE to overcome the energy barrier also increases.

The fraction of molecules with an energy equal to or greater than Ea is given by the exponential term $e^{\frac{-E_a}{RT}}$ in the Arrhenius equation:

$$Ea = Ae^{\frac{-E_a}{RT}} \qquad 2.24$$

- k is the rate constant
- E_a is the activation energy
- R is the gas constant
- T is the temperature in kelvin
- A is frequency factor constant or also known as pre-exponential factor or Arrhenius factor. It indicates the rate of collision and the fraction of collisions with the proper orientation for the reaction to occur.

Taking the natural log of both sides of Equation 2.24 yields the following.

$$lnK = LnA - \frac{E_a}{RT} \qquad 2.25$$

The Gibbs energy of activation has the linear form y = mx + b. Graphing ln k vs $\frac{1}{T}$ yields a straight line with a slope of $\frac{-E_a}{R}$ and a y-intercept of ln A, as shown in graph A.

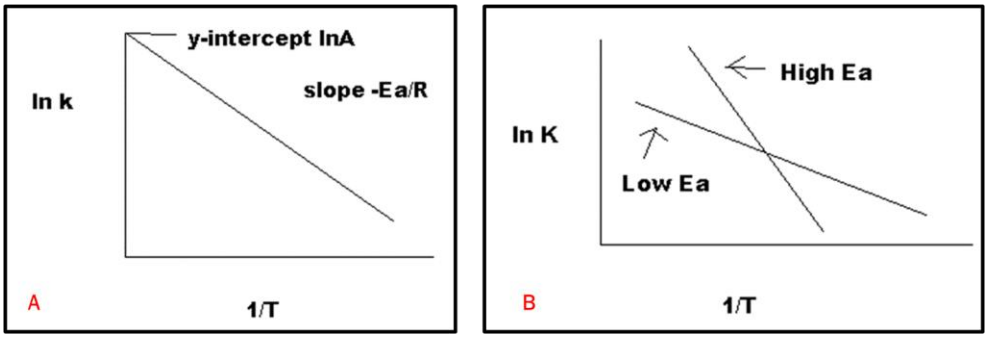

Figure 2.5: Example of inverse and transverse activation energies

As indicated in graph B, the reaction with a higher E_a has a steeper slope; the reaction rate is thus very sensitive to temperature change. On the contrary, the reaction with a lower E_a is less sensitive to a temperature change. Because radicals are extremely reactive, E_a for a radical reaction is 0; an Arrhenius plot of a radical reaction has no slope and is independent of temperature.

2.5. Average intercalation potentials

The voltage of the cell the potential difference between the cathode, anode and specific capacity of the electrode are crucial properties that determines the energy density of a Lithium, sodium, and magnesium ion batteries. Energy density is the product of voltage and specific capacity. To design batteries with high energy densities, the voltage and specific capacity need to be increased. It is important for us to get a coarse measure of the intercalation potentials parameters which thus assess possible energy densities to TiO_2 nano-architectured structures may be capable of integrating. In general, the cell voltage or open-circuit voltage (OCV) is the chemical potential difference between anode the and cathode electrode:

$$V(x) = \frac{\mu_{anode} - \mu_{Cathode}}{e} \qquad 2.26$$

Where e is the magnitude of the charge on the electron, within the anode that is encompassed purely of Lithium/sodium/magnesium metal, the chemical potential is constant and equals to Gibbs free energy of the lithium/sodium/magnesium metal. Electrical energy, E, is obtained by discharging between $A_{x1}TiO_2$ and $A_{x2}TiO_2$ where (A is Li/Na/mg) is calculated by integrating the voltage multiplied by the displaced charge [55]:

$$E = \int_0^{Q_{tot}} V(x)dQ \qquad 2.27$$

$$E = -\left[G\left(A_{x2}TiO_2\right) - G\left(A_{x1}TiO_2\right) - \left(X_2 - X_1\right) G\left(A\right)\right] \qquad 2.28$$

$$E = -\Delta G_r \qquad 2.29$$

The average intercalation potential as a function of lithium intercalated between two intercalation limits x_1 and x_2 ($x_2 > x_1$) is calculated as follows:

$$\overline{V} = -\frac{\Delta G_r}{(X_2 - X_1)F} \qquad 2.30$$

$$\overline{V} = -\frac{G(A_{x2}-TiO_2)-G(A_{x2}-TiO_2)-(x_2-x_1)}{(X_2-X_1)F} \quad 2.31$$

Where G is the Gibbs free energy of the compound, F is the faraday constant, and A is Li/Na/Mg. The Gibbs free energy between the charged and discharged states is given by [56]

$$\Delta \boldsymbol{G_r} = \Delta \boldsymbol{H_r} - \boldsymbol{T}\Delta \boldsymbol{S_r} \quad 2.32$$

where Hr =$\Delta H_r - p\Delta V_r$ is the enthalpy of the system, ΔE_r in its internal energy, P is the pressure, ΔV_r is the charge in volume, T is the simulation temperature and Sr relate of the change in vibrational and configurational entropies of the insertion of the lithium/sodium/magnesium ion. For a quantum mechanical approach such as the density functional, the free energies can be approximated to the internal energies at 0 K because PΔV_r and TΔS_r is much smaller than ΔE_r. Thus equation 2.30 can be approximated to:

$$\overline{\boldsymbol{V}} = -\frac{\boldsymbol{E(A_{x2}-TiO_2)-E(A_{x2}-TiO_2)-(x_2-x_1)E(A)}}{\boldsymbol{(X_2-X_1)F}} \quad 2.33$$

In this study, the simulation model of lithium, sodium, and magnesium intercalation into TiO_2 using the DL_POLY molecular dynamics package is based on Newton's laws where the Li, Ti^{3+}, Ti^{4+}, Na^+, Mg^{2+} and O^{2-} are treated as particulate ions with fixed charge. In this model the term PΔV_r is also much smaller than the internal energy and can be omitted with little error. DL_POLY simulation synthesis at 0 K is not permitted and we thus opted to run our simulations at 1 K instead. DL_POLY does not calculate entropy making it difficult for us to determine if TΔS_r at 1 K is substantial or negligible.

2.6. Intercalation Programme

2.6.1. Overview

The amorphisation and recrystallisation simulation synthesis technique was previously used to generate TiO_2 structures that are amorphous and crystalline with wide and long atom-atom bond length distributions. Thus, it causes an asymmetrical arrangement of TiO_2 atoms resulting in an asymmetrical arrangement of Ti^{4+} and Ti^{3+} crucial for lithium/sodium/magnesium intercalations. An alternative and uncomplicated method presented in Figure 2.1 was utilised since it is strenuous to produce a mathematical formula which carefully recognize all the Ti^{4+} and Ti^{3+} sites. It was developed by Kgatwane K.M using Microsoft Visual C# 2008/2010 software design language where the Li^+, Na^+ and Mg^{2+} insertion programme of amorphisation and recrystallisation generated TiO_2 nanostructures scans identify octahedral coordinate sites along with cations at varying Li^+, Na^+ and Mg^{2+} concentrations. The programme enables intercalations of Li^+, Na^+ and Mg^{2+} ions into TiO_2 polymorphic bulk structures directly into their respective tunnels. The algorithm for detecting coordinative tunnel sites also has the capability of correctly detecting coordinate tunnels sites around the surface of the TiO_2 nanostructures, which consequently allows ion insertion of any surface morphology virtually on all generated TiO_2 nanostructures. The possibility of intercalating a section of the nanosheet, nanoporous and nanosheets is also

permissible. All simulated TiO_2 nanosphere, nanoporous and nanosheet were randomly inserted with varying Li^+, Na^+ and Mg^{2+} ions concentrations where coordinates sites were calculated from the nearest titanium neighbouring atoms.

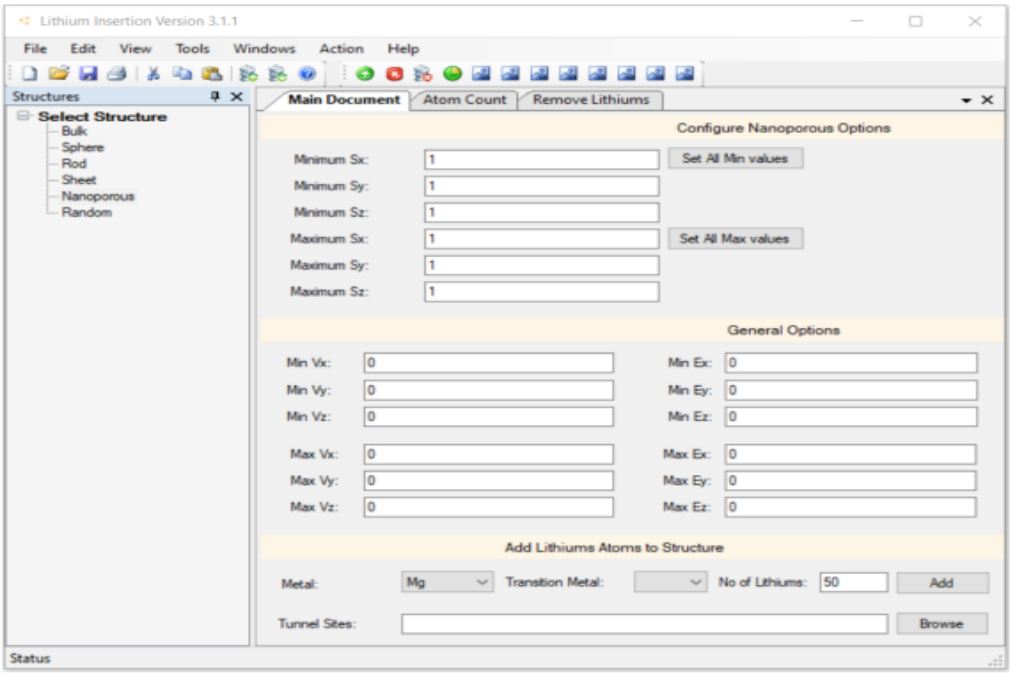

Figure 2.6. Illustrates the main window used for Li^+, Na^+ and Mg^{2+} intercalation program.

2.6.2. Finding Intercalation Sites

The pristine TiO_2 nanostructures are large and comprise 15972 atoms, 5324 titanium atoms and 10648 oxygen atoms. Additionally, they are heavily twinned and noncrystalline making it difficult to easily compute the coordinates of the 1x1 tunnel sites by using the knowledge of symmetry and lattice constants. However, each tunnel is enclosed by four walls of linked edge-sharing TiO_6 octahedral chains with slightly varying distance between the chains. The program uses these twinning octahedral chains to estimate the tunnel sites where lithium ions will be intercalated.

Slicing the TiO_6 octahedral chain planes and rendering the min polyhedral view reveals different the 1x1 tunnel configurations (Figure 6). During intercalation, lithium ions are placed at specific locations in the tunnels, which we denote lithium insertion sites. The estimation of the coordinates of these lithium insertion sites is calculated with the midpoint formula for different tunnel configurations shown in the Figure below.

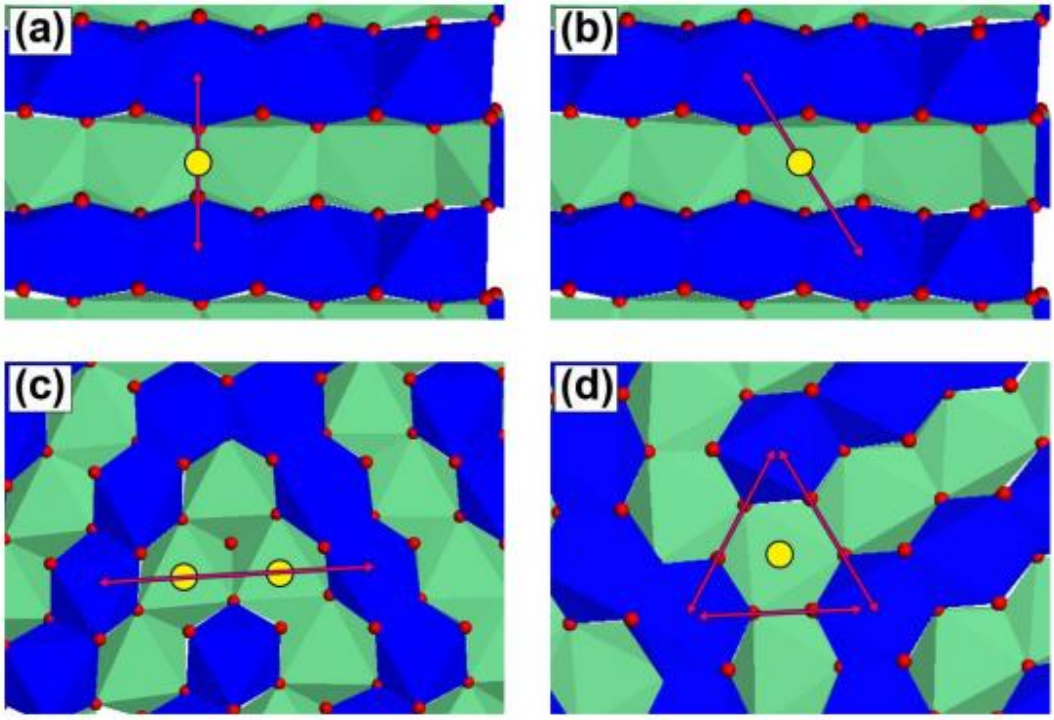

Figure 2.7: slices through the nanostructure showing different tunnel configurations. The yellow circle indicates lithium insertion site.

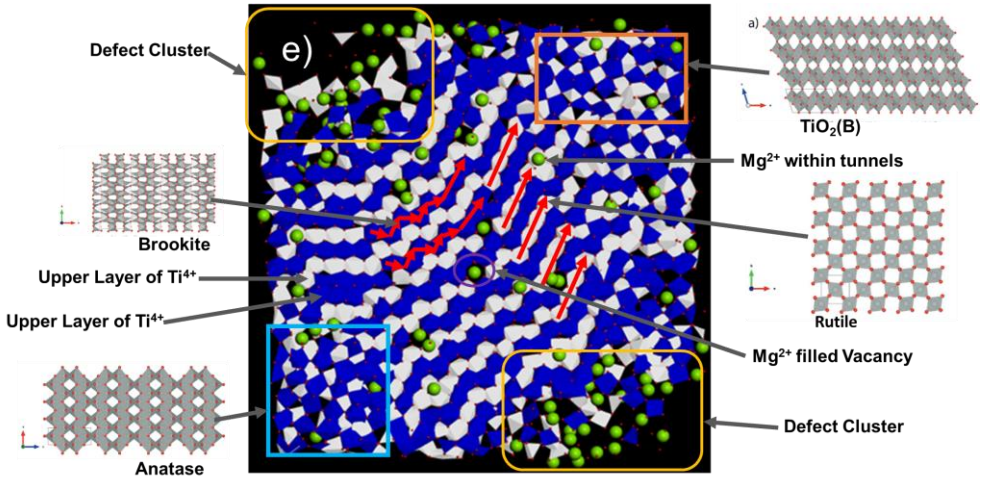

Figure 2.8: Illustrates Interstitial and vacancy defects that exists in $Mg_{0.19}TiO_2$ also on all lithiated, sodiated, and magnesiated TiO_2 nanospheres, nanoporous and nanosheets crystalline patterns on microstructures shown in chapters 3, 4 and 5.

The coordinates of the lithium insertion site (x, y, z) for a tunnel structure in Figure 2.7 (a) is estimated by using the two or three titanium atoms on the same TiO_6 octahedral planes, depicted by the ends of the arrow in the midpoint formula:

$$(\mathbf{x}, \mathbf{y}, \mathbf{z}) = \left(\frac{\mathbf{x_1}+\mathbf{x_2}}{\mathbf{2}}, \frac{\mathbf{y_1}+\mathbf{y_2}}{\mathbf{2}}, \frac{\mathbf{z_1}+\mathbf{z_2}}{\mathbf{2}}\right) \qquad 2.34$$

In Figure 2.7 (b) the estimation of the insertion sites is achieved by applying the midpoint formula twice. Applying the midpoint formula once result in a coordinate in

the middle of the two tunnel sites. Using the newly computed coordinate with the coordinate of one of the manganese atoms at the ends of the arrow in the formula gives the coordinate of the tunnel site (yellow circle):

$$(\mathbf{x},\ \mathbf{y},\ \mathbf{z}) = \left(\frac{\mathbf{x_1}}{\mathbf{2}} + \frac{\mathbf{x_1}+\mathbf{x_2}}{\mathbf{4}}, \frac{\mathbf{y_1}}{\mathbf{2}} + \frac{\mathbf{y_1}+\mathbf{y_2}}{\mathbf{4}}, \frac{\mathbf{z_1}}{\mathbf{2}} + \frac{\mathbf{z_1}+\mathbf{z_2}}{\mathbf{4}}\right) \qquad 2.35$$

In the last case, i.e., in Figure 2.7 (c) I the computation of the tunnel sites is accomplished by using the coordinates of three manganese atoms in the triangle midpoint formula:

$$(\mathbf{x},\ \mathbf{y},\ \mathbf{z}) = \left(\frac{\mathbf{x_1}+\mathbf{x_2}+\mathbf{x_3}}{\mathbf{3}}, \frac{\mathbf{y_1}+\mathbf{y_2}+\mathbf{y_3}}{\mathbf{3}}, \frac{\mathbf{z_1}+\mathbf{z_2}+\mathbf{z_3}}{\mathbf{3}}\right) \qquad 2.36$$

The decision of whether two manganese atoms can be used to compute an insertion site depends on the separation distance between them. The Ti-Ti radial distribution function of the nanostructure provides us with a good estimate of these separation distances.

The program computes the lithium insertion sites by checking the separation distance between each pair of titanium atoms in the range specified by the third, fifth, and ninth peaks in the radial distribution function of a rutile-type structure and using the appropriate form of the midpoint formula. The insertion site is then validated by checking its distance from all atoms within a small cube constructed around the insertion site with dimensions that are slightly larger than the minimum Ti-O (Ti-Ti in rutile-type structure) separation distance. If there is an atom (Ti, O, or Li^+) which is closer to the insertion site by more than 1.6 Å (for pyrolusite) then the insertion site is not valid, and it is discarded. All valid insertion sites are saved in a file that will be used during lithium insertion into various nanostructures.

2.6.3. Intercalation workflows

The program uploads the coordinates of the intercalation sites from the file produced in the previous step, randomly selects a tunnels site, and inserts a cation at a chosen coordinate thus ignoring or by-passing surface intercalation dynamic like surface area, surface terminates, and surface energy barriers. Charge compensation in the structure is achieved by changing the Titanium atoms with 4+ oxidation states (Ti^{4+}) closest to the lithium cation into Jahn-teller active Titanium with 3+ oxidation state (Ti^{3+}). If Li^+ or Mg^{2+} is intercalated then one or two titanium atoms closest to Li^+ or Mg^{2+} ions are reduced to Ti^{3+}. This process is repeated for all the cations inserted into the structure.

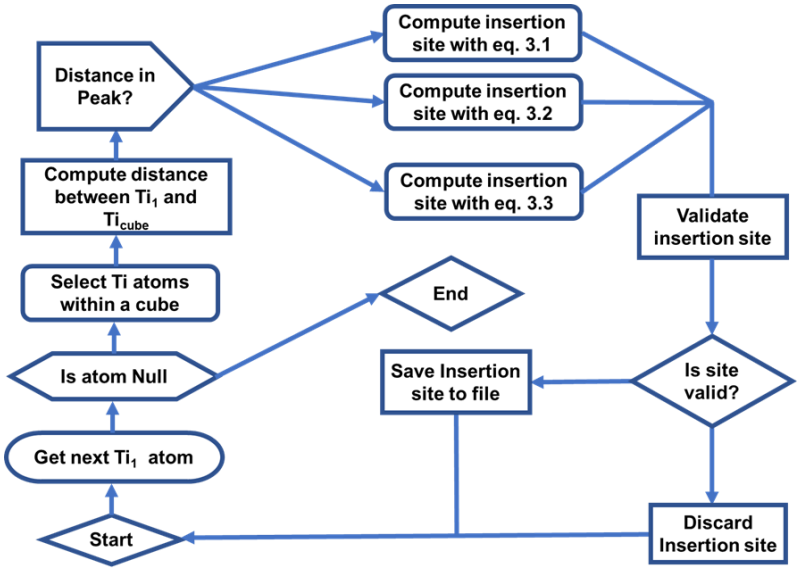

Figure 2.9: Chart showing how the program searches for insertion sites in the uploaded structure.

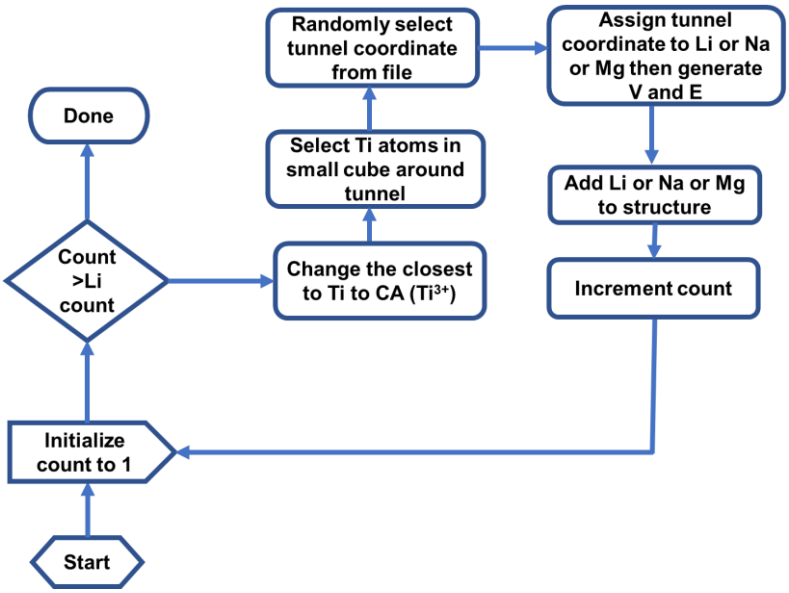

Figure 2.10: A flow chart that indicates the steps taken by the program in the Li, Na and Mg ion intercalation process including charge compensation.

2.6.4. Validation of Intercalations

To validate the intercalation software program and evaluate distributions of intercalated ions, we initially intercalated 0.23Li/Ti into nanosphere, nanoporous and nanosheets architectured structures. A typical 1x1 tunnels found in TiO_2 nano-architectured structures are illustrated in Figure 2.10 where the positions of the octahedral and tetrahedral sites to be intercalated are identified relative to the microstructure's orientation.

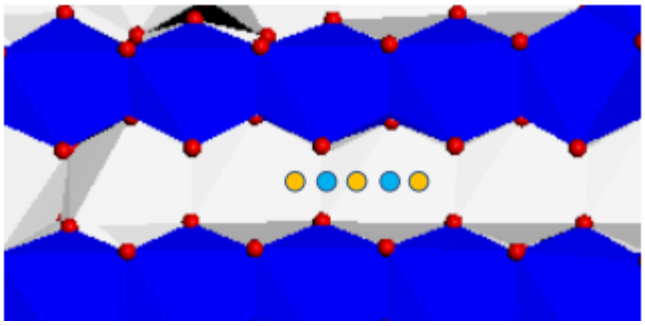

Figure 2.11: Illustrates positions of the octahedral and distorted tetrahedral interstitial sites within the 1x1 tunnel of a rutile structure. Yellow circles represent octahedral sites, whereas cyan circles represent distorted tetrahedral sites.

Microstructure slices cut from nanosphere, nanoporous and nanosheets at 0.23Li/Ti intercalation are shown in Figure 2.7 below. The diagram shows a good placement of lithium ions inside the octahedral sites before molecular dynamics simulations synthesis. Note that the lithium ions can be inserted in two other ways; Li can also be inserted in tetrahedral sites only or in a mixture of tetrahedral and octahedral sites. The ladder is applicable to experimental rutile TiO_2 where the energy difference between the tetrahedral and octahedral sites is small, and the tetrahedral sites are preferable due to their lower energy [59]. In this study, lithiation, sodiation, magnesium at low and high concentrations were achieved by randomly selecting a fraction of the intercalation sites from the total available sites discovered by the program.

Doing this results in an even distribution of lithium cations within the structures. Validating of charge balancing in the nanosphere structure with 0.11 Li/Ti before molecular dynamics simulation synthesis is shown in Figure 2.8 below. It is readily visible that the program perfumed charge compensation, transfer of an electron from lithium ion to neighbouring titanium atom, and property for lithium ions within the red rectangles. Here, each lithium ion is located close to a Titanium 3+ cation lying either on the top octahedral plane represented by a light blue colour or bottom octahedral plane represented by dark green colour. Note that the 1x1 tunnels are closed by four TiO_6 octahedral chains and that the octahedral chains containing Titanium 3+ cations located closer to lithium ions in pink rectangles have been removed to aid clarity. After recrystallisation and cooling synthesis the microstructural visuals contained crystalline polymorphic properties that exist in pure TiO_2 bulk structures illustrated in Figure 2.7 e).

2.7. Atomistic Simulation Details

Computer simulation of matter with atomistic detail has become a very prominent tool in chemistry, physics, life sciences, and material sciences. In this field, simulation results yield the insights needed to interpret experimental measurements that can be used to predict material properties or to design new compounds. Molecular dynamics simulations were all performed using the computer code DL_POLY [166]. DL_POLY is a general-purpose molecular dynamics simulation package continually developed at Daresbury Laboratory by W. Smith and I. T. Todorov under the auspices of EPSRC and NERC in the support of CCP5 [181]. It simulates a wide variety of molecular

systems of ionic liquids and solids, simple liquids, small polar and nonpolar molecular systems, bio- and synthetic polymers, ionic polymers and glasses solutions, simple metals, and alloys. In this work, we used this code to simulate the nanostructures of titanium dioxide. The input files for DL_POLY are CONTROL, FIELD, and CONFIG, which helps us to carry our calculations together with the run script. These mandatory files must be present in the directory when DL_POLY is to run. CONTROL -this file specifies the control conditions for a run of the program. In this file, we specify time step, temperature, pressure, ensemble, Ewald precision, etc. FIELD– defines the force field for the simulation and details of the molecular structures.
CONFIG – defines the positions of all the atoms in the system (in Angstroms) and specifies the simulation cell. It also specifies the atomic velocities and forces.

2.7.1. Potential Model

All atomistic simulation calculation performed in this study were based on the born model of ionic solids. The TiO_2 potentials parameters were previously optimized [151] for the four polymorphs of TiO_2 (rutile, anatase, brookite and TiO_2 II [α-PbO_2 structure]), which then guided us in fitting potential for lithiation, sodiation and Magnetisation to model systems of Ti^{4+}, Ti^{3+}, Li^{+}, Na^{+}, Mg^{2+} and O^{2-} ions to interact via long range coulombic and short-range interaction. These potential parameters were previously used to successfully model the generation of TiO_2 and Li_xTiO_2 (x=0.03, 0.04 and 0.07) bulk, nanosphere, nanoporous and nanosheets sheets through amorphisation and recrystallisation simulation synthesis technique. The parameters for Na-O, Na-Na, Mg-O, and Mg-Mg were fitted to reproduce the lattice parameter and elastic constants of Na_xTiO_2 and Mg_xTiO_2.

2.7.2. Lithium/Sodium/Magnesium Intercalation.

The intercalation program detailed in the prior section was utilised to insert lithium, sodium, and magnesium ions concentration into the nanosphere, nanoporous and nanosheets TiO_2 architectured structures each with 600, 800, 1000 and 1200 corresponding to 0.11, 0.15, 0.19 and 0.23 Li, Na, Mg/Ti fractions respectively. The program uploads the lithium, sodium and magnesium insertion sites from the file produced in the previous step, randomly selects a tunnel site, and inserts a lithium, sodium, and magnesium ion at its coordinates. Charge compensation in the structure is achieved by changing the titanium (4+-oxidation state) closest to the lithium cation into the Jahn-Teller active titanium (3+-oxidation state). This process is repeated for all the lithium ions inserted in the structure. Note that the program randomly selects an insertion site and the corresponding closest trivalent titanium cation, and this can result in different lithium-titanium configurations with different energies. The lithiated, sodiated, and magnesiated structure is not of the lowest energy. To obtain the lowest energy structure, one could intercalate in a Monte Carlo way and then run molecular dynamics simulations on each configuration that would be very time consuming considering the massive size of the nanostructures.

Chapter 3

3. Results and Discussions: Lithium Intercalated TiO_2 Nanoarchitectures

3.1 Recrystallised Structures and Microstructures of Li_xTiO_2 (x=0.11, 0.15, 0.19 and 0.23) nanostructures.

3.1.1. Li_xTiO_2 Nanosphere

Figure 3.1 shows nanosphere structures of a) $Li_{0.11}TiO_2$ b), $Li_{0.15}TiO_2$ c) $Li_{0.19}TiO_2$ and d) $Li_{0.23}TiO_2$. After recrystallization and at higher Li ion concentrations TiO_2 ordered patterns are noted in a), b) and d) but not in c). Moreover, some Li ions have moved/diffused away from the structure at all given concentrations, due to higher electrostatic and repulsive force existing within the Li-Li interactions. Hence, increasing Li ion content within the nanosphere shortens the Li-Li bonds producing intense Li repulsion during and after recrystallisation.

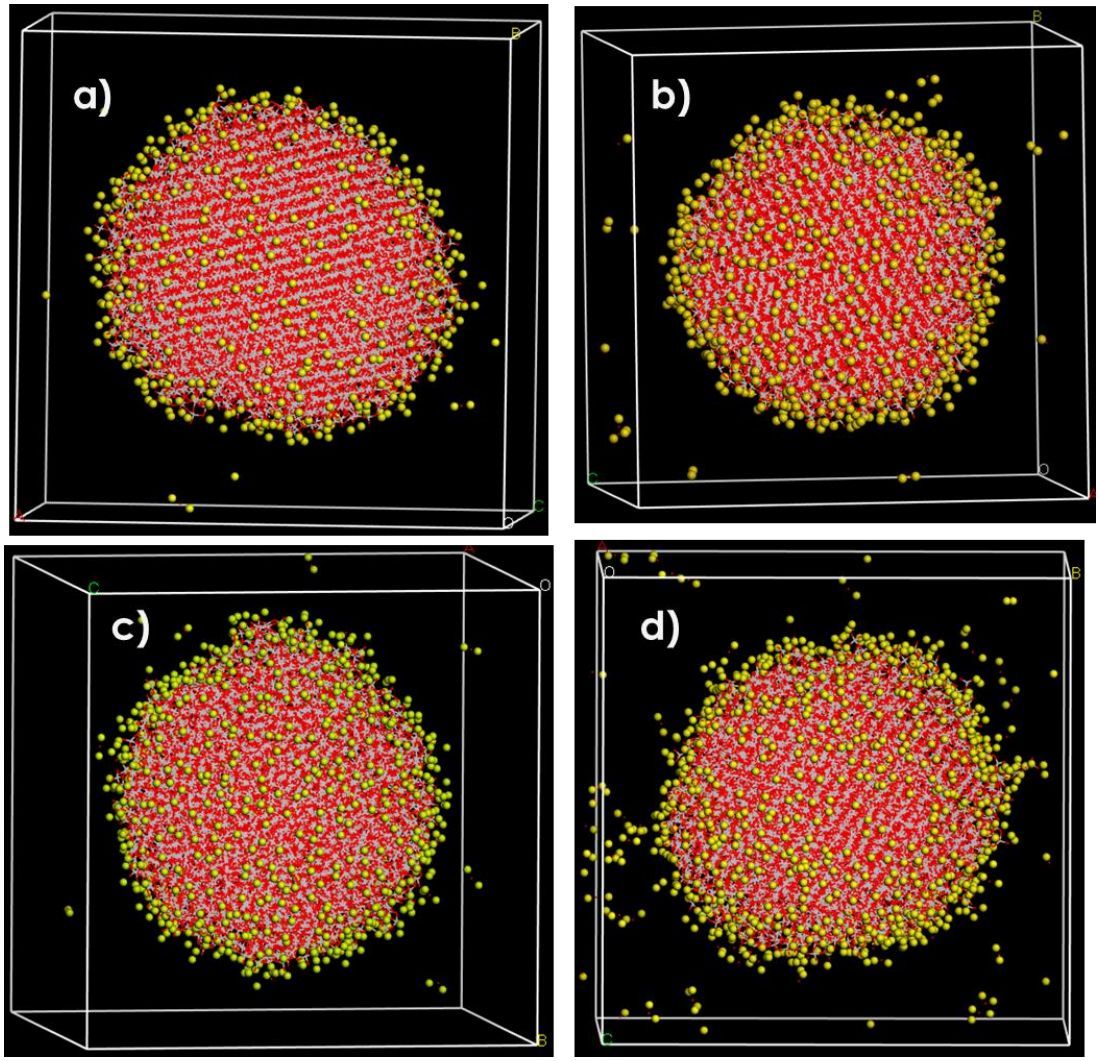

Figure 3.1: Represents nanosphere recrystalised architectures of a) $Li_{0.11}TiO_2$, b) $Li_{0,15}TiO_2$, c) $Li_{0.19}TiO_2$ and d) $Li_{0.23}TiO_2$, respectively.

The recrystallisation on all the nanospheres in figure 3.1 was evident and supported by their microstructural snapshots in figure 3.2 constructed as explained in the methodology section. Figures 3.2 a) $Li_{0.11}TiO_2$, b) $Li_{0.15}TiO_2$, and d) $Li_{0.11}TiO_2$ depict microstructures at different Li concentrations containing zigzag and straight tunnels along with empty and Li filled vacancies, with more Li ions on the edges/surfaces of the microstructures. However, in structure c) a deviant behaviour was noted; the structure did not recrystallise, and this was confirmed by their disordered patterns observed in figure 3.2 c) for $Li_{0.19}TiO_2$. After several trials and errors on the simulated synthesis of a crystalline nanosphere the same results were obtained. The cause of such results could be the size, shape, and imbalances of electron sharing and pairing at a quantum level in the nanosphere.

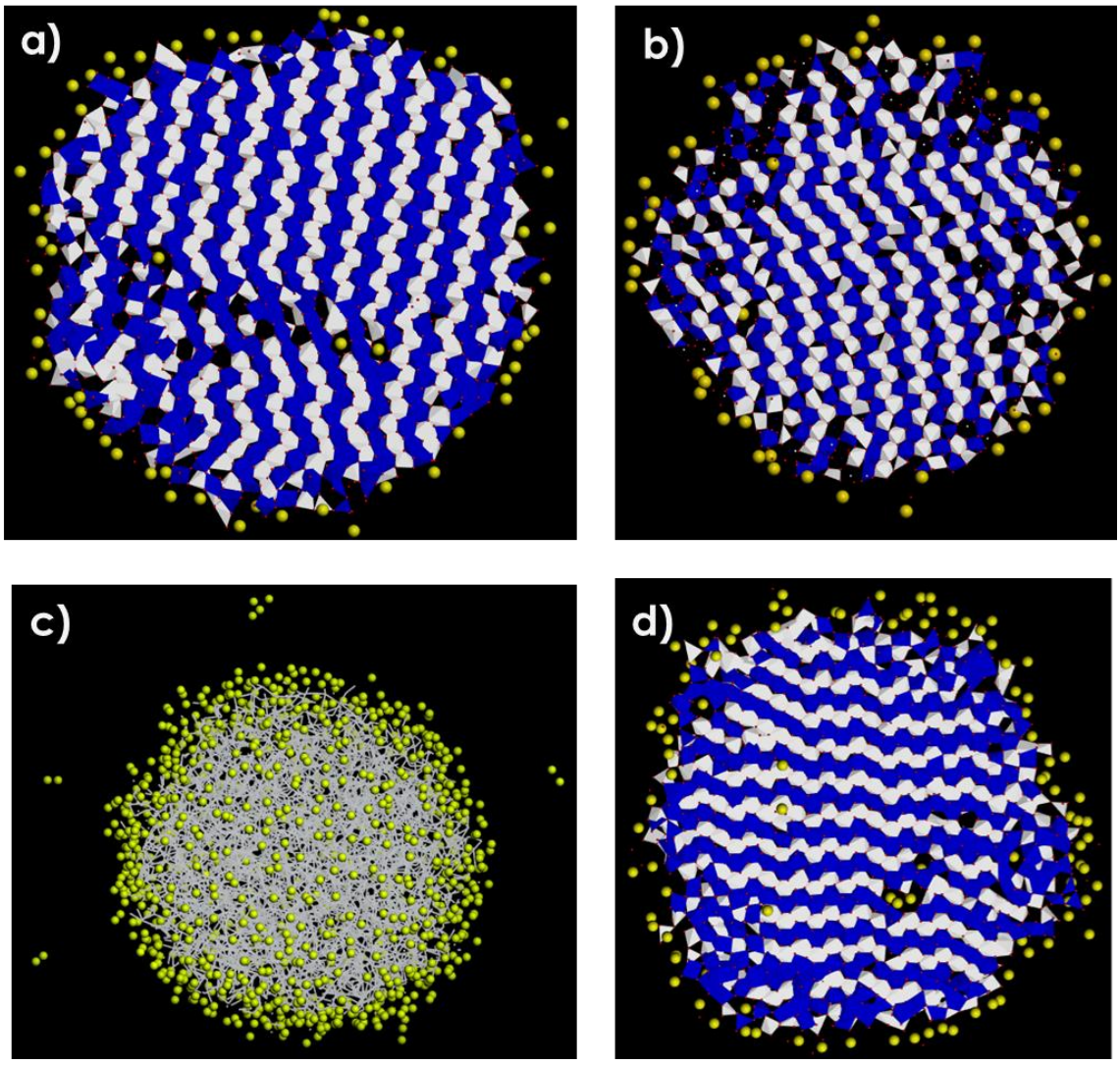

Figure 3.2: Shows recrystallized microstructural snapshots of nanospheres for a) $Li_{0.11}TiO_2$, b) $Li_{0,15}TiO_2$, c) $Li_{0.19}TiO_2$, and d) $Li_{0.23}TiO_2$, respectively.

3.1.2. Li_xTiO_2 nanoporous architecture

Nanoporous structures with different Li concentrations of a) $Li_{0.11}TiO_2$, b) $Li_{0.15}TiO_2$, c) $Li_{0.19}TiO_2$ and d) $Li_{0.23}TiO_2$, given in figure 3.3, were successfully recrystalised. The crystallinity of such structures was evident from a visible ordered pattern with most Li residing around the porous space and inside their structures. The Li content on nanoporous structure c) and d) have closed the porous space more than what is seen on nanoporous a) and b) which is due to the higher Li content in the architecture. Moreover, figure 3.4 gives microstructures of structures a) $Li_{0.11}TiO_2$, b) $Li_{0.15}TiO_2$, c) $Li_{0.19}TiO_2$, and d) $Li_{0.23}TiO_2$ which were constructed to give more evidence of the exact structural appearance after recrystallisation. Consequently, the microstructure on figure 3.4 a) and b) had contain small amount of Li^+ inside the defects because majority of the Li^+ were mostly located within the pore surfaces. The microstructures on a), b), c) and d) have similar characteristics of mostly zigzag (brookite polymorph) and straight (rutile polymorph) tunnels with empty and Li-filled vacancies, which are all

strong characteristics of crystalline structures. Overall, the brookite polymorph is prevalent the rutile phase is apparent in structure b) and most Li content are on the porous surface/edges in all given microstructures.

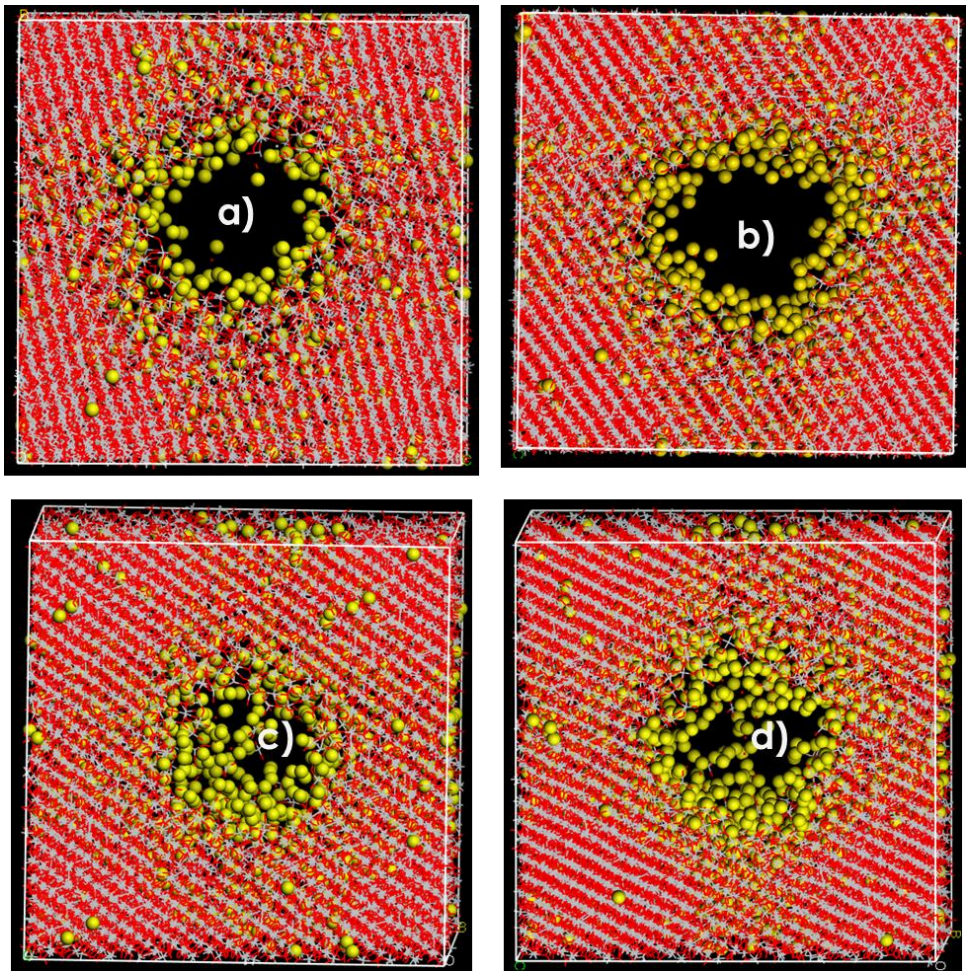

Figure 3.3: Represents recrystalised nanoporous architectures of a) $Li_{0.11}TiO_2$, b) $Li_{0,15}TiO_2$, c) $Li_{0.19}TiO_2$ and d) $Li_{0.23}TiO_2$, respectively.

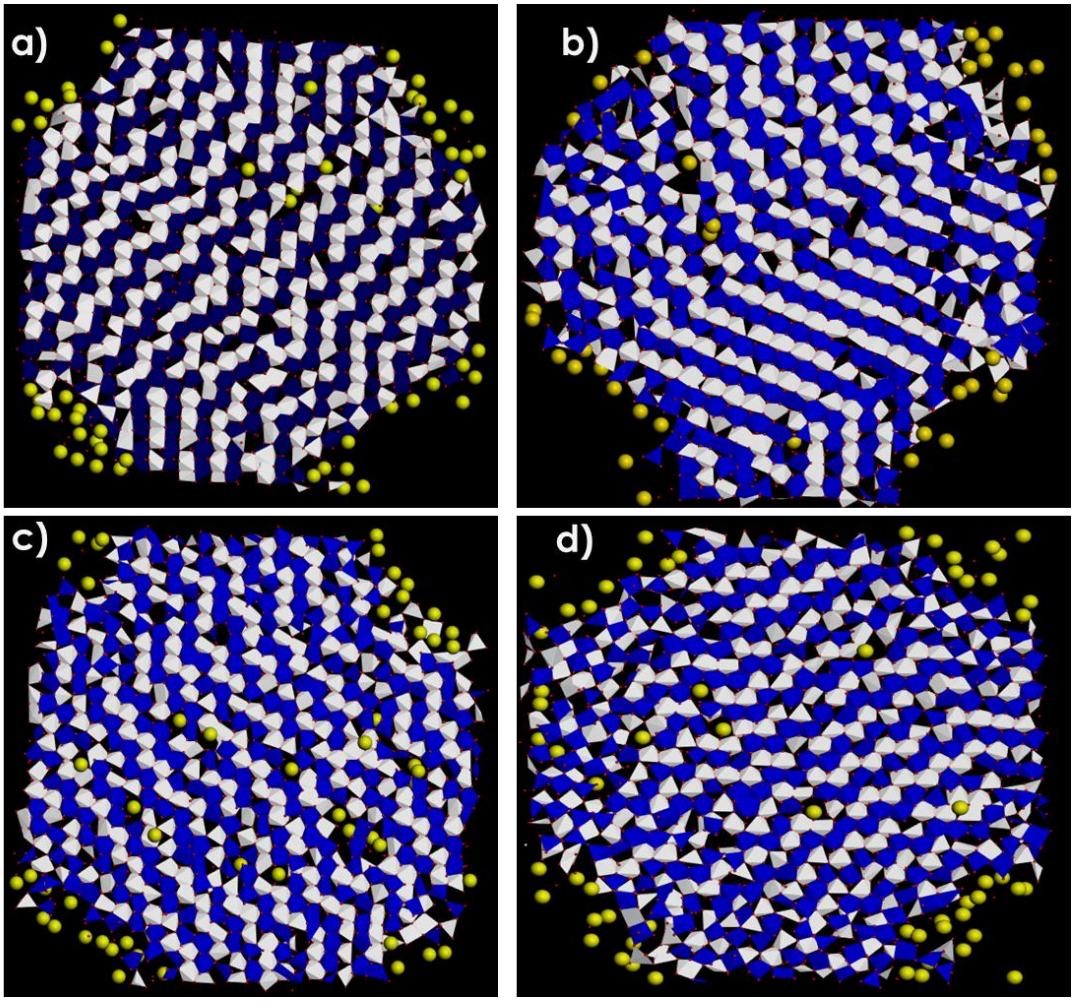

Figure 3.4: Shows recrystallized nanoporous microstructural snapshot for a) $Li_{0.11}TiO_2$, b) $Li_{0,15}TiO_2$, c) $Li_{0.19}TiO_2$ and d) $Li_{0.23}TiO_2$

3.1.3. Li_xTiO_2 Nanosheets

The nanosheet structures, given in figure 3.5 a), b), c) and d), were also synthesised by recrystallization. The observation on all structures given in figure 3.5 has provided the difference that were not evident before recrystallisation where the Li ions are showing to have spread out rather than clustering within the structure, with Li ions diffusing away from the structure in smaller quantities seen on Figure 3.6 a) and b) then higher quantities of Li ions are also seen on c) and d). This could be due to the unavailability and competition of pathways for Li to diffuse through the nanosheets, given the size, shape and atom strain that could be happening inside the structure. Moreover, the microstructure in figure 3.6 a) had lower Li ions when compared to microstructures in Figure 3.6 b),c) and d) this was mainly due to the lower Li content insertions and the equal composition of crystalline and amorphous patterns.

Crystallisation of nanosheets in figure 3.5 was confirmed by viewing microstructural snapshots presented at various Li^+ concentrations in figure 3.6 a), b), c) and d) Crystalline phases are noted at all given concentrations consisting of zigzag and straight tunnels that are associated with twinned rutile and brookite polymorphs; and

are dominant at lower concentrations. Highly disordered portions, or changes in orientations are also observed and become abundant at higher Li concentrations where they occupy half of the snapshot. Most Li^+ ions are accommodated in the latter and on the surface and edges of the microstructures.

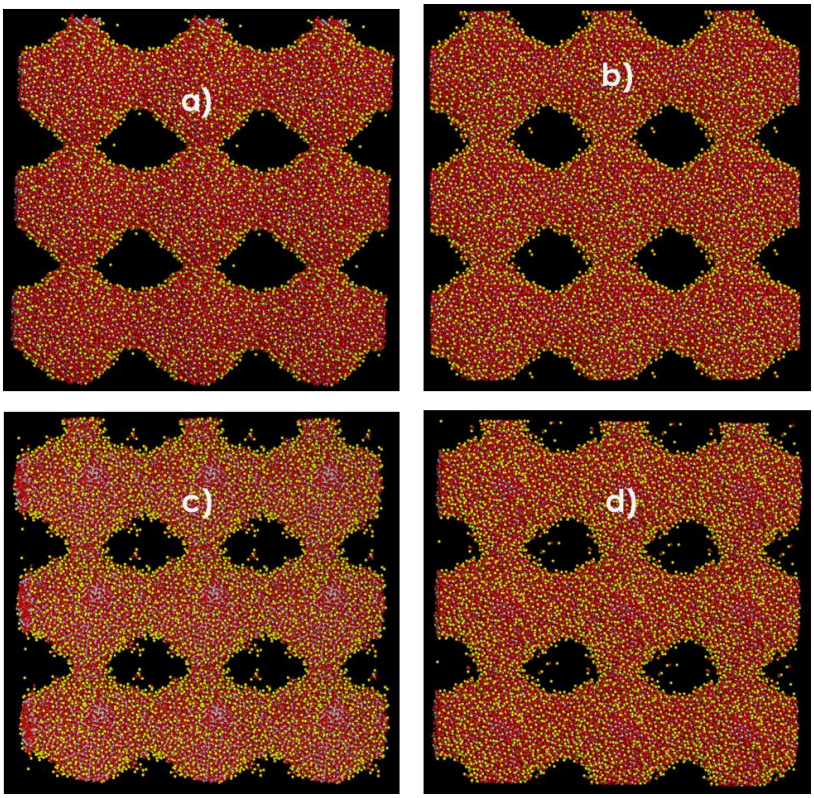

Figure 3.5: Represents nanosheet recrystalised architectures of a) $Li_{0.11}TiO_2$, b) $Li_{0,15}TiO_2$, c) $Li_{0.19}TiO_2$, and d) $Li_{0.23}TiO_2$, respectively.

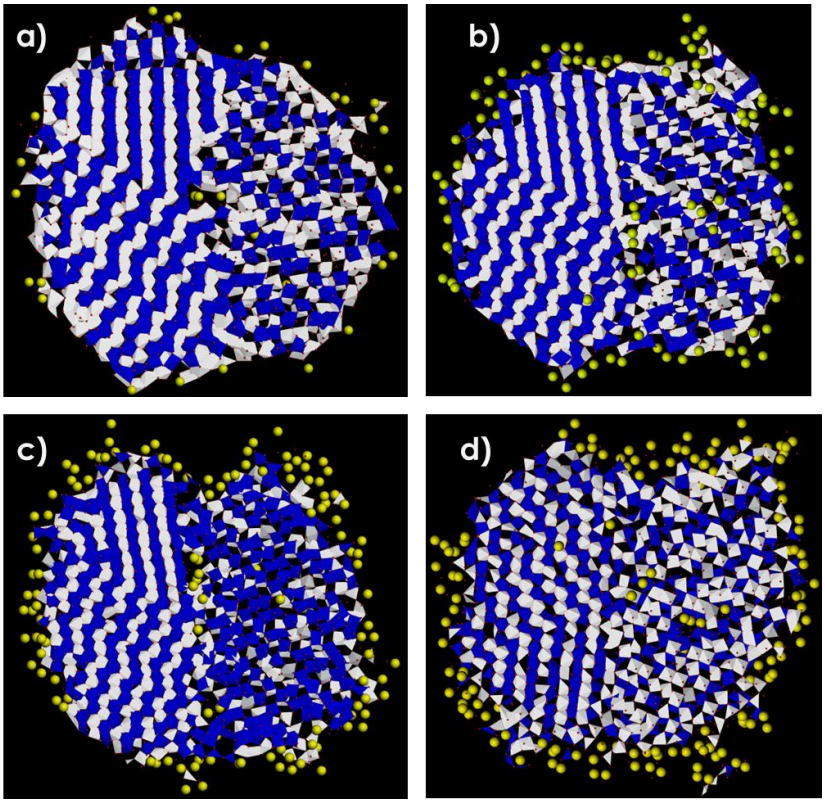

Figure 3.6: Shows recrystallised microstructural snapshots for nanosheets a) $Li_{0.11}TiO_2$, b) $Li_{0,15}TiO_2$, c) $Li_{0.19}TiO_2$ and d) $Li_{0.23}TiO_2$.

3.2. Cooled Structures and Microstructures of Li_xTiO_2 (x=0.11, 0.15, 0.19 and 0.23) Nanostructures.

3.2.1. Li_xTiO_2 nanosphere

Structural variation of recrystallized $Li_{0.11}TiO_2$ nanosphere was studied at different reduced temperatures, namely i) 1500 K, ii) 1000 K, iii) 500 K then iv) 0 K as in figure 3.7. Similar structural patterns are observed in all nanospheres. Their microstructures, in figure 3.8, also confirm similar atomic arrangements. Overall, the microstructures are well defined and better in quality than those at the recrystallization temperature of 2000 K in Figure 3.2 a) through i) to iv) in Figure 3.8. Moreover, straight, and zigzag tunnels corresponding to rutile and brookite, respectively, are visibly showing in Figure 3.8 at i) and ii), then only zigzag tunnels of brookite is only showing in Figure 3.8 at iii) and iv) indicating a rutile polymorph disappearing at lower temperatures. There are also emptier, and Li filled vacancies at iii) and iv) than at i) and ii) along with more Li ions on their edges.

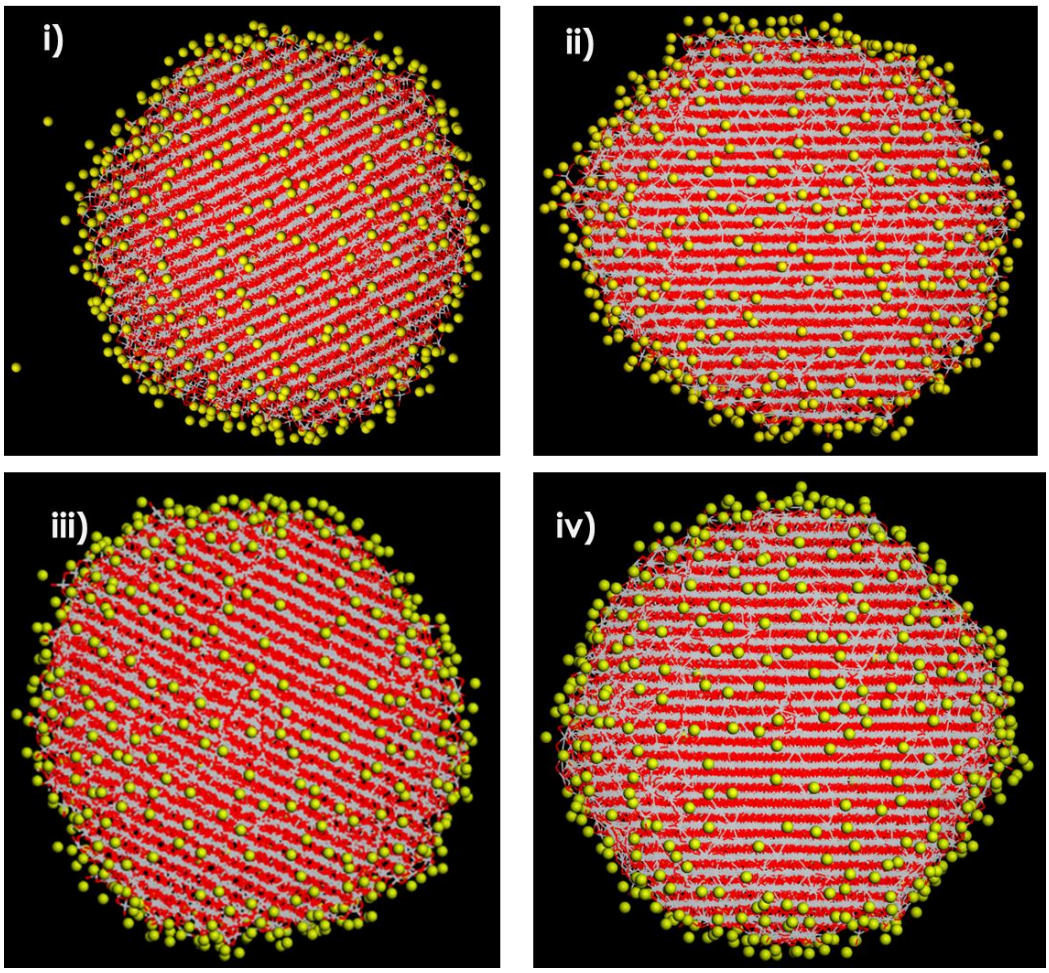

Figure 3.7: Cooled structures of the $Li_{0.11}TiO_2$ nanosphere at i) 1500 K, ii) 1000 K, iii) 500 K and iv) 0 K.

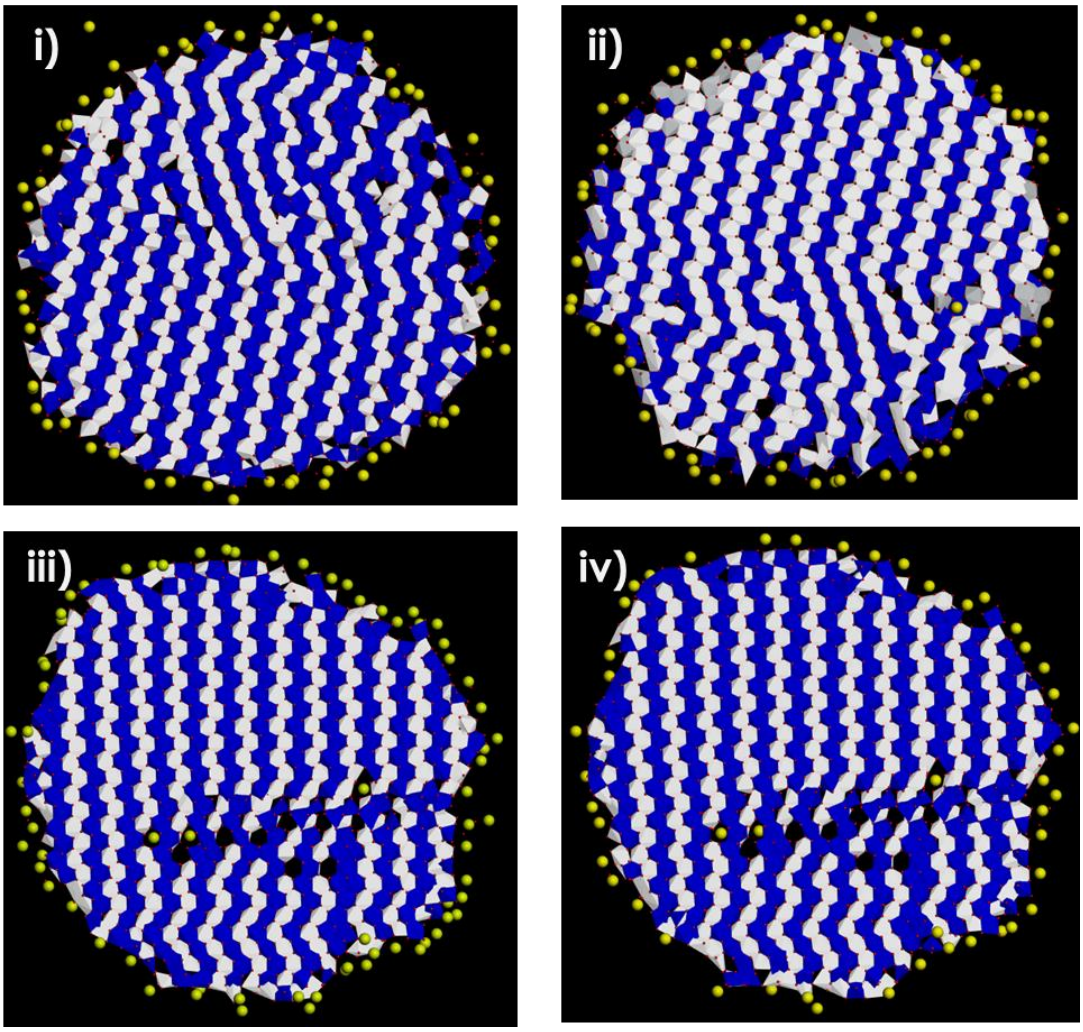

Figure 3.8: Cooled microstructures of $Li_{0.11}TiO_2$ nanosphere at i) 1500 K, ii) 1000 K, iii) 500 K, and iv) 0 K.

Figure 3.9 shows snapshots of nanosphere structures for $Li_{0.15}TiO_2$ at different reduced temperatures, where all structures reflect crystalline patterns. In addition, most Li ions appear to be inside and on the surface of nanospheres at all given temperatures, but only a few seem to have moved away. Their corresponding microstructures in figure 3.10 at i), ii), iii) and iv) strongly support what is noted in figure 3.9 at i), ii), iii) and iv), respectively, where highly crystalline patterns characterised by straight and zigzag tunnels corresponding to rutile and brookite polymorphs along with Li ions in tunnels and Li ions filled vacancies at i), ii) and iv) are present. The cooled structures and microstructures of $Li_{0.19}TiO_2$ nanosphere are hence, not shown owing to their unsuccessful recrystallisation as confirmed in figures 3.1 c) and 3.2 c).

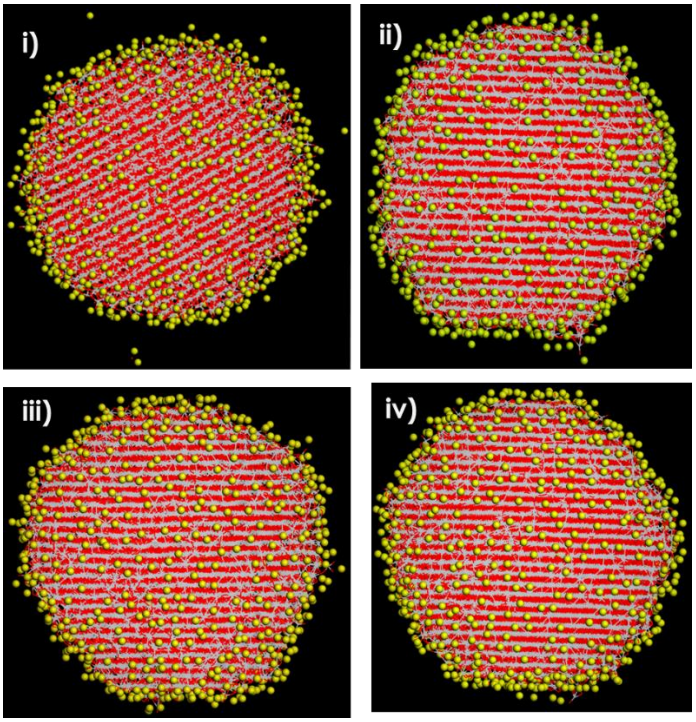

Figure 3.9: Cooled structures of nanosphere $Li_{0.15}TiO_2$ at i) 1500 K, ii) 1000 K, iii) 500 K and 0 K.

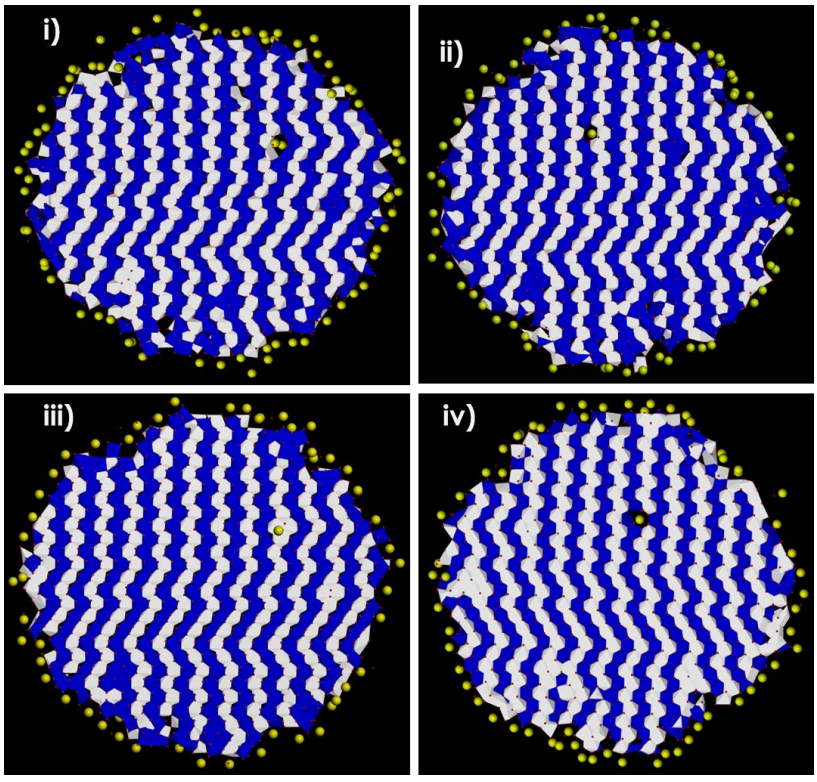

Figure 3.10: Cooled microstructures of $Li_{0.15}TiO_2$ nanosphere at i) 1500 K, ii) 1000 K, iii) 500 K and iv) 0 K.

$Li_{0.23}TiO_2$ nanosphere was also cooled to explore its structural behaviour at lower temperatures as illustrated in figure 3.11. Figure 3.11 i) indicates an accumulation of Li^+ ions on the surface but fewer diffusing away from the surface. However, the structure seems to shrink at this cooled temperature because of the high diffused Li content around and away of its surface. Furthermore, lowering the temperature tends to retain Li^+ on the surface and within the nanosphere, as seen in figure 3.11 ii), iii) and iv). The crystallinity of $Li_{0.23}TiO_2$ of all systems in Figure 3.11 was highly maintained and mainly at low (0 K) temperature synthesis as seen in Figure 3.11 iv), with most Li^+ on the surface and inside the structure. These observations were confirmed by their microstructural slices displaying structural stability from 1500 K to 0 K as noted in Figure 3.12 i), ii), iii) and iv). Also observed are dominant straight and zigzag tunnels associated with rutile and brookite polymorphs, along with empty Ti^{4+} vacancies, Li filled Ti^{4+} vacancies and some Li^+ have occupied the lower Ti^{4+} tunnels. Structural integrity was maintained throughout cooling synthesis in $Li_{0.23}TiO_2$ as seen in its microstructure in Figure 3.12.

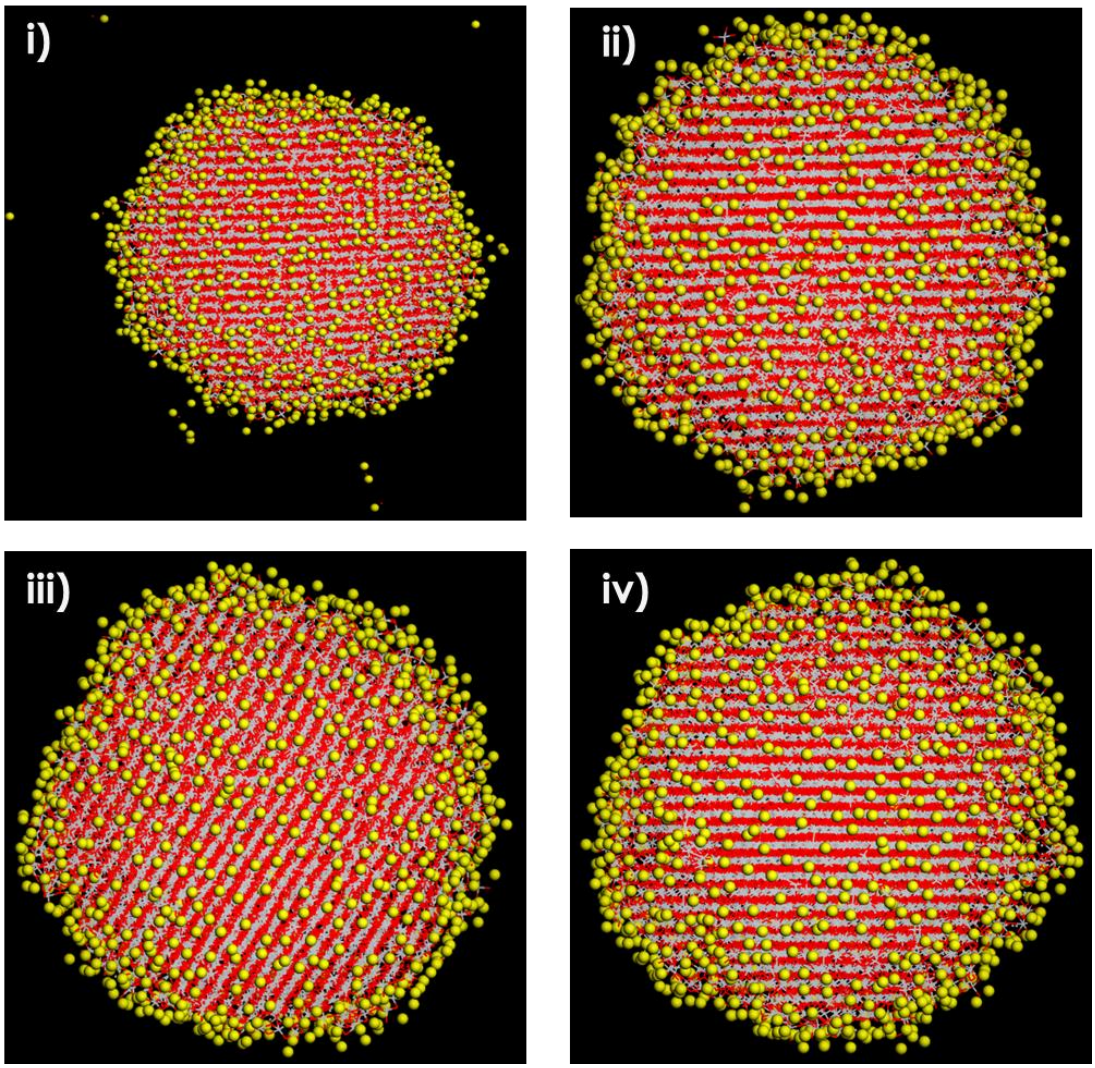

Figure 3.11: Cooled structures of nanosphere $Li_{0.23}TiO_2$ at i)1500 K, ii) 1000 K, iii) 500 K and iv) 0 K.

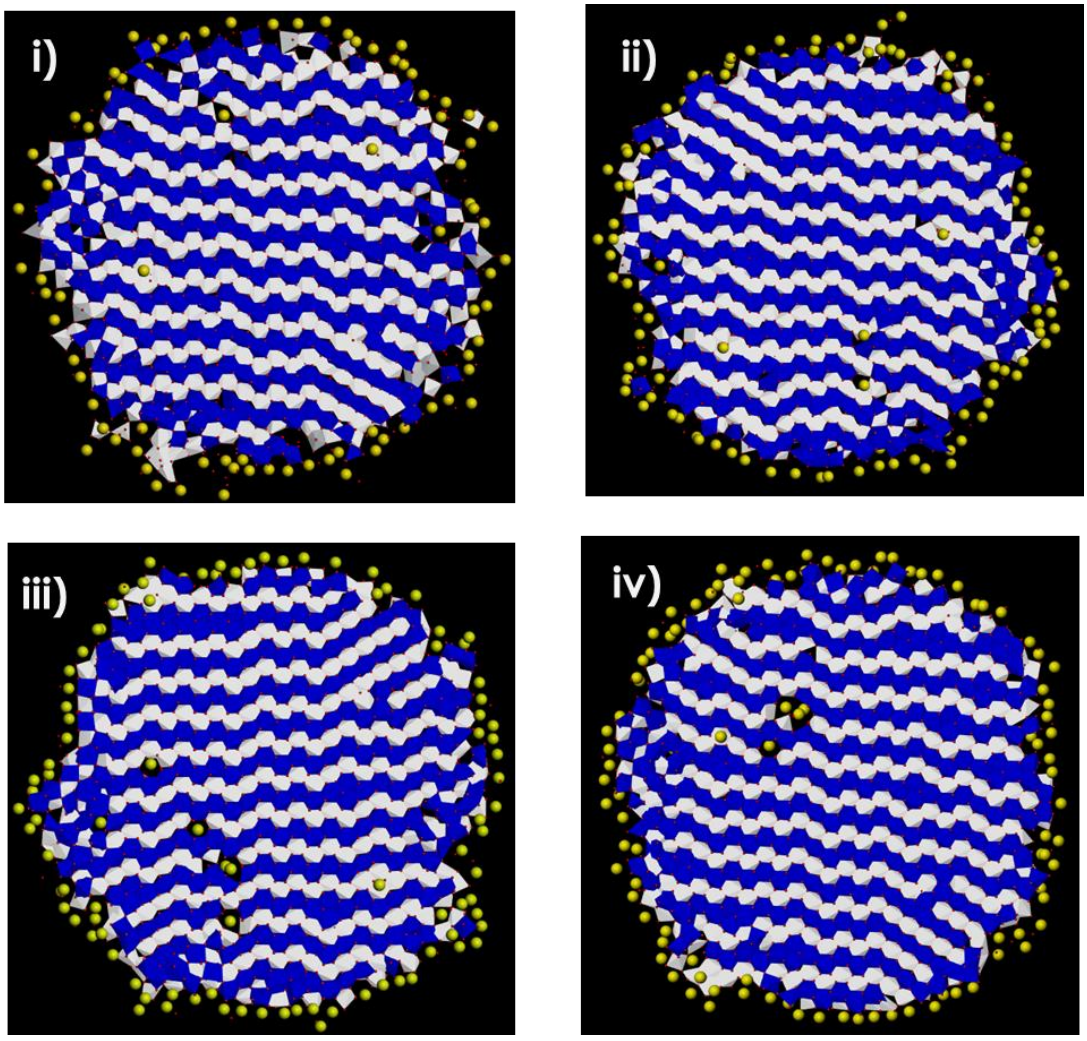

Figure 3.12: Cooled microstructures of nanosphere $Li_{0.23}TiO_2$ at i) 1500 K, ii) 1000 K, iii) 500 K and iv) 0 K.

3.2.2. Li_xTiO_2 Nanoporous

To confirm structural integrity and crystallinity within the nanoporous Li_xTiO_2 system after recrystallisation, the $Li_{0.11}TiO_2$ nanoporous structure in figure 3.3 a) was cooled to temperatures i) 1500 K, ii) 1000 K, iii) 500 K and iv) 0 K as shown in figures 3.13. Such structures provide evidence of crystallinity through ordered TiO_2 patterns from high to low temperatures. More Li^+ settled within pores than in tunnels which will influence its diffusion. The extent of crystallinity in figure 3.13 seems to be increasing with a decrease in temperature and illustrated by their structures in i), ii), iii) and iv) along with their porous opening. Microstructural snapshots of $Li_{0.11}TiO_2$ are shown in figure 3.14. They depict similar crystalline characteristics throughout all reduced temperatures, having zigzag and straight tunnels of rutile and brookite phases along with empty vacancies and Li filled vacancies. However, not many Li^+ ions are residing in the brookite and rutile tunnels.

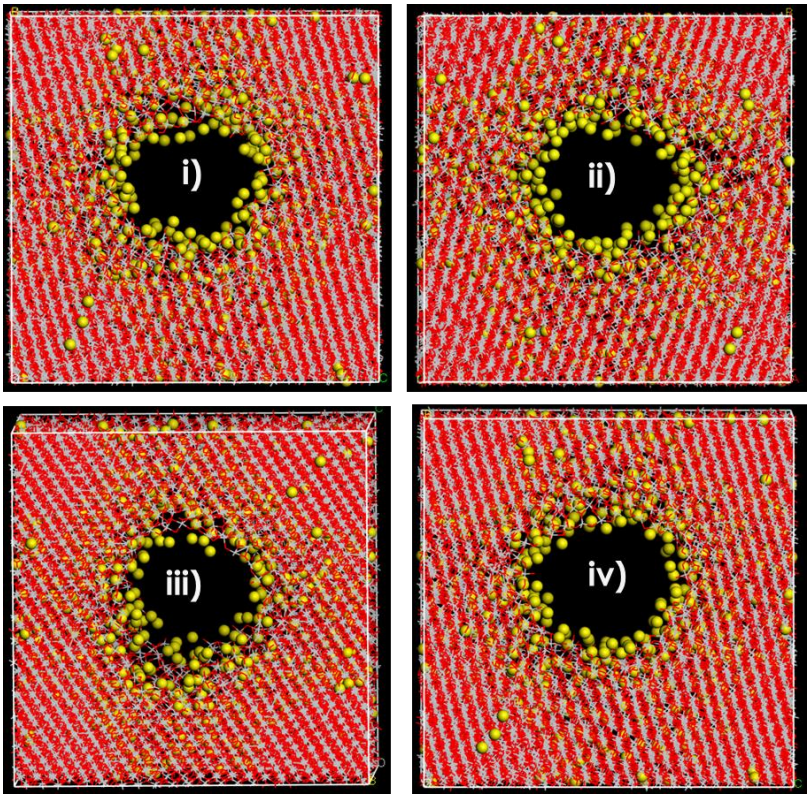

Figure 3.13: Cooled structures of nanoporous $Li_{0.11}TiO_2$ at i)1500 K, ii) 1000 K, iii) 500 K and 0 K.

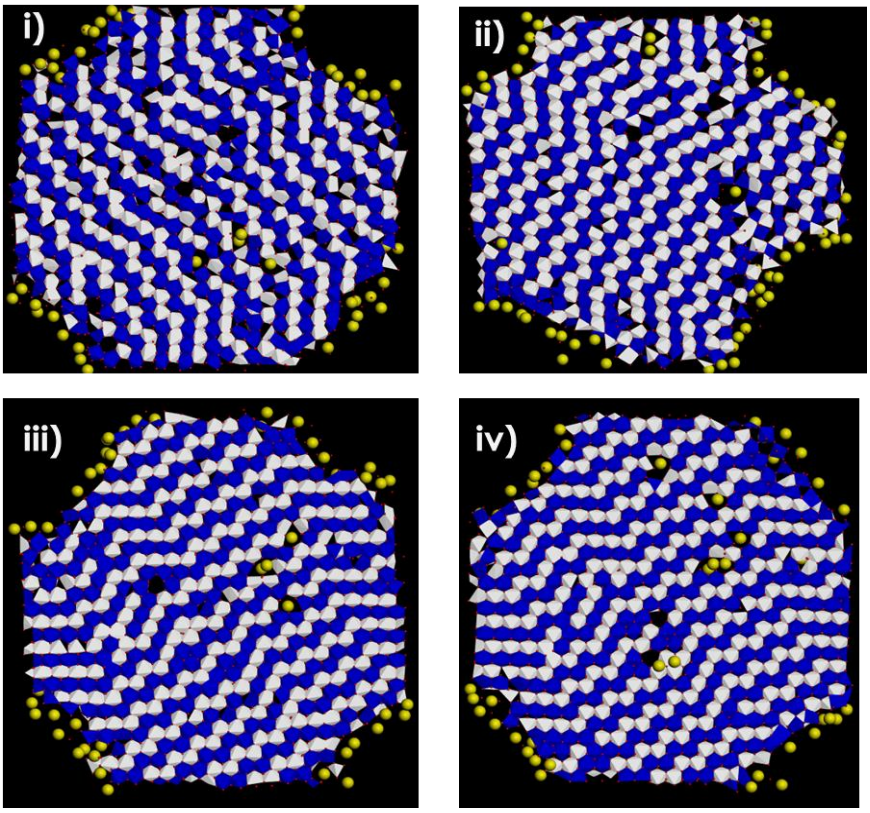

Figure 3.14: Cooled microstructures of nanoporous $Li_{0.11}TiO_2$ at i) 1500 K, ii) 1000 K, iii) 500 K and 0 K.

Figure 3.15 represents the $Li_{0,15}TiO_2$ nanoporous at cooled temperatures from 1500 K to 0 K respectively, at i) 1500 K and ii) 1000 K the nanoporous shows to have some partial aligned crystalline patterns whereas at iii) 500 K and 0 K the nanoporous shows to have well fully aligned crystalline patterns and their porosity is wide open where the Li^+ are situated right at the edges. Therefore, the crystallinity increases with a decrease in the temperature; hence their porosity. The microstructural snapshots in figure 3.16 i), ii), iii), and iv) show two layers of Ti^{4+} tunnels sliced on each structure in figure 3.15 i) ii) iii) and iv) to expose internal atomic arrangements. All microstructures in figure 3.16 have straight and zigzag tunnels, corresponding to rutile and brookite phases, and contain many Ti^{4+} empty vacancies and Li filled vacancies. However, there are fewer Li^+ ions in the tunnels of the microstructures.

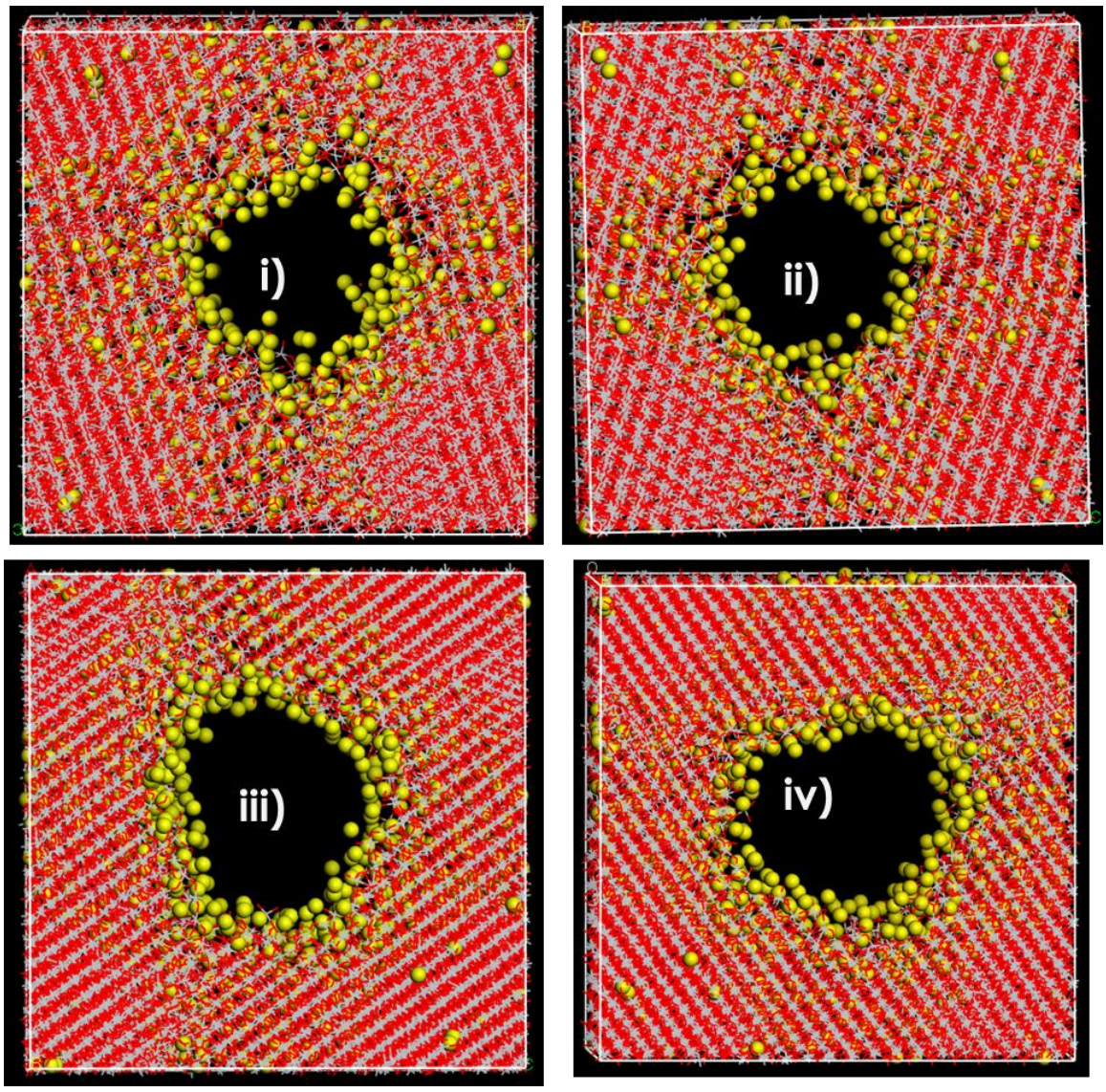

Figure 3.15: Cooled structures of nanoporous $Li_{0.15}TiO_2$ at i)1500 K, ii) 1000 K, iii) 500 K and iv) 0 K.

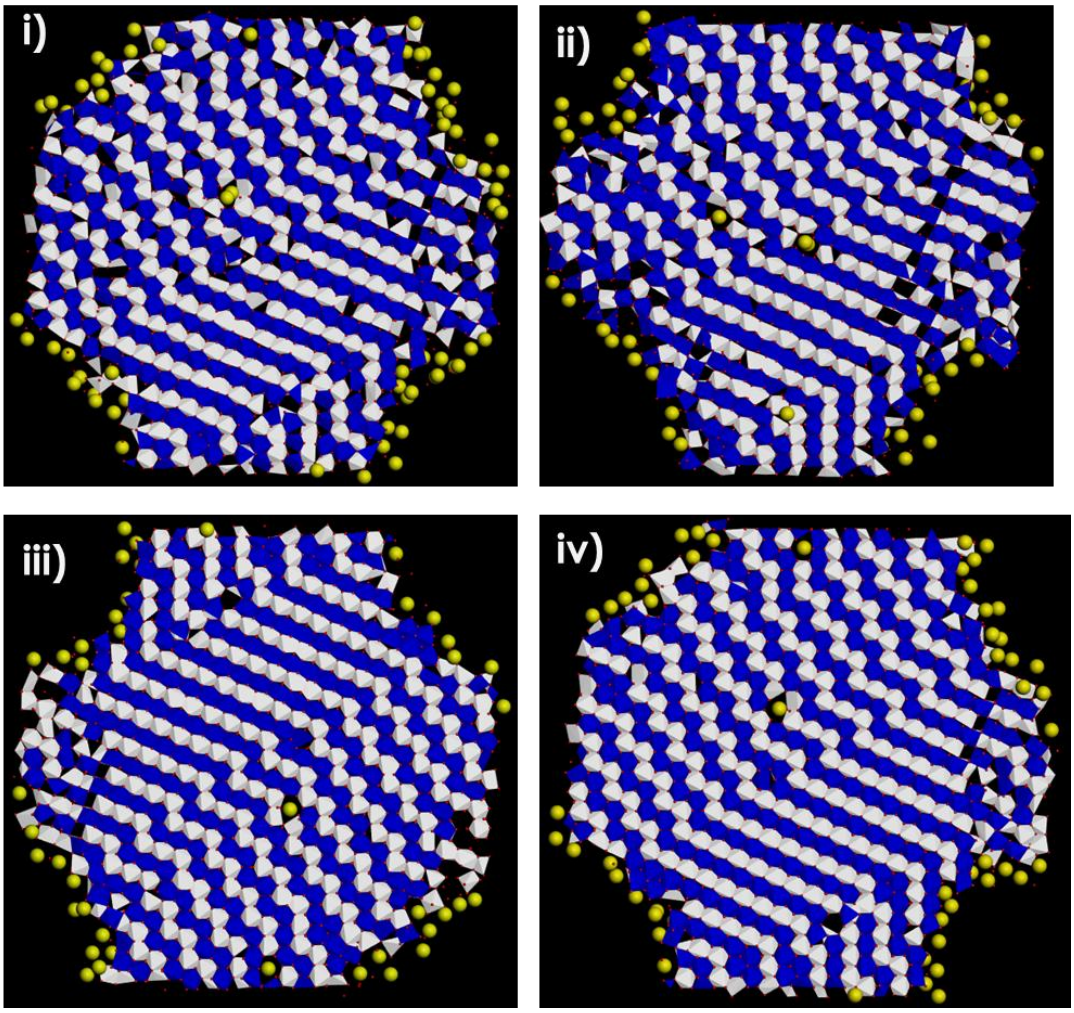

Figure 3.16: Cooled microstructures of nanoporous $Li_{0.15}TiO_2$ at i) 1500 K, ii) 1000 K, iii) 500 K and iv) 0 K.

Increasing the Li^+ content has slight impact on the TiO_2 nanoporous structure. What is noted for $Li_{0.19}TiO_2$, in figure 3.17, has almost similar crystalline patterns as that in figures 3.13 and 3.15. However, the Li^+ arrangements for such structures are unlike the $Li_{0.19}TiO_2$ since the pores are being slightly closed by increased Li^+ content. Similarly, to figures 3.13 and 3.15, the crystallinity observed in figure 3.17 i), ii), iii) and iv) increases with a decrease in temperature. Hence the higher crystalline patterns observed on their microstructural snapshots in figure 3.18 possess dominant zigzag tunnels depicting a strong brookite polymorphs with highly Li^+ filled Ti^{4+} vacancies along with fewer empty Ti^{4+} vacancies. Lastly, more Li^+ ions in $Li_{0.19}TiO_2$ appear in the tunnels of the microstructures at all temperatures, than in nanoporous structures with lower Li concentrations.

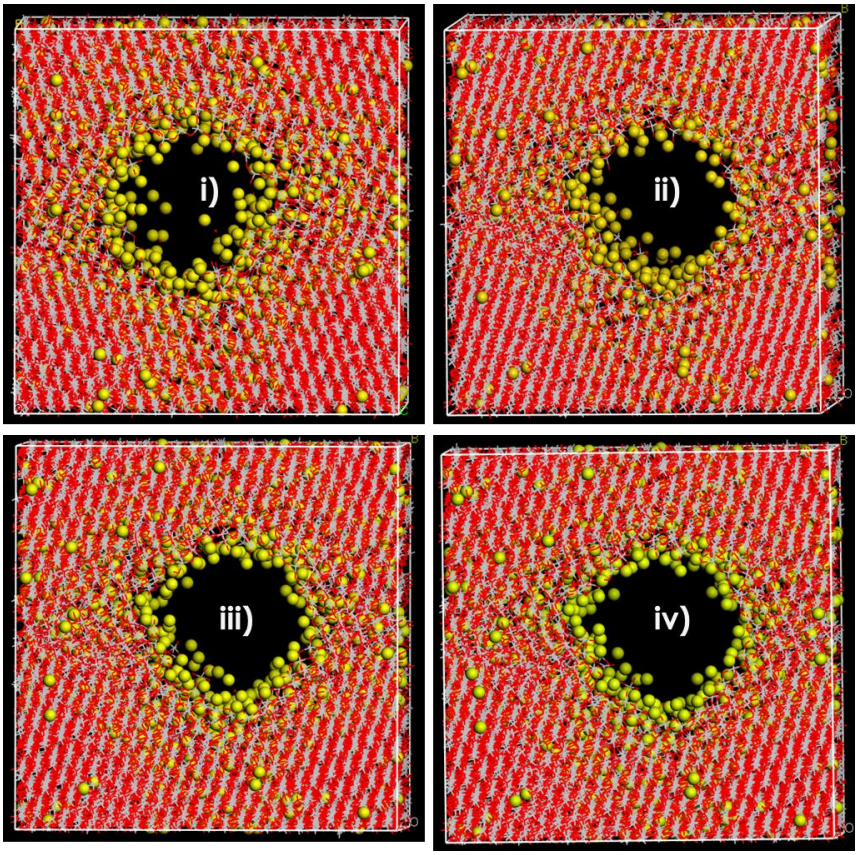

Figure 3.17: Cooled structures of nanoporous $Li_{0.19}TiO_2$ at i)1500 K, ii) 1000 K, iii) 500 K and iv) 0 K.

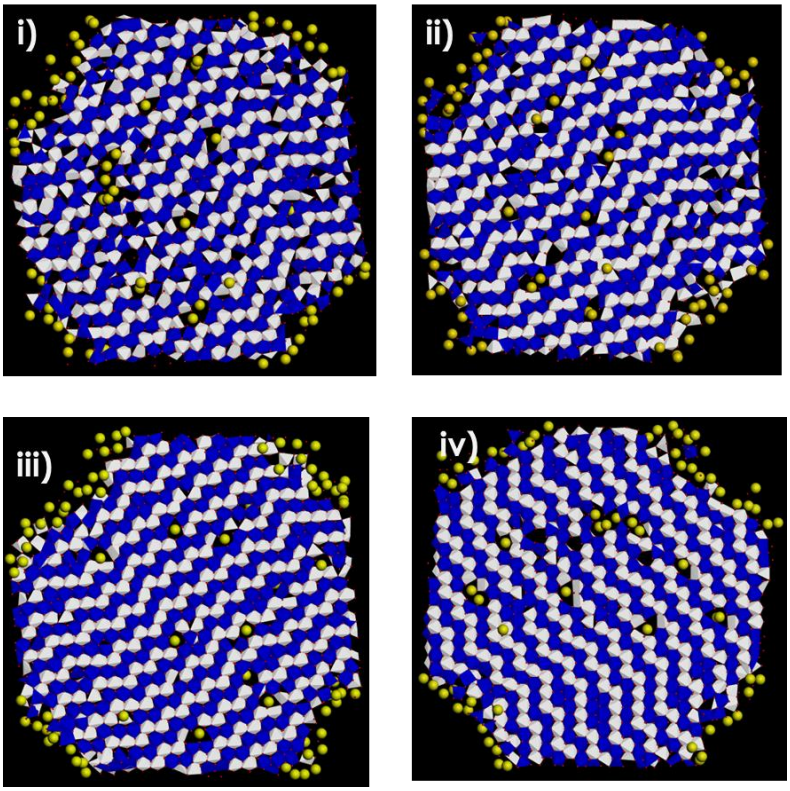

Figure 3.18: Cooled microstructures of nanoporous $Li_{0.19}TiO_2$ at i) 1500 K, ii) 1000 K, iii) 500 K and iv) 0 K.

The highly Li^+ populated recrystalised nanoporous $Li_{0.23}TiO_2$, in Figure 3.3 d), was cooled and resulted in structures shown in Figure 3.19 i) 1500 K, ii)1000K, iii) 500 K, and iv) 0 K . The cooled structures in Figure 3.19 contain highly crystalline patterns at all temperatures, with more Li^+ ions in the pores closing the large opening of the nanoporous structure and maintaining structural stability. The microstructural snapshots reflect sliced Ti^{4+} layers in Figure 3.20 i), ii), iii) and iv). They are also consistent at all low temperatures, showing highly crystalline patterns of straight and zigzag tunnels of rutile and brookite polymorphs, where the latter is dominant. Consistent with $Li_{0.19}TiO_2$ nanoporous structure, we also note more Li^+ ion filled tunnels and vacancies and empty vacancy than in $Li_{0.11}TiO_2$.and $Li_{0.15}TiO_2$.

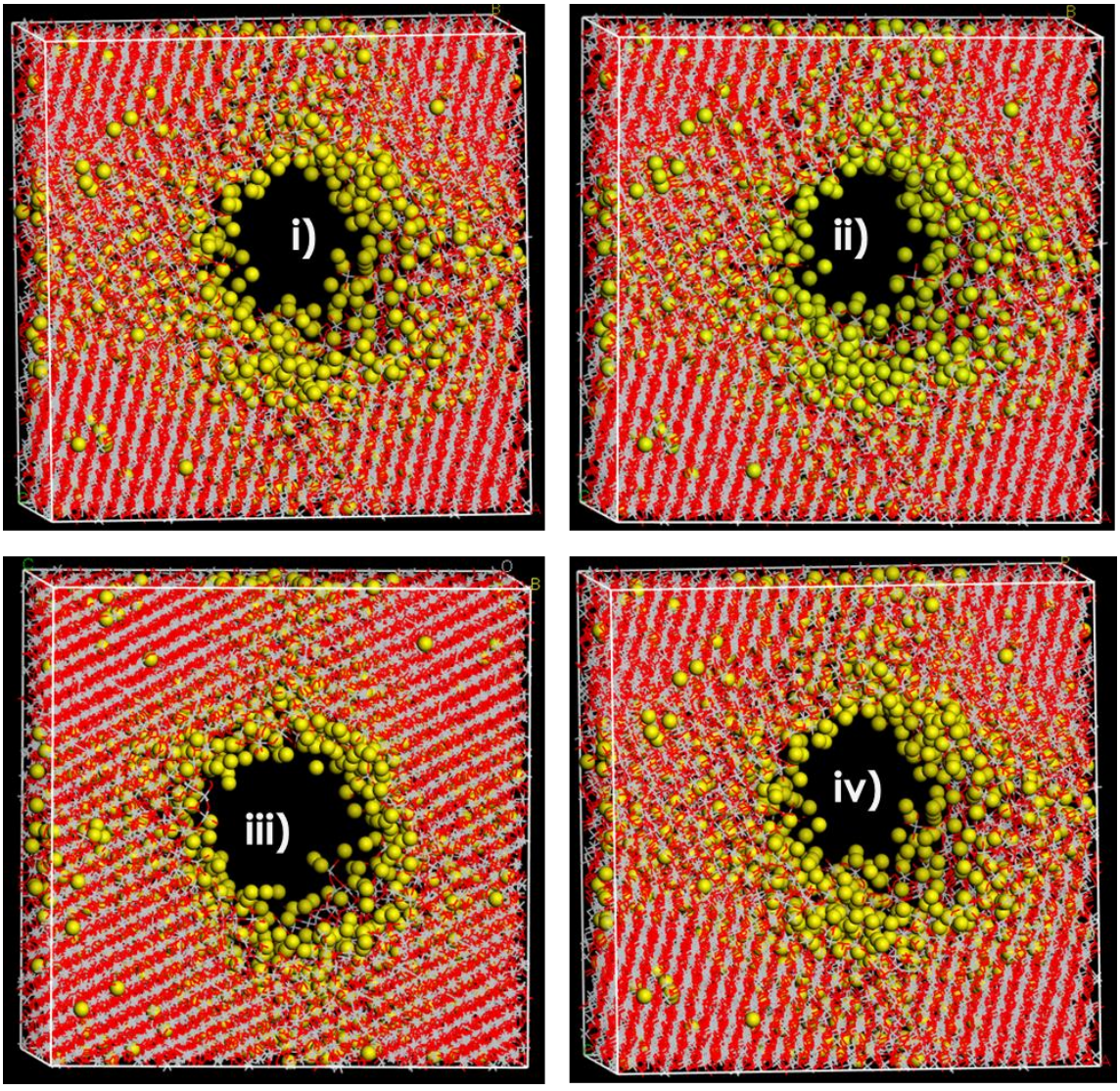

Figure 3.19: Cooled structures of nanoporous $Li_{0.23}TiO_2$ at i)1500 K, ii) 1000 K, iii) 500 K and iv) 0 K.

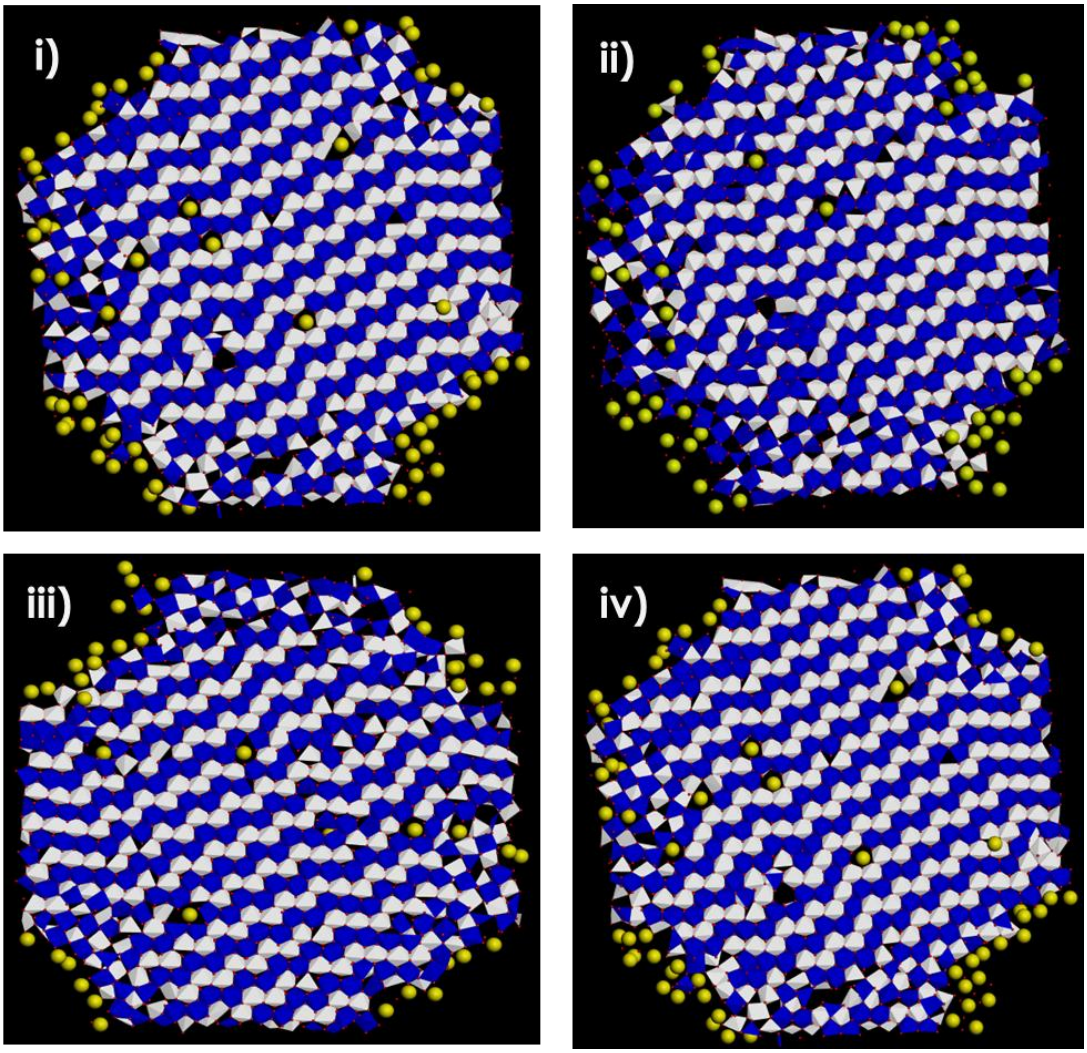

Figure 3.20: Cooled microstructures of nanoporous $Li_{0.23}TiO_2$ at i) 1500 K, ii) 1000 K, iii) 500 K and iv) 0 K.

3.2.3. Li_xTiO_2 Nanosheets

The recrystallized $Li_{0.11}TiO_2$ nanosheet, in figure 3.5, was cooled from 1500 to 0 K The cooled structures at i) 1500 K, ii) 1000 K, iii) 500 K and iv) 0 K are shown in Figure 3.21. Microstructural snapshots in figure 3.22 show 50 % portion that is highly crystalline, with brookite and rutile polymorphs, and the remaining part that is disordered with dislocations, grain boundaries, and intrinsic (point) defect. Li^+ ions are very scarce in the crystalline tunnels and some are noted in the disordered portion of the microstructure; a substantial number resides on the edges and surface of the nanosheet. The variation in temperature does not appear to change the microstructure and its composition significantly.

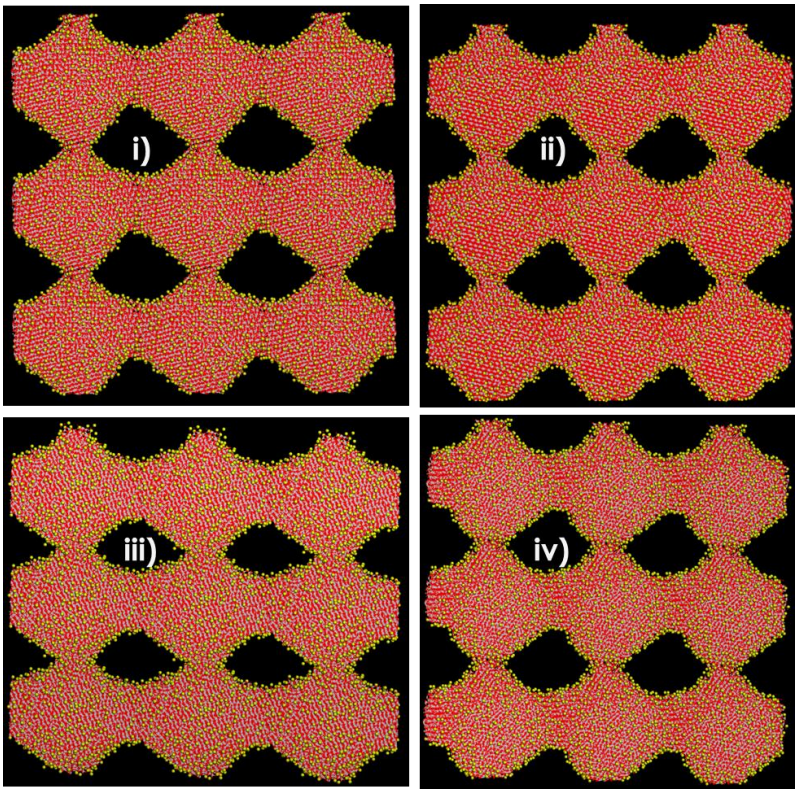

Figure 3.21: Cooled structures of $Li_{0.11}TiO_2$ nanosheet at i) 1500 K, ii) 1000 K, iii) 500 K and iv) 0 K.

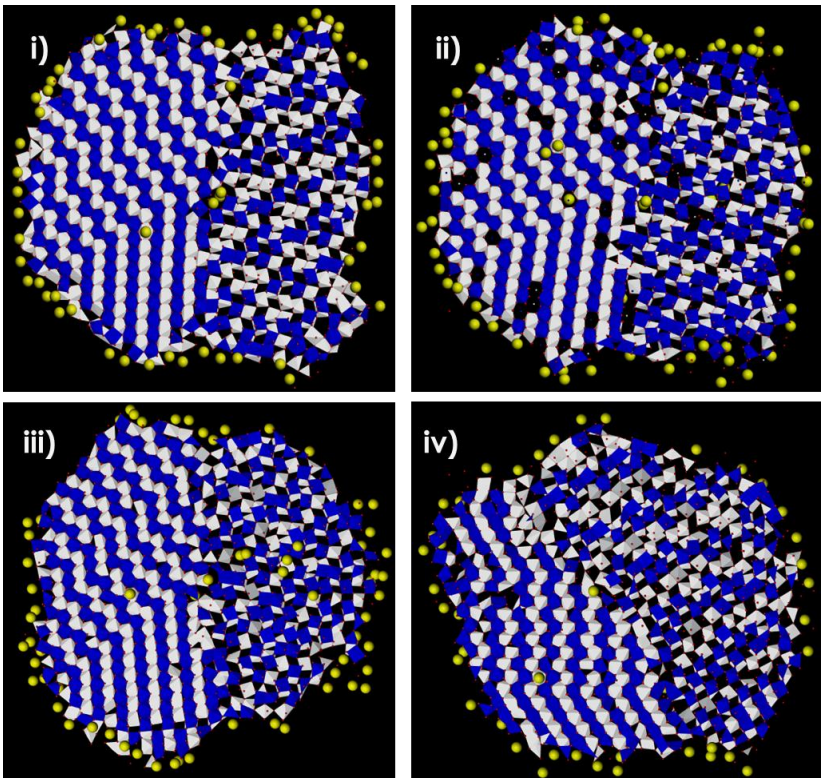

Figure 3.22: Cooled microstructures of nanosheets $Li_{0.11}TiO_2$ at i) 1500 K, ii) 1000 K, iii) 500 K and iv) 0 K.

The recrystallized nanosheets of $Li_{0.15}TiO_2$, $Li_{0.19}TiO_2$ and $Li_{23}TiO_2$ in figure 3.4 ii), iii) and iv) respectively were cooled and resulted in structures that appear in figures 2.23, 2.25 and 3.27 respectively all temperatures i) 1500 K, ii) 1000 K, iii) 1500K and iv) 0 K. Such cooled structures demonstrate similar structural view of Li^+ distribution and arrangement, which only differed by amounts of Li^+ settled inside the systems. However, figure 3.27 i), for $Li_{23}TiO_2$ nanosheet, shows a different Li^+ distribution where it freely diffuses away from the surface owing to its high content when compared to other nanosheets. Furthermore, Li^+ is returns to the nanosheet when the temperature was reduced to 0 K as in figure 3.27 iv). The structural arrangements of the Li_xTiO_2 nanosheets with increase Li^+ contents after cooling were further characterised by their slicing two layers of microstructural planes to observe and study their interstitial Ti^{4+} and Li^+ distributions after cooling simulation synthesis. Microstructural snapshots of the three cooled nanosheets, i.e. $Li_{0.15}TiO_2$, $Li_{0.19}TiO_2$ and $Li_{23}TiO_2$ are shown in figures 3.24, 3.26 and 3.28 respectively. Likewise, all such microstructures contain partial crystalline and partial disordered patterns which host Li^+.

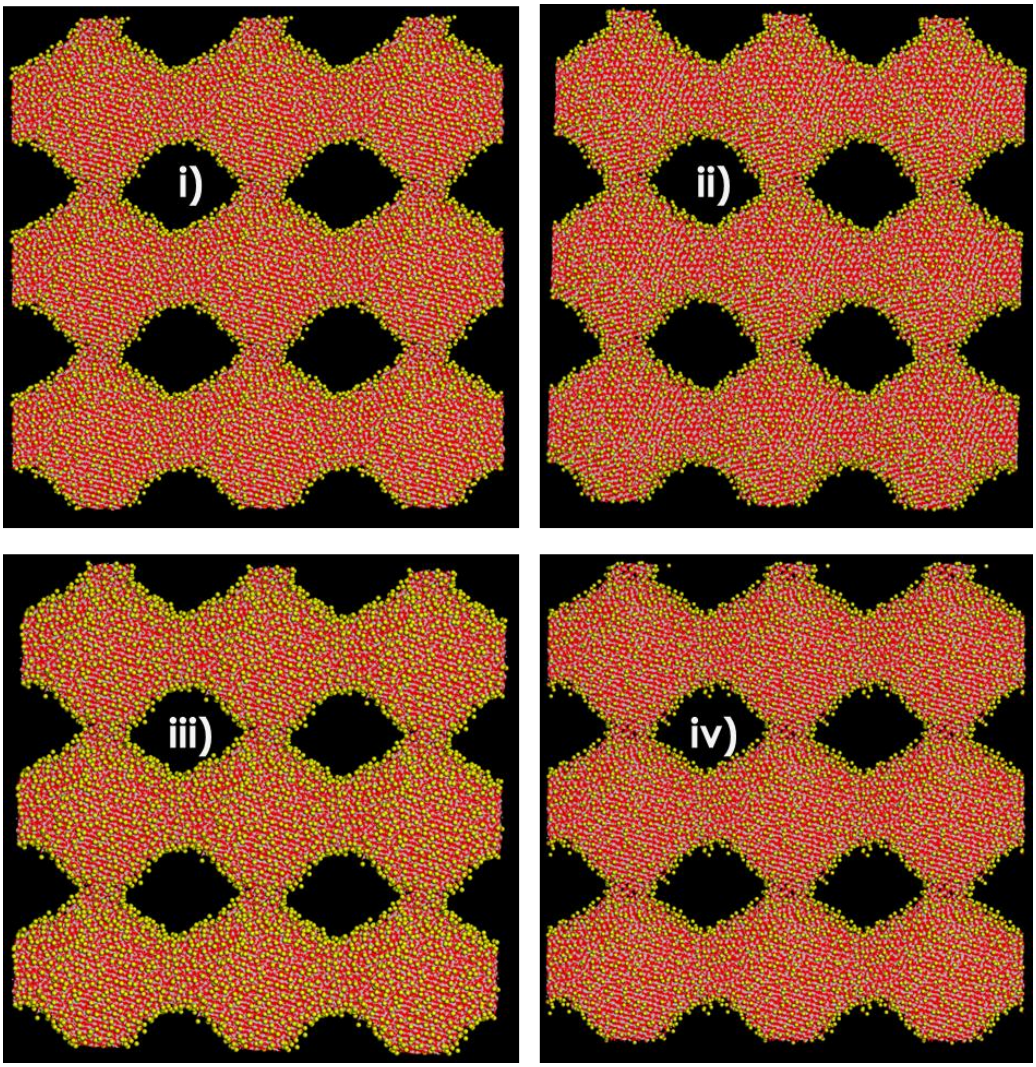

Figure 3.23: Cooled structures of $Li_{0.15}TiO_2$ nanosheet at i)1500 K, ii) 1000 K, iii) 500 K and iv) 0 K.

Tunnels on the microstructure snapshots have straight and zigzag patterns corresponding to rutile and brookite polymorphs, which are mainly seen on the crystalline regions of the microstructure. However, different Ti^{4+} non-crystalline patterns are observed in the disordered region. It is apparent that, at all temperatures, few Li^{+} ions are hosted in the crystalline portion of the microstructure, and many are located on the edge surfaces whilst some settled in the Ti^{4+} vacancies and in the upper and lower tunnels.

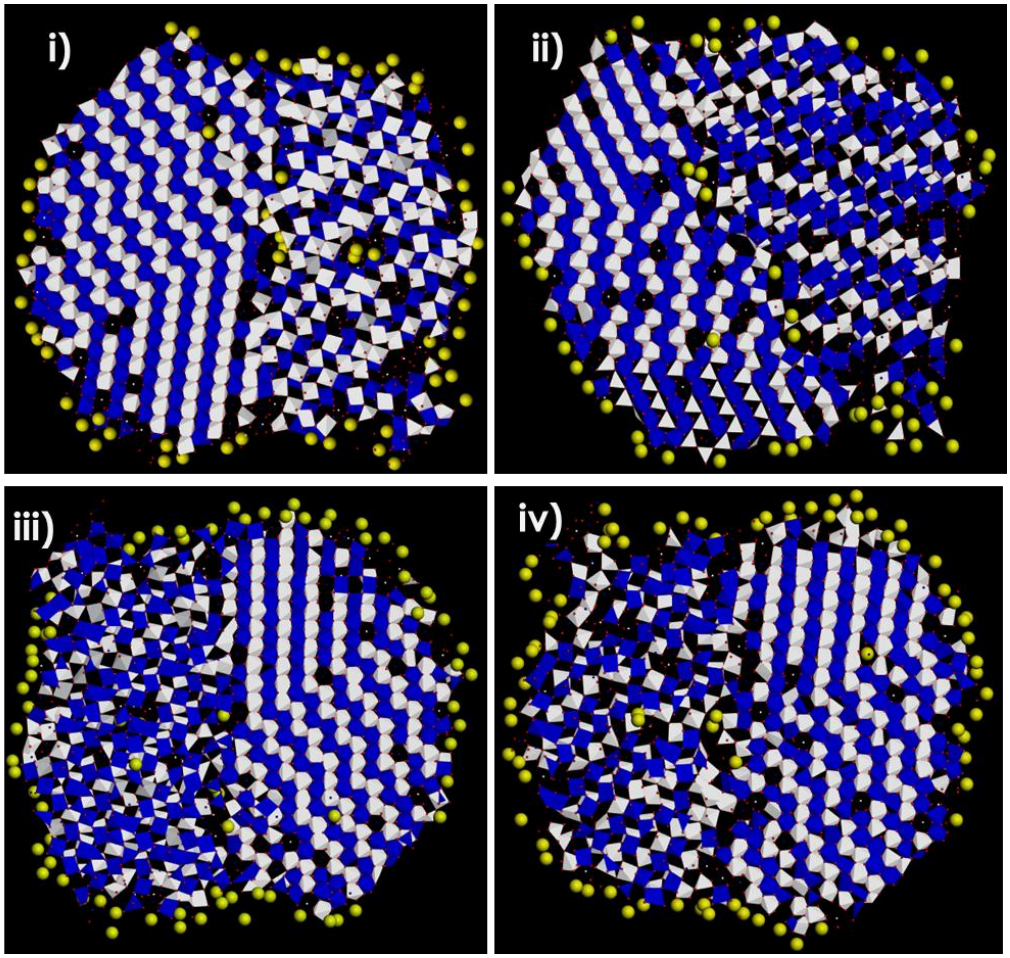

Figure 3.24: Cooled microstructures of $Li_{0.15}TiO_2$ nanosheets at i) 1500 K, ii) 1000 K, iii) 500 K and iv) 0 K.

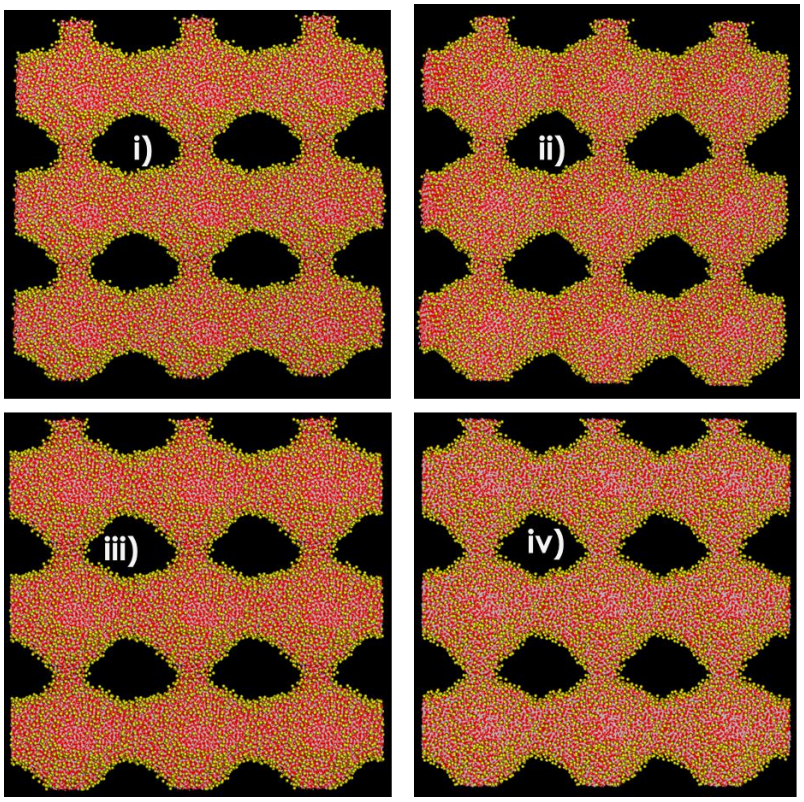

Figure 3.25: Cooled structures of $Li_{0.19}TiO_2$ nanosheet at i)1500 K, ii) 1000 K, iii) 500 K and iv) 0 K.

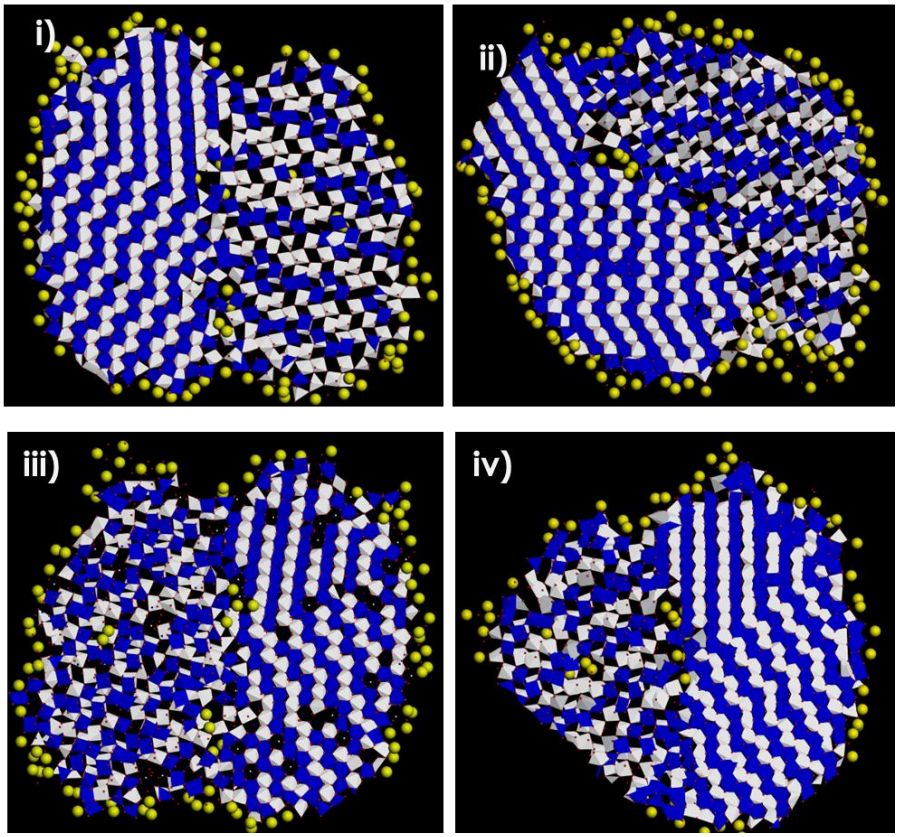

Figure 3.26: Cooled microstructures of $Li_{0.19}TiO_2$ nanosheets at i) 1500 K, ii) 1000 K, iii) 500 K and iv) 0 K.

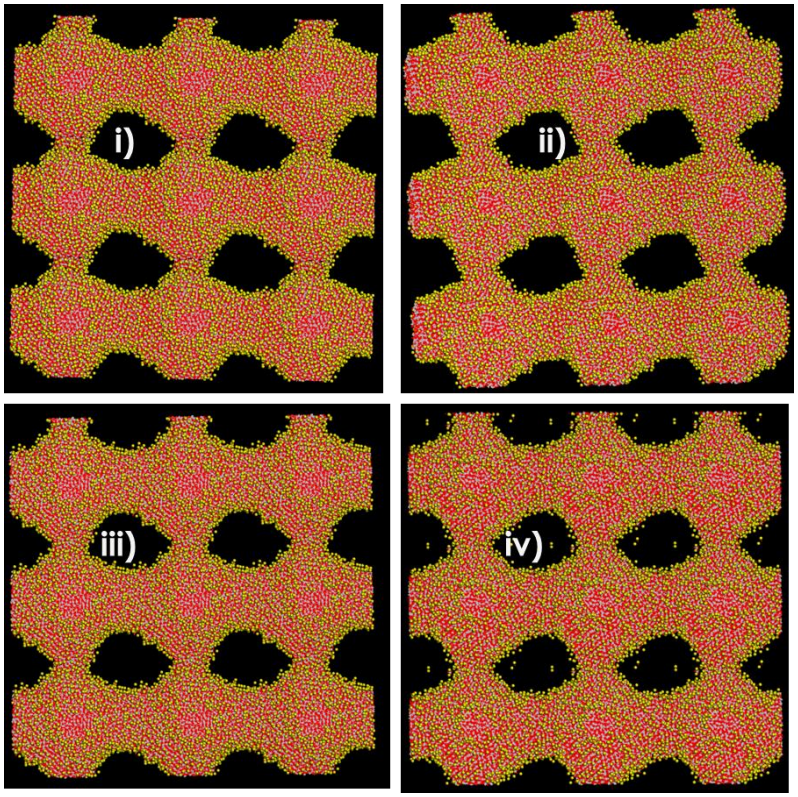

Figure 3.27: Cooled structures of $Li_{0.23}TiO_2$ nanosheet at i)1500 K, ii) 1000 K, iii) 500 K and iv) 0 K.

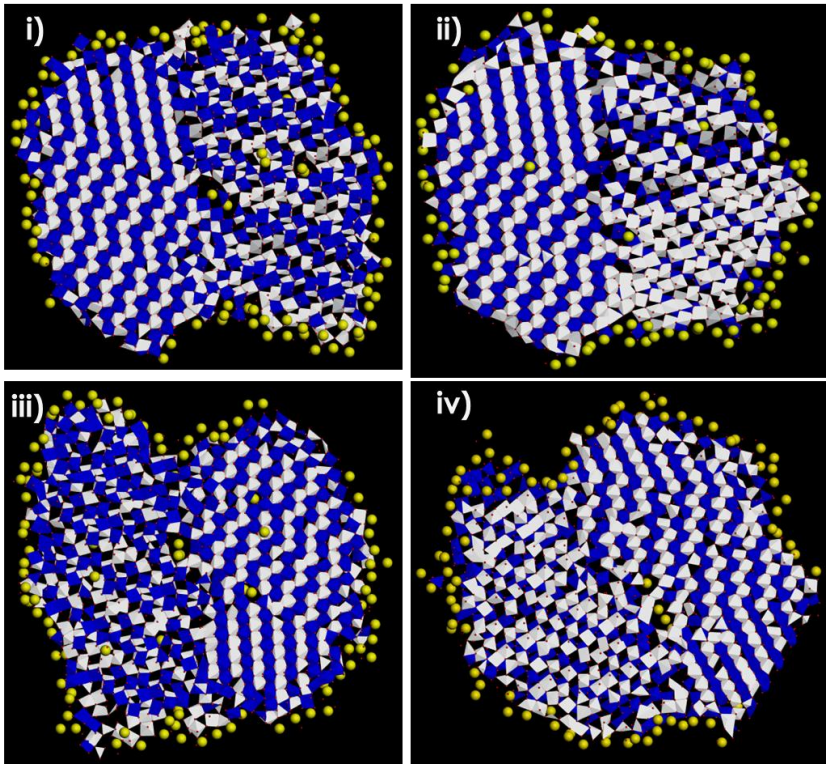

Figure 3.28: Cooled microstructures of nanosheets $Li_{0.23}TiO_2$ at i) 1500 K, ii) 1000 K, iii) 500 K and 0 K.

3.3. RDFs of Li_xTiO_2 (x=0.11, 0.15, 0.19 and 0.23) Nanostructures

The RDFs plots of Li_xTiO_2 nanosphere, nanoporous, and nanosheets, with x=0.11 ,015, 0.19 and 0.23, for Ti-O pairs at 0 K, 500 K,1000 K,1500 K and 2000 K are shown in figures 3.29 to 3.40.

3.3.1. Li_xTiO_2 Nanosphere

The RDFs of Ti-O pairs in $Li_{0.11}TiO_2$, $Li_{0.15}TiO_2$, $Li_{0.19}TiO_2$ and $Li_{23}TiO_2$ nanospheres from low (0 K) to high (2000 K) temperatures are featured in figures 3.29 3.30, 3.31 and 3.32 respectively, consisting of almost 2Å bond length. Total RDFs of the $Li_{0.11}TiO_2$ nanosphere are presented in figure 3.29 (Ti-O). They show similar trend of the peaks throughout the graph, especially near around peak of 2 Å. At peak of 2 Å we observe a clear trend of peaks as the smallest peak corresponds to the temperature of 2000 K, followed by the peak of temperature of 1500 K, followed by the peak of temperature of 1000 K, then peak of 500 K and ultimately a peak of 0K. Throughout the graphs of RDFs we observe a peak of 0 K being the sharpest and highest implying that the system has properly crystallised. Consequently nanosphere peaks between 3Å and 5Å were magnified at all Li^+ concentrations ($Li_{0.11}TiO_2$, $Li_{0.15}TiO_2$, $Li_{0.19}TiO_2$ and $Li_{23}TiO_2$ shown in figures 3.29 3.30, 3.31 and 3.32 respectively) for better viewing also and to confirm the extent of crystallinity from the sharpness of peaks for all temperatures. The $Li_{0.11}TiO_2$, $Li_{0.15}TiO_2$ and $Li_{0.23}TiO_2$ structures were highly crystalline at low temperatures while the order of crystallinity decreased with an increase in temperature i.e., 0 K > 500 K > 1000 K >1500 K >2000 K. However, the $Li_{0.19}TiO_2$ nanosphere was noncrystalline after cooling, as shown in figure 3.31 and its non-crystallinity increased with an increase in temperature i.e., 0 K < 500 K < 1000 K <1500 K<2000 K. Consequently, structural crystallinity within TiO_2 nanosphere could be maintained at varied temperatures and Li^+ concentrations, except for $Li_{0.19}TiO_2$, suggesting it to be good for anode electrodes in Li-ion batteries.

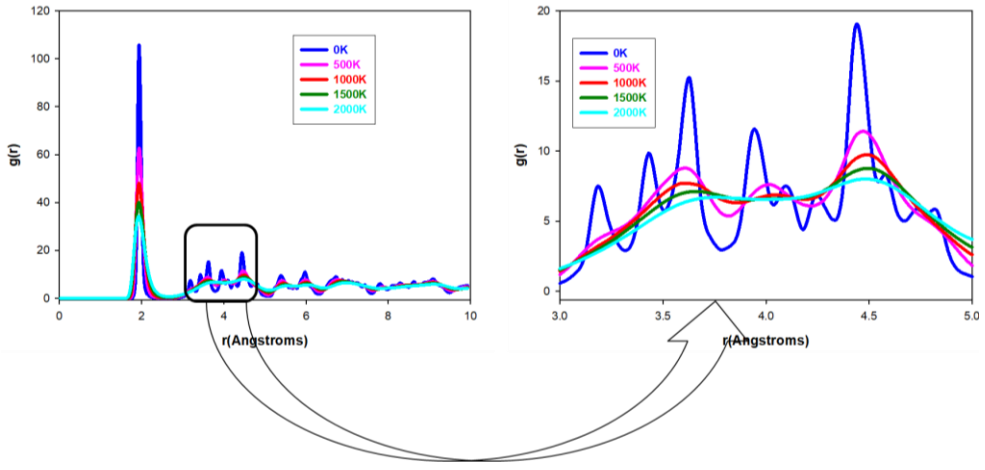

Figure 3.29: Shows simulated RDFs plots for the $Li_{0.11}TiO_2$ nanosphere at low and high temperatures with a magnified RDFs portion between 3 and 5 Å for better visualisation.

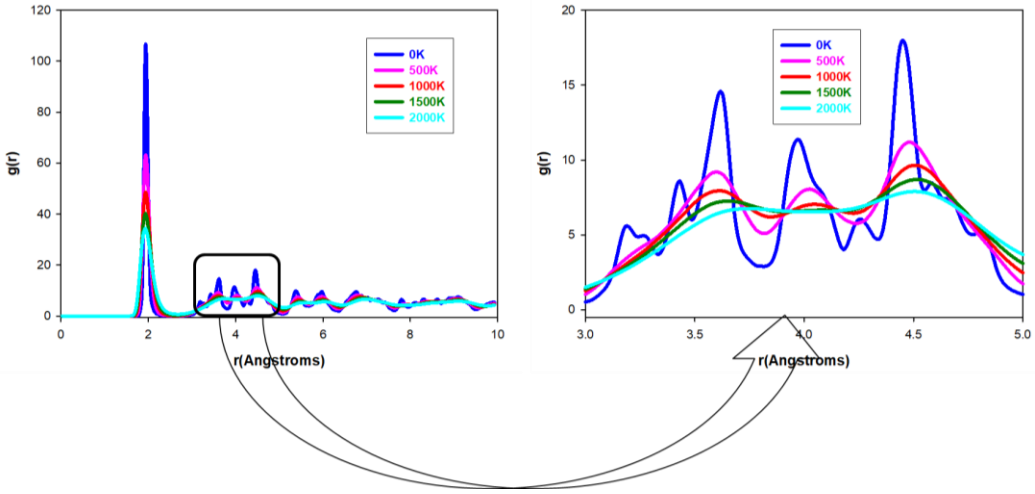

Figure 3.30: Shows simulated RDFs plots for the $Li_{0.15}TiO_2$ nanosphere at low and high temperatures with a magnified RDFs portion between 3 and 5 Å for better visualisation.

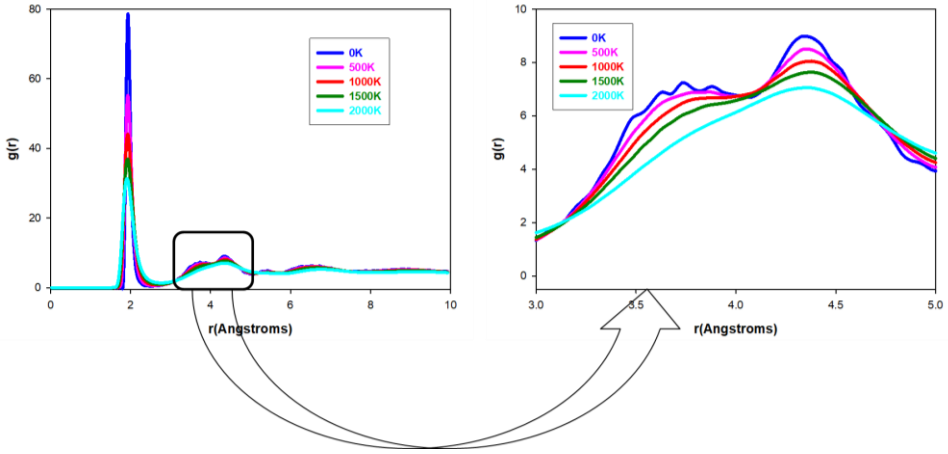

Figure 3.31: Shows simulated RDFs plots for the $Li_{0.19}TiO_2$ nanosphere at low and high temperatures with a magnified RDFs portion between 3 and 5 Å for better visualisation.

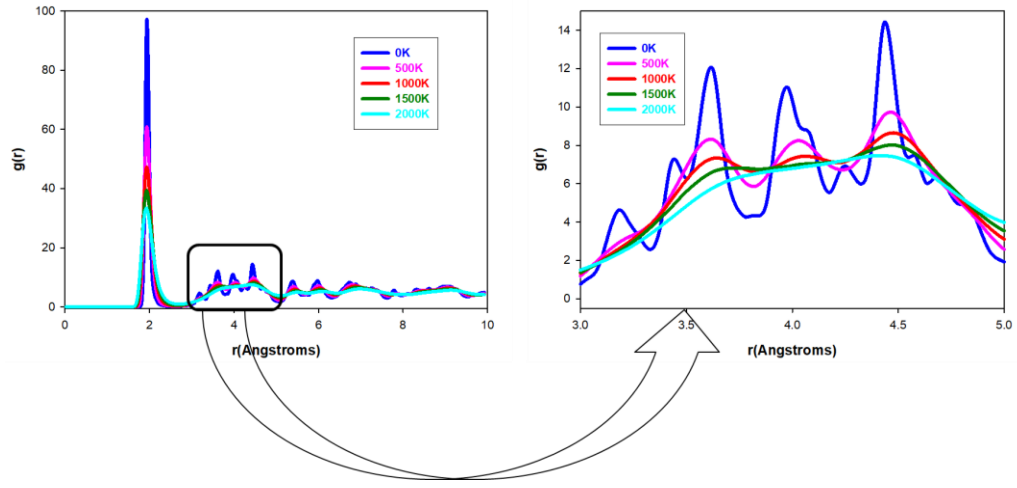

Figure 3.32: Shows simulated RDFs plots for the $Li_{0.23}TiO_2$ nanosphere at low and high temperatures with a magnified RDFs portion between 3 and 5 Å for better visualisation.

3.1.2. Li_xTiO_2 Nanoporous

The simulated RDFs plots for Ti-O pairs in $Li_{0.11}TiO_2$, $Li_{0.15}TiO_2$, $Li_{0.19}TiO_2$, and $Li_{0.23}TiO_2$ nanoporous systems analysed between low (0 K) and high (2000 K) temperatures, in a 500 K intervals, are displayed from Figure 3.39 to Figure 3.42 for the purpose of determining the coordination of numbers of Ti atoms and their bond lengths. The bonds lengths of Li_xTiO_2 nanoporous systems are almost similar to those of Li_xTiO_2 nanospheres demostrated in figures 3.33 to 3.36 when rounded to 2Å. A combination of tetrahedral, pentahedral, and octahedral coordinations is suggested which is confirmed by their microstructral snapshots viewed at high temperatures and low temperatures and illustrated in figures 3.14, 3.16, 3.18 and 3.20. As in nanospheres, such RDFs of nanoporous systems show similar peak feautures where the crystallinity increases with a decrease in temperature and therefore are all highly crystalline at low (0 K) temperatures with crystallinity trend of, i.e., 0 K > 500 K > 1000 K >1500 K >2000 K and near amorphous at higher temperatures (2000 K) at all varied Li^+ concentrations. The first peak intensities of the RDFs of nanoporous structures at different Li concentrations and temperatures are lower than those of nanospheres, although the peaks are sharp and well defined. The same applies to the magnified peaks between 3Å and 5Å. The analysis firmly confirms that high temperatures on a highly lithiated TiO_2 nanoporous structure induces disorder on the Ti-O pairs while maintaining the structural frameworks for better Li^+ diffusivity.

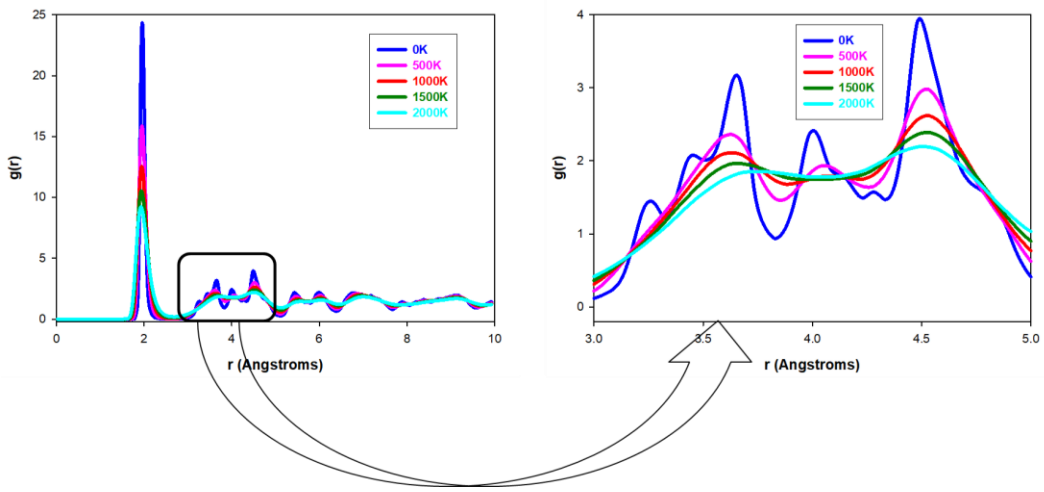

Figure 3.33: Shows simulated RDFs plots for $Li_{0.11}TiO_2$ nanoporous at low and high temperatures with a magnified RDFs portion between 3 and 5 Å for better visualisation.

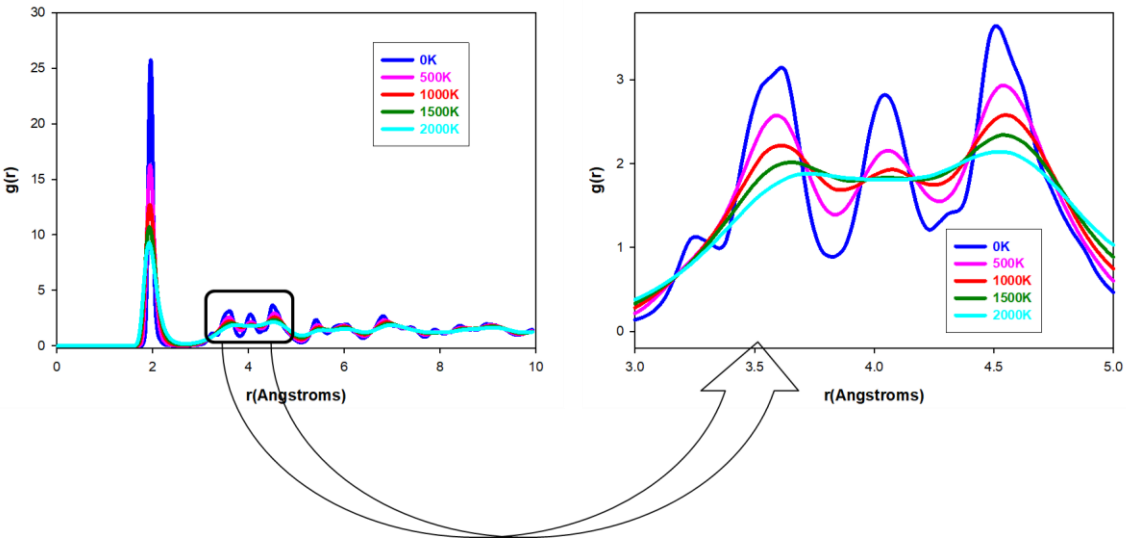

Figure 3.34: Shows simulated RDFs plots for $Li_{0.15}TiO_2$ nanoporous at low and high temperatures with a magnified RDF portion between 3 and 5 Å for better visualisation.

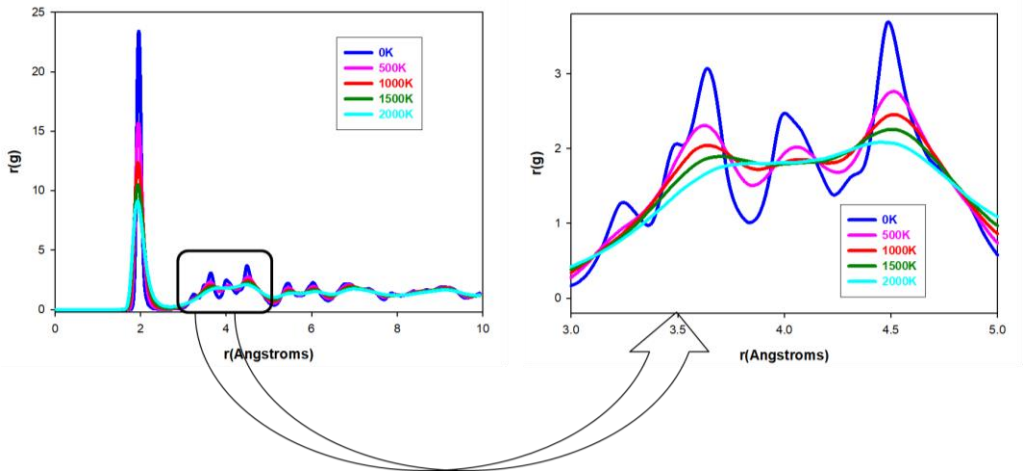

Figure 3.35: Shows simulated RDFs plots for $Li_{0.19}TiO_2$ nanoporous at low and high temperatures with a magnified RDF portion between 3 and 5 Å for better visualisation.

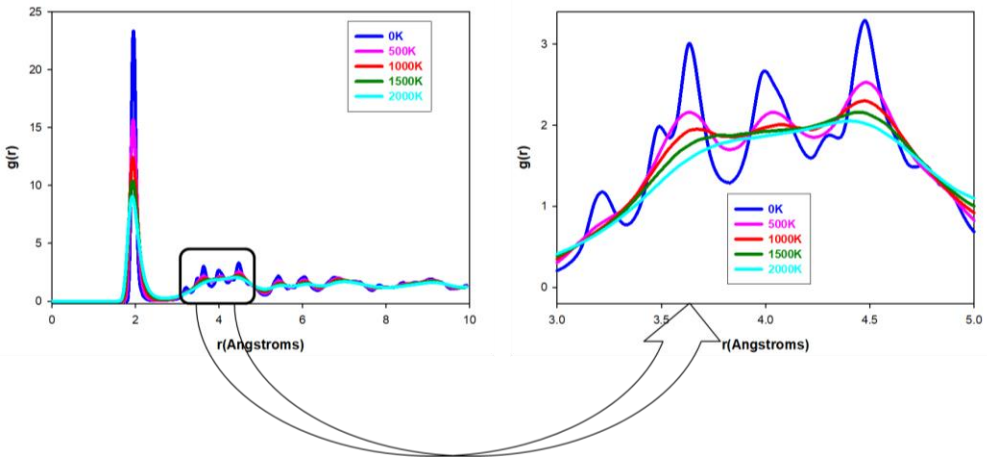

Figure 3.36: Shows simulated RDFs plots for $Li_{0.23}TiO_2$ nanoporous at low and high temperatures with a magnified RDF portion between 3 and 5 Å for better visualisation.

3.1.3. Li_xTiO_2 Nanosheets

The calculated RDFs plots for Ti-O pairs in $Li_{0.11}TiO_2$, $Li_{0.15}TiO_2$, $Li_{0.19}TiO_2$ and $Li_{0.23}TiO_2$ nanosheets at 0 K, 500 K,1000 K,1500 K and 2000 K are perfectly portrait in figures 3.37, 3.38, 3.39 and 3.40 respectively. As in nanospheres and nanoporous structures, such RDFs of nanosheets show similar peak feautures where the crystallinity increases with a decrease in temperature and therefore are all highly crystalline at low (0 K) temperatures with crystallinity trend of, i.e., 0 K > 500 K > 1000 K >1500 K >2000 K and near amorphous at higher temperatures (2000 K) at all varied Li^+ concentrations. The first peak intensities of the RDFs of nanosheets at different Li concentrations and temperatures are lower than those of nanospheres but higher than those of nanoporous systems, although the peaks are sharp and well defined. The same applies to the magnified peaks between 3Å and 5Å. The analysis firmly confirms that high temperatures on a highly lithiated TiO_2 nanosheet induces disorder on the Ti-O pairs while maintaining the structural frameworks for better Li^+ diffusivity.

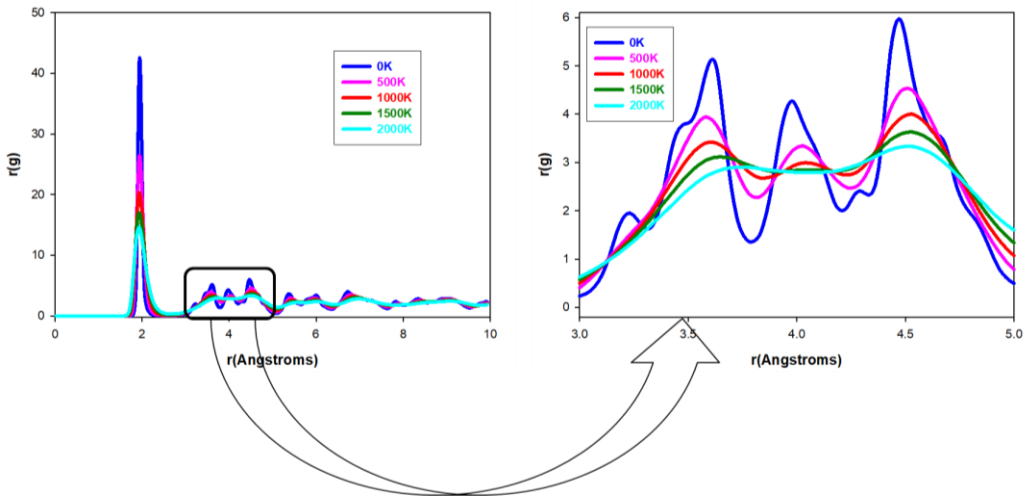

Figure 3.37: Shows simulated RDFs plots for $Li_{0.11}TiO_2$ nanosheets at low and high temperatures with a magnified RDFs portion between 3 and 5 Å for better visualisation.

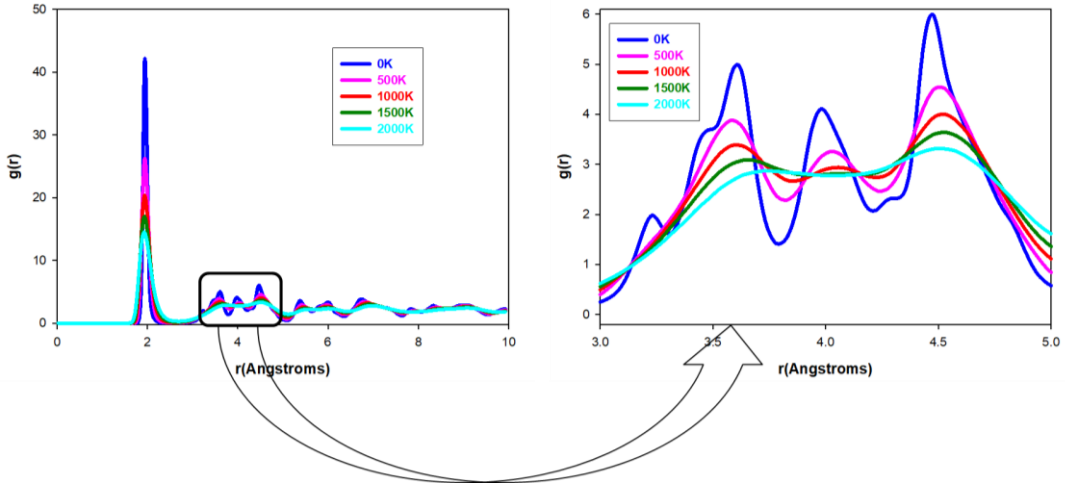

Figure 3.38: Shows simulated RDFs plots for $Li_{0.15}TiO_2$ nanosheets at low and high temperatures with a magnified RDFs portion between 3 and 5 Å for better visualisation.

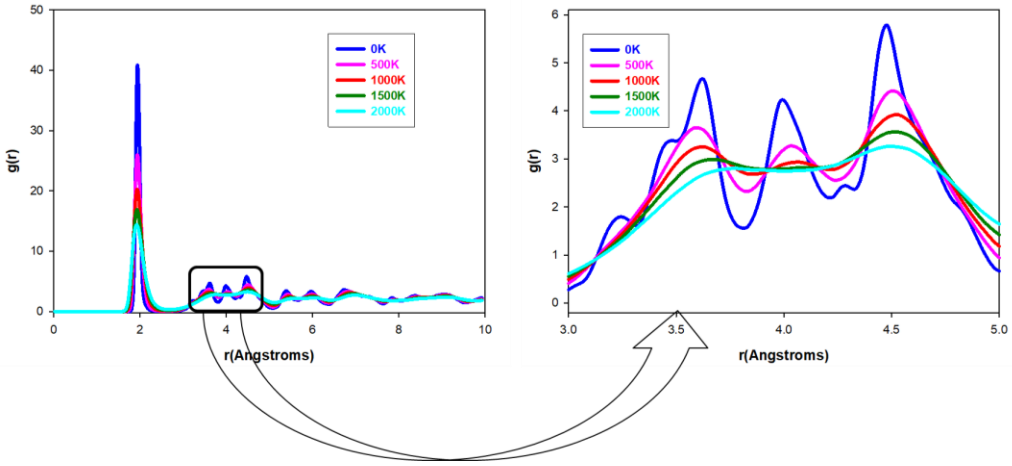

Figure 3.39: Shows simulated RDFs plots for $Li_{0.19}TiO_2$ nanosheets at low and high temperatures with a magnified RDFs portion between 3 and 5 Å for better visualisation.

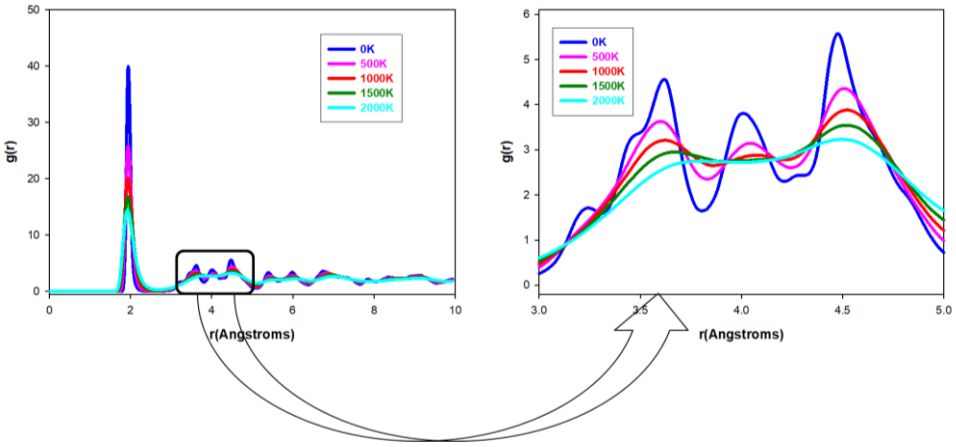

Figure 3.40: Shows simulated RDFs plots for $Li_{0.23}TiO_2$ nanosheets at low and high temperatures with a magnified RDFs portion between 3 and 5 Å for better visualisation.

3.4. XRDs of Li_xTiO_2 (x=0.11, 0.15, 0.19 and 0.23) Nanostructure

The simulated X-ray diffraction patterns (XRD) for nanosphere, nanoporous and nanosheets Li_xTiO_2 with x= 0.11, 0.15, 0.19 and 0.23 Li ion concentrations characterised at high (2000 K) and low (0 K) temperature conditions were calculated using the reflex module within Biovia Material studio software over the 2Θ range of 20º to 80º with a step size of 0.05 and the Cu Kα (λ=1.54Å). The calculated XRDs patterns of the computationally generated nanostructures were compared with XRD patterns of pure TiO_2 synthesised using different experimental methods illustrated in [24,151]

3.4.1. Li_xTiO_2 Nanosphere

The calculated XRDs patterns in figure 3.41 for $Li_{0.11}TiO_2$ nanosphere had high sharp peaks at 2Θ values 25º, 30º, 35º and 55º corresponding to reflections by the (120), (111), (121), (012), (131) and (101), (105) planes of brookite and anatase polymorphs respectively, at both 2000 K and 0 K temperature. Moreover, low broad peaks were also observed at 2Θ values of 38º, 41º, 42º, 62º and 65º corresponding to the reflection by (200), (111), (120), (610) and (211) of rutile, brookite, and anatase polymorphs seen at both 2000 K of the (200) plane of the anatase phase had emerged at 0 K, which suggested a peak shift and 0 K temperature conditions, however another low intense peak at 2Θ value 46º positions from high to lower temperatures. So, the structure of $Li_{0.11}TiO_2$ nanosphere architecture contained the rutile, anatase, and brookite polymorphs, where the brookite phase was highly dominant with very intense peaks at both 2000 K and 0 K and more present at 0 K.

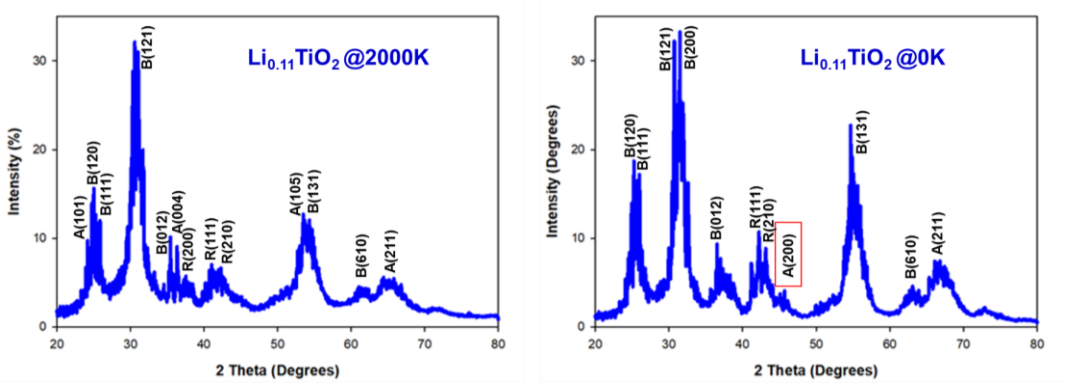

Figure 3.41: Simulated XRDs patterns of $Li_{0.11}TiO_2$ nanosphere at high (2000 K) and low (0 K) temperatures conditions for structural characterisations.

The calculated XRDs patterns for $Li_{0.15}TiO_2$ nanosphere in figure 3.42 show almost similar peak positions to that of $Li_{011}TiO_2$ nanosphere in figure 3.41. The difference is the multiplicity separations and the intensity of peaks where $Li_{011}TiO_2$ nanosphere had highest peaks of 34 % and 39% at 2000 K and 0 K respectively to that of $Li_{0.15}TiO_2$ nanosphere which had maximum intense peak of 29% and 25% at 2000 K and 0 K respectively. Consequently, the brookite polymorphs was also a dominant phase inside the $Li_{0.15}TiO_2$ nanosphere under both temperature conditions illustrated in figure 3.42. However, the present peaks multiplicity on the same 2Θ positions also suggested the possibility of few rutile and anatase phases which were highly difficult to point due to their very close separation, hence only few reflections planes were indexed. The XRDs patterns for $Li_{0.15}TiO_2$ and $Li_{011}TiO_2$ nanospheres are consistent

with their microstructural snapshots shown in figure 3.10 iv), figure 3.2 b) and figure 3.8 iv), figure 3.2 i).

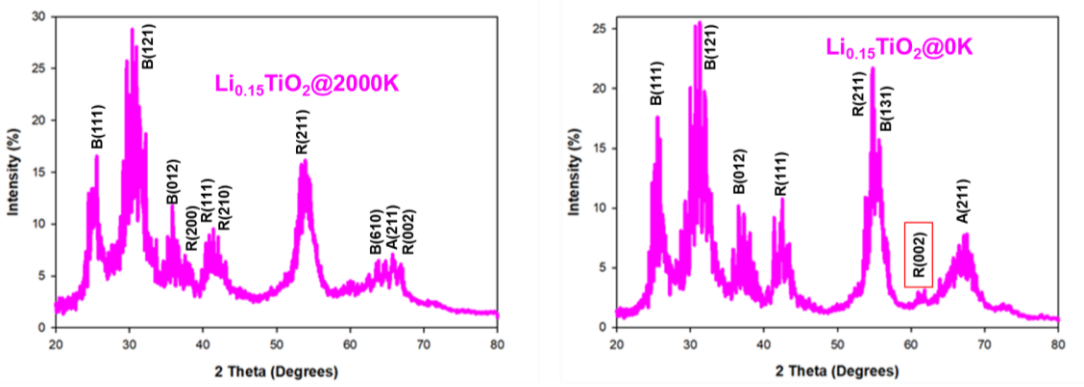

Figure 3.42: Simulated XRDs patterns of $Li_{0.15}TiO_2$ nanosphere at high (2000 K) and low (0 K) temperatures conditions for structural characterisations.

Moreover, the XRDs patterns for $Li_{0.19}TiO_2$ nanosphere in figure 3.43 were also calculated and found to be inconsistent to the calculated XRD pattern of $Li_{0.11}TiO_2$, $Li_{0.15}TiO_2$ and $Li_{0.23}TiO_2$ nanosphere in figures 3.48, 3.49 and 3.51 respectively. The characterised XRD patterns of $Li_{0.19}TiO_2$ nanosphere in figure 3.43 had very broad peaks and had only two maximum indexed peaks at 2Θ position of 30º and 55º corresponding to the reflections by the (121) and (211) (220) of brookite and rutile polymorphs. The wide broadness of the peaks confirms a highly amorphous system both at 2000 K and 0 K consistent with their RDF of Ti-O pairs in figure 3.37 hence the microstructure of the recrystalised system was not presented along with their structures at cooled due to the highly disordering of Li, Ti, and O atoms framework. Therefore, the $Li_{0.19}TiO_2$ systems was highly unfavourable to recrystallisation and cooled synthesis so we can conclude that these systems cannot withstand high temperature conditions.

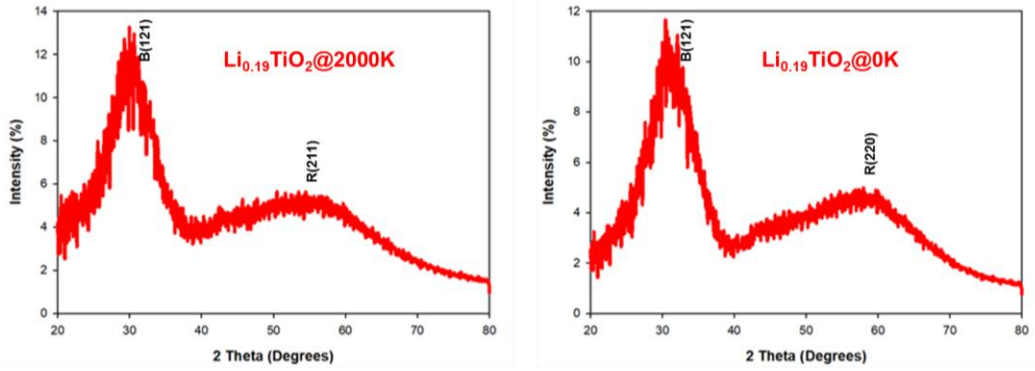

Figure 3.43: Simulated XRD patterns of $Li_{0.19}TiO_2$ nanosphere under high (2000 K) and low (0 K) temperatures for structural characterisations.

The simulation of the XRD patterns of $Li_{0.23}TiO_2$ nanosphere system shown in figure 3.44 was also characterised to study and compare its structural crystallinity phases at 2000 K and 0 K. The XRD patterns in Figure 3.44 had very highly intense peaks at 2Θ values of 25º,30º,33º,42º,42º,55º,56º and 65º observed at both temperature conditions but that at 2000 K was more intense with maximum intensity of 39% than that at 0 K

with 27% intensity. These two values correspond to the reflection by the (111), (121), (200), (012), (004), (111), (210), (105), (131) and (211) planes for brookite, anatase and rutile phase in no chronological order. Moreover, the (111) plane for rutile only appeared at 2000 K, while the (200) (012) planes for brookite and (200) for rutile plane appeared at 0 K which suggested equal phase transformation dominance from high temperature to low temperatures.

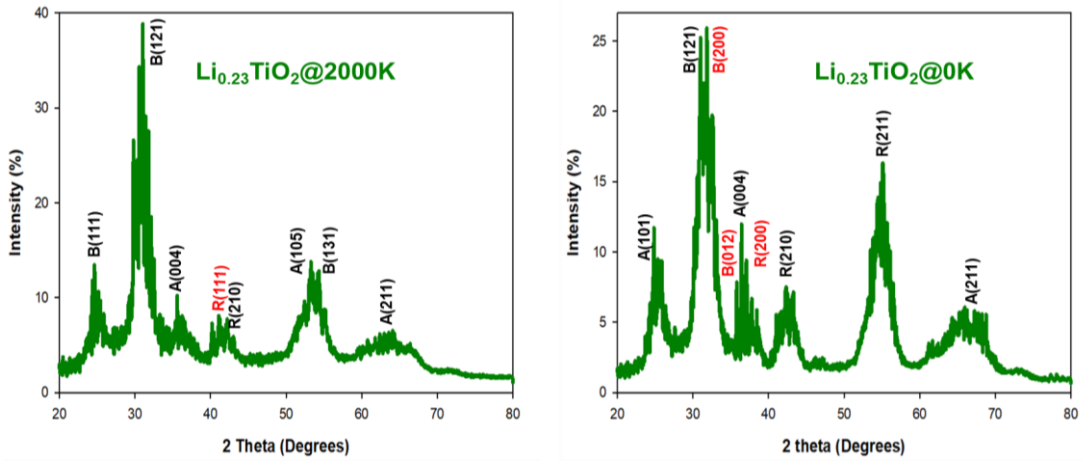

Figure 3.44: Simulated XRD patterns of $Li_{0.23}TiO_2$ nanosphere under high (2000 K) and low (0 K) temperatures for structural characterisations.

3.4.2. Li_xTiO_2 Nanoporous

Interestingly, the XRD patterns for the Li_xTiO_2 nanoporous (x = 0.11, 0.15, 0.19 and 0.23) under both temperature conditions showed intensities higher intense with distinguishable close multiple peaks on the same 2Θ positions when compared to XRD patterns of the Li_xTiO_2 nanospheres. The XRD patterns for $Li_{0.11}TiO_2$ nanoporous simulated at 2000 K and 0 K are shown in figure 3.45 where very high intense peaks dominance appeared at 2Θ values of 25º,30º,35º,41º,43º,54º,55º and 65º correlating to the reflection by the (120), (111), (121), (004), (200), (210), (105), (131), (211) and (301) planes which are linked to mixtures brookite, anatase and rutile phases. However, the (101) and (301) planes for rutile polymorphs had only visibly appeared at 0 K and the (131) plane for brookite phase had only appeared at 2000 K suggesting a high brookite polymorphs dominance at high temperature and rutile dominance at lower temperatures. The higher multiplicity of intense peaks seen in figure 3.52 proves and confirm a very high crystalline phases influenced by both high and lower temperature.

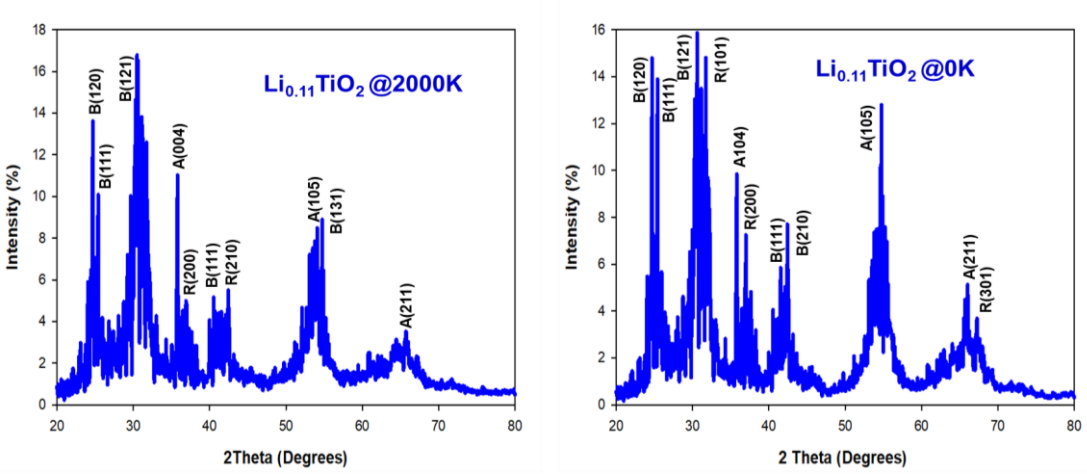

Figure 3.45: Simulated XRD patterns of $Li_{0.11}TiO_2$ nanoporous at high (2000 K) and low (0 K) temperatures conditions for structural characterisations.

The crystalline phases were further observed in the $Li_{0.15}TiO_2$ nanoporous structures confirmed by their highly intense peaks illustrated in figure 3.46 with maximum intensity of 25% and 22% at 2000 K, and 0 K respectively. The simulated XRD patterns shown in Figure 3.46 have similar peak positions observed in XRD patterns shown in figure 3.52. However the XRD patterns in figure 3.46 contained more peaks noises and are highly intense. The simulated XRD patterns for $Li_{0.15}TiO_2$ nanoporous at 2000 K had indexed peaks with brookite and rutile dominance while the $Li_{0.15}TiO_2$ nanoporous at 0 K had a mixture of rutile, anatase and brookite phases. The reflections by the planes (101), (111), (110), (121), (004), (210), (200), (211), (301), (116) and (112) were indexed between 2Θ values of 23º to 70º both at 2000 K and 0 K, moreover the (200) (116) and (112) planes for brookite, anatase and rutile phases had strongly appeared more on XRD patterns at 0 K than at 2000 K. Thus, the crystallinity increased with a decrease in temperature.

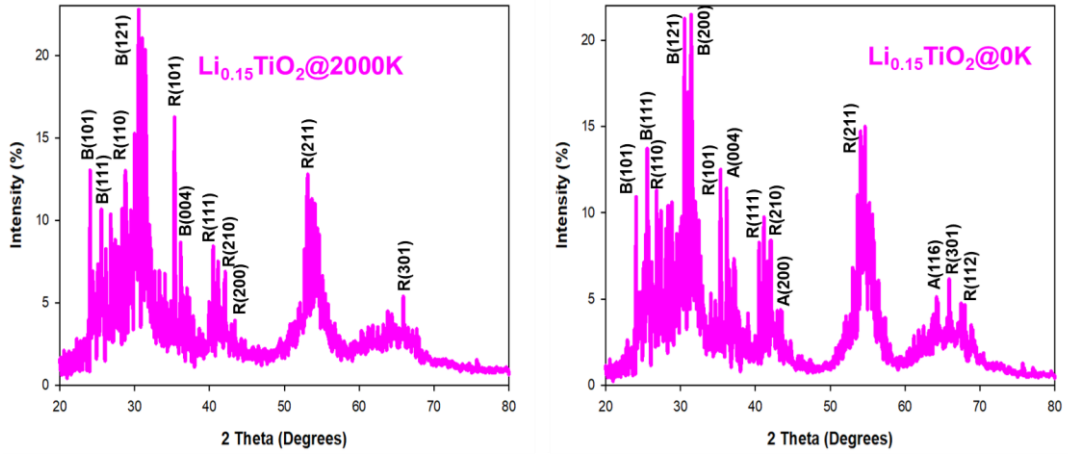

Figure 3.46: Simulated XRD patterns of $Li_{0.15}TiO_2$ nanoporous at high (2000 K) and low (0 K) temperatures for structural characterisations.

Since the peak intensity of Li_xTiO_2 nanoporous shown from figure 3.45 to 3.48 was influenced by increased Li^+ concentrations confirmed the high crystalline phase contained in the structures. The simulated XRDs patterns of $Li_{0,19}TiO_2$ nanoporous

system at 2000 K and 0 K, given in figure 3.47, have more intense peaks with less noises than XRDs patterns in figure 3.45 and figure 3.46 at 2Θ values of 25º, 30º, 35º, 41º, 43º, 54º, 55º, 61º, 65º and 68º corresponding to the reflections by (120), (121), (101), (111), (210), (004), (211), (002), (112), (116) and (220) planes corresponding to rutile, brookite and anatase polymorphs by which proves a highly crystalline system . The XRD peaks were more intense at 2000 K than those at 0 K

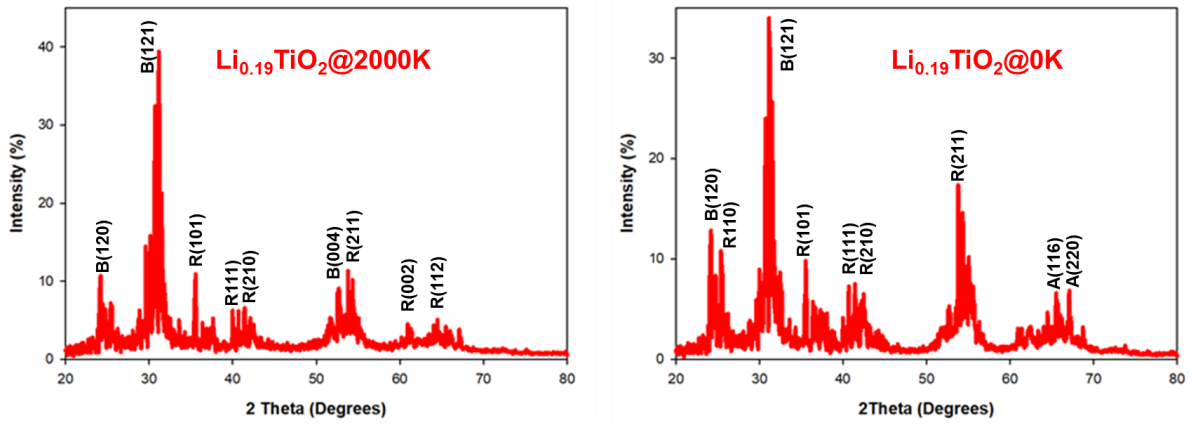

Figure 3.47: Simulated XRD patterns of $Li_{0.19}TiO_2$ nanoporous at high (2000 K) and low (0 K) temperatures for structural characterisations.

More Li^+ insertion into TiO_2 nanoporous have influenced the structural framework into higher dimensions, figure 3.48 is the simulated XRD patterns for $Li_{0.23}TiO_3$ nanoporous ran at 2000 K and 0 K. The XRD peaks have the same 2Θ positions at both temperatures with different peaks intensities. Both XRD patterns at both temperatures contain a mixture of the three dominant polymorphs of rutile, anatase and brookite indexed at 2Θ values of 25º, 30º, 35º, 41º, 43º, 54º, 55º, 61º, 65º and 68º corresponding to reflections by (111), (121), (004), (111), (210), (211), (220), (002) and (310) planes.

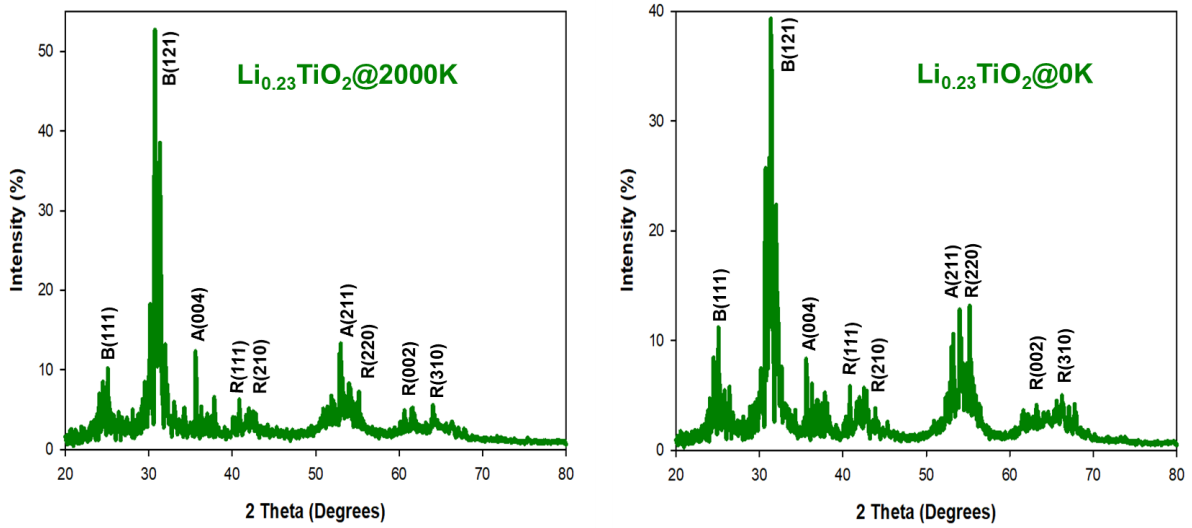

Figure 3.48: Simulated XRD patterns of $Li_{0.23}TiO_2$ nanoporous at high (2000 K) and low (0 K) temperatures for structural characterisations.

3.4.3. Li_xTiO_2 Nanosheets

The simulated XRD patterns for $Li_{0.11}TiO_2$ $Li_{0.15}TiO_2$ $Li_{0.19}TiO_2$ and $Li_{0.23}TiO_2$ nanosheets illustrated in figures 3.49, 3.50, 3.51 and 3.52 consecutively show similar peaks positions but different peak intensity characteristics. They all contain an indexed peak position at 2Θ values of 25º, 26º, 31º, 35º, 37º, 41º, 55º, 61º and 65º representing reflection of (101), (110), (121), (004), (111), (211) and (310) planes with mixture of brookite, anatase and rutile polymorphs at both simulated temperatures of 2000 K and 0 K. The peak intensities were increasing with an increase in Li^+ concentration, therefore, the XRD peaks in figure 3.52 were more intense than the peaks shown in figure 3.49, 3.50 and 3.51 following an intensity peaks trend of $Li_{0.11}TiO_2$ > $Li_{0.15}TiO_2$ > $Li_{0.19}TiO_2$ and $Li_{0.23}TiO_2$. However, there is an emerging peak in the XRDs patterns of $Li_{0.23}TiO_2$ nanosheets at 0 K positions at 2Θ value 56º indexed with (211) plane of rutile polymorphs. The peaks were well separated/split more than what was seen on other XRDs patterns at 0 K for the three Li^+ concentrations. The simulated XRD patterns of Li_xTiO_2 nanosphere, nanoporous and nanosphere confirms that the structural integrity was confirmed and improved at elevated temperature and Li^+ concentrations on the nanostructures.

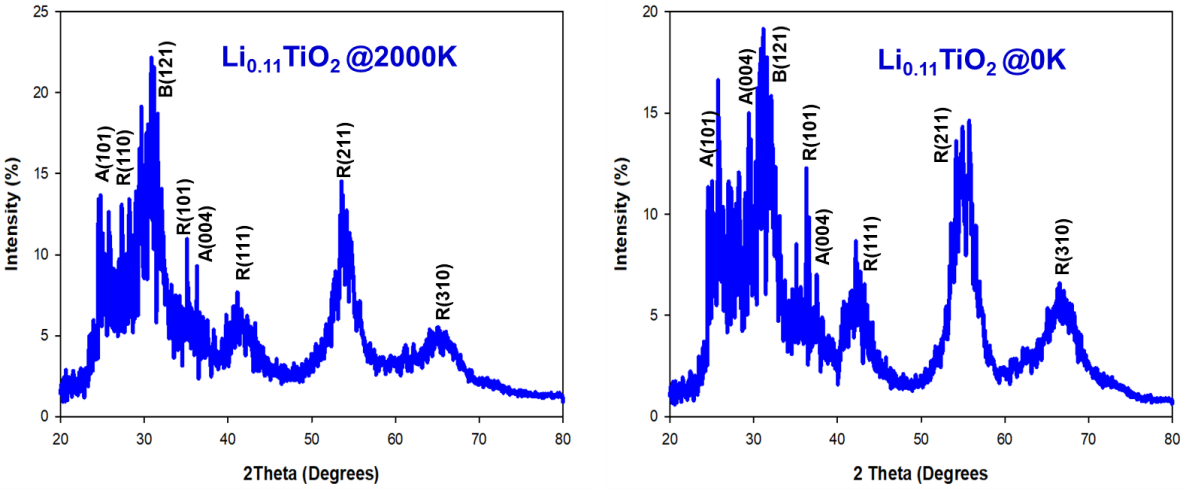

Figure 3.49: Simulated XRD patterns of $Li_{0.11}TiO_2$ nanosheets at high (2000 K) and low (0 K) temperatures for structural characterisation.

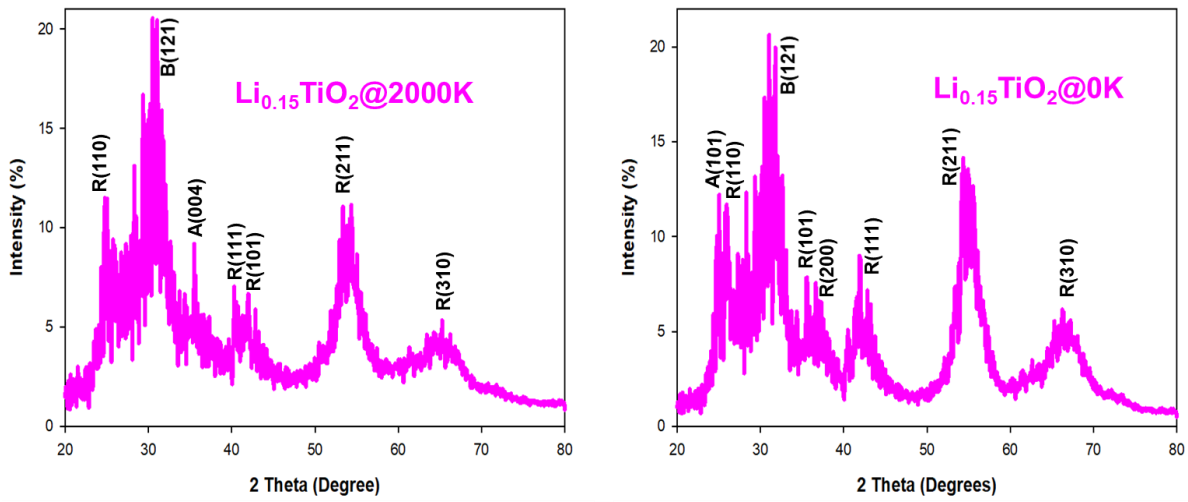

Figure 3.50: Simulated XRD patterns of $Li_{0.15}TiO_2$ nanosheets at high (2000 K) and low (0 K) temperatures for structural characterisation.

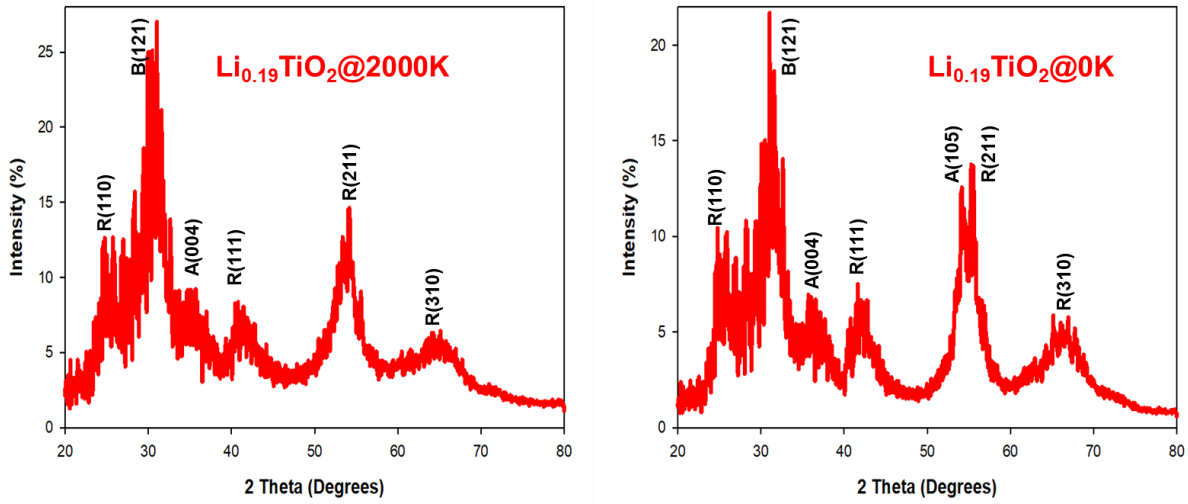

Figure 3.51: Simulated XRDs patterns of $Li_{0.19}TiO_2$ nanosheets at high (2000 K) and low (0 K) temperatures conditions for structural characterisation.

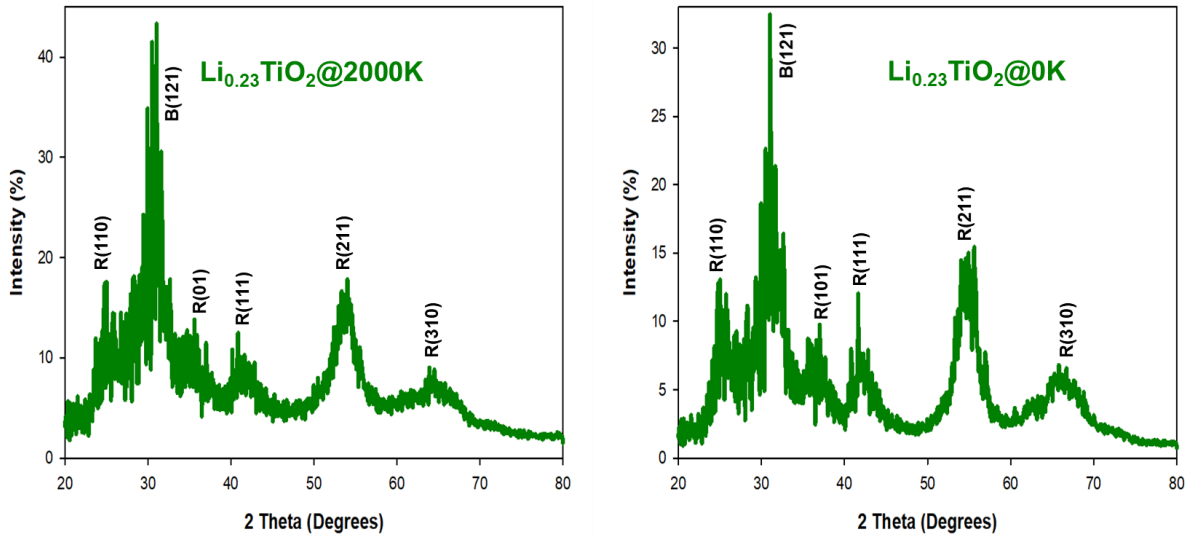

Figure 3.52: Simulated XRD patterns of $Li_{0.23}TiO_2$ nanosheets at high (2000 K) and low (0 K) temperatures for structural characterisation.

3.5. Diffusion Coefficients of Li_xTiO_2 (x=0.11, 0.15, 0.19 and 0.23) Nanoarchitectures

Li transport in the nanostructure is important for its consideration as a good anode. In the current study, Li^+ mobility was investigated from low (0 K) to high (2000 K) temperatures in the nanosphere (0-D), nanoporous (3-D) and nanosheets (2-D). The Li^+ transport was captured by diffusion coefficients vs temperature calculations and the energy required for the Li^+ to diffuse by their activation energies calculations.

3.5.1. Li_xTiO_2 Nanosphere

The variation of diffusion coefficient of Li with temperature for $Li_{0.11}TiO_2$, $Li_{0.15}TiO_2$, $Li_{.19}TiO_2$, and $Li_{0.23}TiO_2$ nanospheres, is shown in figure 3.53. Between 100 and 1300 K diffusion coefficients of Li^+ in $Li_{0.19}TiO_2$ nanosphere was above zero and higher than the rest. Those of $Li_{0.11}TiO_2$, $Li_{0.15}TiO_2$, $Li_{.23}TiO_2$ nanospheres were near zero and superimposed up to 700 K. A marked increase and splitting of the $Li_{.23}TiO_2$ nanosphere diffusion coefficient curve from that of $Li_{0.11}TiO_2$ and $Li_{0.15}TiO_2$ is noted beyond 1200 K, though the latter two, together with $Li_{.19}TiO_2$, increased moderately up to 2000 K. The anomalous behaviour of $Li_{.19}TiO_2$ nanosphere could be attributed to its amorphous phase since it could not crystallise as shown in figure 3.2.

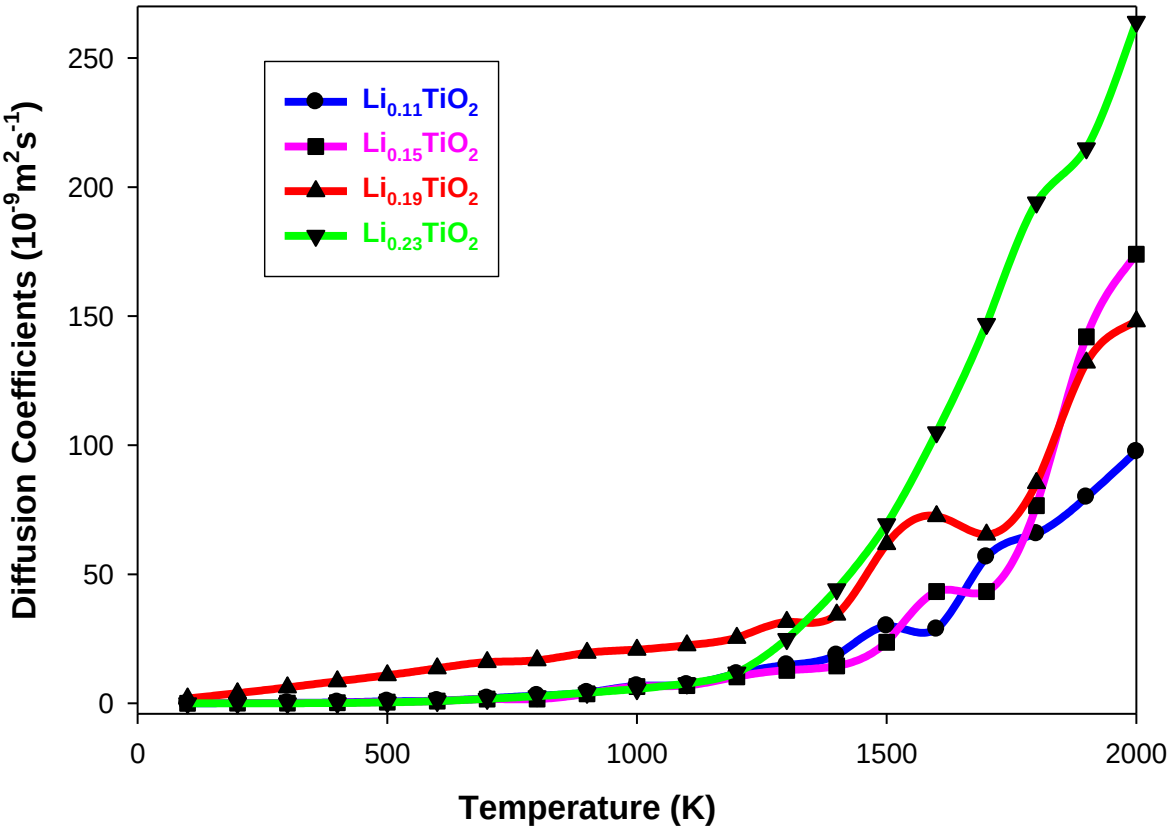

Figure 3.53: Represents graph of Li^+ diffusion coefficients at varied temperature within TiO_2 nanospheres with 0.11, 0.15, 0.19 and 0.23 Li^+ concentrations on the same axis.

3.5.2. Li_xTiO_2 Nanoporous

Plots of diffusion coefficients of Li with temperature in $Li_{0.11}TiO_2$, $Li_{0.15}TiO_2$, $Li_{0.19}TiO_2$ and $Li_{0.23}TiO_2$ nanoporous structures are shown in figure 3.54. All plots completely overlap and show minimal diffusion of Li^+ from 0 to 500K; noticeable diffusion commences above this temperature. Furthermore, the plots begin to separate beyond 800 K where the diffusion coefficient of $Li_{.23}TiO_2$ nanoporous structure slightly prevails above others and $Li_{0.15}TiO_2$, $Li_{0.19}TiO_2$ continue to be intertwined whilst $Li_{0.11}TiO_2$ lingers slightly below up to 2000 K . From 1300 K the trend of diffusion coefficients in different nanoporous structures emerges as $Li_{0.23}TiO_2$ > $Li_{0.19}TiO_2$ ~ $Li_{0.15}TiO_2$ > $Li_{0.11}TiO_2$.

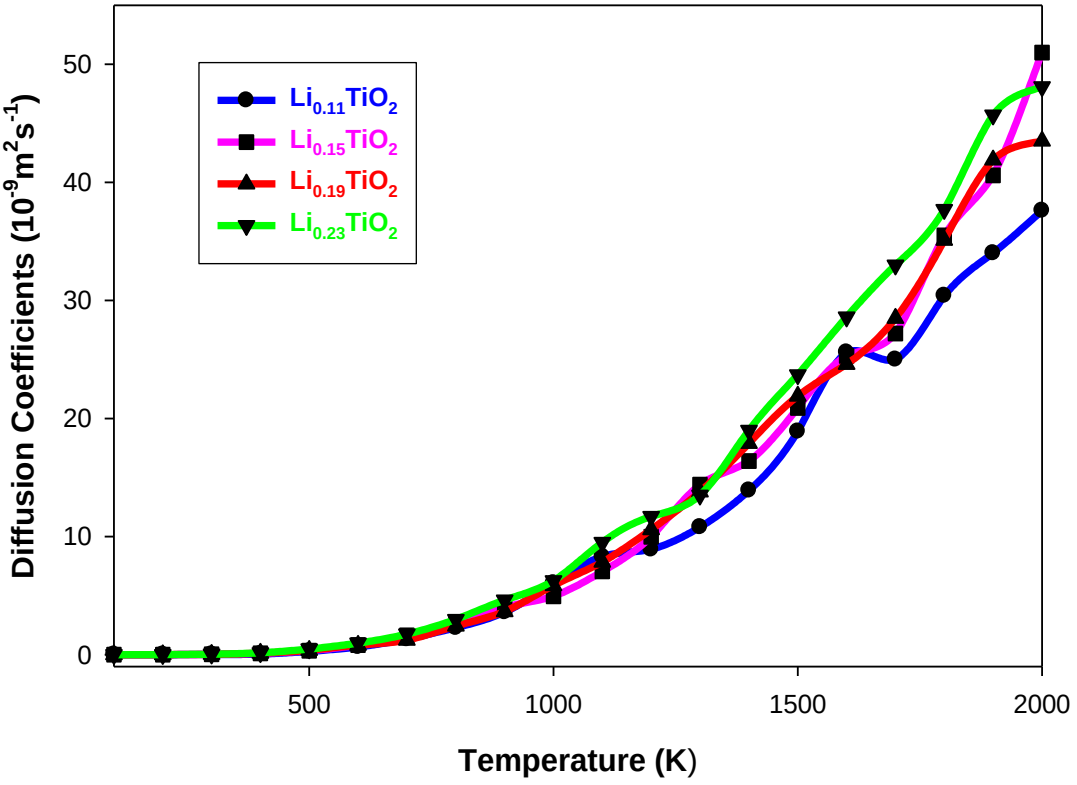

Figure 3.54: Represents graph of Li^+ diffusion coefficients at varied temperature in TiO_2 nanoporous architecture with 0.11, 0.15, 0.19 and 0.23 Li^+ concentrations.

Plots of diffusion coefficients of Li against temperature in $Li_{0.11}TiO_2$, $Li_{0.15}TiO_2$, $Li_{0.19}TiO_2$, and $Li_{0.23}TiO_2$ nanosheets are shown in figure 3.55. All plots completely overlap and show minimal Li^+ diffusion from 100 to 500K. Diffusion coefficients begin to increase above such temperature and plots continue to mostly overlap up to 1300 K where the diffusion of $Li_{0.23}TiO_2$ nanosheet is predominant up to 2000 K. On the

whole, a comparison diffusion coefficient in the various nanosheets, above 1300 K shows that $Li_{0.23}TiO_2$ > $Li_{0.19}TiO_2$ **>** $Li_{0.15}TiO_2$ ~ $Li_{0.11}TiO_2$.

3.5.3. Li_xTiO_2 Nanosheets

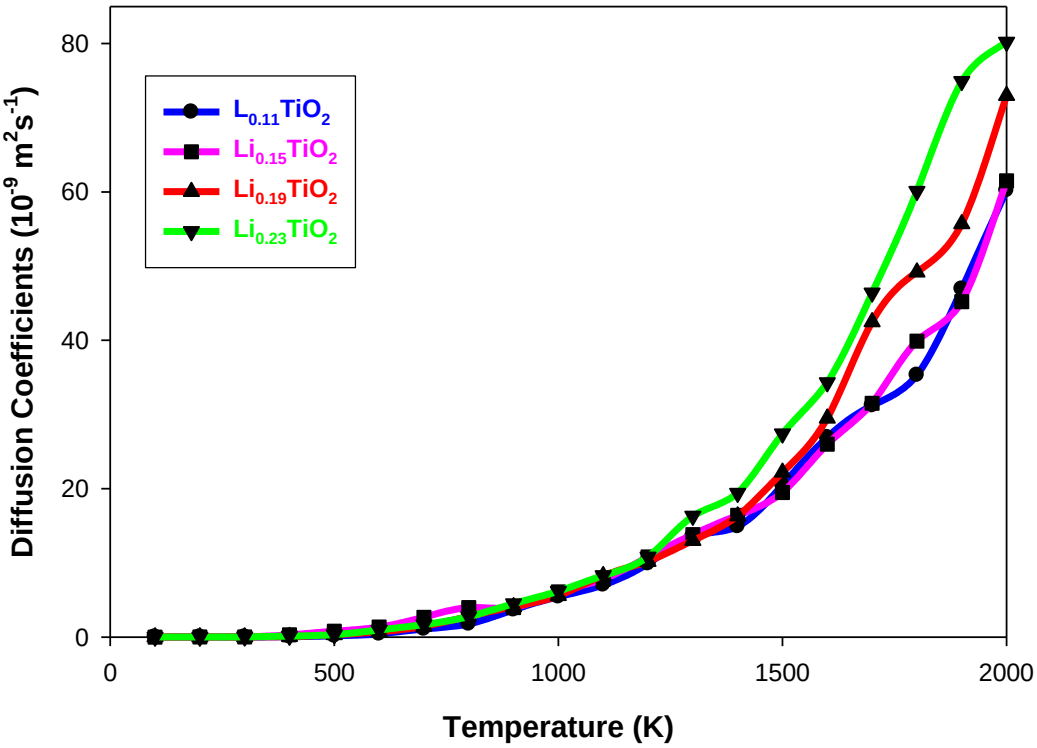

Figure 3.55: Represents graph of Li^+ diffusion coefficients at varied temperatures for Li_xTiO_2 nanosheets with x = 0.11, 0.15, 0.19 and 0.23.

3.6. Activation Energies of Li_xTiO_2 (x = 0.11, 0.15, 0.19 and 0.23) Nanoarchitectures.

Figures 3.56, 3.57 and 3.58 show the logarithm of diffusion coefficients vs. the inverse temperatures between 1000 and 2000 K in $Li_{0.11}TiO_2$, $Li_{0.15}TiO_2$, $Li_{0.19}TiO_2$ and $Li_{0.23}TiO_2$ nanosphere, nanoporous and nanosheets architectures, respectively.

3.6.1. Li_xTiO_2 Nanosphere

Calculated activation energies for $Li_{0.11}TiO_2$, $Li_{0.15}TiO_2$, $Li_{01.9}TiO_2$ and $Li_{0.23}TiO_2$ nanospheres, from 1.0 K^{-1} to 2.0 K^{-1}, are 0.25eV, 0.29eV, 0.18eV and 0.37eV respectively, as shown in figure 5.56. The highest calculated AE was for the $Li_{0.23}TiO_2$ nanosphere, followed by $Li_{0.15}TiO_2$ and $Li_{0.11}TiO_2$. The lowest AE corresponds to $Li_{0.19}TiO_2$ nanosphere, implying that it requires least energy for Li to be activated in the range 1.0 K^{-1} to 2.0 K^{-1}. This has led to achievement of higher diffusion coefficients at lower temperatures. The latter could be partly ascribed to the amorphous phase of $Li_{0.19}TiO_2$ nanosphere since it could not be recrystallized as shown in figure 3.2.

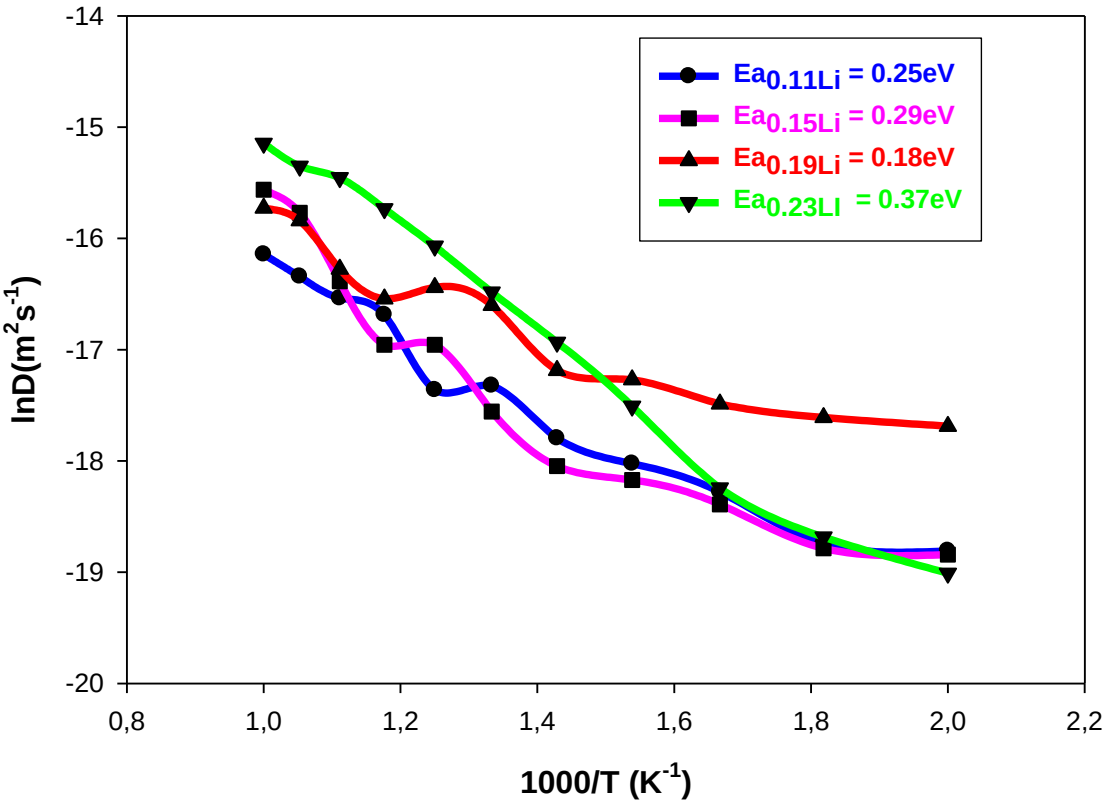

Figure 3.56: Represents graphs of lnD vs 1000/T for Li_xTiO_2 nanospheres with x = 0.11, 0.15, 0.19 and 0.23.

3.6.2. Li_xTiO_2 Nanoporous

Calculated activation energies for $Li_{0.11}TiO_2$, $Li_{0.15}TiO_2$, $Li_{01.9}TiO_2$ and $Li_{0.23}TiO_2$ nanoporous structures, between 1.0 K^{-1} to 2.0 K^{-1}, are 0.165eV, 0.194eV, 0.1775eV and 0.1778eV respectively, as shown in figure 3.57. Although there are slight variations, on the whole the activation energies are close to each other as supported by corresponding plots of diffusion coefficients in figure 3.53.

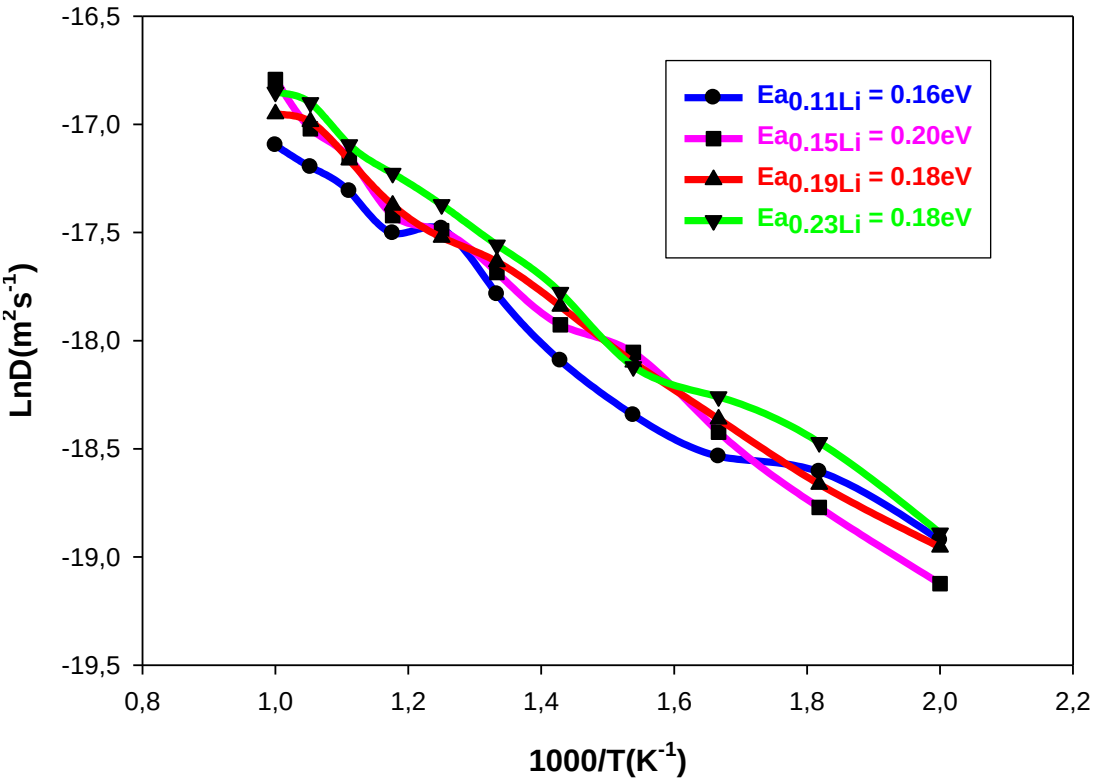

Figure 3.57: Represents graphs of lnD vs 1000/T for Li_xTiO_2 nanoporous structures with x = 0.11, 0.15, 0.19 and 0.23.

3.6.3. Li_xTiO_2 Nanosheets

Calculated activation energies for $Li_{0.11}TiO_2$, $Li_{0.15}TiO_2$, $Li_{01.9}TiO_2$ and $Li_{0.23}TiO_2$ nanosheets, between 1.0 K^{-1} to 2.0 K^{-1}, are 0.20 eV, 0.19 eV, 0.22 eV and 0.23 eV respectively, as shown in figure 3.58. Although there are slight variations, on the whole the activation energies are close to each other as supported by corresponding plots of diffusion coefficients in figure 3.54.

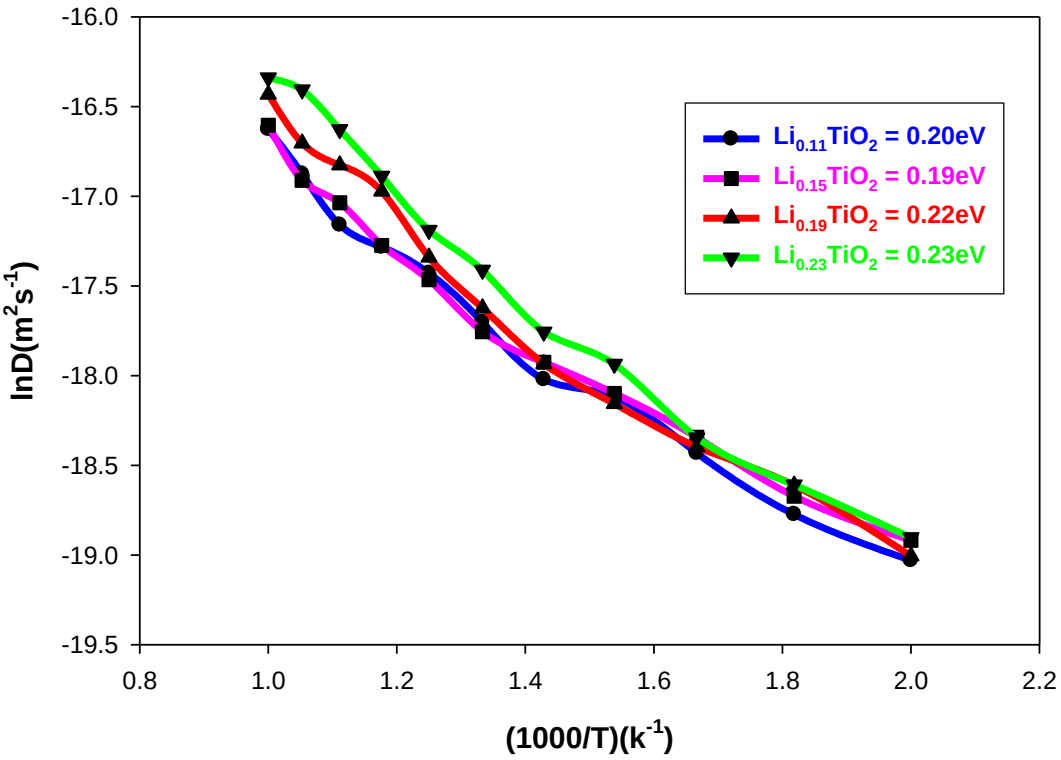

Figure 3.58: Represents graphs of lnD vs 1000/T for Li_xTiO_2 nanosheets with x = 0.11, 0.15, 0.19 and 0.23.

3.7. Summary

Different lithium concentrations were inserted in amorphous precursors of TiO_2 nanospheres (0D), nanoporous (3D) and nanosheets (2D) to produce $Li_{0.11}TiO_2$, $Li_{0.15}TiO_2$, $Li_{0.19}TiO_2$ and $Li_{0.23}TiO_2$ nano-architectures. These were recrystallised at 2000 K followed by cooling from 1500 K to 0 K in 500 K intervals and were subsequently heated from 0 to 2000 K in 100 K intervals. With exception of $Li_{0.19}TiO_2$ nanosphere all Li_xTiO_2 crystallised well for all nano-architectures and microstructures, RDFs and XRDs depicted high crystallinity at low temperatures. Microstructures showed tunnels with zigzag and straight tunnels that provide pathways for Li transport which correspond to brookite and rutile polymorphs respectively. The presence of the two polymorphs were confirmed by XRDs at various temperatures, which on the whole confirmed the degree of crystallinity.

The Li ions were distributed in tunnels depicted on microstructures to a varying degree and some could be located in vacancies. In nanoporous structures some Li ions accumulated on the edges of the channels as lithium concentration is increased. Generally, Li_xTiO_2 nanosheets consisted of two portions, one with rutile and brookite tunnels and another consisting of highly disordered portions, or changes in orientations are also observed and become abundant at higher Li concentrations where they occupy half of the snapshot. Since there was no crystallisation for $Li_{0.19}TiO_2$ nanosphere microstructural patterns could not be observed. Instead, wide and broad peaks in the corresponding RDF and XRD patterns were observed.

On Li transportation, diffusion coefficients were mostly near zero at low temperatures and increase gradually above 500 K and significantly at higher temperatures beyond 1000 K, for most Li concentrations and nano-architectures. The diffusion coefficient of the amorphous $Li_{0.19}TiO_2$ nanosphere is elevated at low temperatures, however, it is exceeded by those of other concentrations at higher temperatures. On the whole the activation energies of Li inside TiO_2 nanosphere, nanoporous and nanosheet structures were consistent with observed transport properties. The results in this chapter confirm that lithium inserted TiO_2 nanosphere, nanoporous, and nanosheet architectures can serve as good anode materials for Li-ion batteries during charging and discharging.

Chapter 4

4. Results and Discussion: Sodium Intercalated TiO_2 Nanoarchitectures

4.1. Recrystallised Structures and Microstructures of Na_xTiO_2 (x=0.11, 0.15, 0.19 and 0.23) Nanostructures

4.1.1. Na_xTiO_2 Nanosphere

The amorphous Na_xTiO_2 (x = 0.11,0.15,0.19 and 0.23) nanosphere structures were recrystallised through atomistic simulation synthesis, at 2000K, and resultant nanosphere are shown in Figure 4.1 a) $Na_{0.11}TiO_2$ b) $Na_{0.15}TiO_2$ c) $Na_{0.19}TiO_2$ and d) $Na_{0.23}TiO_2$ respectively. The structures in Figure 4.1 a) and b) have crystalline patterns confirmed by the ordered arrangements of Ti, O atoms influenced by the Na^+ settling inside the architecture. Moreover, few Na^+ ions were observed to have been repelled away from the nanosphere and most Na^+ were seen right on the edges of the nanosphere framework, this is a similar phenomenon observed in Figure 4.1 b), c) and d).

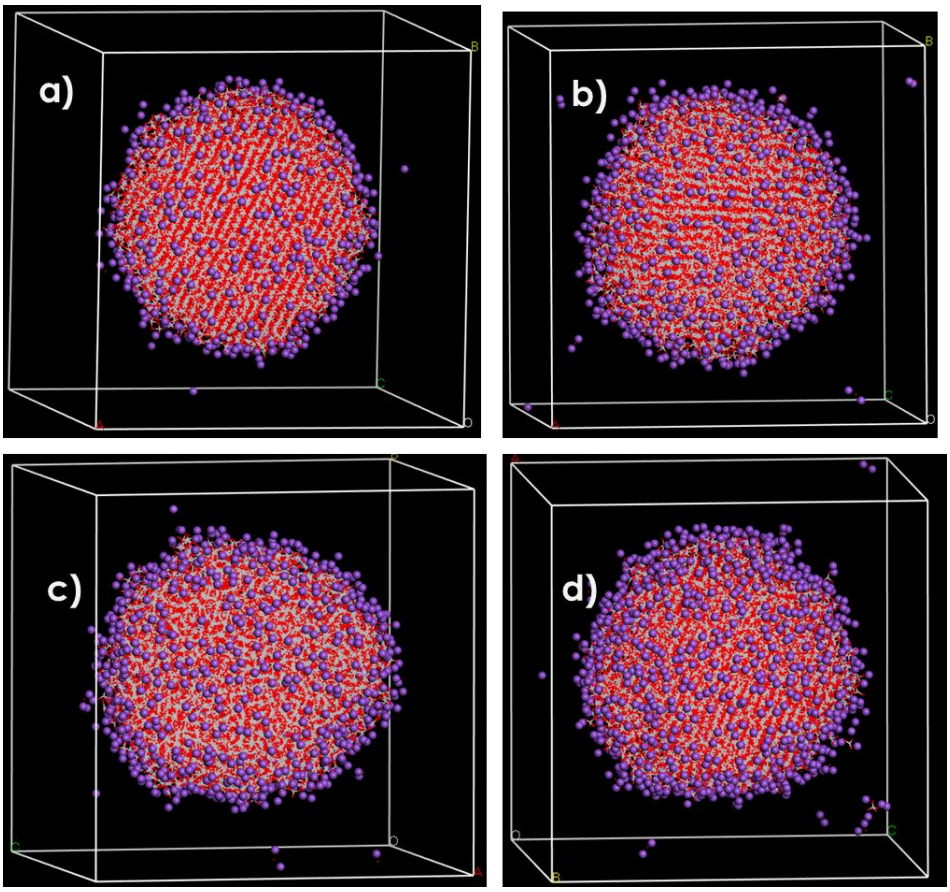

Figure 4.1: Represents recrystalised nanospheres for a) $Na_{0.11}TiO_2$, b) $Na_{0,15}TiO_2$, c) $Na_{0.19}TiO_2$, and d) $Na_{0.23}TiO_2$, respectively.

However, the nanosphere structure in Figure 4.1 c) did not recrystallise at all but rather has melted, the melting was confirmed by the noncrystalline pattens of the disordered Ti, O atoms arrangements seen on the structures. Similar results were also observed

in $Li_{0.19}TiO_2$ nanosphere structure illustrated by Figure 3.1 c) which attests that TiO_2 nanosphere structure cannot handle the hosting of 0.19 Li^+ and 0.19 Na^+ ions concentrations. Surprisingly Figure 4.1 d) had shown some crystalline patterns verified by the Ti, O ordered systems seen on the structure different from what was observed in Figure 4.1 c). So, the Na_xTiO_2 nanosphere structure was successfully recrystallised with 0.11, 0.15 and 0.23 Na^+ concentrations and was unsuccessful with 0.19 Na^+ concentration. Two layers of Ti^{4+} (blue and white) on each recrystallised Na_xTiO_2 nanosphere structure shown in Figure 4.1 a), b), c) and d) were sliced to obtain their microstructural defect morphologies inside the architectures. The sliced microstructural snapshots are shown in Figure 4.2 a), b), c) and d) respectively. Figure 4.2 a) and b) have pure crystalline patterns of zigzag and straight tunnels associated with the brookite and rutile polymorphs respectively, along with empty and Na^+ filled vacancies and majority of the Na^+ were observed on the edges of the microstructures.

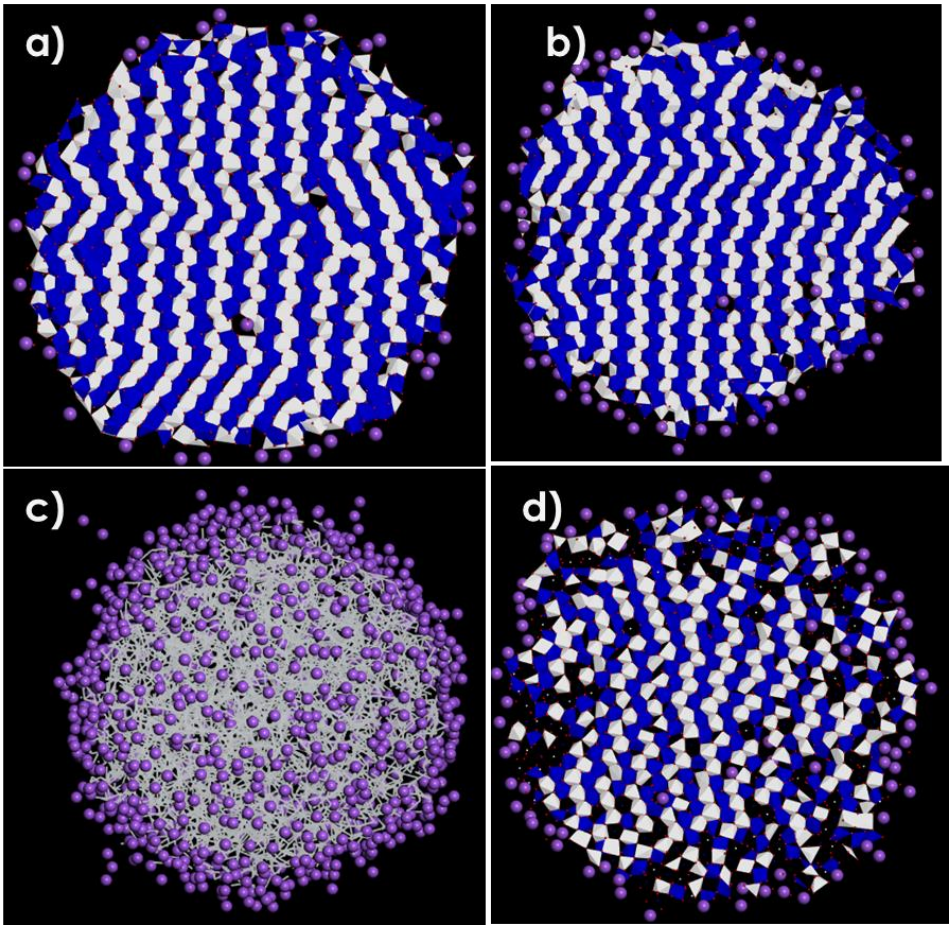

Figure 4.2: Shows a recrystallised microstructural snapshots nanospheres at concentrations a) $Na_{0.11}TiO_2$, b) $Na_{0,15}TiO_2$, c) $Na_{0.19}TiO_2$ and d) $Na_{0.23}TiO_2$, respectively.

So, since the Figure 4.1 c) could not recrystallise, there was no microstructural snapshots for it due to the impossibility and difficulty of obtaining two Ti^{4+} layers hence Figure 4.2 c) was obtained. Figure 4.2 c) simply shows the extents of how the Ti atoms were disordered surrounded by their inserted Na^+. Furthermore, the microstructures shown by Figure 4.2 d) contained some crystallinity that was highly dominated by zigzag patterns corresponding to the brookite phase with most Na^+ settling right on

their edges and within Ti^{4+} vacancies. The microstructural results obtained in Figure 4.2 a), b), c) and d) were consistent with results in Figure 4.1 a), b), c) and d) respectively.

4.1.2. Na_xTiO_2 Nanoporous

The recrystallised Na_xTiO_2 nanoporous structures are illustrated in Figure 3.3 a), b), c) and d) had similar characteristics of highly crystalline Ti, O patterns with most Na^+ segregation towards the open pores. Figure 3.3 a) had a very wide-open pore filled with most Na^+ right on a pore edge, while the open pores in Figure 3.3 d) were highly filled up by Na^+ where segregation of Na^+ was influenced by the charge compensation within the structures.

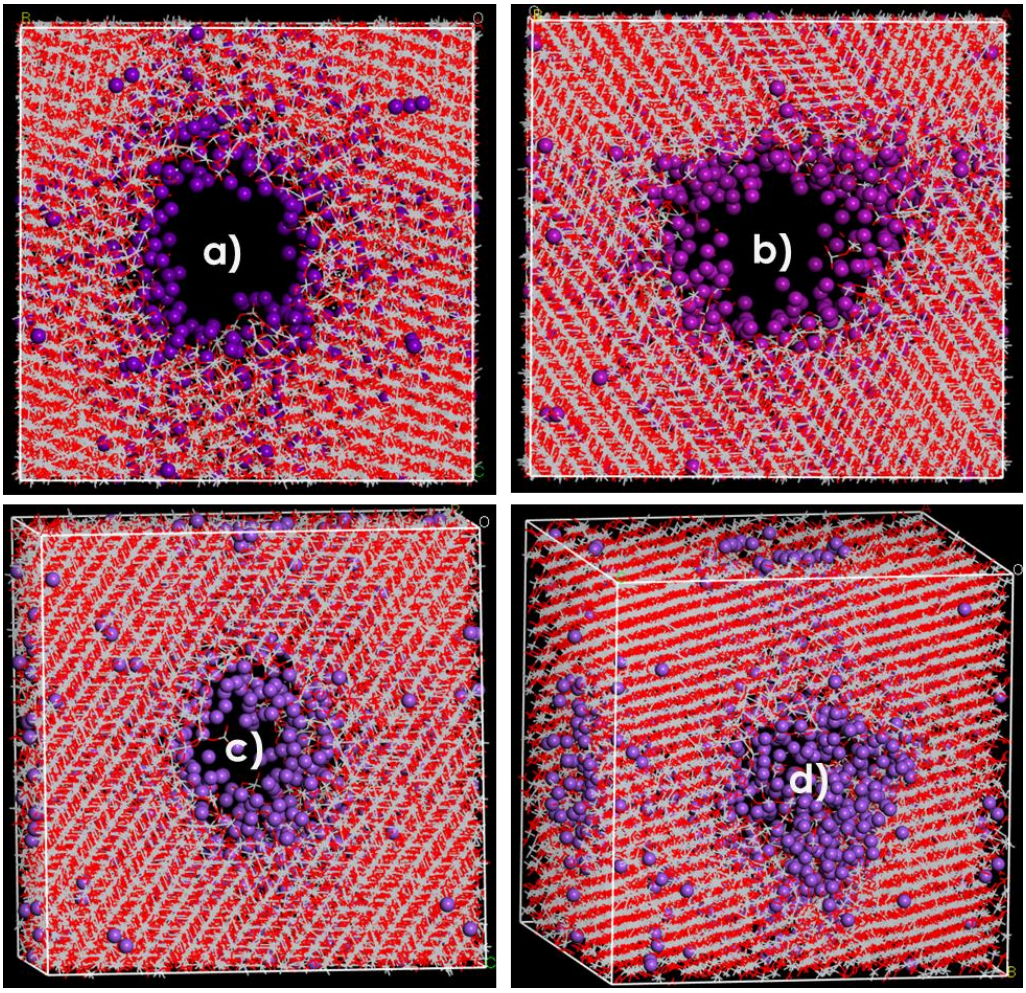

Figure 4.3: Represents recrystalised nanoporous architectures with concentrations of a) $Na_{0.11}TiO_2$, b) $Na_{0,15}TiO_2$, c) $Na_{0.19}TiO_2$ and d) $Na_{0.23}TiO_2$.

The nucleation and growth that occurred on Na_xTiO_2 nanoporous was verified by defect morphology through microstructural snapshot characterization conveyed in Figure 3.4 a), b), c) and d) respectively. All microstructures in Figure 3.4 had similar crystalline characteristics of straight and zigzag tunnels corresponding to the rutile and brookite phase along with empty and Na^+ filled vacancies, as well as some Na^+ were on the edges of the pores.

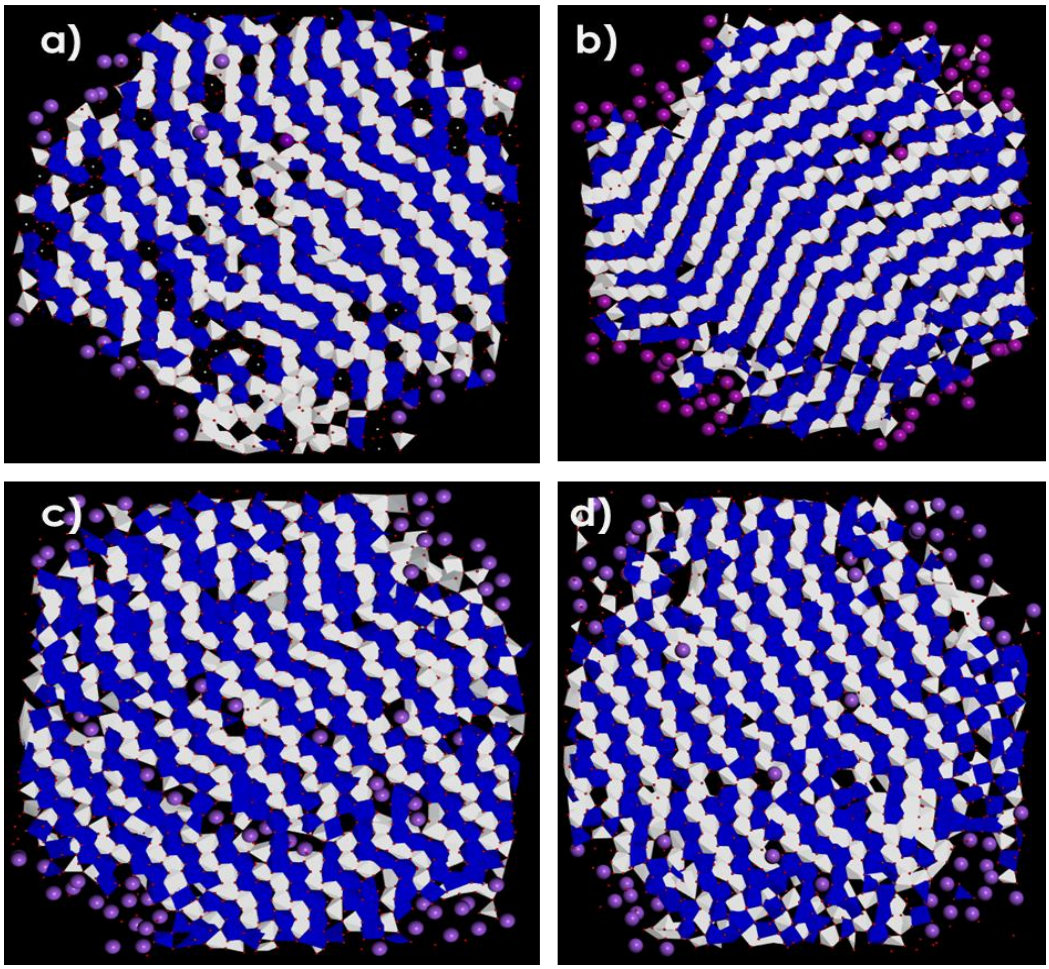

Figure 4.4: Shows microstructural snapshots for recrystallised nanoporous architecture with concentrations of a) $Na_{0.11}TiO_2$, b) $Na_{0,15}TiO_2$, c) $Na_{0.19}TiO_2$ and d) $Na_{0.23}TiO_2$.

4.1.3. Na_xTiO_2 Nanosheets

Figure 4.5 a) $Na_{0.11}TiO_2$, b) $Na_{0.15}TiO_2$, c) $Na_{0.19}TiO_2$ and d) $Na_{0.23}TiO_2$ are recrystallised nanosheet structures showing similar partially amorphous and partly crystalline Ti, O patterns n all structures where some Na^+ were actively diffusing away from the structure influenced by high thermal repulsion force and high Na^+ concentrations illustrated in Figure 4.5 c) and d). Na_xTiO_2 nanosheet structures shown in Figure 4.5 a) $Na_{0.11}TiO_2$, b) $Na_{0.15}TiO_2$, c) $Na_{0.19}TiO_2$ and d) $Na_{0.23}TiO_2$ were very much consistent with their respective microstructural snapshots in Figure 4.6 a), b), c) and d) which had partly crystalline and amorphous phases which then proves that the structures have indeed gone recrystallisation synthesis.

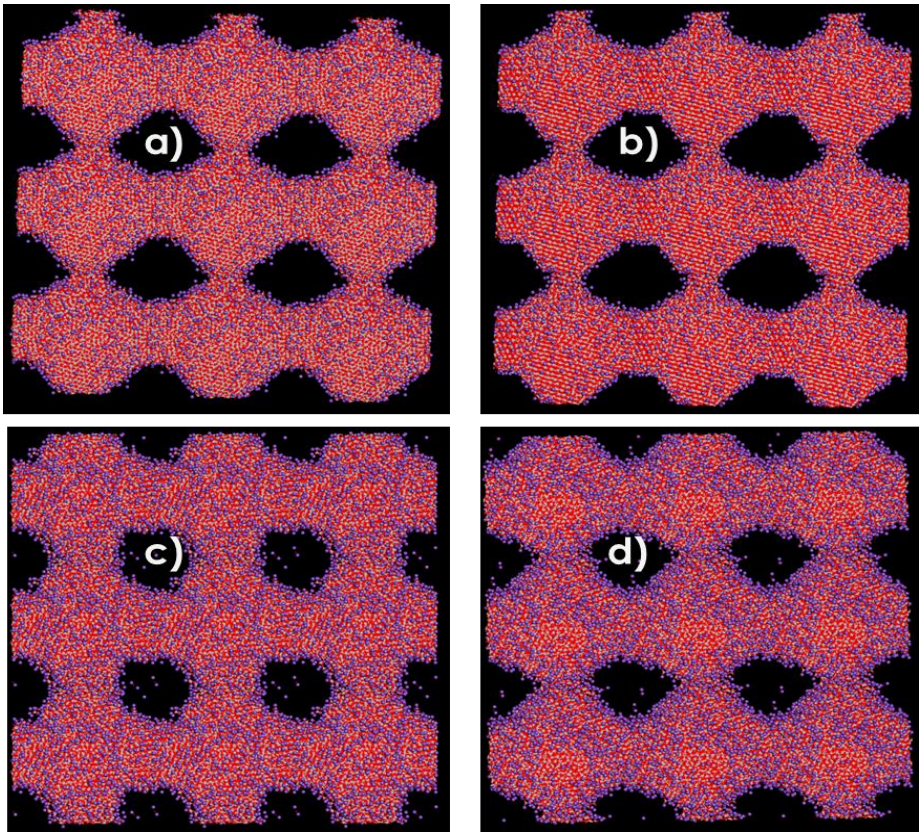

Figure 4.5: : Represents recrystallised nanosheets of Na_xTiO_2 with varying Na concentrations a) $Na_{0.11}TiO_2$, b) $Na_{0,15}TiO_2$, c) $Na_{0.19}TiO_2$ and d) $Na_{0.23}TiO_2$.

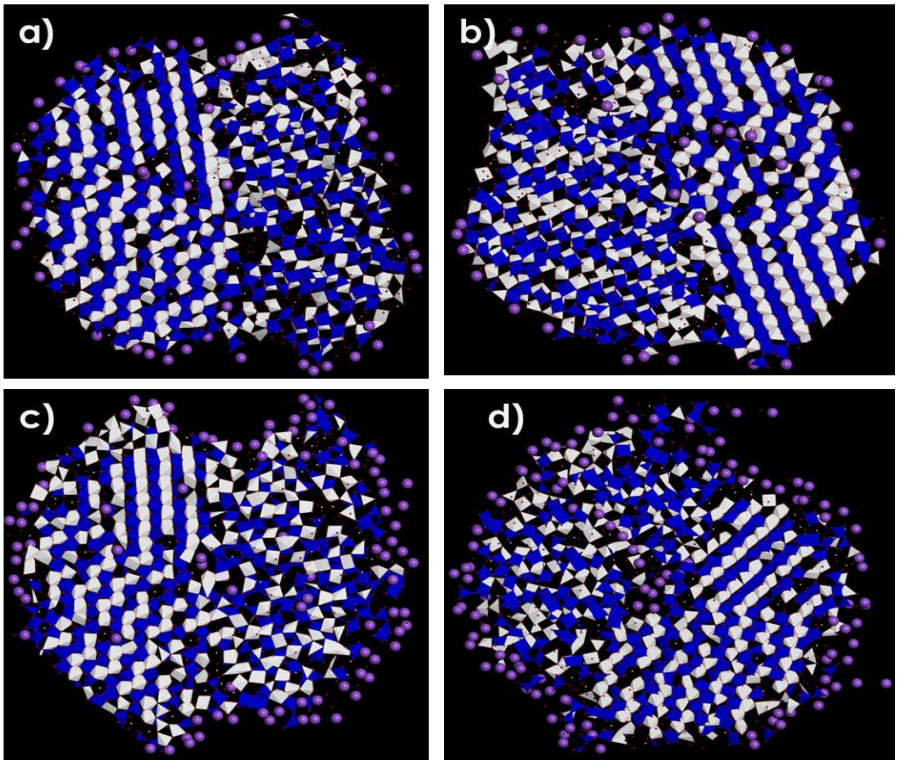

Figure 4.6: Shows recrystallised microstructural snapshots of Na_xTiO_2 nanosheets with varying Na concentrations; a) $Na_{0.11}TiO_2$, b) $Na_{0,15}TiO_2$, c) $Na_{0.19}TiO_2$, and d) $Na_{0.23}TiO_2$.

4.2. Cooled Structures and Microstructures of Na_xTiO_2 (x=0.11, 0.15, 0.19 and 0.23) nanostructures.

The recrystallised nanosphere, nanoporous and nanosheet architectures in Figure 4.1, Figure 4.3, and Figure 4.5 were then cooled from 1500 K, 1000 K, 500 and 0 K within 500 K intervals; the process was proceeded to influence further crystallinity and to verify the extent of structural Ti, O orderings at lower temperatures.

4.2.1. Na_xTiO_2 Nanosphere

Structural behaviour of $Na_{0.11}TiO_2$ nanosphere was studied at temperatures different from 2000 K, at which recrystallisation occurred, which are i) 1500 K ii) 1000 K iii) 500 K and iv) 0 K as illustrated in Figure 4.7 having similar structural patterns of atoms arrangements of that of Li^+ in Figure 3.7. These crystalline phases were confirmed by their microstructural snapshots illustrated in Figure 4.8 i), ii), iii) and iv) respectively, showing highly pure zigzag and straight tunnels associated with brookite and rutile polymorphs along with empty and Na^+ filled vacancies.

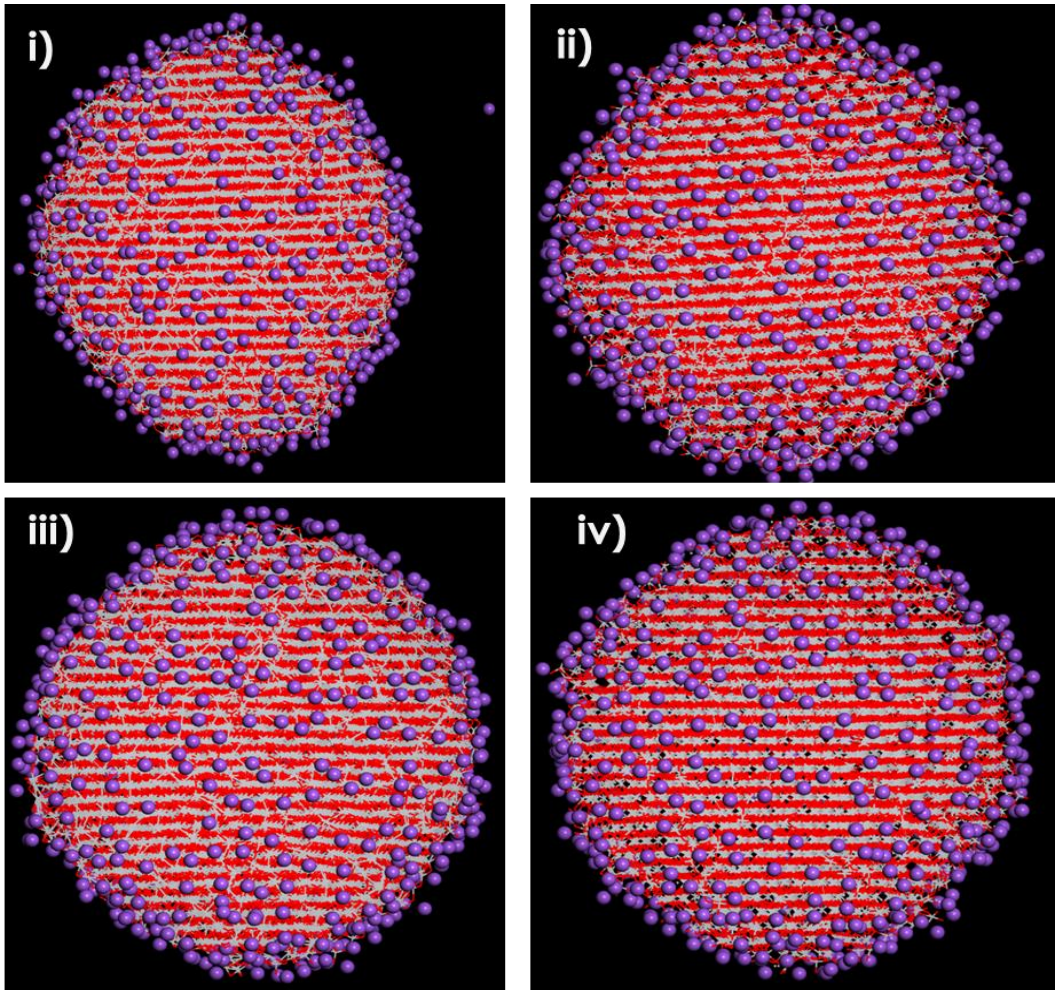

Figure 4.7: Cooled structures of nanosphere $Na_{0.11}TiO_2$ at i)1500 K, ii) 1000 K, iii) 500 K and 0 K.

Most Na^+ have settled inside the $Na_{0.11}TiO_2$ nanosphere architecture; however, some Na^+ were also noticed on the edges similarly to their respective microstructures in Figure 4.8. Increasing Na^+ inside the TiO_2 nanosphere with 0.15, 0.19 and 0.23 did

not affect any of the Ti, O framework patterns as seen in Figure 4.9, Figure 4.11 and Figure 4.13 respectively; consequently, their corresponding microstructures shown in Figure 4.10, Figure 4.12 and Figure 4.14 have similar characteristics as seen in Figure 4.8 which had zigzag and straight tunnels corresponding to brookite and rutile polymorphs along with empty and Na^+ filled vacancies.

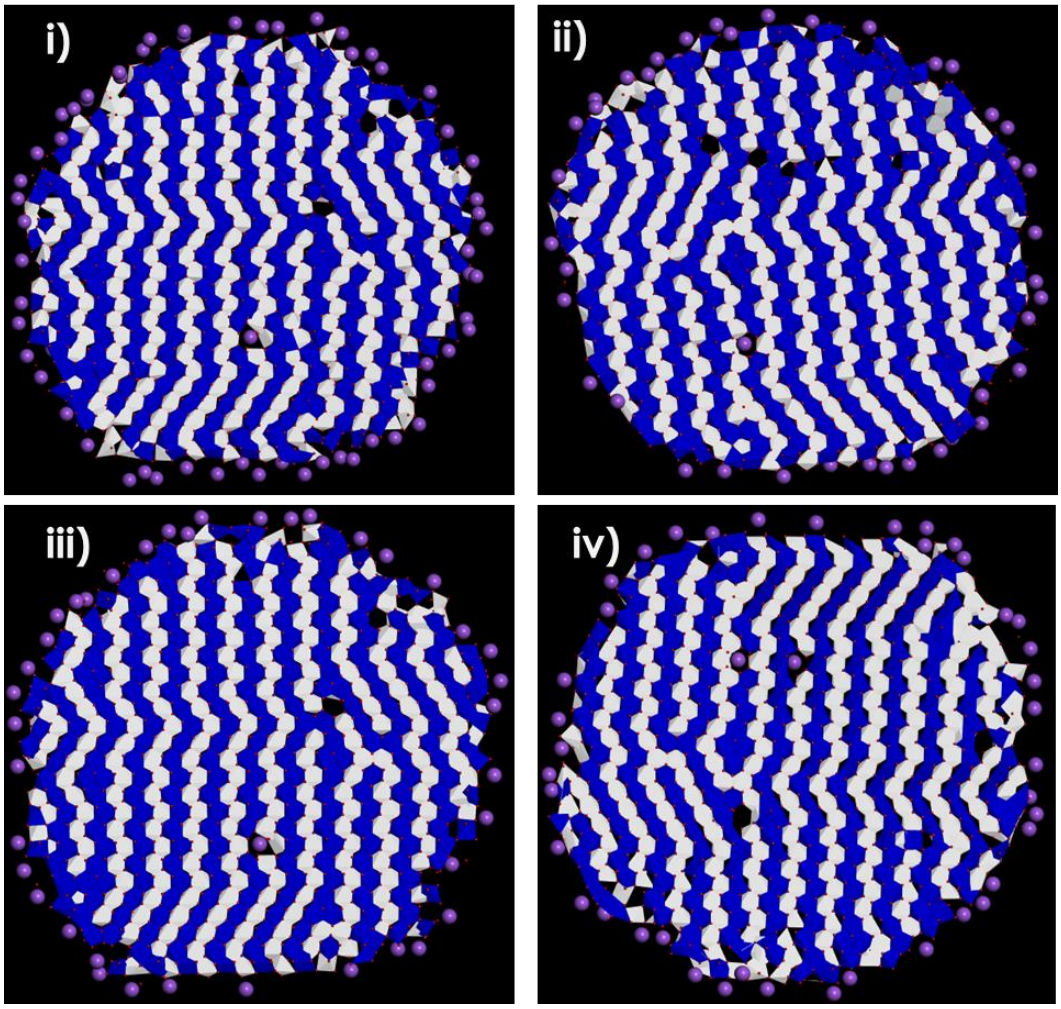

Figure 4.8: Cooled microstructures of nanosphere $Na_{0.11}TiO_2$ at i) 1500 K, ii) 1000 K, iii) 500 K and iv) 0 K.

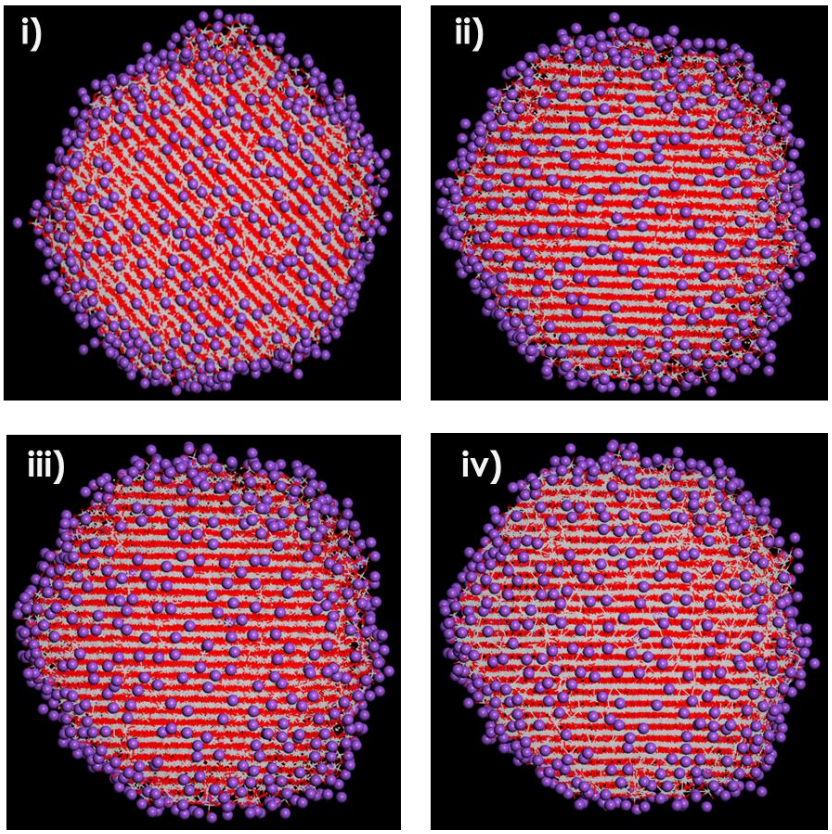

Figure 4.9: Cooled structures of nanosphere $Na_{0.15}TiO_2$ at i)1500 K, ii) 1000 K, iii) 500 K and 0 K.

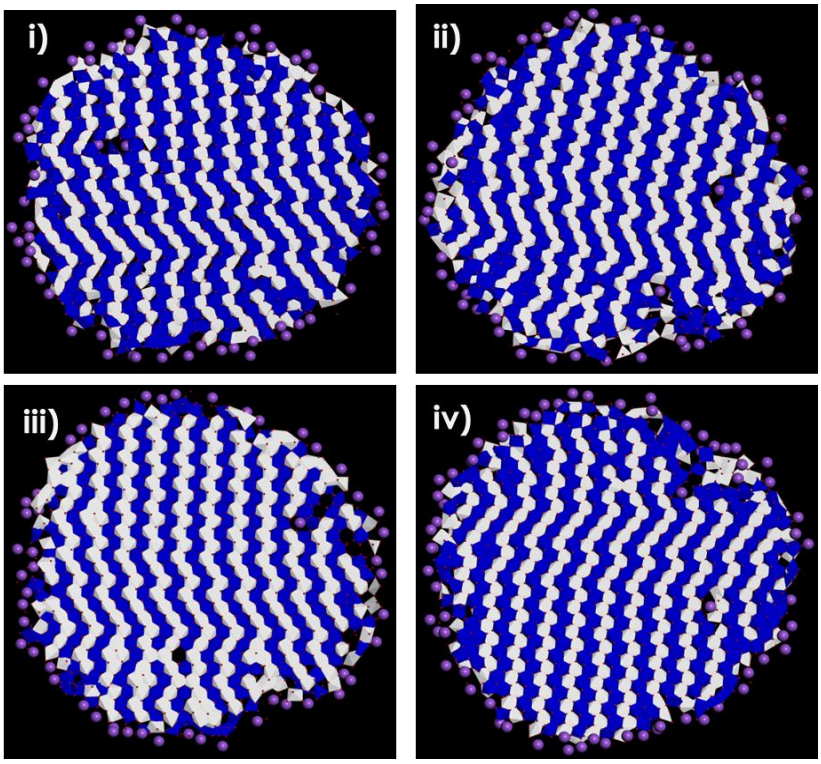

Figure 4.10: Cooled microstructures of nanosphere $Na_{0.15}TiO_2$ at i) 1500 K, ii) 1000 K, iii) 500 K and iv) 0 K.

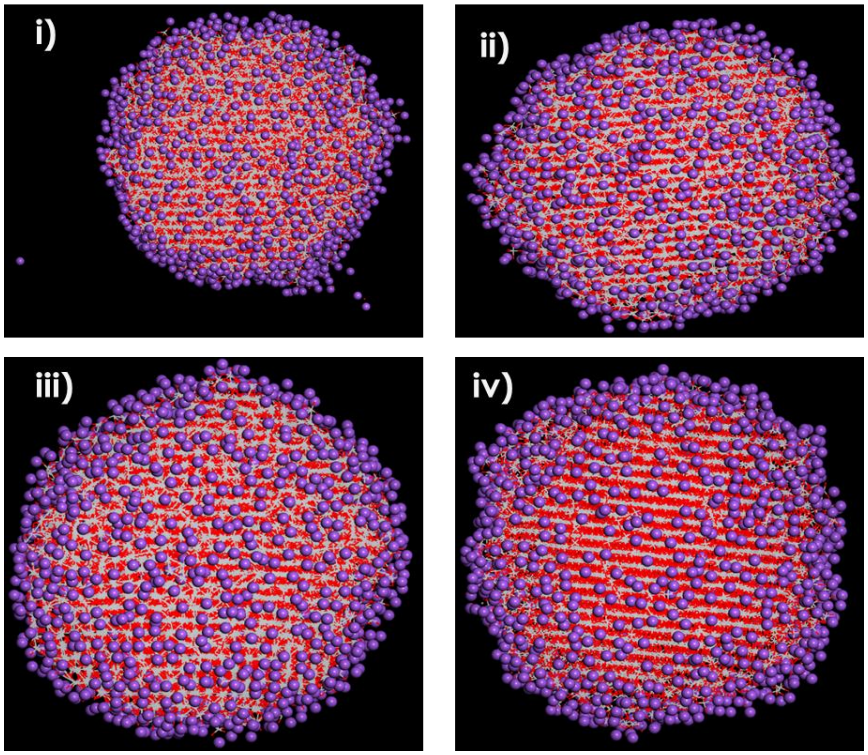

Figure 4.11: Cooled structures of nanosphere $Na_{0.23}TiO_2$ at i)1500 K, ii) 1000 K, iii) 500 K and 0 K.

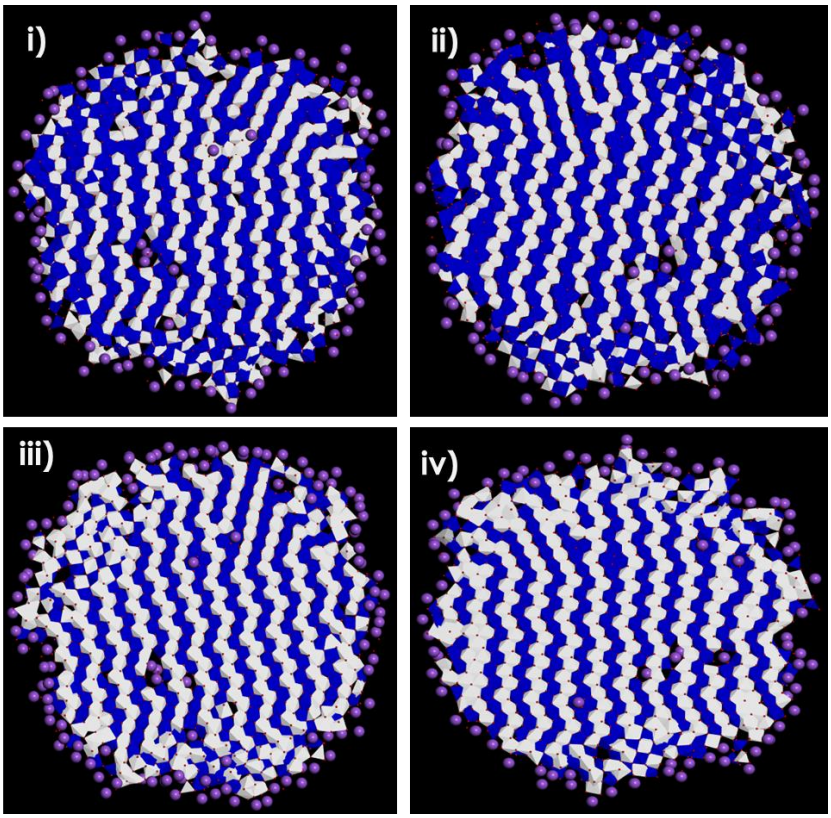

Figure 4.12: Cooled microstructures of nanosphere $Na_{0.23}TiO_2$ at i) 1500 K, ii) 1000 K, iii) 500 K and iv) 0 K.

4.2.2. Na_xTiO_2 Nanoporous

Recrystallised nanoporous architectures with concentrations $Li_{0.11}TiO_2$, $Li_{0.15}TiO_2$, $Li_{0.19}TiO_2$ and $Li_{0.23}TiO_2$ were cooled to i) 1500 K ,ii) 1000 K, iii) 500 K and iv) 0 K in order to enhance their crystallinity at low temperature. Such cooled nanoporous structures are featured in figures 4.13, 4.15, 4.17 and 4.19 along with their microstructural snapshots showing similar and familiar structural patterns of straight and zigzag tunnels related to rutile and brookite polymorphs also having some empty and Na^+ filled vacancies better viewed in figures 4.14, 4.16, 4.18 and 4.20 respectively.

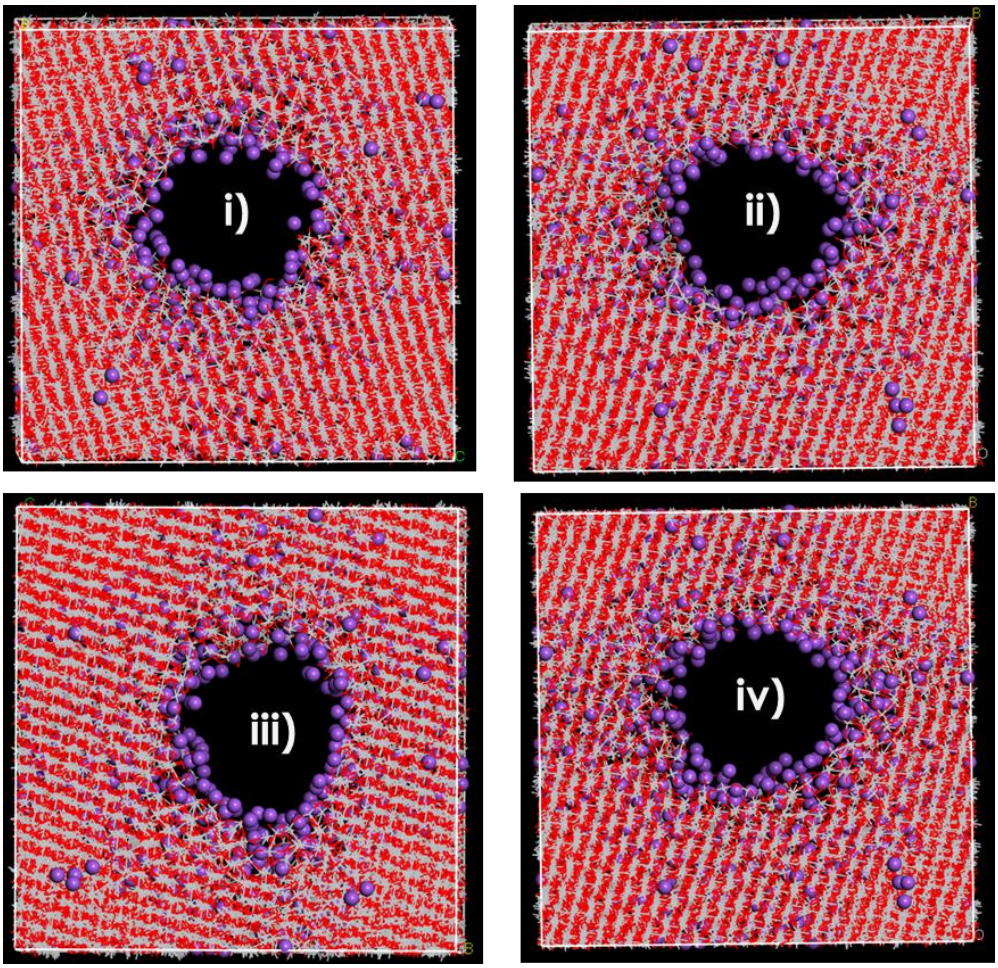

Figure 4.13: Cooled structures of nanoporous $Na_{0.11}TiO_2$ at i)1500 K, ii) 1000 K, iii) 500 K and iv) 0 K.

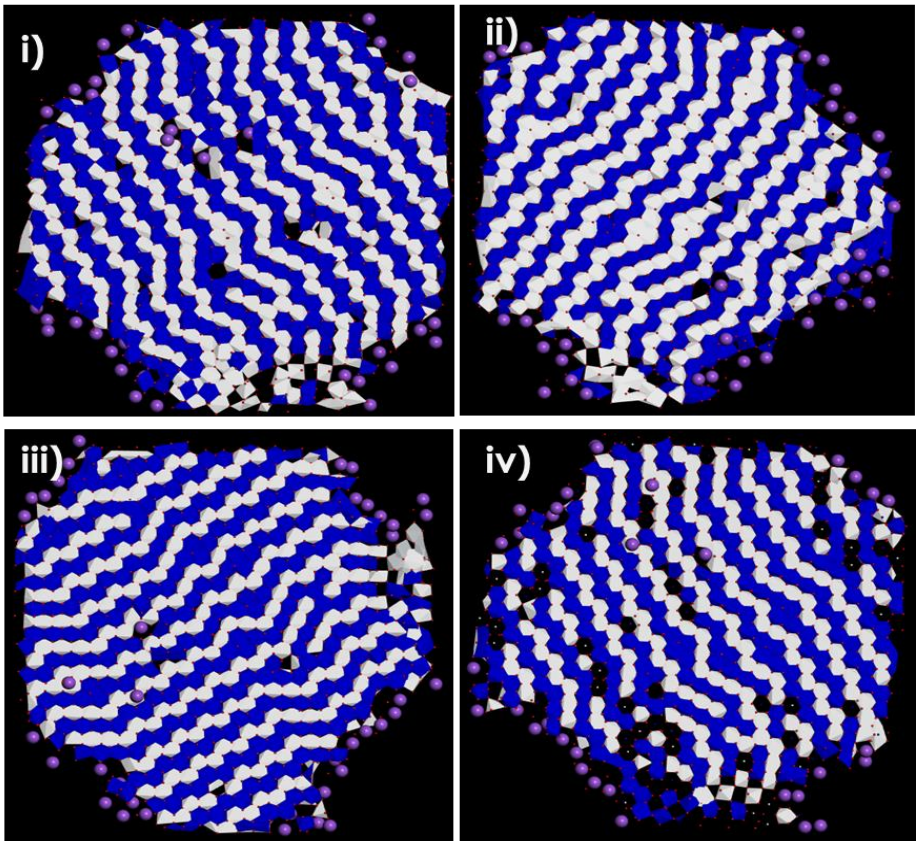

Figure 4.14: Cooled microstructures of nanoporous $Na_{0.11}TiO_2$ at i) 1500 K, ii) 1000 K, iii) 500 K and iv) 0 K.

Cooling the nanoporous Na_xTiO_2 gradually increases the crystallinity and structural defects without affecting the Ti, O atom ordering. It also influences the wide opening of the pores by drawing the Na^+ towards the pore edges and channels. Interestingly, all microstructural defects of nanoporous Na_xTiO_2 illustrated in figures 4.14, 4.16, 4.18 and 4.20 have similar structural defects as those of Li_xTiO_2 nanoporous shown in figures 3.14, 3.16, 3.18 and 3.20 respectively, the strong familiarity of structural defects is due to the Li^+ and Na^+ properties which have an almost similar ion exchange and equilibrium constant properties. It may be surmised that TiO_2 nanoporous architecture is an excellent configuration for hosting high Na^+ and Li^+ concentrations and can withstand high temperature conditions without damaging the crystalline ordered patterns on the system; hence is appropriate for sodium ion batteries anodes.

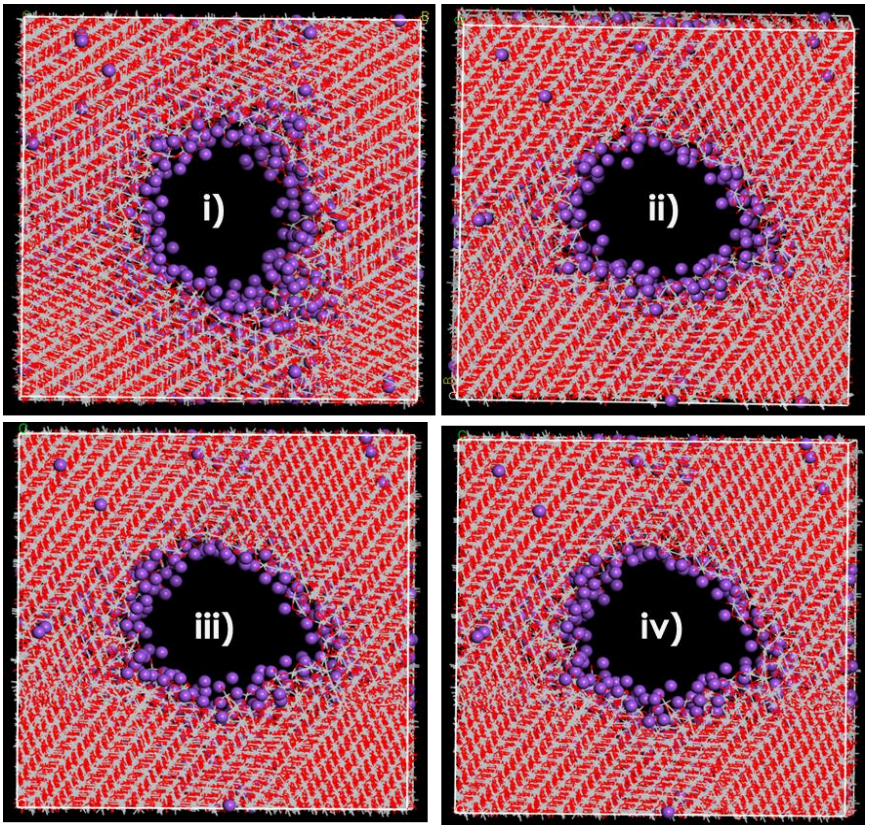

Figure 4.15: Cooled structures of nanoporous $Na_{0.15}TiO_2$ at i) 1500 K, ii) 1000 K, iii) 500 K and iv) 0 K.

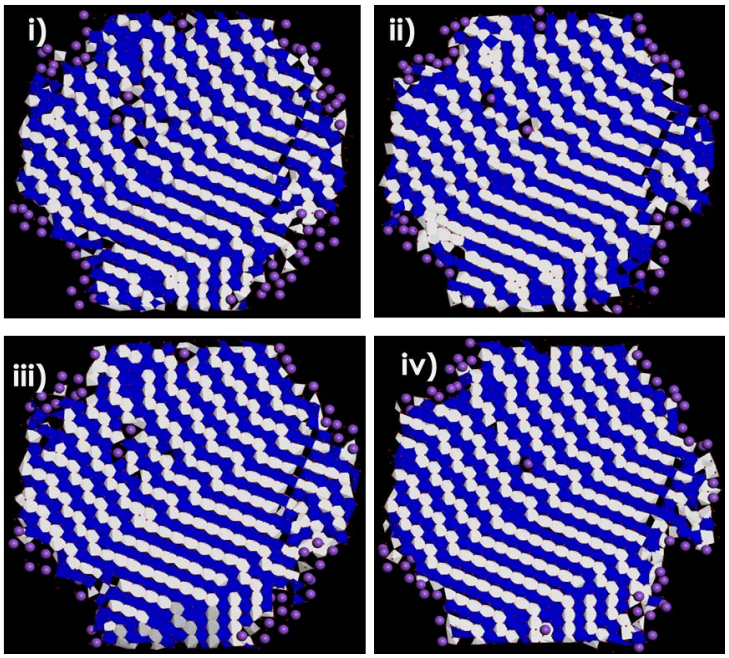

Figure 4.16: Cooled microstructures of nanoporous $Na_{0.15}TiO_2$ at i) 1500 K, ii) 1000 K, iii) 500 K and iv) 0 K.

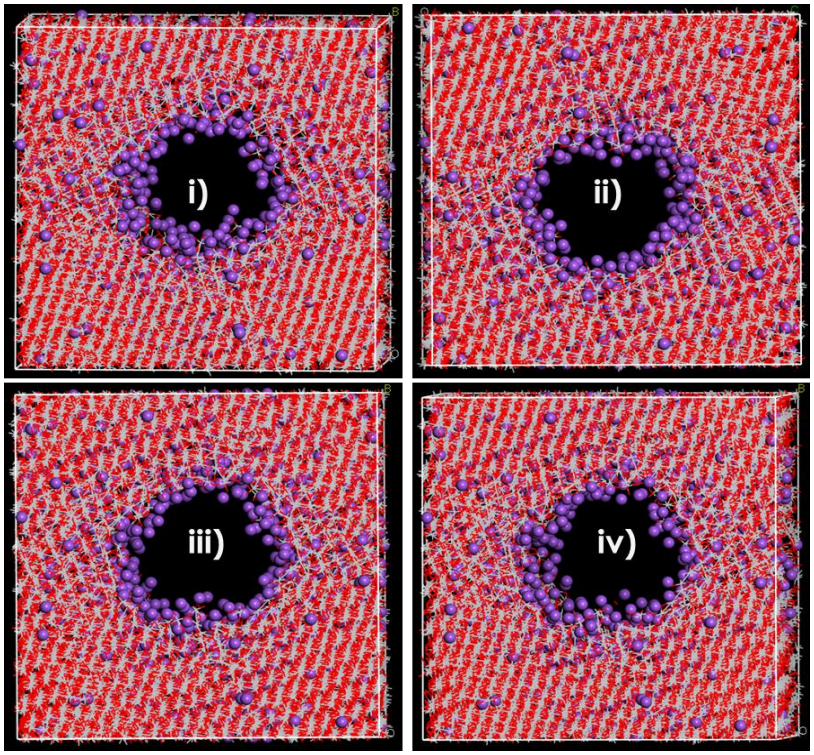

Figure 4.17: Cooled structures of nanoporous $Na_{0.19}TiO_2$ at i) 1500 K, ii) 1000 K, iii) 500 K and iv) 0 K.

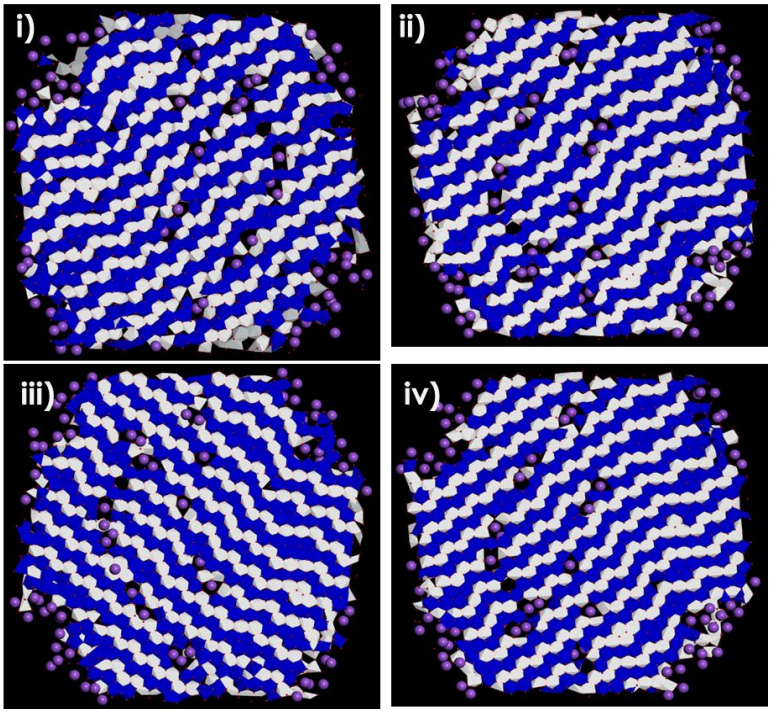

Figure 4.18: Cooled microstructures of nanoporous $Na_{0.19}TiO_2$ at i) 1500 K, ii) 1000 K, iii) 500 K and iv) 0 K.

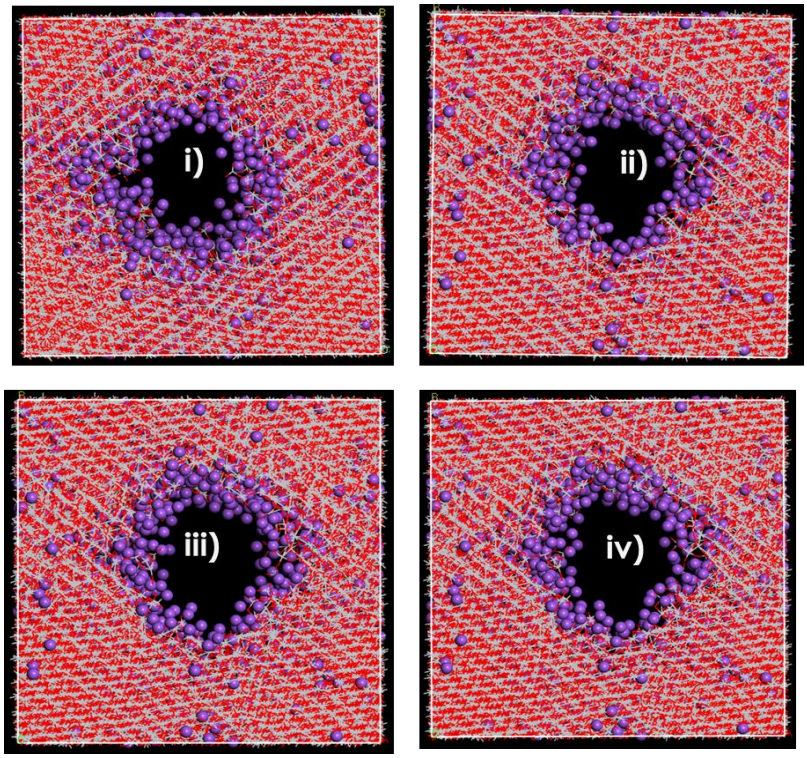

Figure 4.19: Cooled structures of nanoporous $Na_{0.23}TiO_2$ at i)1500 K, ii) 1000 K, iii) 500 K and iv) 0 K.

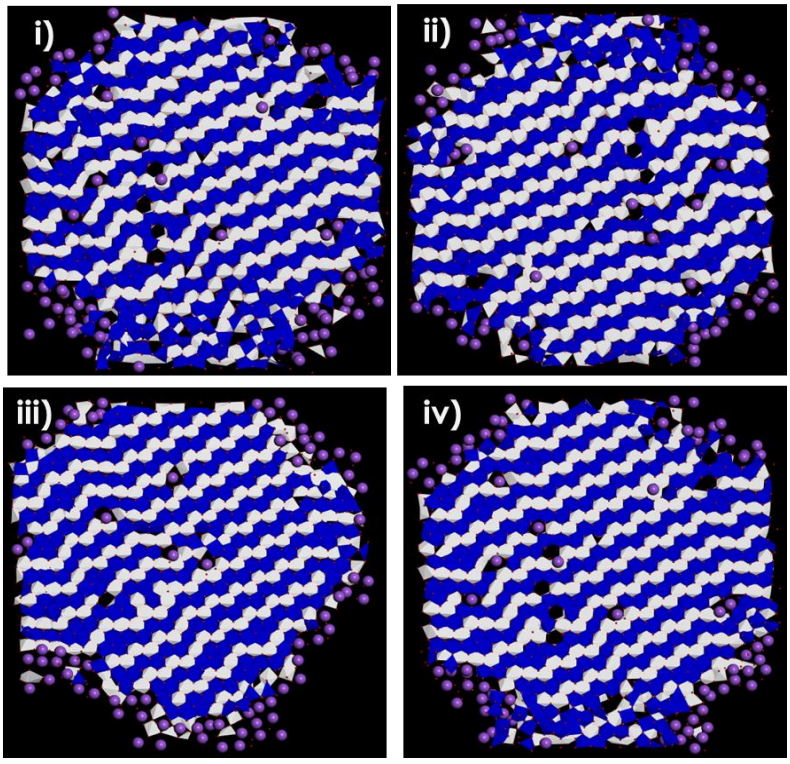

Figure 4.20: Cooled microstructures of nanoporous $Na_{0.23}TiO_2$ at i) 1500 K, ii) 1000 K, iii) 500 K and iv) 0 K.

4.2.3. Na_xTiO_2 Nanosheets

Furthermore, the cooling synthesis was also performed on the $Na_{0.11}TiO_2$, $Na_{0.15}TiO_2$ $Na_{0.19}TiO_2$ $Na_{0.23}TiO_2$ nanosheets architecture structures from i)1500 K, ii) 1000 K, iii) 500 K then iv) 0 K to improve the ordering for better Na^+ diffusivity and excellent pathways via their structural and microstructural snapshot's view shown from Figure 4. 21 to Figure 4.28. Cooled nanosheet structures shown in Figure 4.21, Figure 4.23, Figure 4.25 and Figure 4.27 have similar ordered patterns, however increasing the Na^+ inside the TiO_2 nanosheets has expanded the structures then made the systems to be more Na^+ filled by allowing dispersed Na^+ distribution without them aggregating.

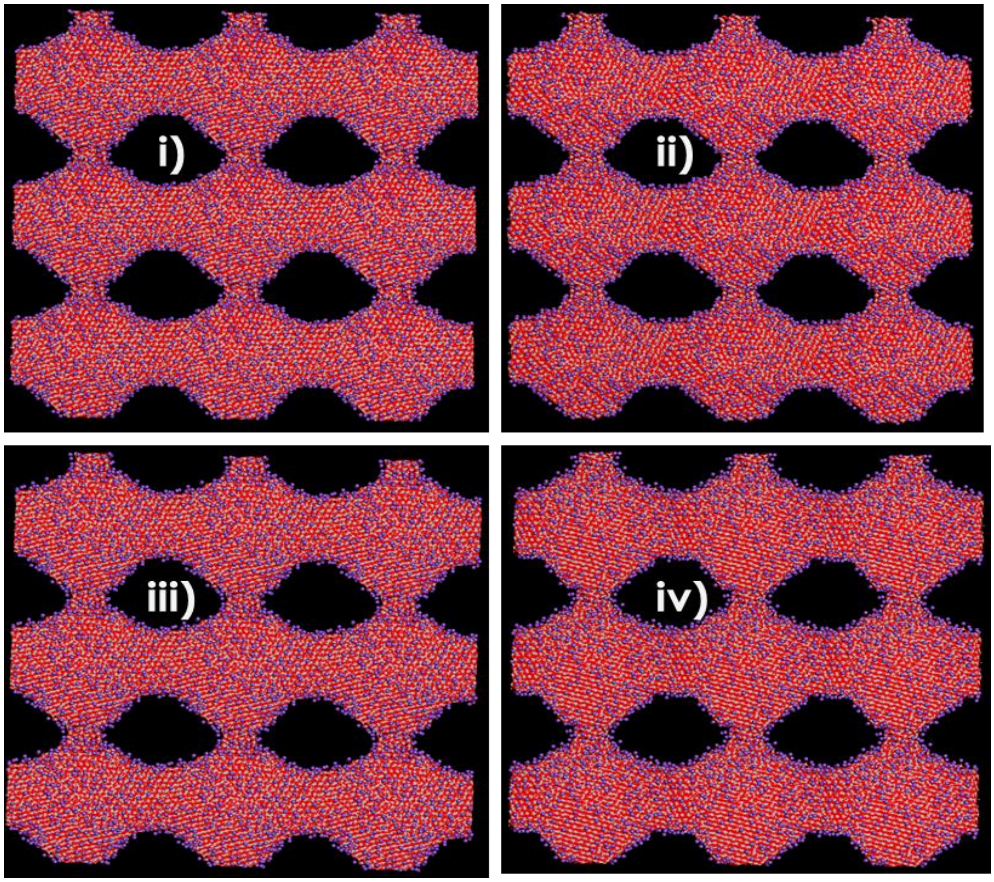

Figure 4.21: Cooled structures of $Na_{0.11}TiO_2$ nanosheets at i) 1500 K, ii) 1000 K, iii) 500 K and iv) 0 K.

The previous observation was confirmed by the microstructural snapshots to compare the defect properties at all given Na^+ concentrations and cooled temperatures. All microstructures shown by Figure 4.22, Figure 4.24, Figure 4.26 and Figure 4.28 agrees well with their respective structures where more Na^+ are observed to be right inside the partial non-crystalline and partial crystalline tunnels with more straight and zigzag tunnels corresponding to the rutile and brookite polymorphs respectively along with emptier and Na^+ filled vacancies on the highly crystalline part of the microstructures.

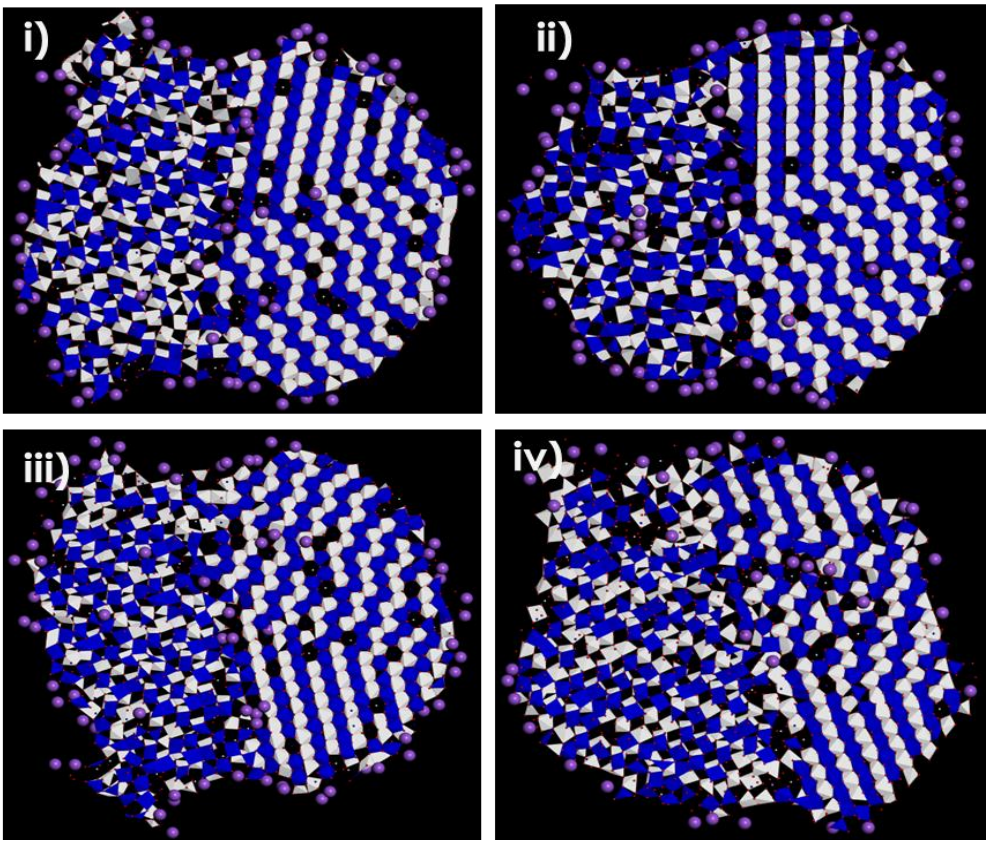

Figure 4.22: Cooled microstructures of $Na_{0.11}TiO_2$ nanosheets at i) 1500 K, ii) 1000 K, iii) 500 K and iv) 0 K.

The partial amorphous and partial crystalline patterns inside the nanosheets structure allows structural stabilities inside during and after higher exposure temperature conditions and seeing that their microstructures do not change even at low temperatures it improves high Na^+ diffusivity during charging and discharging. Therefore, Na_xTiO_2 (0.11, 0.15, 0.19 and 0.23) nanosheets showed very excellent structural stability after cooling synthesis which is very good for future anode electrode materials for sodium ion batteries.

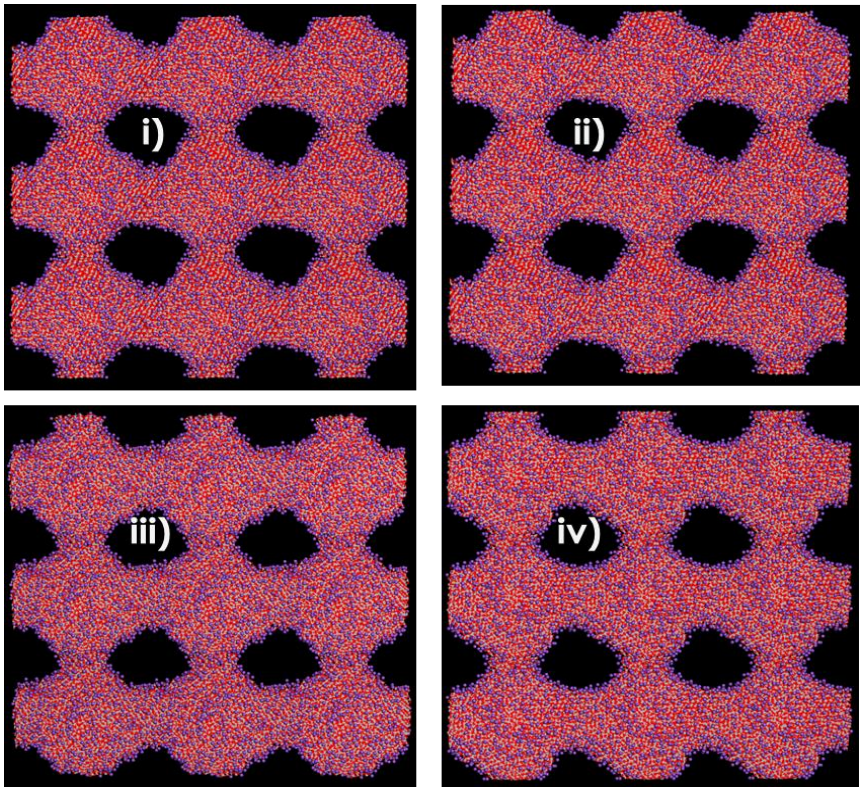

Figure 4.23: Cooled structures of $Na_{0.15}TiO_2$ nanosheets at i)1500 K, ii) 1000 K, iii) 500 K and 0 K.

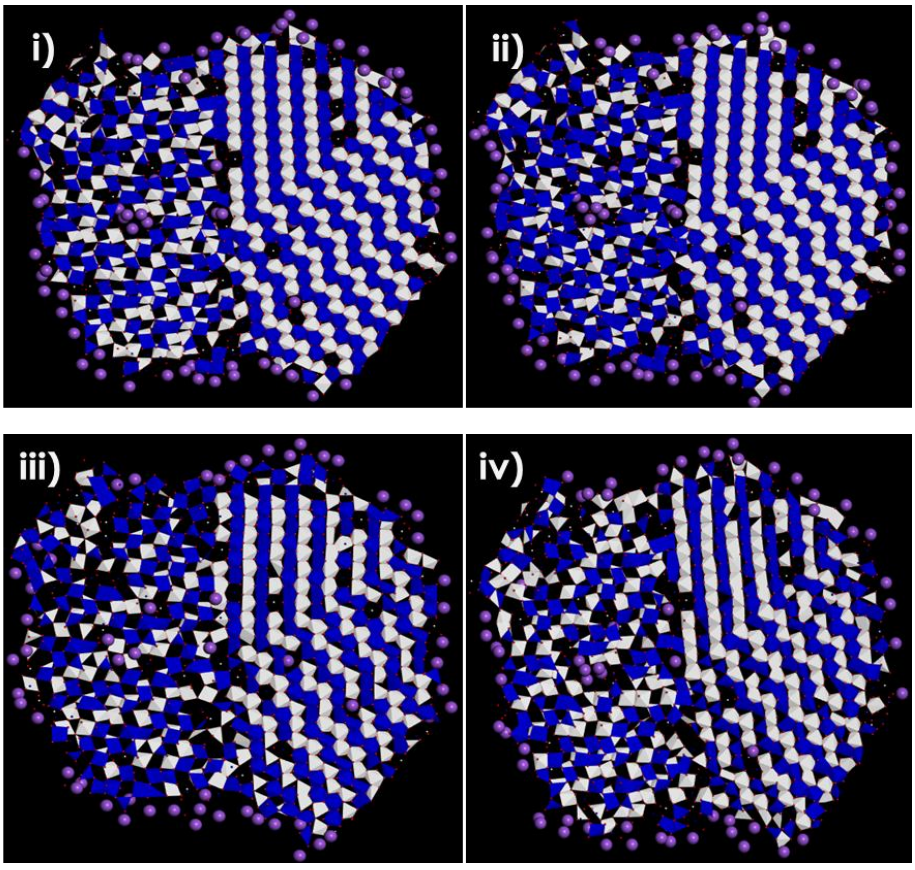

Figure 4.24: Cooled microstructures of $Na_{0.15}TiO_2$ nanosheets at i) 1500 K, ii) 1000 K, iii) 500 K and iv) 0 K.

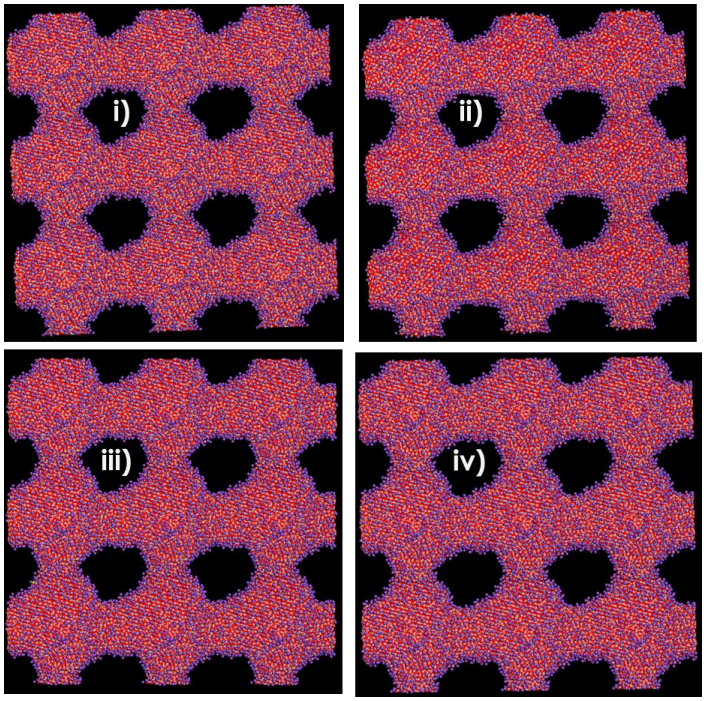

Figure 4.25: Cooled structures of $Na_{0.19}TiO_2$ nanosheets at i) 1500 K, ii) 1000 K, iii) 500 K and 0 K.

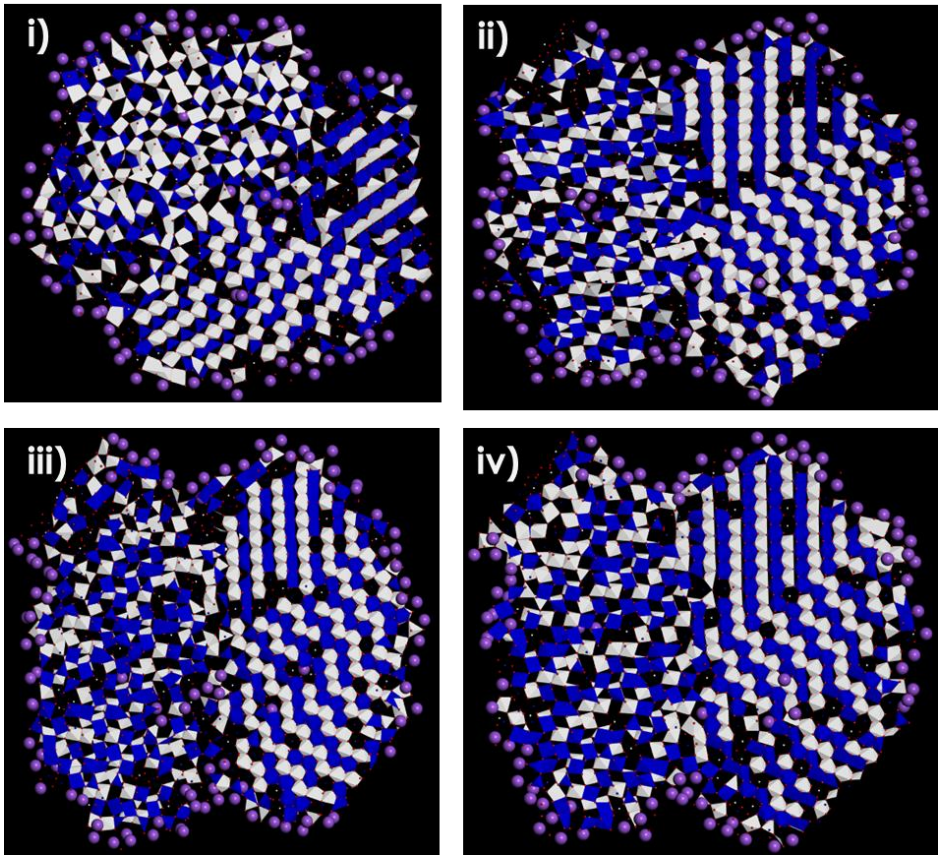

Figure 4.26: Cooled microstructures of $Na_{0.19}TiO_2$ nanosheets at i) 1500 K, ii) 1000 K, iii) 500 K and iv) 0 K.

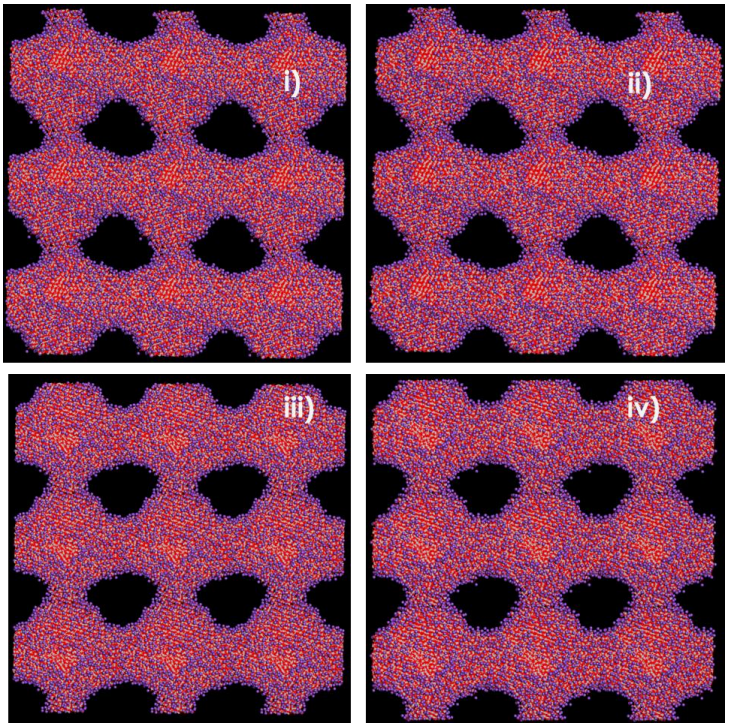

Figure 4.27: Cooled structures of $Na_{0.23}TiO_2$ nanosheets at i) 1500 K, ii) 1000 K, iii) 500 K and iv) 0 K.

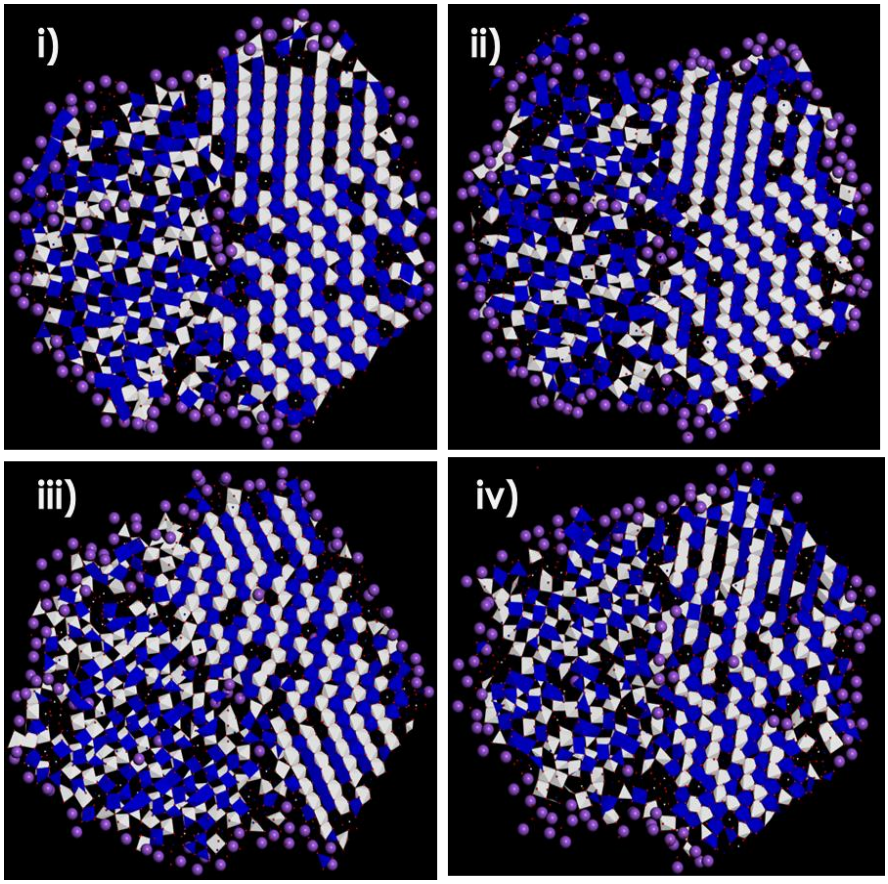

Figure 4.28: Cooled microstructures of $Na_{0.23}TiO_2$ nanosheets at i) 1500 K, ii) 1000 K, iii) 500 K and iv) 0 K.

4.3. RDFs of Na_xTiO_2 Nanostructures (x= 0.11, 0.15, 0.19 and 0.23)

In a crystal RDFs have finite number of sharp peaks whose separation and height are characteristics of the lattice structure.

4.3.1. Na_xTiO_2 Nanosphere

The RDFs plots of $Na_{0.11}TiO_2$, $Na_{0.15}TiO_2$, $Na_{0.19}TiO_2$ and $Na_{0.23}TiO_2$ nanospheres cooled from 1500 K to 0 K within 500 K intervals are illustrated in figures 4.29, 4.30, 4.31 and 4.32 respectively. These RDFs plots consist of an almost 2Å bond length equivalent to calculated bond length and G(r) maxima values of first peaks of Li_xTiO_2 and Mg_xTiO_2 nanosphere Ti-O pairs RDFs plots observed in chapters 3 and 5. This observation confirms that temperature did not distort the Ti-O positions but only improved the extent of crystallinity. Hence, no change was seen in RDFs peak positions but rather only the variation of the broadening of peaks was noted. The RDFs shown in figures 4.29, 4.30 and 4.32 show very distinct sharp peaks at low (0 K) temperatures indicating a highly crystalline structure, then their crystallinity reduced with an increase in temperature as indicated by their broader reflected in the trend 0 K > 500 K >1000 K >1500 K > 2000 K. However, the RDF peaks in figure 4.31 have broad peaks at all reduced temperatures although the broadness was clearly decreased at the very low (0 K) temperature, which then proves the $Na_{0.19}TiO_2$ was not crystalline but rather amorphous at all temperatures below 2000. Similar peak characteristics were also reflected in $Li_{0.19}TiO_2$.

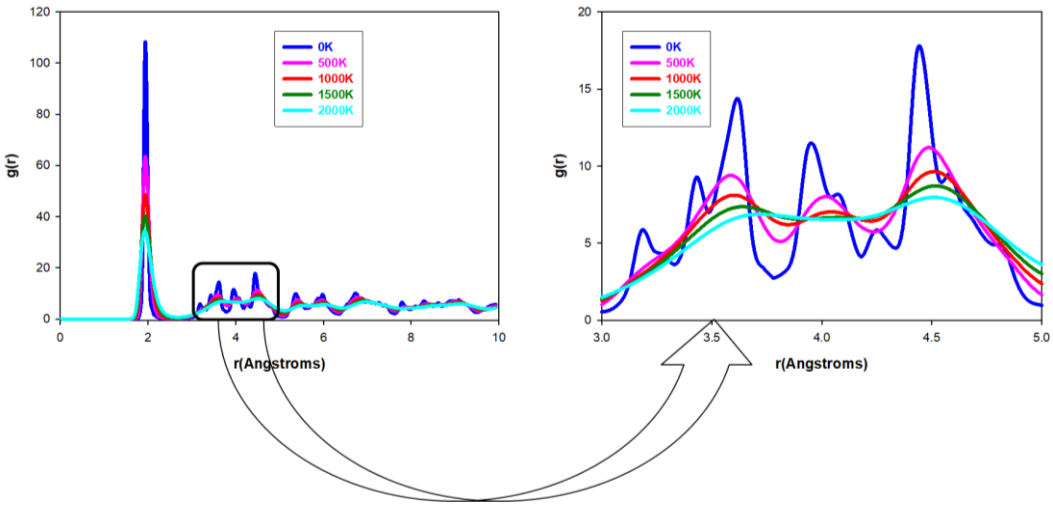

Figure 4.29: Shows simulated RDFs plots for $Na_{0.11}TiO_2$ nanosphere at all temperatures with a magnified RDFs portion between 3 and 5 Å for better visualisation.

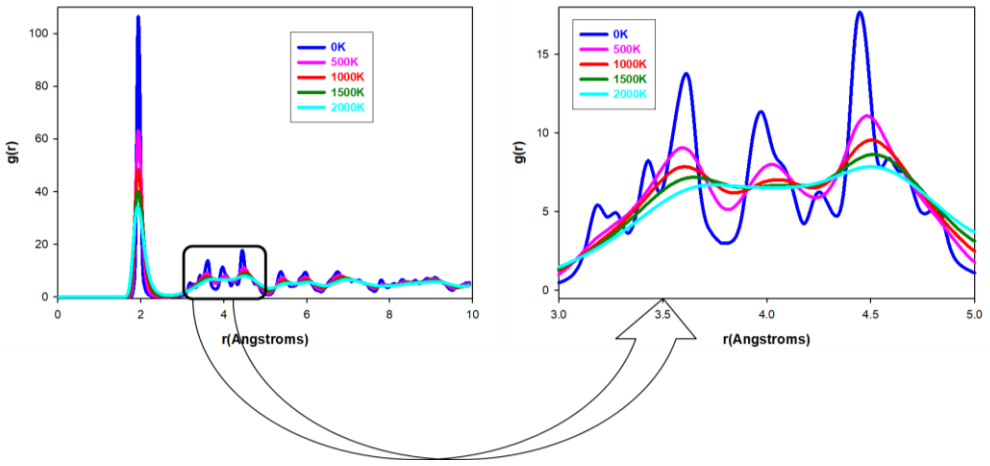

Figure 4.30: Shows simulated RDFs plots for $Na_{0.15}TiO_2$ nanosphere at all temperatures with a magnified RDFs portion between 3 and 5 Å for better visualisation.

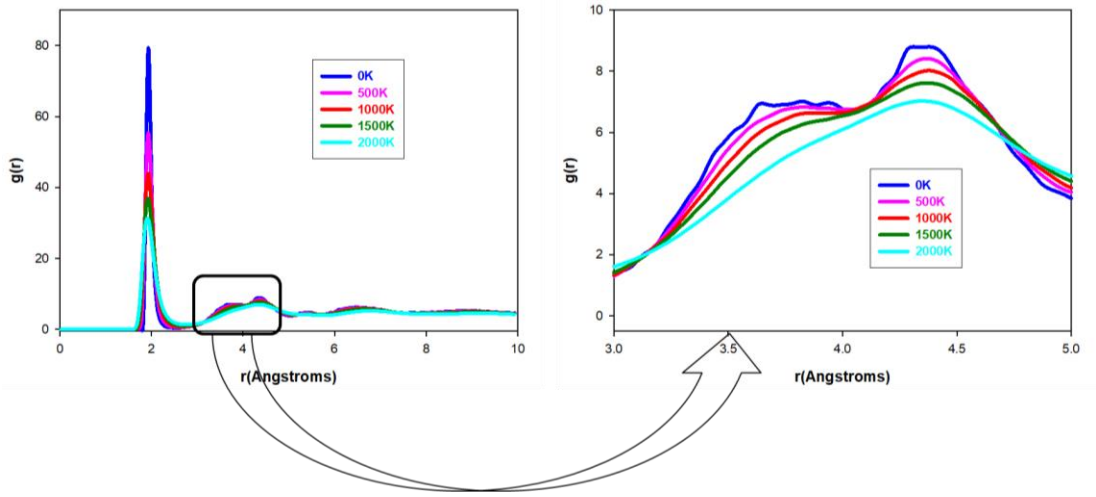

Figure 4.31: Shows simulated RDFs plots for $Na_{0.19}TiO_2$ nanosphere at at all temperatures with a magnified RDFs portion between 3 and 5 Å for better visualisation.

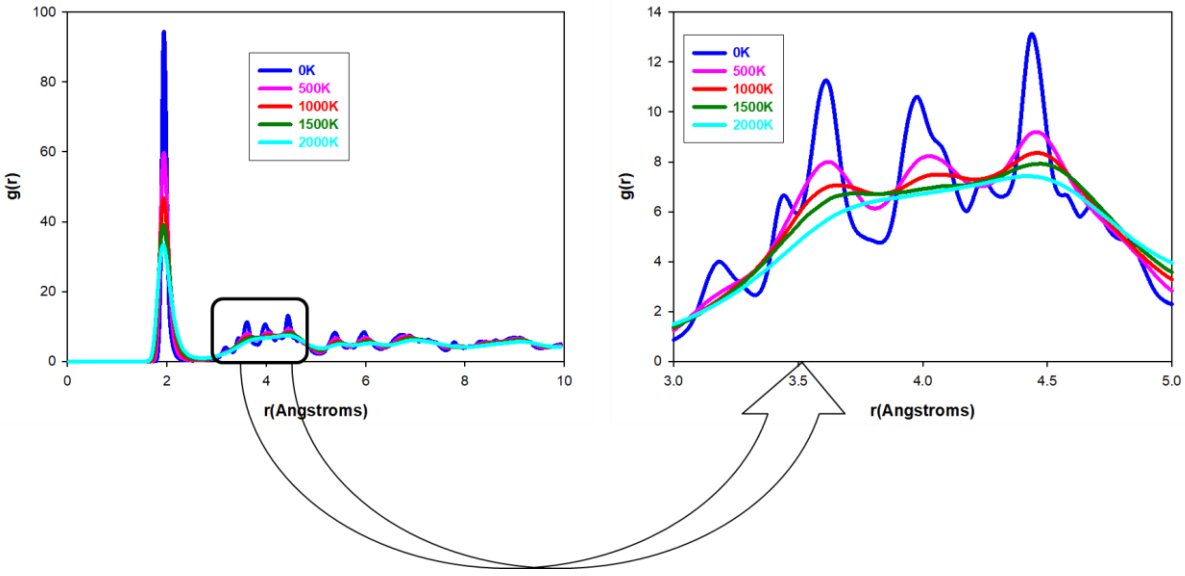

Figure 4.32: Shows simulated RDFs plots for $Na_{0.23}TiO_2$ nanosphere at all temperatures with a magnified RDFs portion between 3 and 5 Å for better visualisation.

4.3.2. Na_xTiO_2 Nanoporous

The Ti-O RDF analysis in $Na_{0.11}TiO_2$, $Na_{0.15}TiO_2$, $Na_{0.19}TiO_2$ and $Na_{0.23}TiO_2$ nanoporous systems are presented in figures 4.33, 4.35, 4.36 and 4.37 respectively. All the RDFs peaks show that the crystallinity decreases with increasing temperature, below 2000 K. These RDF data analysis of Na_xTiO_2 nanoporous confirms that cooling down the systems greatly improves the extent of crystallisation, which is important in electrochemical properties of the anodes. The bond length and the G (r) observed in figures 4.33 to 4.37 are the similar to those of Li_xTiO_2 nanoporous the only difference being peak sharpness, peak splitting and peak intersections as seen on the magnified RDFs sections for each Ti-O pair. Furthermore, more Na^+ intercalation into TiO_2 nanoporous systems reduces peak sharpness

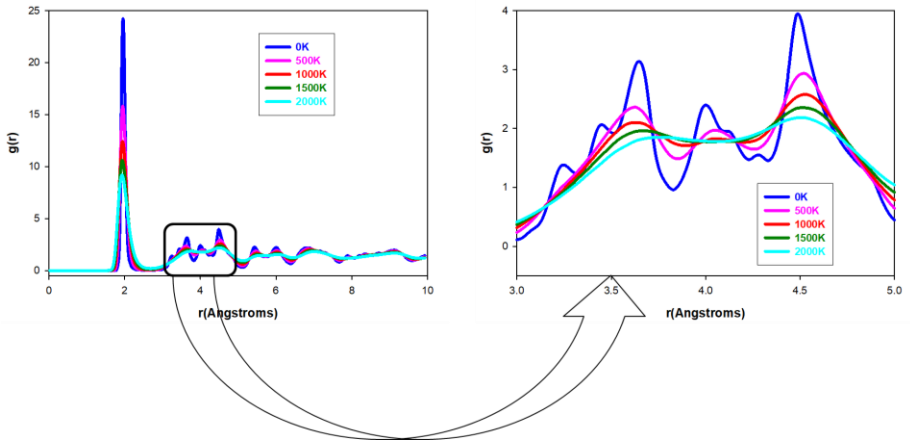

Figure 4.33: Shows simulated RDFs plots for $Na_{0.11}TiO_2$ nanoporous at all temperatures with a magnified RDFs portion between 3 and 5 Å for better visualisation.

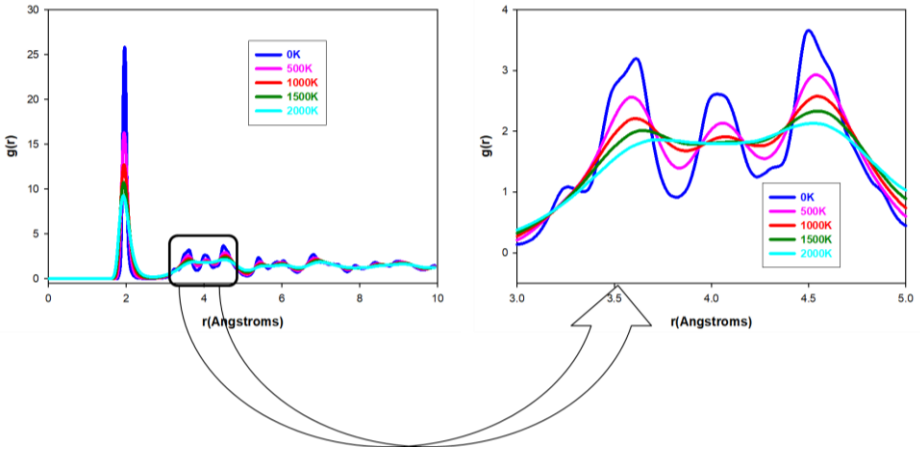

Figure 4.34: Shows simulated RDFs plots for $Na_{0.15}TiO_2$ nanoporous at all temperatures with a magnified RDFs portion between 3 and 5 Å for better visualisation.

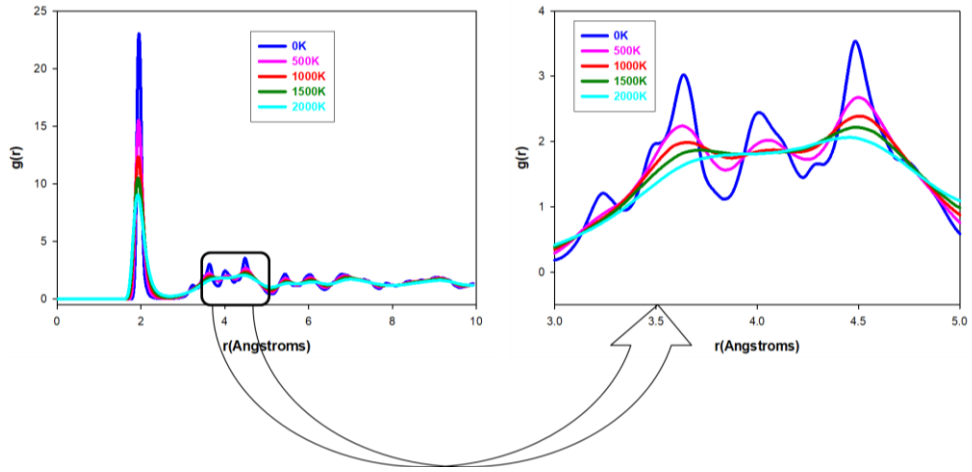

Figure 4.35: Shows simulated RDFs plots for $Na_{0.19}TiO_2$ nanoporous at all temperatures with a magnified RDFs portion between 3 and 5 Å for better visualisation.

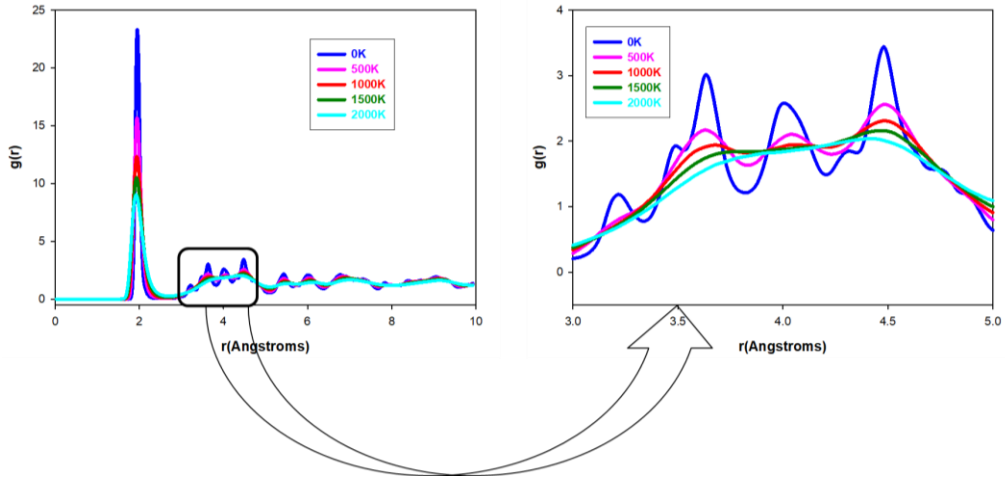

Figure 4.36 Shows simulated RDFs plots for $Na_{0.23}TiO_2$ nanoporous at all temperatures with a magnified RDFs portion between 3 and 5 Å for better visualisation.

4.3.2. Na_xTiO_2 Nanosheets

Ti-O RDFs for $Na_{0.11}TiO_2$, $Na_{0.15}TiO_2$, $Na_{0.19}TiO_2$ and $Na_{0.23}TiO_2$ nanosheets are presented in figures 4.37 to 3.40 respectively, all showing high and sharp peaks mostly at low (0K) temperatures influenced by partly crystalline portions observed in microstructures. As with other nanoarchitectures, Ti-O RDF peak sharpness reduced with increasing temperatures at all Na^+ concentrations and the crystallinity trend is reflected as 0K>500K>1000K>1500K>2000K.

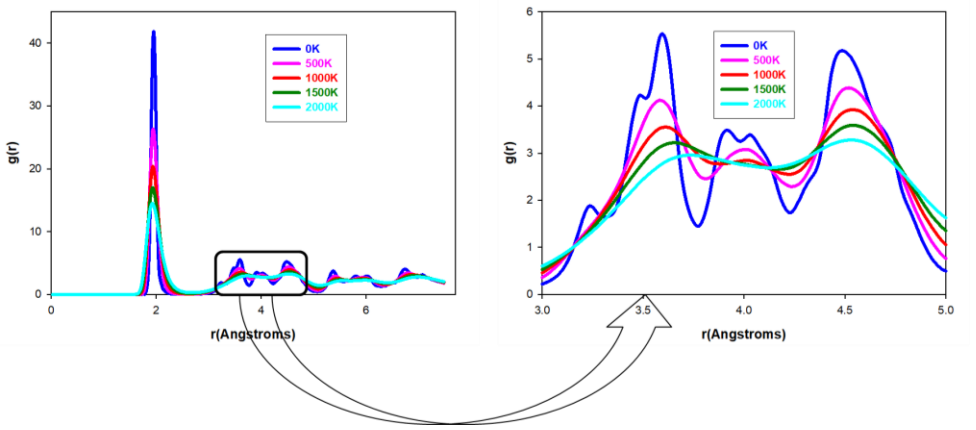

Figure 4.37: Shows simulated RDFs plots for $Na_{0.11}TiO_2$ nanosheets all temperatures with a magnified RDFs portion between 3 and 5 Å for better visualisation.

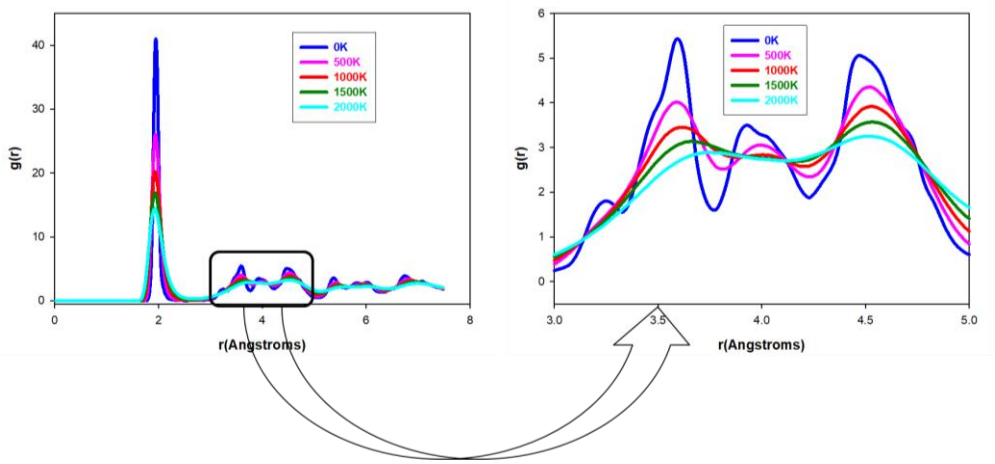

Figure 4.38: Shows simulated RDFs plots for $Na_{0.15}TiO_2$ nanosheets at all temperatures with a magnified RDFs portion between 3 and 5 Å for better visualisation.

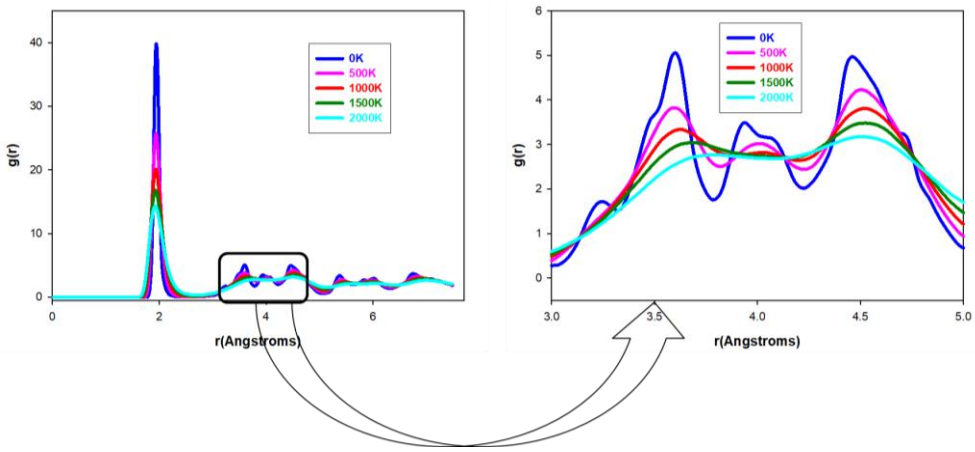

Figure 4.39: Shows simulated RDFs plots for Na0.19TiO2 nanosheets at all temperatures with a magnified RDFs portion between 3 and 5 Å for better visualisation.

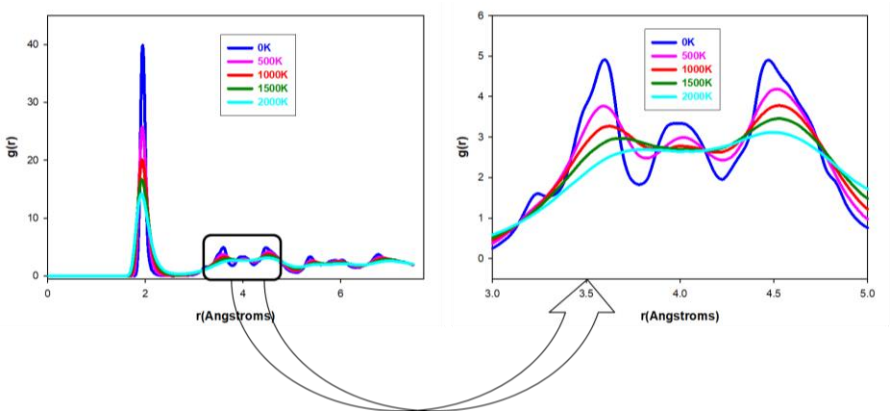

Figure 4.40: Shows simulated RDFs plots for $Na_{0.23}TiO_2$ nanosheets at all temperatures with a magnified RDFs portion between 3 and 5 Å for better visualisation.

4.4. XRDs of Na_xTiO_2 (x = 0.11, 0.15, 0.19 and 0.23) Nanoarchitectures

4.4.1. Na_xTiO_2 Nanosphere

Figures 4.41, 4.42, 4.43 and 4.44 depict XRD patterns for $Na_{0.11}TiO_2$, $Na_{0.15}TiO_2$, $Na_{0.19}TiO_2$ and $Na_{0.23}TiO_2$ systems respectively, which revealed well defined sharp peaks positioned at 2Θ = 25º, 31º, 35º, 41º, 55º,61º and 65º corresponding to the reflections by the (111), (101), (120), (121), (200), (012), (210), (211), (131), (610), (002) and (200) representing crystalline nanospheres at both high (2000 K) and low (0 K) temperatures. However, the XRD patterns for $Na_{0.19}TiO_2$ have much wider broader peaks which are positioned at 30º, 55º and 60º 2Θ angles at 2000 K and 0 K , which both suggested an extremely amorphous system.

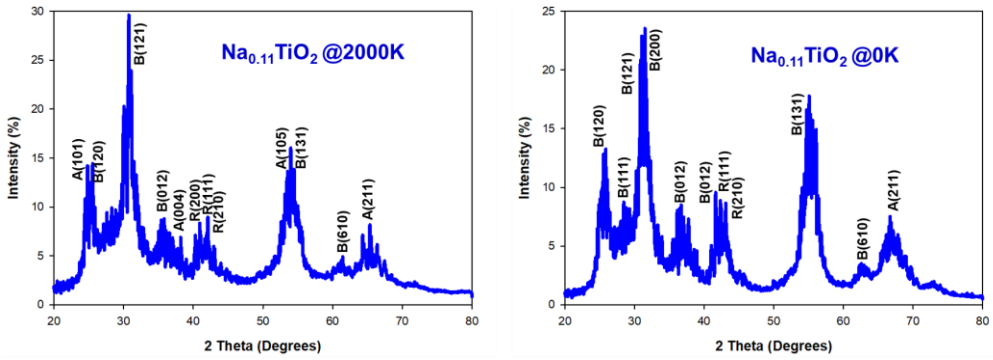

Figure 4.41: Illustrates simulated XRDs plots of $Na_{0.11}TiO_2$ nanosphere at recrystallised (2000 K) and cooled (0 K) temperatures for structural characterisations.

The high intensities and sharp peaks have influenced an increase in crystallinity patterns on all Na_xTiO_2 nanosphere systems, hence the $Na_{0.23}TiO_2$ nanosphere system had the highest intensity peaks followed by $Na_{0.15}TiO_2$, then $Na_{0.11}TiO_2$ nanosphere system and lastly the $Na_{0.11}TiO_2$ nanosphere systems, so higher Na^+ intercalation in TiO_2 greatly increased and improves crystals when heated to 2000 K and cooled to 0 K. These highly intense peaks observed in figures 4.41, 4.42 and 4.44

are peaks belonging to brookite (B120 and B121) polymorph; which was followed by a rutile phase (B131). The two polymorphs were also noted in tunnels deduced from snapshots of microstructures and provide pathways for Na ions hence rendering Na_xTiO_2 nanospheres excellent anode electrode for large grid energy storage applications; except for the concentration $Na_{0.19}TiO_2$.

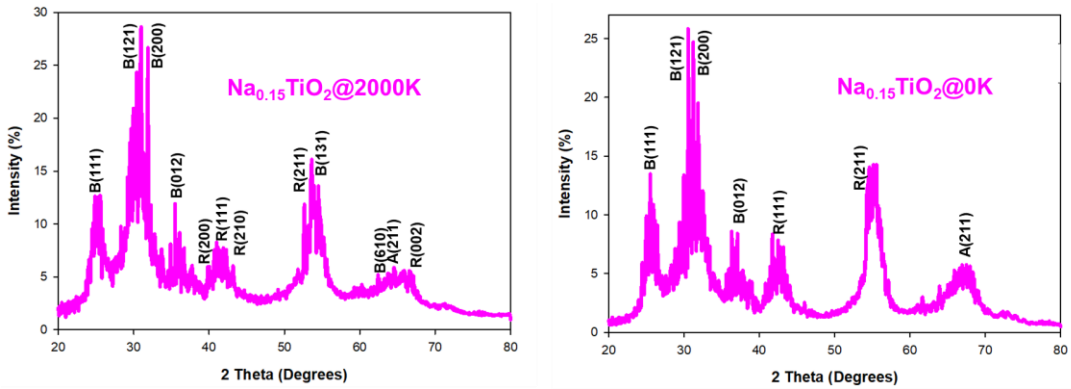

Figure 4.42: Illustrates simulated XRDs plots of $Na_{0.15}TiO_2$ nanosphere at recrystallised (2000 K) and cooled (0 K) temperatures for structural characterisations.

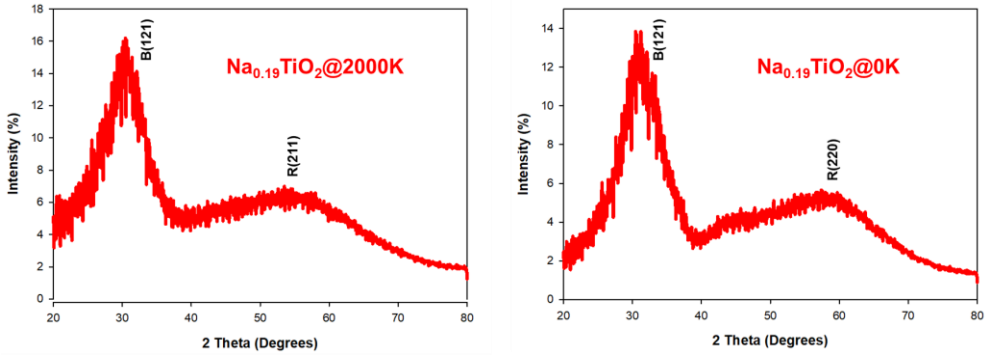

Figure 4.43: Illustrates simulated XRDs plots of $Na_{0.19}TiO_2$ nanosphere in recrystallised (2000 K) and cooled (0 K) temperatures for structural characterisations.

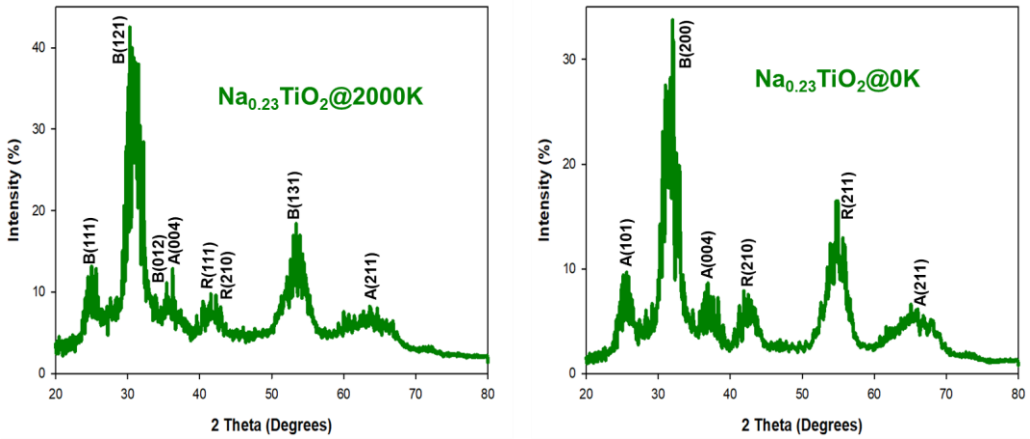

Figure 4.44: Illustrates simulated XRDs plots of $Na_{0.23}TiO_2$ nanosphere in recrystallised (2000 K) and cooled (0 K) temperatures for structural characterisations.

4.4.2. Na_xTiO_2 Nanoporous

The simulated XRD patterns were also analysed for the Na_xTiO_2 nanoporous structures heated to 2000 K and cooled to 0 K to study and compare their crystalline characteristics. Similar peak positions and intensities are observed in $Na_{0.11}TiO_2$, $Na_{0.15}TiO_2$, $Na_{.19}TiO_2$ and $Na_{0.23}TiO_2$ at high (2000 K) and low (0 K) temperatures, as illustrated in figures 4.45, 4.46, 4.47, and 4.48 respectively. Highly intense sharp peaks were observed on all simulated XRD patterns for Na_xTiO_2 nanoporous structures as seen from figure 4.45 to figure 4.48 which then confirms a highly crystalline system observed at 2Ɵ values of 25º, 26º, 30º, 35º, 36º, 40º, 43º, 55º, 56º and 64º corresponding to the reflections by the (120), (111), (121), (101), (004), (200), (210), (105), (131), (211) and (301) planes belonging to brookite, rutile and anatase crystal structures which are consistent with the dominant zigzag and straight tunnels inside the structures confirmed by their microstructural snapshots. Furthermore, the maximum peak intensities were shown to increase with increasing Na^+ intercalation in TiO_2 nanoporous which followed a crystalline trend of $Na_{0.23}TiO_2$ (Figure 4.48)>$Na_{.19}TiO_2$ (Figure 4,47)> $Na_{0.15}TiO_2$ (Figure 4.46)> $Na_{0.11}TiO_2$ (Figure 4,45) respectively; hence, the sodiation highly increases and creates more smooth tunnels and channels for fast Na^+ diffusing during heating and after cooling.

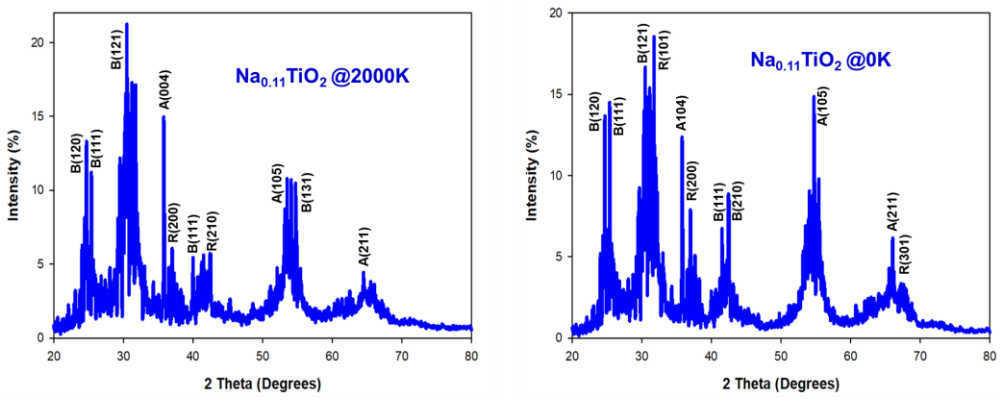

Figure 4.45: Illustrates simulated XRDs plots of $Na_{0.11}TiO_2$ nanoporous at recrystallised (2000 K) and cooled (0 K) temperatures conditions for structural characterisations.

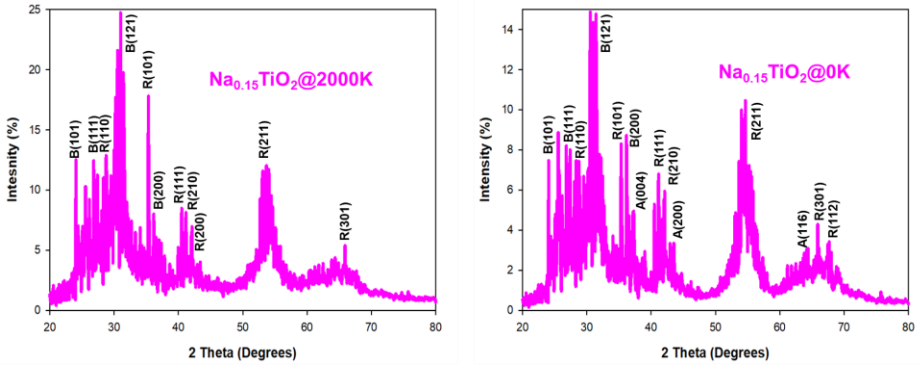

Figure 4.46: Illustrates simulated XRDs plots of $Na_{0.15}TiO_2$ nanoporous at recrystallised (2000 K) and cooled (0 K) temperatures conditions for structural characterisations.

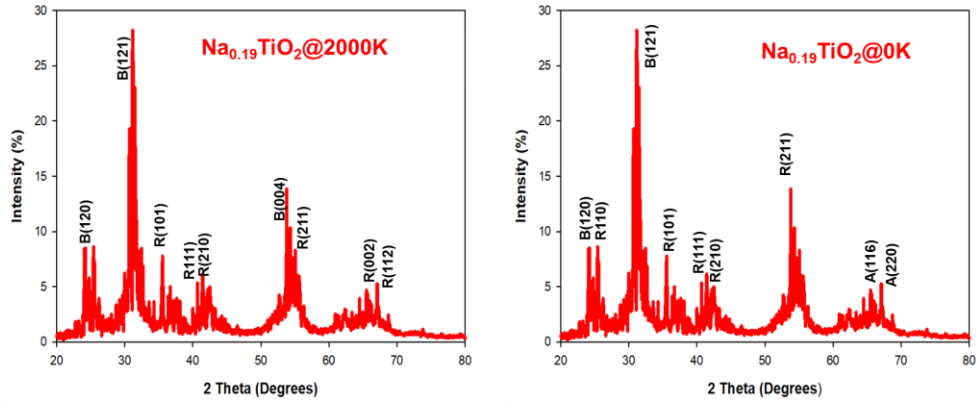

Figure 4.47: Illustrates simulated XRDs plots of $Na_{0.19}TiO_2$ nanoporous at recrystallised (2000 K) and cooled (0 K) temperatures conditions for structural characterisations.

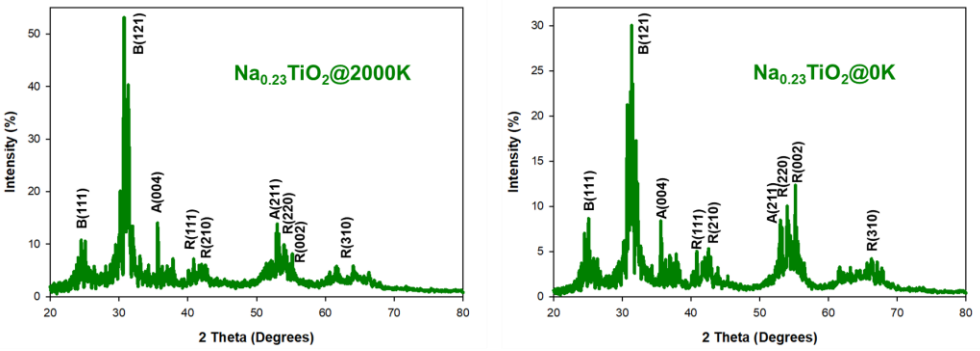

Figure 4.48: Illustrates simulated XRDs plots of $Na_{0.23}TiO_2$ nanoporous at recrystallised (2000 K) and cooled (0 K) temperatures conditions for structural characterisations.

4.4.3. Na_xTiO_2 Nanosheets

The Na_xTiO_2 nanosheets had broader surface areas at lower intensities then sharp peaks with many noises at higher intensities confirmed by their simulated XRD patterns shown in figures 4.49, 4.50, 4.51 and 4.52 corresponding to $Na_{0.11}TiO_2$, $Na_{0.15}TiO_2$, $Na_{.19}TiO_2$ and $Na_{0.23}TiO_2$ nanosheets respectively. The broader and sharper peaks illustrate the presence of disordered and crystalline polymorph infusions on each nanosheets, this observation was also confirmed by their microstructural snapshots after heating (2000 K) and cooling (0 K) in figures 4.6 (a to d), 4.22 (iv), 4.24 (iv), 4.26 (iv), and 4.28 (iv) respectively. The sharp peaks at 2Ɵ values of 23º,25º,30º,35º, 37º,40º, 55º and 65º congruent to the planes reflections e (101), (110), (121), (004), (111), (211) (200), (105) and (310) are associated with the rutile and brookite polymorphs in the Na_xTiO_2 nanosheet. The peak intensities were highly inconsistent to the increase in Na^+ insertions also with the heating and cooling, but rather Na^+ insertion from 0.11 to 0.19 Na^+ increased peak intensities at 2000 K and not so much at 0 K. It can generally be concluded that the broad XRD peaks of the nanosheets are associated with the higher content of disorder as depicted by microstructures.

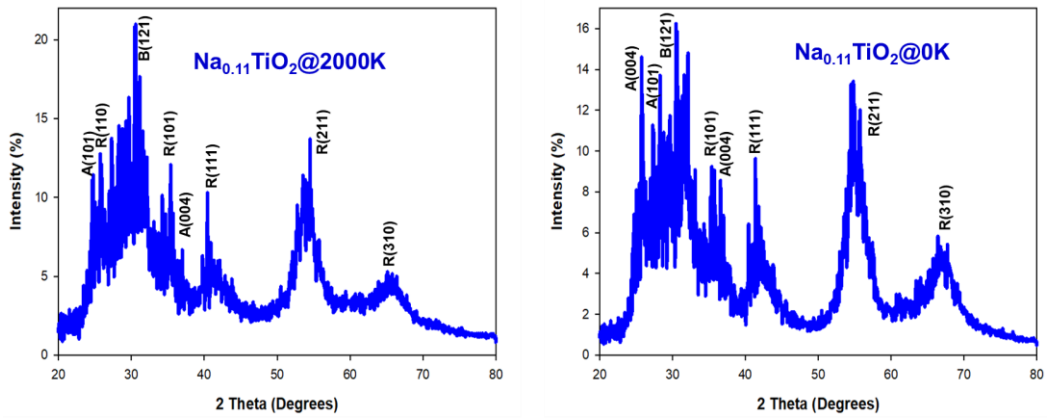

Figure 4.49: Illustrates simulated XRDs plots of $Na_{0.11}TiO_2$ nanosheets at recrystallised (2000 K) and cooled (0 K) temperatures conditions for structural characterisations.

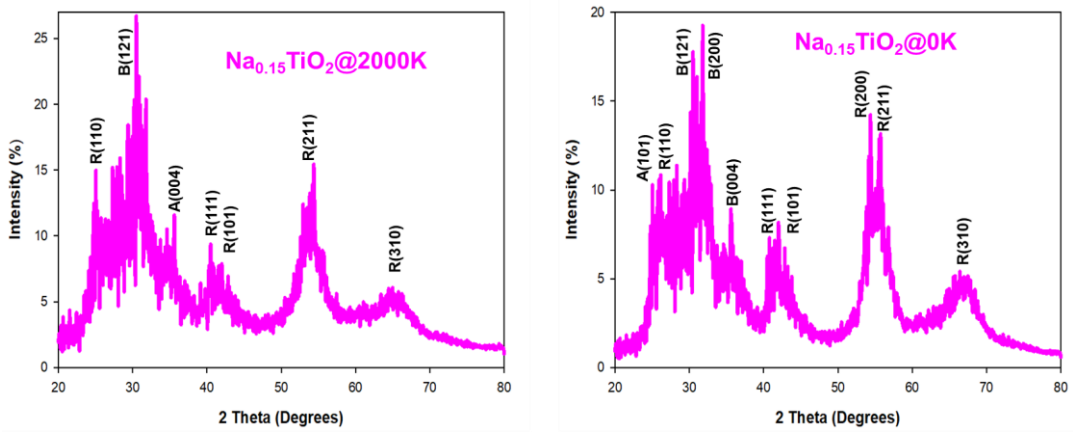

Figure 4.50: Illustrates simulated XRDs plots of $Na_{0.15}TiO_2$ nanosheets at recrystallised (2000 K) and cooled (0 K) temperatures conditions for structural characterisations.

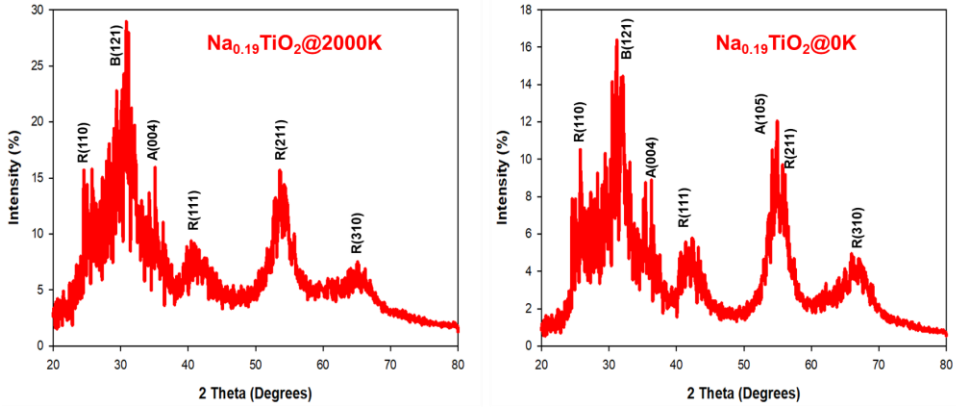

Figure 4.51: Illustrates simulated XRDs plots of $Na_{0.19}TiO_2$ nanosheets at recrystallised (2000 K) and cooled (0 K) temperatures conditions for structural characterisations.

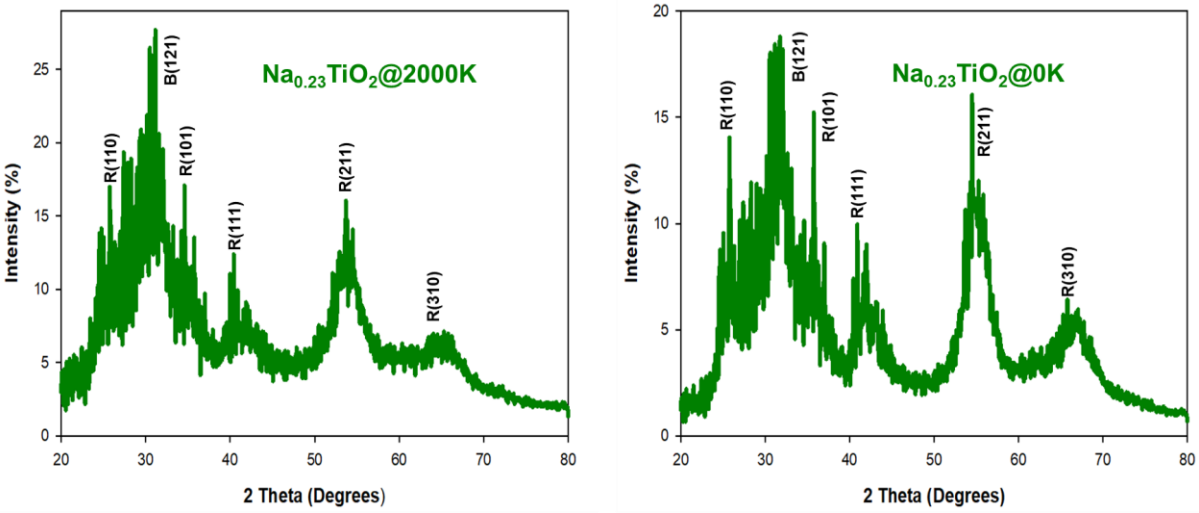

Figure 4.52: Illustrates simulated XRDs plots of $Na_{0.23}TiO_2$ nanosheets at recrystallised (2000 K) and cooled (0 K) temperatures conditions for structural characterisations.

3.5. Diffusion Coefficients of Na_xTiO_2 (x=0.11, 0.15, 0.19 and 0.23) Nanoarchitectures.

The Na^+ diffusion transport was calculated from 100 to 2000 K in 100 K intervals in TiO_2 nanosphere, nanoporous and nanosheet structures at varied Na^+ concentrations through diffusion coefficients presented by figure 4.63, 4.64 and 4.65 respectively. The blue, pink, red and green line graphs represent diffusion coefficients of Na^+ inside $Na_{0.11}TiO_2$, $Na_{0.15}TiO_2$, $Na_{.19}TiO_2$ and $Na_{0.23}TiO_2$ nano-architectured structures.

3.5.1. Na_xTiO_2 Nanosphere

Sodium ion diffusion coefficients (DC_{Na}) in $Na_{0.11}TiO_2$, $Na_{0.15}TiO_2$, $Na_{.19}TiO_2$, and $Na_{0.23}TiO_2$ nanospheres were simulated from 100K to 2000K to understand and track the Na^+ ion diffusion in the TiO_2 nanospheres. As seen in Figure 4.63 all Na^+ diffusion coefficients were enhanced with an increase in temperature. Na^+ ion in $Na_{0.23}TiO_2$ nanosphere had the highest diffusion coefficient, in the range 100 to 2000 K, when compared to other nanospheres. It is generally followed by $Na_{0.15}TiO_2$ nanosphere and the plots for $Na_{0.11}TiO_2$ and $Na_{0.19}TiO_2$ nanospheres are lower and mostly overlap. The low diffusion in $Na_{0.19}TiO_2$ can be attributed to its non-crystalline phase and lack of open wide channels for convenient transport of Na^+ ion as confirmed by their RDFs and XRDs patterns in figures 4.31 and 4.43. It may also be surmised that high Na^+ content in TiO_2 enhances diffusion coefficients; except for the concentration that did not allow crystallisation.

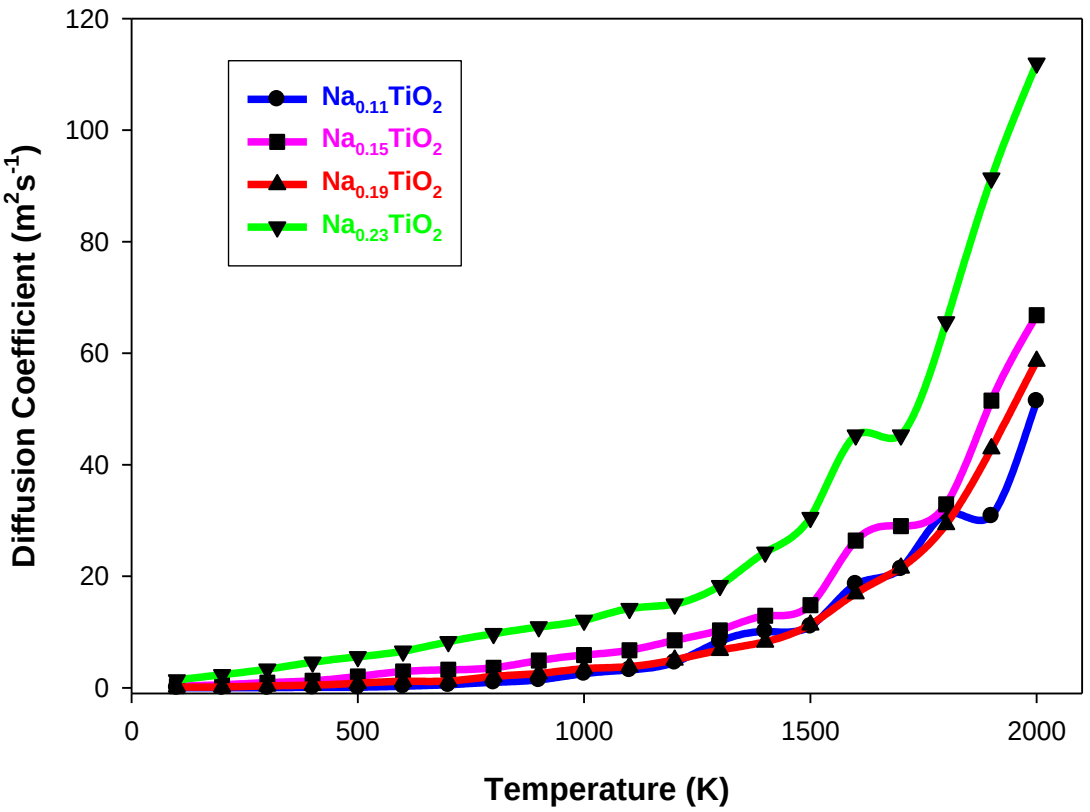

Figure 4.53: Represents graph of Na^+ diffusion coefficients at various temperatures in TiO_2 nanospheres with 0.11, 0.15, 0.19 and 0.23 Na^+ concentrations.

4.5.2. Na_xTiO_2 Nanoporous Architecture

Plots of diffusion coefficients of Na^+ with temperature in $Na_{0.11}TiO_2$, $Na_{0.15}TiO_2$, $Na_{.19}TiO_2$ and $Na_{0.23}TiO_2$ nanoporous structures are shown in Figure 4.63. All plots completely overlap and show no diffusion of Na^+ from 100 to 400K; diffusion commences above this temperature. Furthermore, the plots begin to separate above 1000 K where the diffusion of $Na_{.11}TiO_2$ is initially prevalent. From 1500 K the trend of diffusion coefficients in different nanoporous structures emerges as $Na_{0.23}TiO_2$ >$Na_{0.19}TiO_2$ > $Na_{0.15}TiO_2$ > $Na_{.11}TiO_2$. All snapshots of microstructures, with different Na^+ content, have orderly patterns of tunnels corresponding to the brookite and rutile polymorphs. XRDs and RDFs also show reasonable level of crystallinity. However, there are also several Na ions located on the edges of the channels. The zero diffusion coefficients of Na^+ at low temperature is due to the high static force involved within the Na_xTiO_2 structure, hence a lot of energy is required to allow the onset of Na^+ activation.

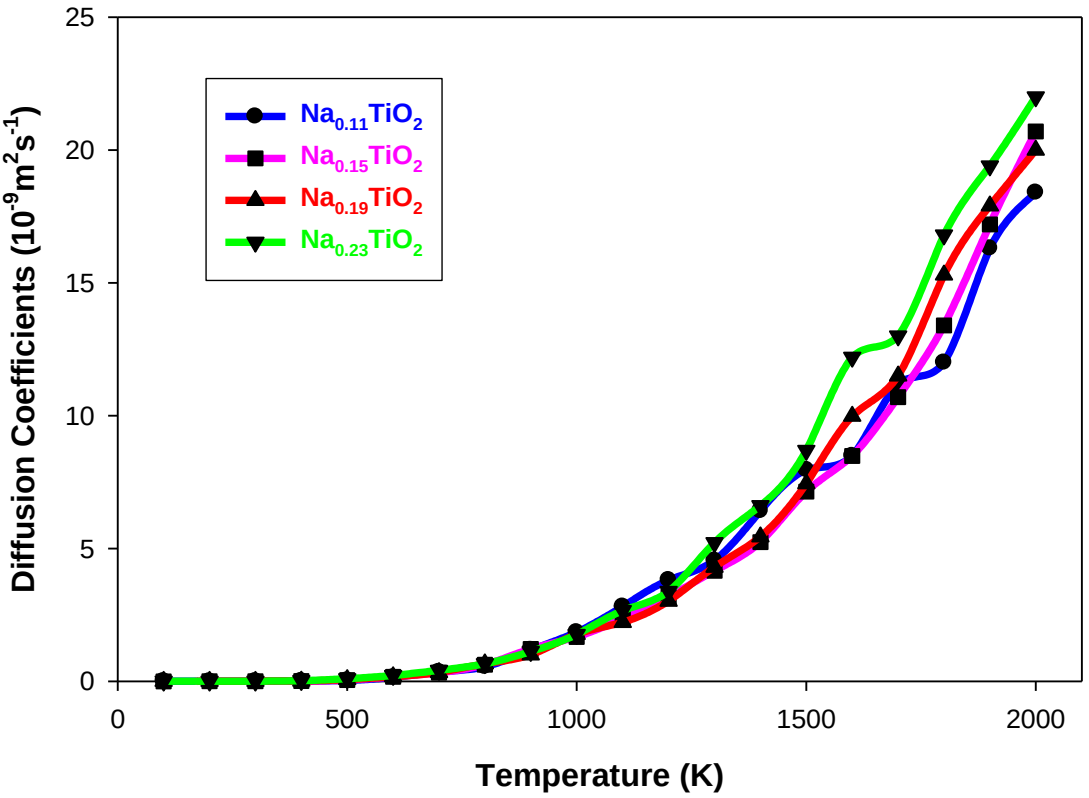

Figure 4.54: Represents graph of Na^+ diffusion coefficients at varied temperatures in TiO_2 nanoporous architecture with 0.11, 0.15, 0.19 and 0.23 Na+ concentrations.

3.5.3. Na_xTiO_2 Nanosheets

Plots of diffusion coefficients of Na^+ as a function of temperature in $Na_{0.11}TiO_2$, $Na_{0.15}TiO_2$, $Na_{.19}TiO_2$ and $Na_{0.23}TiO_2$ nanosheets are given in figure 4.64. As in nanoporous structures, all plots completely overlap and show no diffusion of Na^+ from 100 to 600 K; diffusion commences above this temperature. Furthermore, the plots begin to separate above 1000 K, and the diffusion of $Na_{.11}TiO_2$ is dominant from 1200 to 1700 K whilst those of other nanosheets are lower with several intersections. From 1750 K the trend of diffusion coefficients in different nanosheets aligns to $Na_{0.23}TiO_2$ > $Na_{0.15}TiO_2$ > $Na_{0.19}TiO_2$ > $Na_{0.11}TiO_2$; with that of $Na_{0.23}TiO_2$ increasing substantially. Generally the magnitudes of diffusion coefficients of Na in the nanosheets are twice as much as those of the nanoporous architectures. In nanosheets, half of the snapshot of the microstructure consists of well-defined brookite and rutile tunnels. The other half reflect disorder and possibly change in the orientation of channels. The combination of the two tend to contribute to the broadening of XRD peaks when compared to nanoporous structures. Hence, several Na ions, in nanosheets, could be settling in the grain boundaries and consequently adding to the diffusion as the temperature increases. At very high temperatures nanosheets with high Na^+ concentrations begin to have high diffusions.

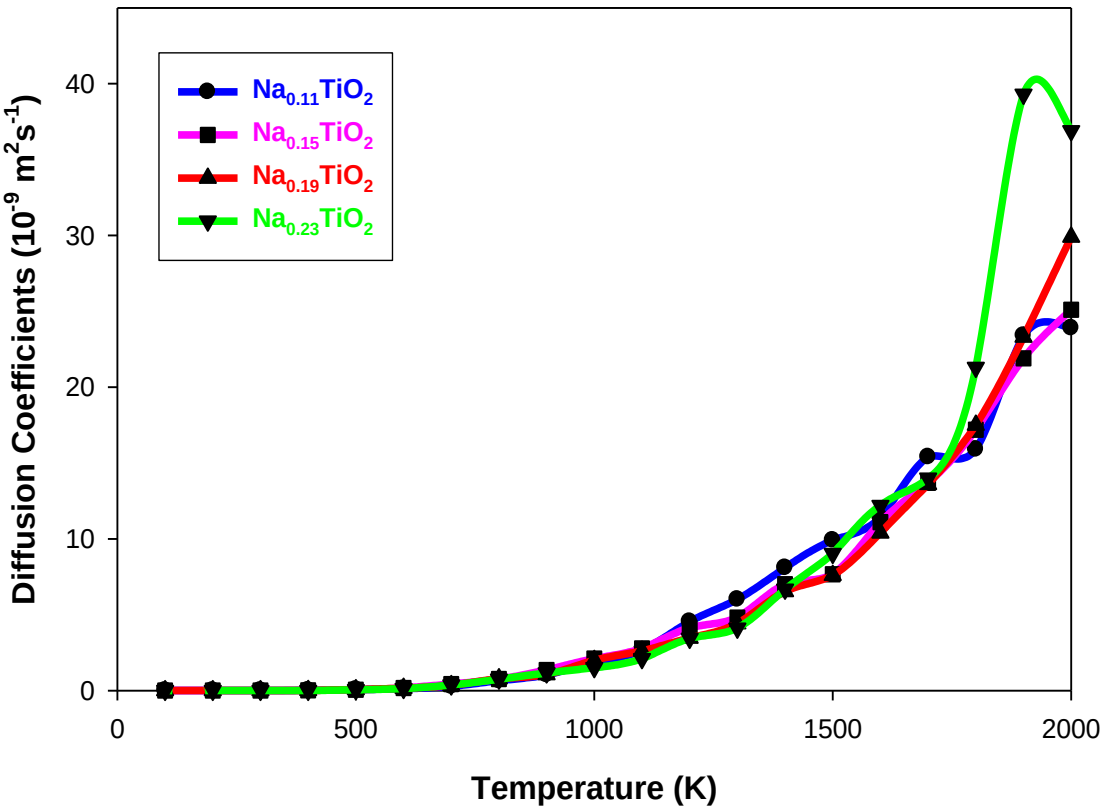

Figure 4.55: Represents graph of Na^+ diffusion coefficients at varied temperature inside TiO_2 nanosheets with 0.11, 0.15, 0.19 and 0.23 Na^+ concentrations.

4.6. Activation Energies of Na_xTiO_2 (x=0.11, 0.15, 0.19 and 0.23) Nanostructures

Since Na atoms were randomly inserted into TiO_2 nanosphere, nanoporous, and nanosheets architectures, it is expected that the Na^+ to freely diffuse within the TiO_2 nanostructures without being limited by their site defects, no restriction was introduced before, during and after molecular dynamics simulation synthesis. The calculated activation energies presented in these theses were within between 1.0 K^{-1} and 2.0 K^{-1}.

4.6.1. Na_xTiO_2 Nanosphere

The activation energy in Na_xTiO_2 nanosphere illustrated in Figure 4.66 decreased with increasing Na^+ content in TiO_2 with a calculated activation energy value of 0.256 eV, 0.248 eV, 0.209 eV and 0.190 eV which followed a trend of $Na_{0.11}TiO_2$>$Na_{0.15}TiO_2$>$Na_{0.19}TiO_2$>$Na_{0.23}TiO_2$ respectively. The $Na_{0.23}TiO_2$ and $Na_{0.19}TiO_2$ nanosphere had an almost equal Na^+ activation energy value of 0.2eV while $Na_{0.11}TiO_2$ and $Na_{0.15}TiO_2$ had an almost of equal Na^+ activation value of 0.25eV which indicates that the Na^+ is diffusing at almost equal rate for all given temperatures. lnD was decreasing with an increase in K^{-1} in all nanosphere systems as observed in Figure 4.56 with maximum lnD value at around -16 belonging to $Na_{0.23}TiO_2$ nanosphere structure.

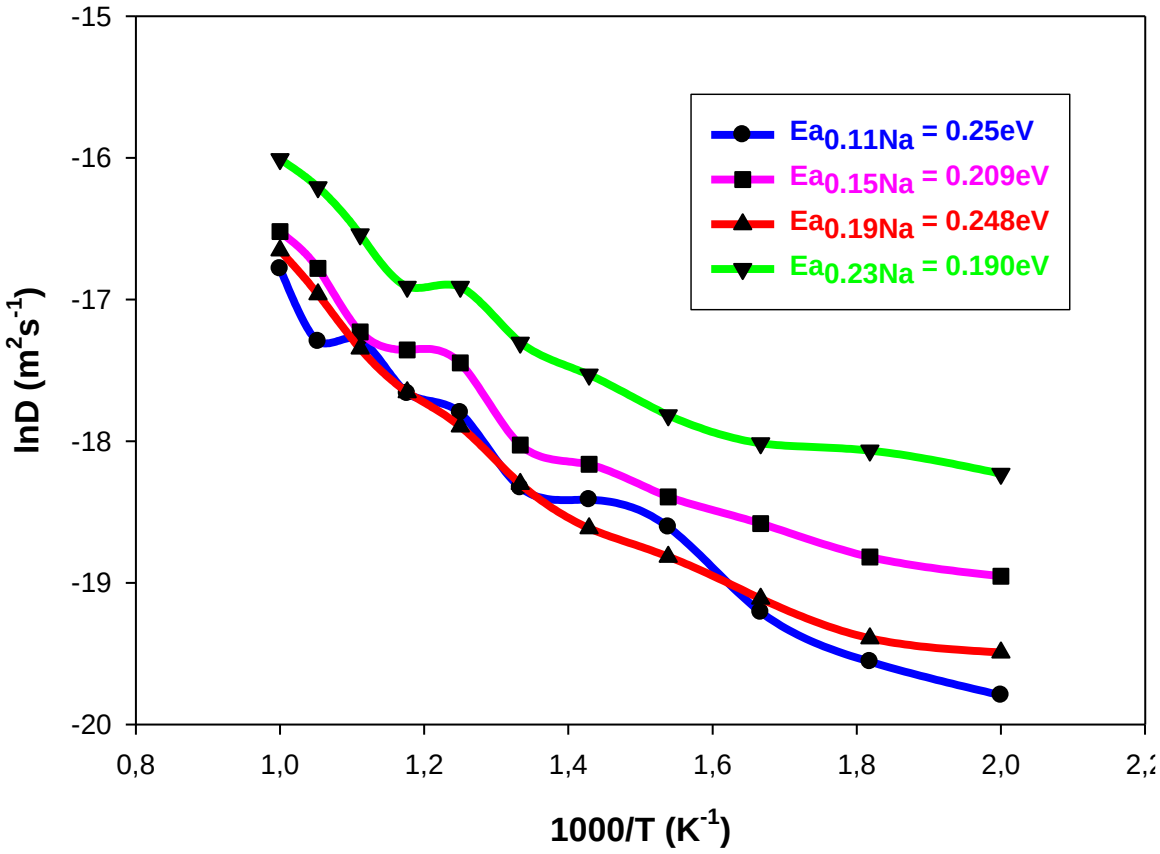

Figure 4.56: Represents graph of activation energies of Na^+ inside TiO_2 nanospheres with 0.11, 0.15, 0.19 and 0.23 Na^+ concentrations.

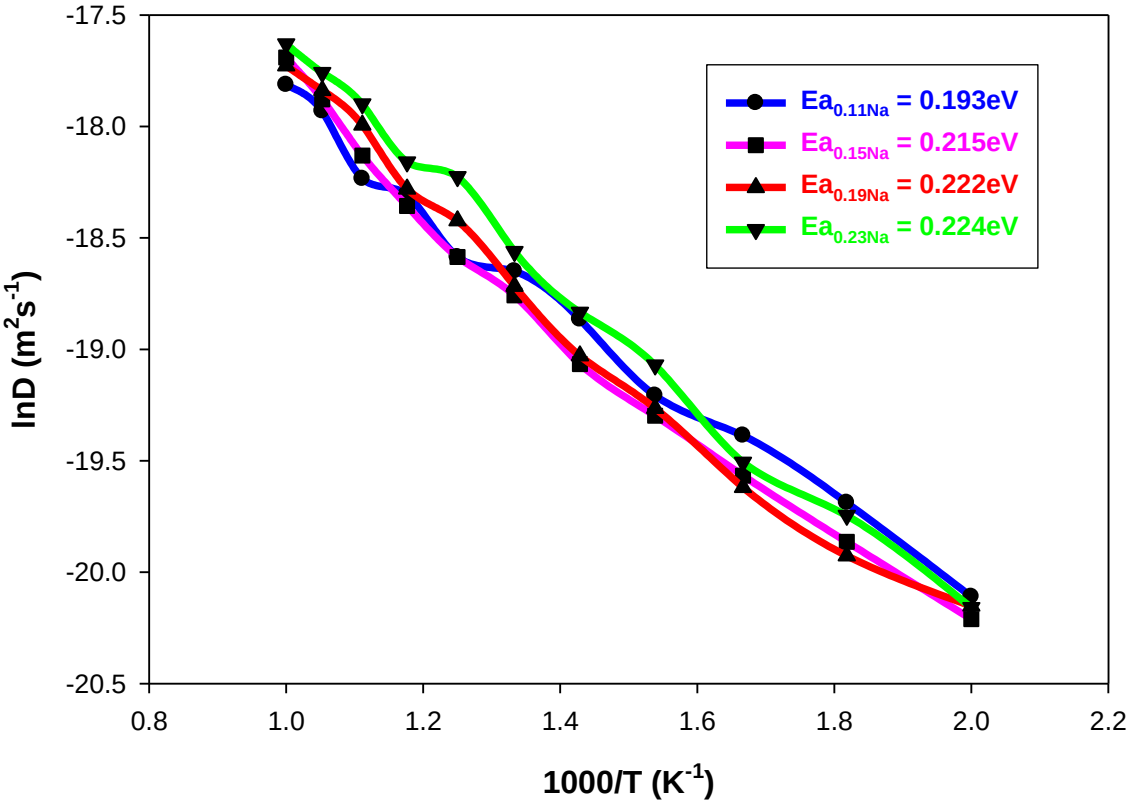

Figure 4.57: Represents graph of activation energies of Na^+ inside TiO_2 nanoporous structures with 0.11, 0.15, 0.19 and 0.23 Na^+ concentrations.

4.6.2. Na_xTiO_2 Nanoporous

The activation energies of Na^+ in the Na_xTiO_2 nanoporous shown in Figure 4.57 was quite different to AE observed in Figure 4.56 because in Figure 4.57 the AE for Na^+ in $Na_{0.11}TiO_2$, $Na_{0.15}TiO_2$, $Na_{0.19}TiO_2$ and $Na_{0.23}TiO_2$ was diffusion at an equal rate with an AE value close to 0.2eV at all given temperatures, thus too much too much line overlapping and splitting. This observation indicates that the Na_xTiO_2 nanoporous had an almost equal diffusion barriers with open channels and pores which allowed fast Na^+ diffusivity to this extends and had much higher maximum lnD value of about -17.4 which belonged to $Na_{0.23}TiO_2$ nanoporous system.

4.6.3. Na_xTiO_2 Nanosheets

The calculated activation energies for Na^+ within the Na_xTiO_2 nanosheets have almost equal AE values of close to 0.2eV, as shown in figure 4.67 of Na_xTiO_2. This suggests equivalent Na^+ diffusion barriers in the Na_xTiO_2 nanosheets, even though $Ea_{0.11Na} < Ea_{0.15Na} < Ea_{0.19Na} < Ea_{0.23Na}$. Such equivalence is also mostly reflected in the plots of Na diffusion coefficients.

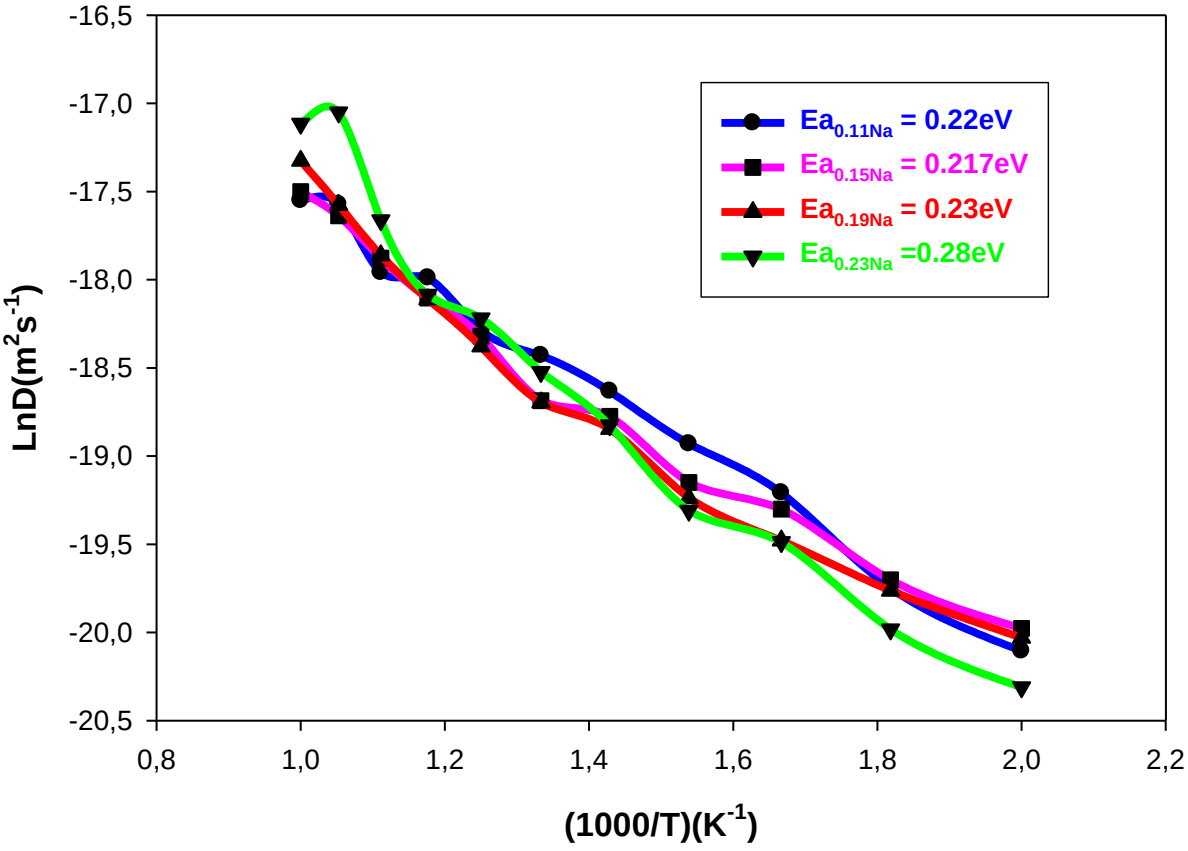

Figure 4.58: Represent graph of activation energies of Na^+ inside TiO_2 nanosheets with 0.11, 0.15, 0.19 and 0.23 Na^+ concentrations on the same axis.

4.7. Summary

The sodium ion was inserted into amorphous TiO_2 nanosphere, nanoporous and nanosheets architectures, with concentrations of $Na_{0.11}TiO_2$, $Na_{0.15}TiO_2$, $Na_{0.19}TiO_2$ and $Na_{0.23}TiO_2$. This was followed by recrystallisation, cooling and heating at different temperatures. The resultant crystallised nano-architectures featured similar structural and microstructural characteristics consisting of straight and zigzag tunnels corresponding to rutile and brookite polymorphs respectively. Generally, Na_xTiO_2 nanosheets consisted of two portions, one with rutile and brookite tunnels and another consisting of highly disordered portions, or changes in orientations; and at higher Na concentrations they occupy half of the microstructural snapshot. Consequently, some Na^+ ions were located inside tunnels and vacancies causing high surfaces distortions mostly with higher Na^+ contents. However, the $Na_{0.19}TiO_2$ nanosphere could not recrystallise and this anomaly was also observed for $Li_{0.19}TiO_2$ nanosphere, in figure 3.2 of chapter 3.

This confirms that the 0.19 Na ion concentration does not favour nucleation and growth of crystals but rather a more complex disordered (amorphous) system. Hence further exploration on such hindrance is required. Analysis of the RDFs and XRDs results substantiates observations on each structural and microstructural snapshots, where crystallinity was maintained in $Na_{0.11}TiO_2$, $Na_{0.15}TiO_2$ and $Na_{0.23}TiO_2$ nanospheres, $Na_{0.11}TiO_2$, $Na_{0.15}TiO_2$, $Na_{0.19}TiO_2$ and $Na_{0.23}TiO_2$ nanoporous and nanosheets except for the $Na_{0.19}TiO_2$ nanosphere. In all nano-architectures diffusion coefficients of Na^+, below 500 K, remained almost near zero and constant except for crystallised nanospheres with higher Na concentrations.

The DCs subsequently increase gradually above 500 K to substantial at higher temperatures, with DCs of higher Na concentration nano-architectures tending to be highest. The activation energy of the nanosphere with the higher Na concentration was low, consistent with the trend of non-zero diffusion coefficients at low temperatures. The AEs of nanoporous structures at different Na contents were equivalent and related DCs almost overlap in the 500 to 1000 K range. In the case of nanosheets AEs are also almost equal for all Na_xTiO_2 with that of the $Na_{x0.23}TiO_2$ (highest Na concentration) being highest resulting in a slightly lower diffusivity, except at very high temperatures. These results provide insights and an understanding on how much such TiO_2 nano-architectures can enable operations of sodium ion batteries.

Chapter 5

5. Results and Discussions: Magnesium Intercalated TiO_2 Nanoarchitectures

5.1. Recrystallised Structures and Microstructures of Mg_xTiO_2 (x=0.11, 0.15, 0.19 and 0.23) nanostructures.

Amorphisation and recrystallisation synthesis was run on Mg_xTiO_2 (x=0.11, 0.15, 0.19 and 0.23) nanosphere, nanoporous, and nanosheets to study their structural properties as influenced by low- and high temperature conditions.

5.1.1. Mg_xTiO_2 Nanosphere

Mg^{2+} ions with concentrations of 0.11, 0.15, 0.19 and 0.23 were inserted into amorphous TiO_2 nanosphere, at 2000K, which influenced disordered Ti-O patterns before recrystallisation. Figure 5.1 a) $Mg_{0.11}TiO_2$, b) $Mg_{0.15}TiO_2$, c) $Mg_{0.19}TiO_2$ and d) $Mg_{0.23}TiO_2$ show recrystallised nanospheres after Mg^{2+} insertions where all structures have highly crystalline patterns confirmed by ordered Ti-O patterns with zigzag and straight tunnels associated with brookite and rutile crystalline polymorphs, with sliced microstructural snapshots illustrated in Figure 5.2 a), b), c) and d) respectively. Both structures and microstructures of Mg_xTiO_2 nanosphere in Figure 5.1 and Figure 5.2 respectively contain crystal patterns with most Mg^{2+} ions situated on the surface/edges which surely validate open channels and frameworks to successfully accommodate more Mg^{2+} ions.

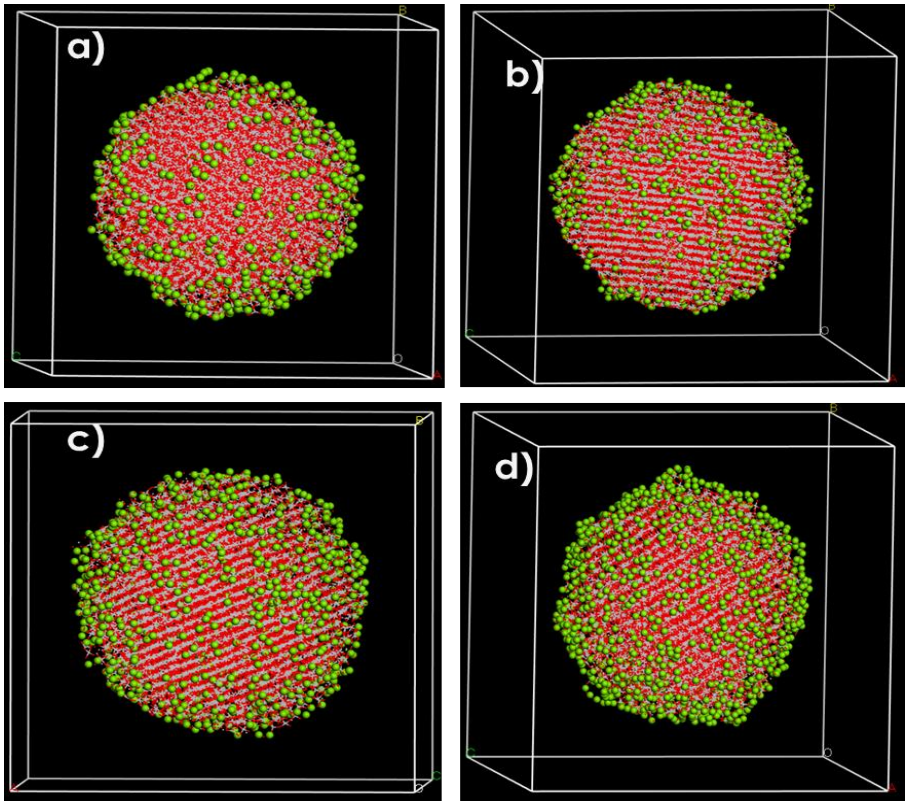

Figure 5.1: Represents recrystalised nanospheres of a) $Mg_{0.11}TiO_2$, b) $Mg_{0,15}TiO_2$, c) $Mg_{0.19}TiO_2$ and d) $Mg_{0.23}TiO_2$ at 2000K. Green balls represent Mg.

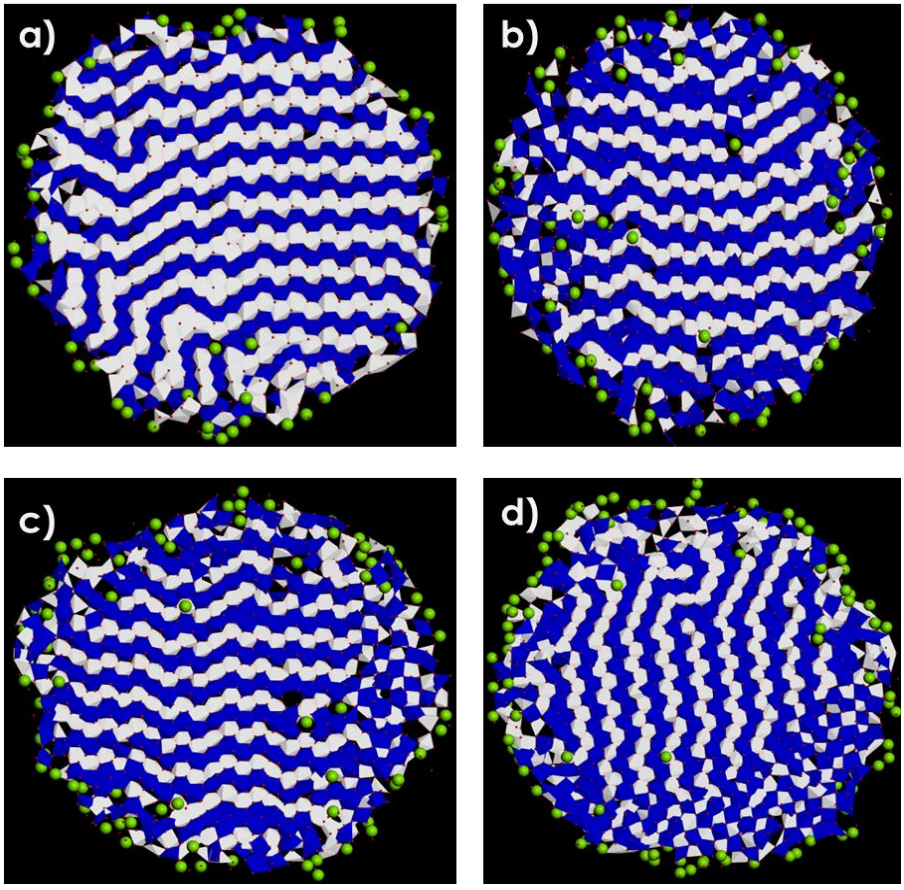

Figure 5.2: Shows microstructures from slices of nanospheres for a) $Mg_{0.11}TiO_2$, b) $Mg_{0,15}TiO_2$, c) $Mg_{0.19}TiO_2$ and d) $Mg_{0.23}TiO_2$, respectively, at 2000K.

5.1.2. Mg_xTiO_2 Nanoporous

Recrystallised structures and microstructures of a) $Mg_{0.11}TiO_2$, b) $Mg_{0.15}TiO_2$, c) $Mg_{0.19}TiO_2$, and d) $Mg_{0.23}TiO_2$ nanoporous architectures are illustrated in Figure 5.3 and 5.4 respectively, at 2000K. Figure 5.3 a) have crystalline patterns with some Mg^{2+} ions on open pore edges and inside the TiO_2 frameworks which agrees well with its respective microstructure in Figure 5.4 a) which contains most of straight and zigzag tunnels associated to rutile and brookite polymorphs of TiO_2 crystal structures. A recrystallised TiO_2 nanoporous structure with 0.15 Mg^{2+} is shown in Figure 5.3 b) where the pore seems to have been reduced in size when compared to Figure 5.3 a) these observation are influenced by the divalent electrons of Mg atoms that are inside the TiO_2 nanoporous, which then expands the total volume of the system, hence the reduced pore size seen in Figure 5.3b), also the crystal patterns observed on the system in Figure 5.3 b) confirms that the systems was fully recrystallised, which were confirmed by its microstructural snapshots provided in Figure 5.4 b) that contained straight and zigzag tunnels, which are related to rutile and brookite TiO_2 polymorphs similar to the microstructure of $Mg_{0.11}TiO_2$ nanoporous systems in Figure 5.4 b). However, the pores in the nanoporous structures of $Mg_{0.19}TiO_2$ and $Mg_{0.23}TiO_2$ shown by Figure 5.3 c) and Figure 5.3 d) have doubled in size more than the pore in Figure 5.3 a), this increase in size and shape in Figure 5.3 c) and d) was altered by the high number of Mg^{2+} on the porous edges/surface more than those settled inside the TiO_2

nanoporous framework, so the weight of the divalent Mg atom causes the wide opening of the pores in Figure 5.3 c) and d) respectively. Moreover, after recrystallisation, the synthesis of the $Mg_{0.19}TiO_2$ nanoporous structure seen in Figure 5.4 c) have produced high ordered Ti-O patterns within the microstructures and disordered Ti-O patterns at the edges/surfaces where most of Mg^{2+} were situated hence the pore was enlarged. Furthermore Figure 5.3 d) also experienced similar structural atom arrangement seen in Figure 5.3 c) however the pore size had become narrower and bigger then shifted towards the simulation box on the right due to the atomic weight of Mg^{2+} which then influenced a Ti-O atom shift towards the left side of the simulations box as seen in Figure 5.3 d) hence no microstructural snapshots were viewed due to the amorphous state of the systems. Recrystallisation synthesis of $Mg_{0.23}TiO_2$ nanoporous structure had influenced amorphisation and phase transformation which implies that the TiO_2 nanoporous structure could not handle being accommodated with 0.23 fraction of Mg^{2+} but rather caused structural instability. The sliced microstructures of $Mg_{0.11}TiO_2$, $Mg_{0.15}TiO_2$ and $Mg_{0.19}TiO_2$ in Figure 5.4 a), b) and c respectively all had zigzag and straight tunnels correlating to brookite and rutile polymorphs with most empty and Mg^{2+} filled vacancies, which are good properties for fast ion diffusivity and electrochemical properties. Furthermore Figure 5.4c) has highly dispersed Mg^{2+} inside (crystalline) and on the edge (noncrystalline) of the microstructure consistent to what was observed on Figure 5.3 c).

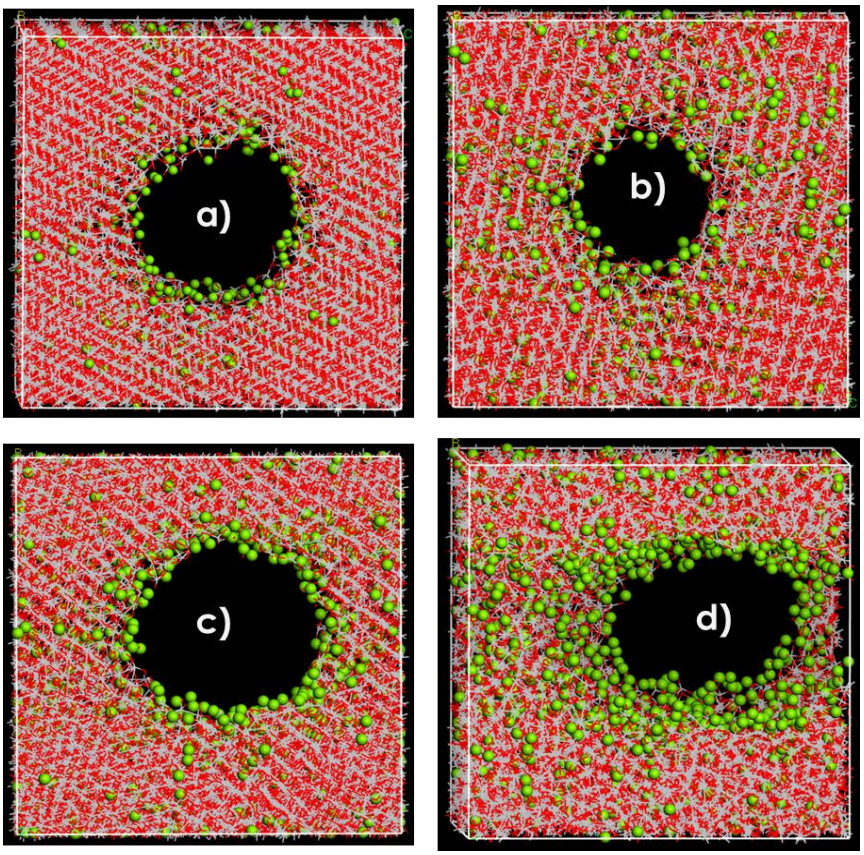

Figure 5.3: Represents nanoporous recrystalised architectures of a) $Mg_{0.11}TiO_2$, b) $Mg_{0,15}TiO_2$, c) $Mg_{0.19}TiO_2$ and d) $Mg_{0.23}TiO_2$.

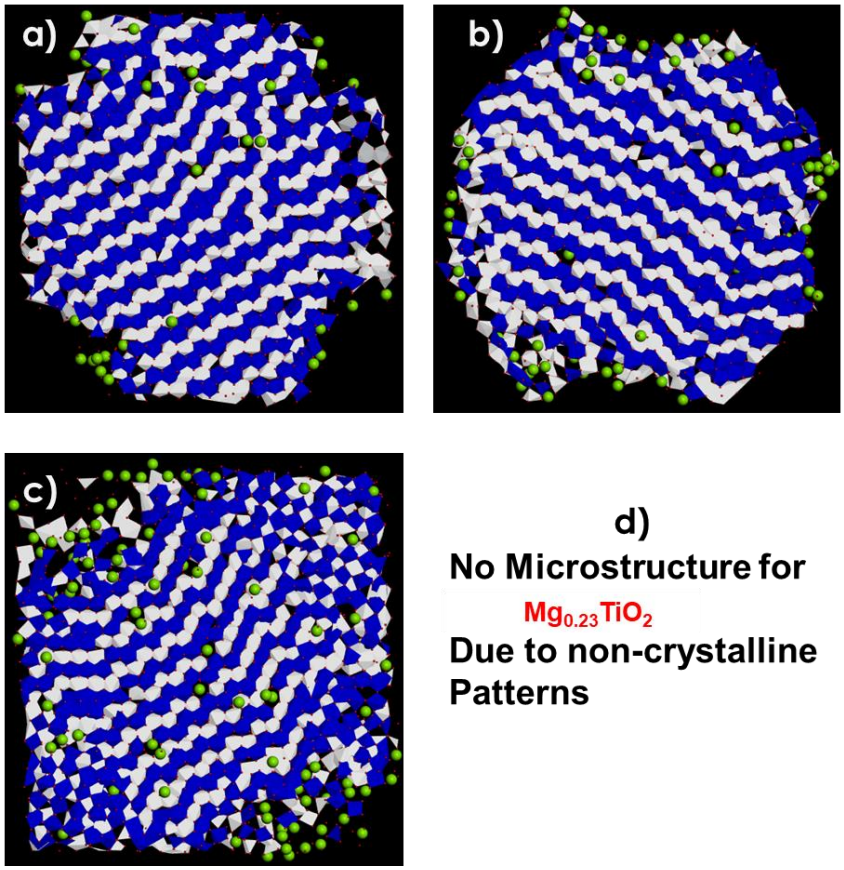

Figure 5.4: Shows microstructures from a slice of nanoporous architecture for a) $Mg_{0.11}TiO_2$, b) $Mg_{0,15}TiO_2$, c) $Mg_{0.19}TiO_2$ and d) $Mg_{0.23}TiO_2$, respectively.

5.1.3. Mg_xTiO_2 Nanosheets

Figure 5.5 displays snapshots of a) $Mg_{0.11}TiO_2$, b) $Mg_{0.15}TiO_2$, c) $Mg_{0,19}TiO_2$ and d) $Mg_{0.23}TiO_2$ nanosheet structures after being recrystallised at atomic scale. Each nanosheet structure illustrated in Figure 5.5 a), b) and c) possesses partial crystalline and amorphous patterns with most Mg^{2+} evenly dispersed inside each system. Recrystallisation synthesis has promoted structural volume expansion in Figure 5.5 b) $Mg_{0.15}TiO_2$ and d) $Mg_{0.23}TiO_2$ nanosheet systems, where their open space between the sheets have greatly reduced as seen in Figure 5.5 d), which even led to a complete closing of the open space between the sheets as seen in Figure 5.5 d) which then influenced a complete disordered Ti-O patterns. So, Figure 5.5 d) was completely amorphous which generated a structural morphology of nano-flat sheet structure. The structural observations of Mg_xTiO_2 in Figure 5.5 a), b) and c) are consistent with their related microstructures in Figure 5.6 a), b) and c). The latter reflect partial crystalline patterns with zigzag and straight tunnels corresponding to brookite and rutile polymorphs, with most Mg^{2+} occupying vacancies on 1x1 tunnels. Also noted are empty vacancies and partial disordered portions which are good features for long life cycle of the battery system. However, the microstructure of the $Mg_{0.23}TiO_2$ nanosheet structure in Figure 5.5 d) is not depicted due to its amorphous phase and Ti-O disordered states; hence the new generated nano-flat sheet structure is shown in Figure 5.6 d).

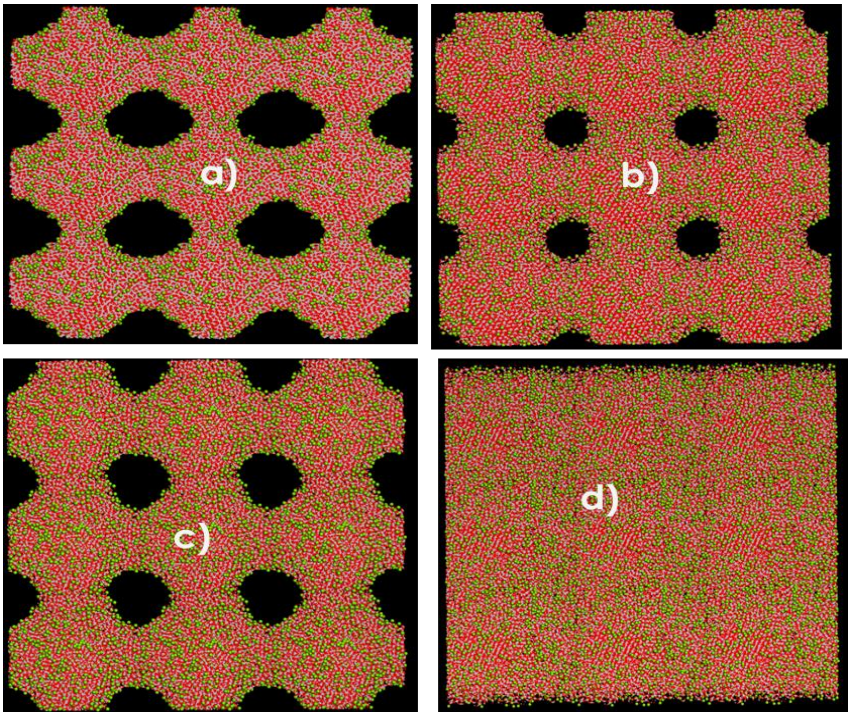

Figure 5.5: Represents recrystalised nanosheets of a) $Mg_{0.11}TiO_2$, b) $Mg_{0,15}TiO_2$, c) $Mg_{0.19}TiO_2$ and d) $Mg_{0.23}TiO_2$ at 2000K.

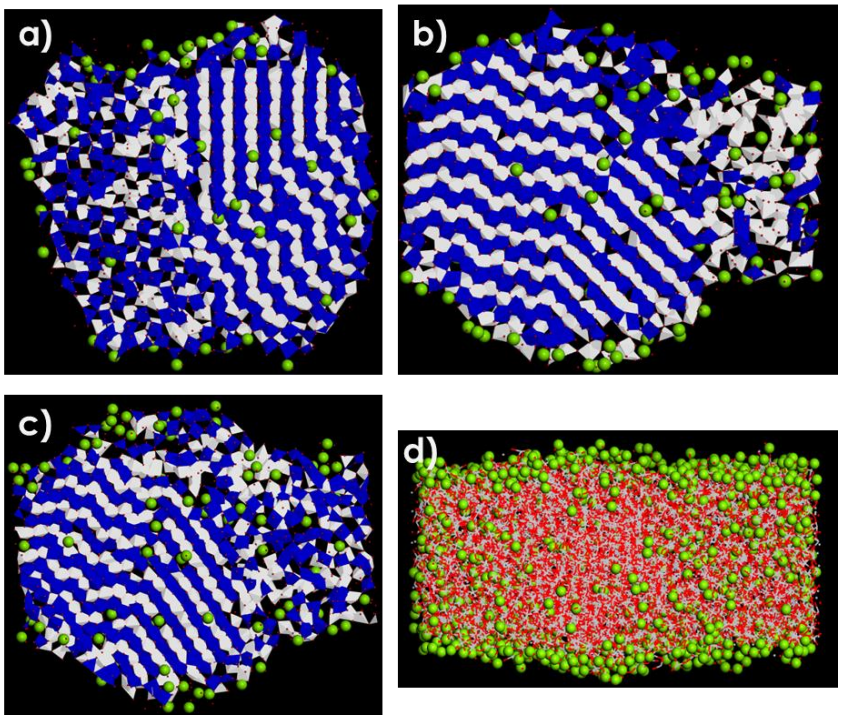

Figure 5.6: Shows microstructures from slices of nanosheets for a) $Mg_{0.11}TiO_2$, b) $Mg_{0,15}TiO_2$, c) $Mg_{0.19}TiO_2$ and d) $Mg_{0.23}TiO_2$, at 2000K.

5.2. Cooled Structures and Microstructures of Mg_xTiO_2 (x=0.11, 0.15, 0.19 and 0.23) nanostructures

Molecular dynamics simulation was used to cool (from 2000 to 0K) all recrystallised Mg_xTiO_2 nanosphere, nanoporous and nanosheets structures, presented in Figures 5.1, 5.3 and 5.5, respectively to study its impact of all Mg^{2+} ion concentrations.

5.2.1. Mg_xTiO_2 Nanosphere

The cooling of the $Mg_{0.11}TiO_2$ nanosphere from i) 1500 K, ii) 1000 K, iii) 500 K to iv) 0 K was successfully simulated from a recrystallised structure. As depicted in Figure 5.7, the structural integrity is reflected in crystalline and ordered patterns for all nanosphere structures from Figure 5.7 i), ii), iii) and iv), respectively. Since $Mg_{0.11}TiO_2$ is the lowest concentration in this study, Mg^{2+} ions are located inside 1x1 tunnels and on the facets of the cooled nanosphere. The extent of crystallinity observed in $Mg_{0.11}TiO_2$ nanosphere in Figure 5.7 i), ii), iii) and iv) correlated well with the microstructural snapshots shown in Figure 5.8, sliced from each nanosphere in Figure 5.7. The microstructures viewed in Figure 5.8 i), ii), iii) and iv) all have straight and zigzag tunnels related to rutile and brookite polymorphs with empty and Mg^{2+} filled vacancies. Most Mg^{2+} are located on the facets than in tunnels, as seen on the microstructures. Cooling has significantly enhanced crystallinity in the $Mg_{0.11}TiO_2$ nanosphere as illustrated in Figure 5.7 i) to iv), hence at 0 K the Ti-O bonds are much more distinct than those at 1500 K.

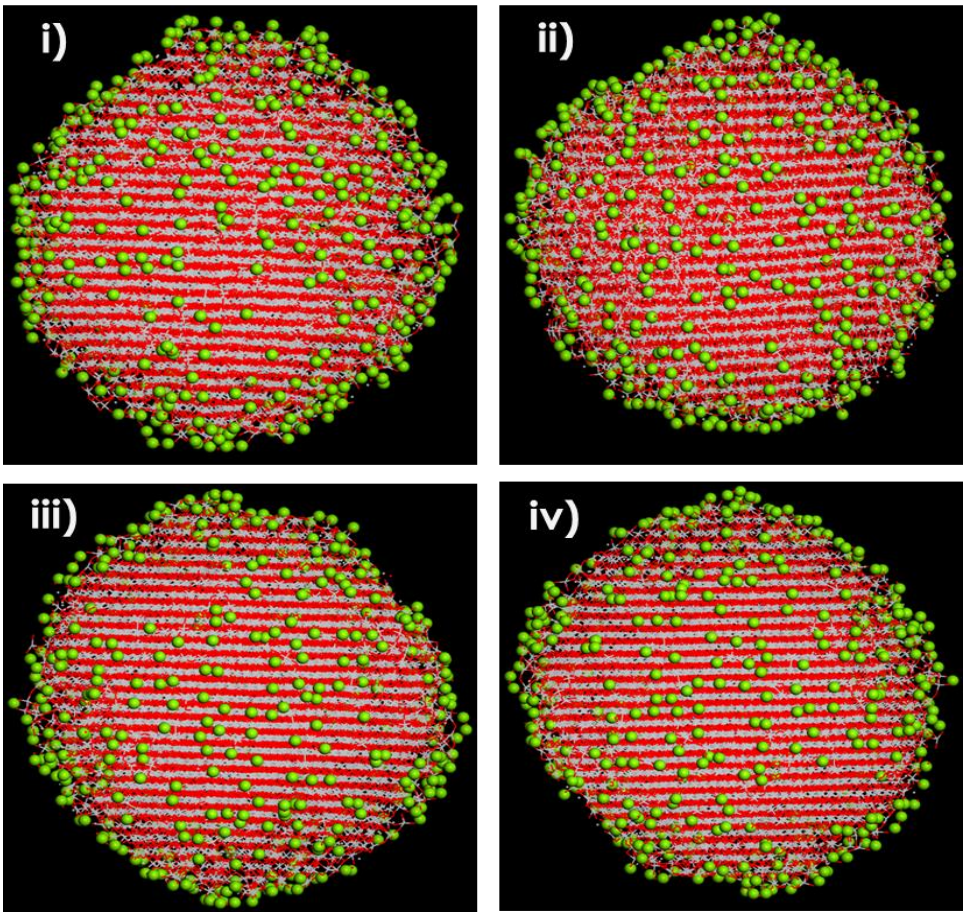

Figure 5.7: Cooled structures of nanosphere $Mg_{0.11}TiO_2$ at i)1500 K, ii) 1000 K, iii) 500 K and iv) 0 K.

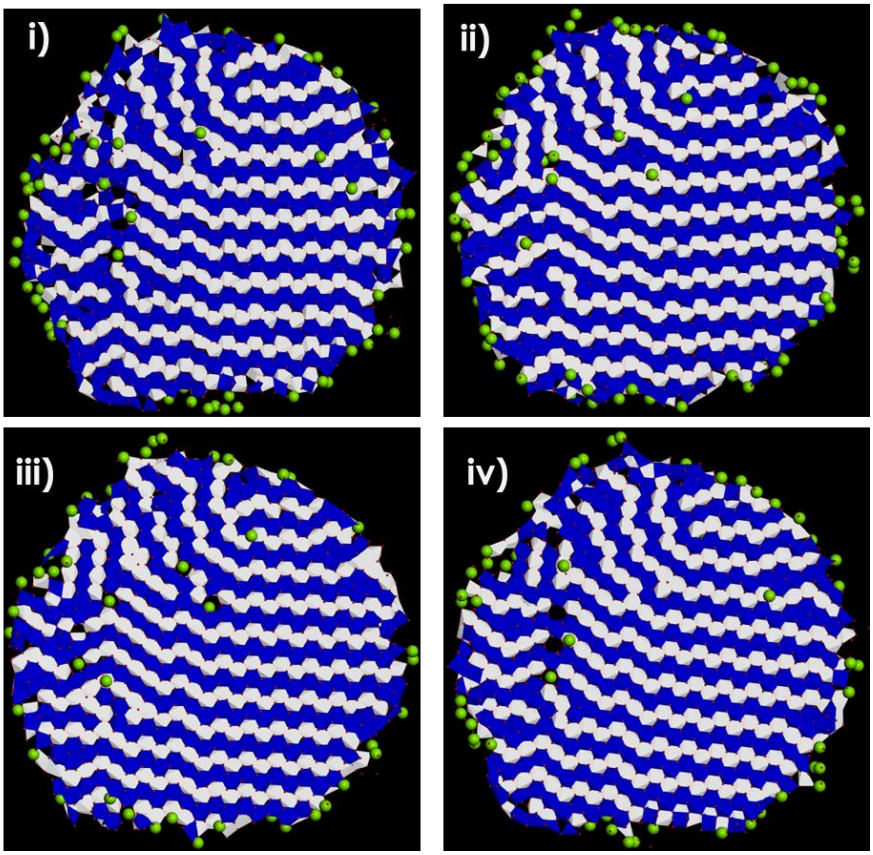

Figure 5.8: Cooled microstructures of $Mg_{0.11}TiO_2$ nanosphere at i) 1500 K, ii) 1000 K, iii) 500 K and iv) 0 K.

The effect of cooling was further analysed on $Mg_{0.15}TiO_2$, $Mg_{0.19}TiO_2$ and $Mg_{0.23}TiO_2$ nanospheres from 1500 K, 1000 K, 500 K then finally to 0 K where structural and microstructural snapshots were compared for further insights. All structures and microstructures illustrated in Figures 5.9, 5.11, 5.13 and Figures 5.10, 5.12, 5.14 respectively obtained at i) 1500 K, ii) 1000K, iii) 500 K and i) 0 K for the $Mg_{0.15}TiO_2$, $Mg_{0.19}TiO_2$ and $Mg_{0.23}TiO_2$ nanosphere systems show similar characteristics of high crystallinity and ordered Ti-O patterns with straight and zigzag tunnels corresponding to rutile and brookite polymorphs. Furthermore, microstructures in Figures 5.10, 5.12 and 5.14, at all simulated temperatures, were consistent with their respective structural snapshots in Figures 5.9, 5.11, 5.13, containing empty and Mg^{2+} filled vacancies with most Mg^{2+} occupying open tunnels inside and on surfaces of nanospheres. It appears that high Mg^{2+} concentrations at elevated and low temperatures have introduced disordered Ti-O patterns mainly on the surface/outer surroundings of the nanosphere as noted in Figure 5.12 and Figure 5.14 from i) to iv). Furthermore, the Ti-O disordered patterns, though not extensive, are confirmed by microstructural snapshots of the $Mg_{0.23}TiO_2$ nanosphere. However, on the whole, these structural and microstructural snapshots indicate that the structural integrity is maintained inside $Mg_{0.11}TiO_2$ $Mg_{0.15}TiO_2$, $Mg_{0.19}TiO_2$ and $Mg_{0.23}TiO_2$ nanospheres after recrystallisation and cooling hence enabling good and fast Mg^{2+} diffusivity.

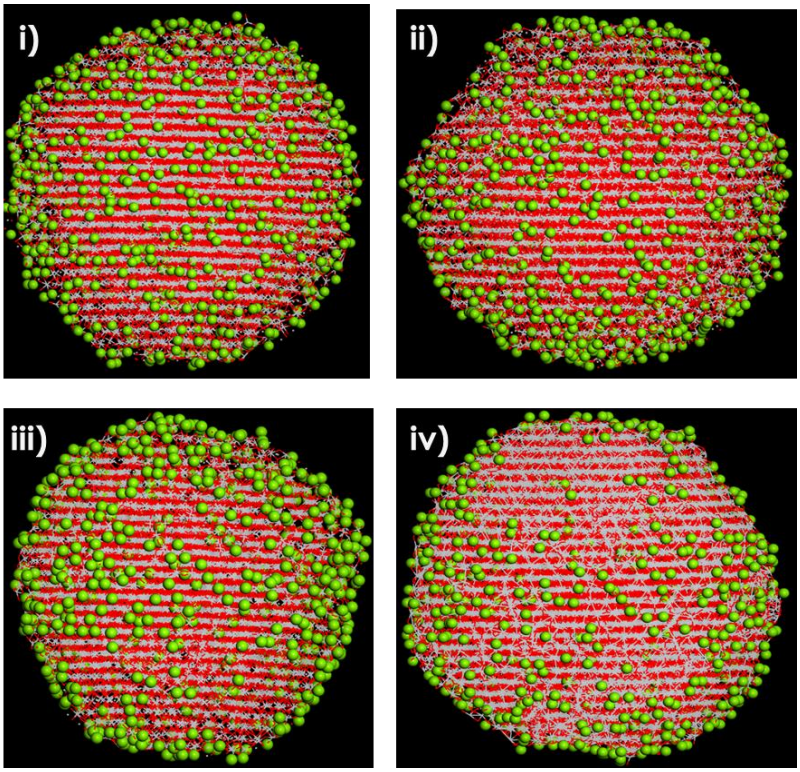

Figure 5.9: Cooled structures of $Mg_{0.15}TiO_2$ nanosphere at i)1500 K, ii) 1000 K, iii) 500 K and iv) 0 K.

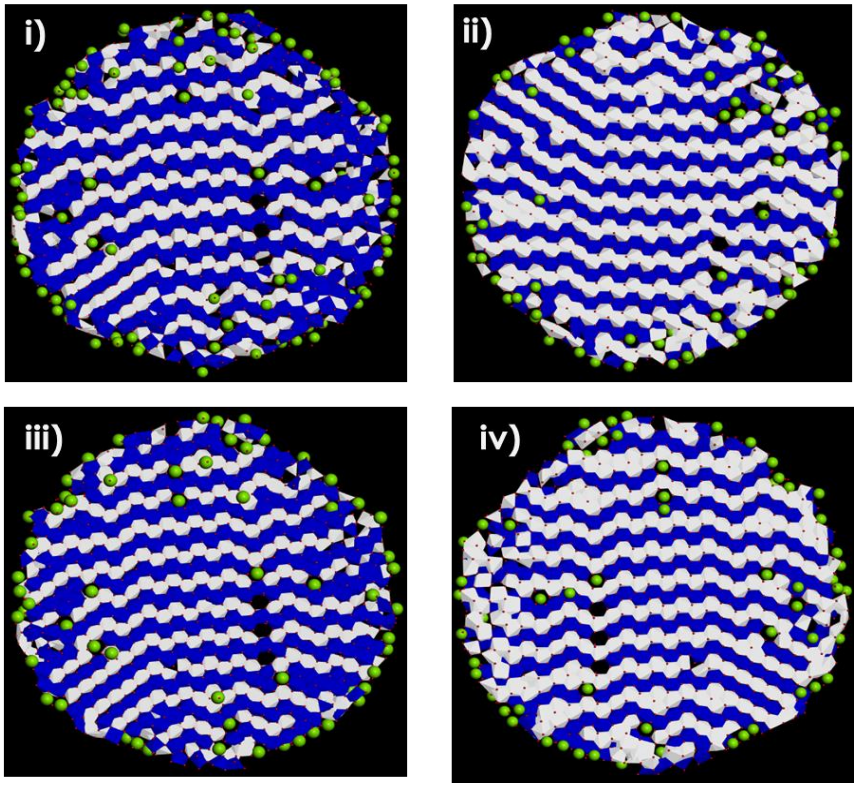

Figure 5.10: Cooled microstructures of $Mg_{0.15}TiO_2$ nanosphere at i) 1500 K, ii) 1000 K, iii) 500 K and iv) 0 K.

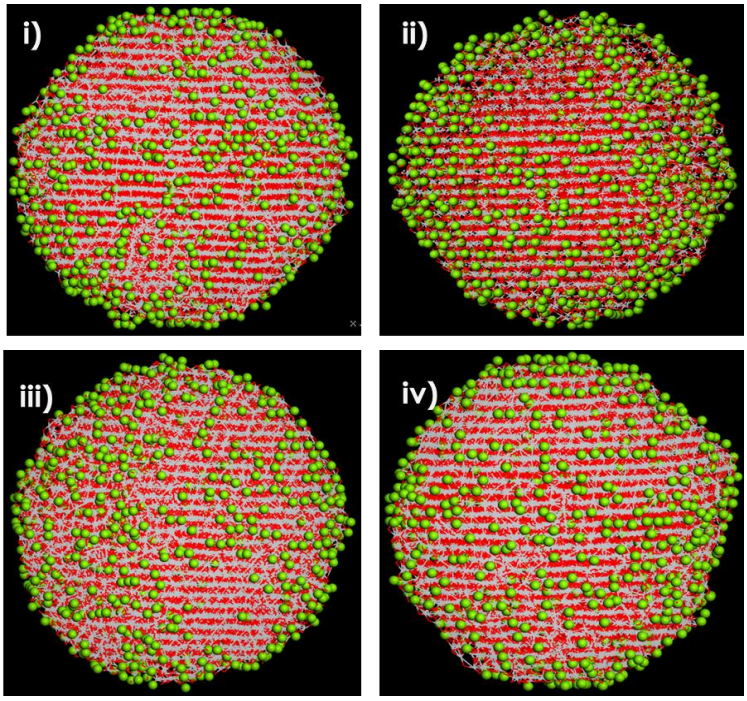

Figure 5.11: Cooled structures of $Mg_{0.19}TiO_2$ nanosphere at i)1500 K, ii) 1000 K, iii) 500 K and iv) 0 K.

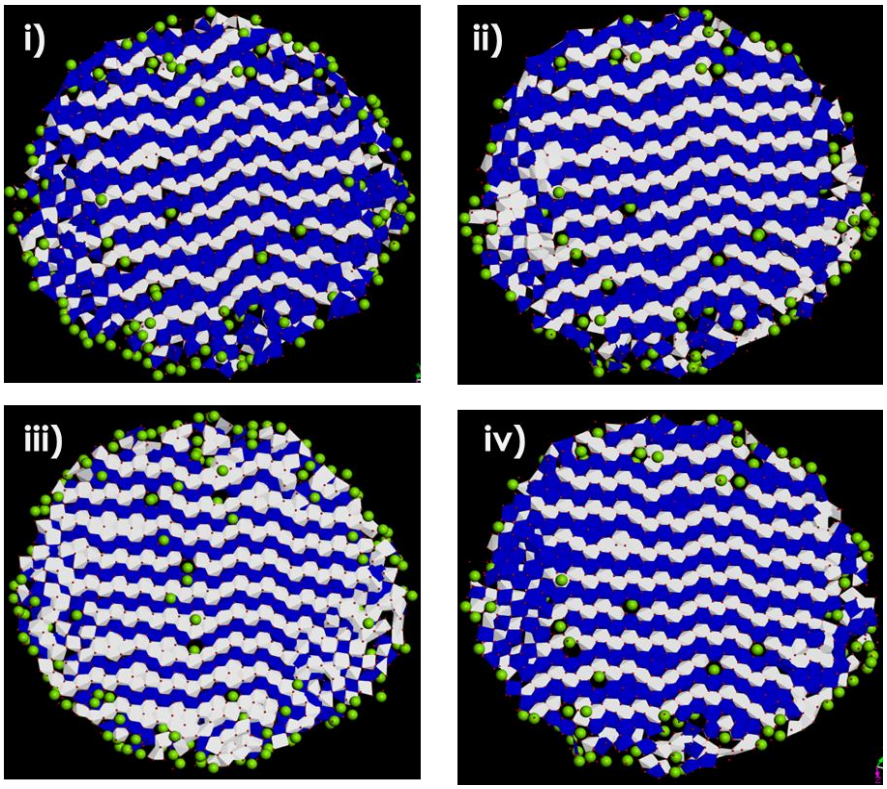

Figure 5.12: Cooled microstructures of $Mg_{0.19}TiO_2$ nanosphere at i) 1500 K, ii) 1000 K, iii) 500 K and iv) 0 K.

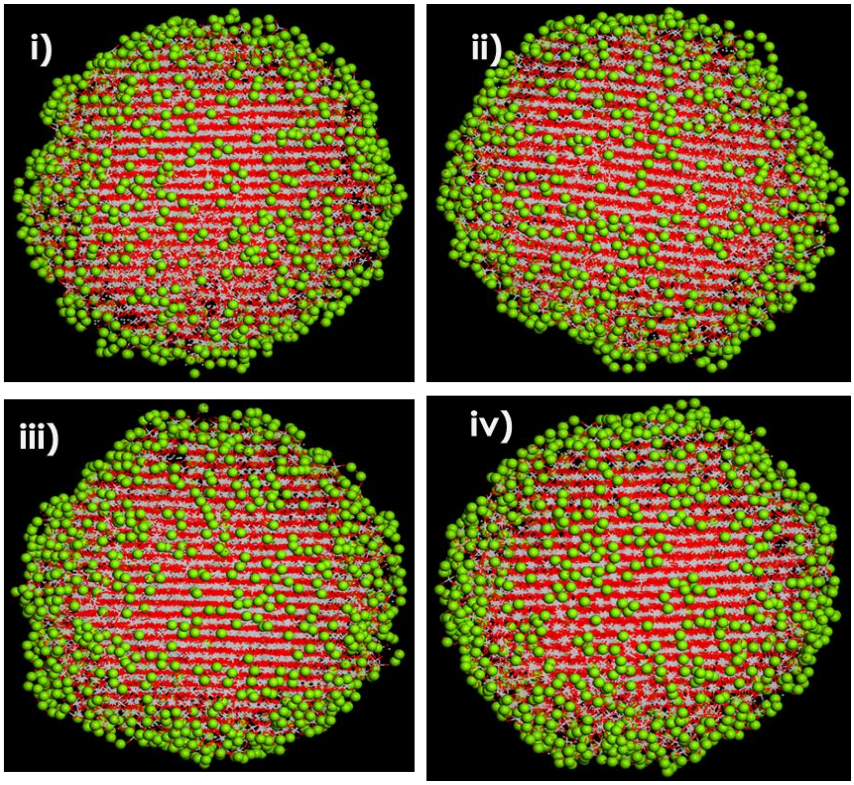

Figure 5.13: Cooled structures of $Mg_{0.23}TiO_2$ nanosphere at i)1500 K, ii) 1000 K, iii) 500 K and iv) 0 K.

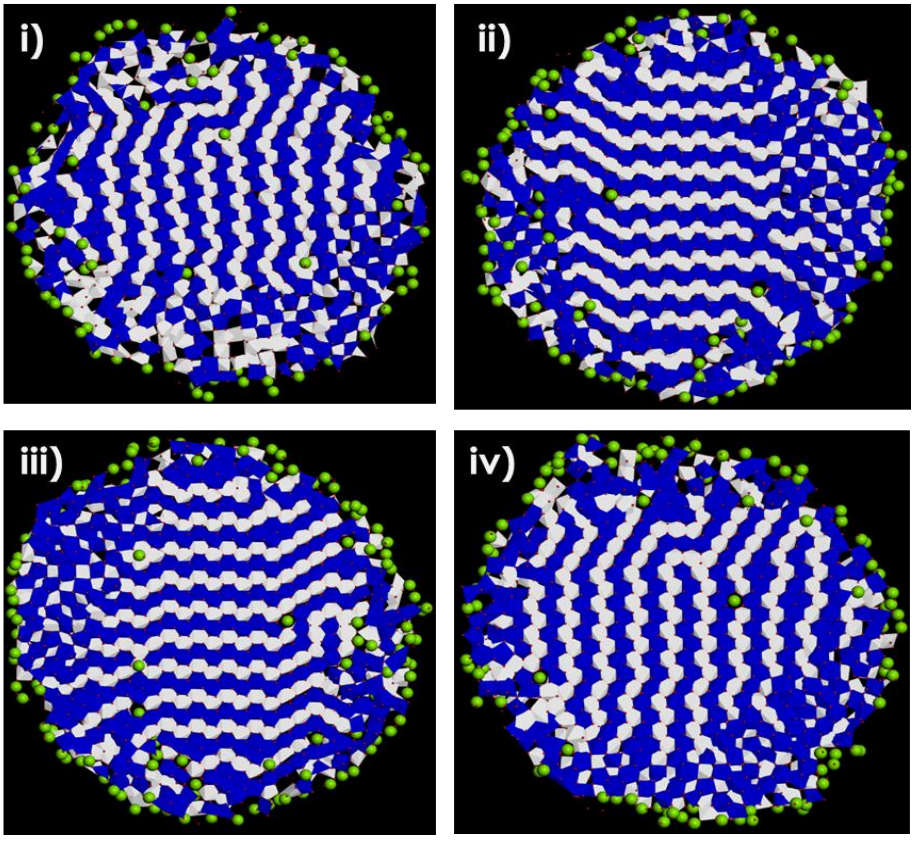

Figure 5.14: Cooled microstructures of $Mg_{0.23}TiO_2$ nanosphere at i) 1500 K, ii) 1000 K, iii) 500 K and iv) 0 K.

5.2.2. Mg_xTiO_2 Nanoporous

All recrystallised Mg_xTiO_2 nanoporous in Figure 5.3 a), b), c) and d) were cooled from 1500 K followed by 1000 K, 500 K and finally 0 K, the cooled structures and microstructures of $Mg_{0.11}TiO_2$, $M_{0.15}TiO_2$ and $Mg_{0.19}TiO_2$ were viewed in Figures 5.15, 5.17, 5.19 and 5.16, 5.18, 5.20 respectively. However, the structural and microstructural snapshots of $Mg_{0.23}TiO_2$ nanoporous architecture are not presented here due to its inability to crystallise. The cooled nanoporous structures from i) 1500 K to iv) 0 K for $Mg_{0.11}TiO_2$, $Mg_{0.15}TiO_2$ and $Mg_{0.19}TiO_2$ systems are illustrated in Figures 5.15, 5.17, 5.19 and they all have similar long-range order characteristics of crystalline patterns where most Mg^{2+} are well located and dispersed within the 1x1 tunnels, inside channels, and right on the open pores edges. The pores sizes have increased with an increased in Mg^{2+} concentrations inside the TiO_2 nanoporous lattice but kept the same after being cooled from i) 1500 K to iv) 0 K, these prior observations was confirmed by their corresponding sliced microstructural snapshots demonstrated in Figures 5.16, 5.18 and 5.20. urthermore, the snapshots of all microstructures for $Mg_{0.11}TiO_2$, $Mg_{0.15}TiO_2$ and $Mg_{0.23}TiO_2$ presented in Figure 5.16, Figure 5.18 and Figure 5.20 contained interstitial defect of zigzag and straight tunnels coinciding with brookite and rutile phases essential for electrochemical properties for energy in magnesium ion batteries during charging and discharging times. Empty vacancies and Mg^{2+} filled vacancies with most Mg^{2+} located on the 1x1 tunnels were observed on all Mg_xTiO_2 nanoporous structures. However, in microstructures with higher Mg^{2+} content, especially in $Mg_{0.19}TiO_2$ (Figure 5.20), clear limited disordered portions are observed, at lower temperatures, which may also be partly ascribed to change in orientation of the microstructure.

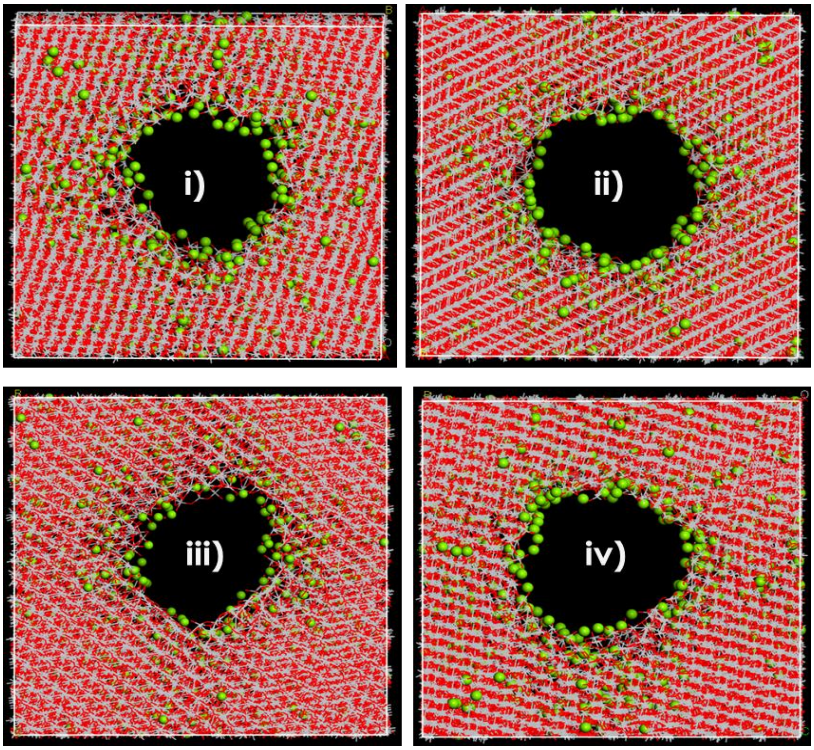

Figure 5.15: Cooled structures of $Mg_{0.11}TiO_2$ nanoporous architecture at i)1500 K, ii) 1000 K, iii) 500 K and iv) 0 K.

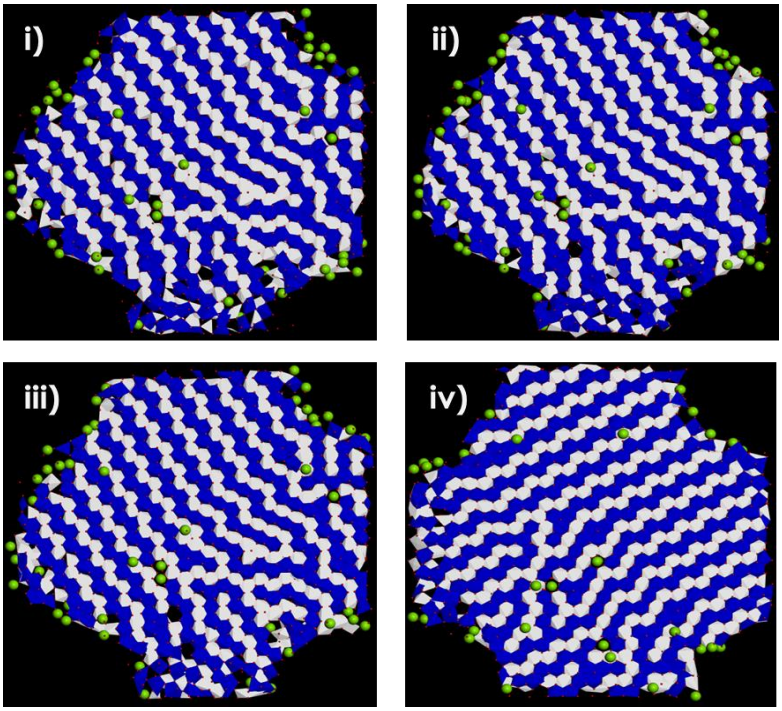

Figure 5.16: Cooled microstructures of $Mg_{0.11}TiO_2$ nanoporous architecture at i) 1500 K, ii) 1000 K, iii) 500 K and iv) 0 K.

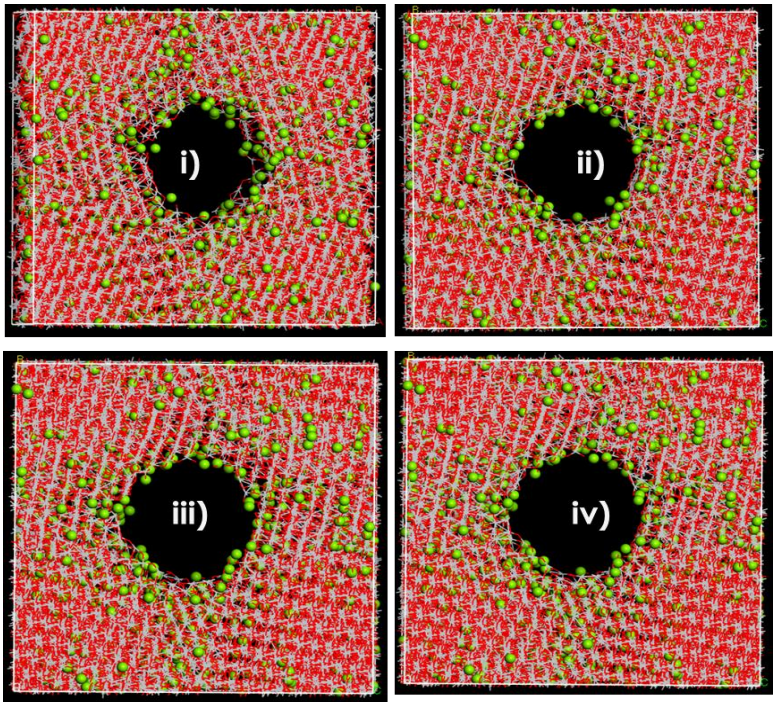

Figure 5.17: Cooled structures of $Mg_{0.15}TiO_2$ nanoporous architecture at i)1500 K, ii) 1000 K, iii) 500 K and iv) 0 K.

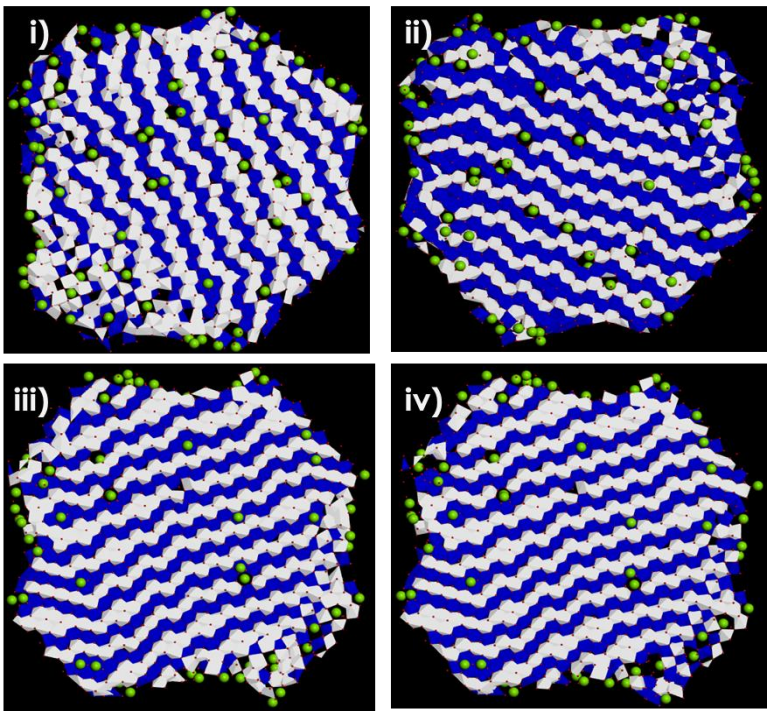

Figure 5.18: Cooled microstructures of $Mg_{0.15}TiO_2$ nanoporous architecture at i) 1500 K, ii) 1000 K, iii) 500 K and iv) 0 K.

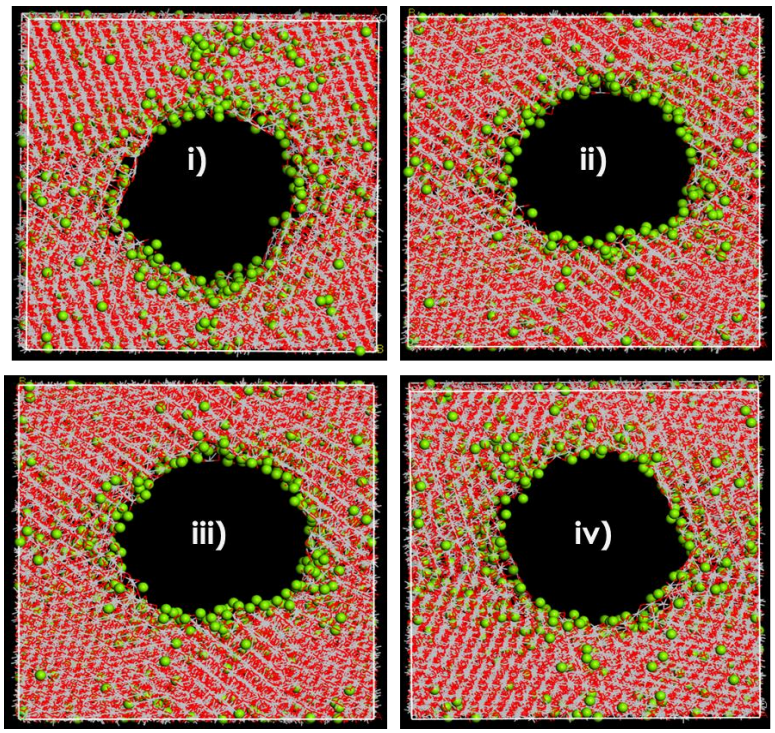

Figure 5.19: Cooled structures of $Mg_{0.19}TiO_2$ nanoporous architecture at i)1500 K, ii) 1000 K, iii) 500 K and iv) 0 K.

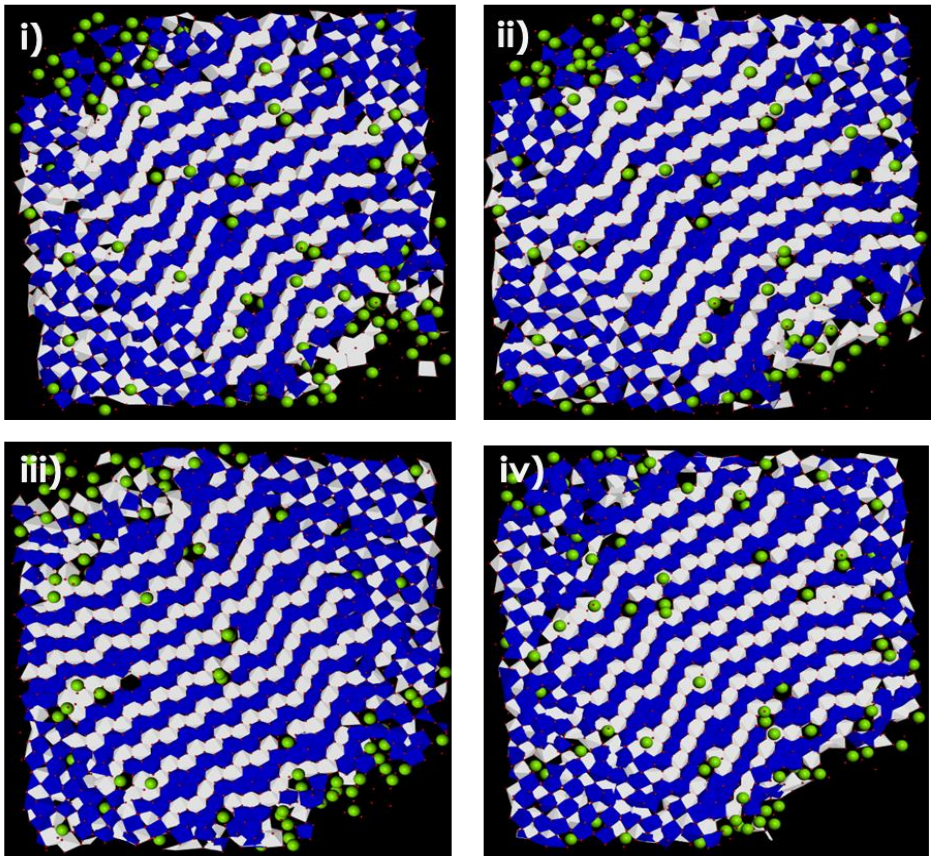

Figure 5.20: Cooled microstructures of $Mg_{0.19}TiO_2$ nanoporous architecture at i) 1500 K, ii) 1000 K, iii) 500 K and iv) 0 K.

5.2.3. Mg_xTiO_2 Nanosheets

The recrystallised nanosheets a) $Mg_{0.11}TiO_2$, b) $Mg_{0.15}TiO_2$ and c) $Mg_{0.19}TiO_2$ discussed in section 5.1 (Figure 5.5) were successfully cooled through molecular dynamics simulations from 1500 K to 0 K in 500 K intervals. Their cooled structures are shown in Figures 5.21, 5.23 and 5.25 where similar characteristics of partial crystalline and disordered patterns (though not too apparent) with well dispersed Mg^{2+} ions on at all Mg^{2+} concentrations and cooled temperature except for $Mg_{0.23}TiO_2$ nanosheets which was not presented due to its high amorphous state even after recrystallisation in Figure 5.5 d). The structural integrity was confirmed by their corresponding microstructural snapshots presented by Figures 5.22, 5.24 and 5.26 for $Mg_{0.11}TiO_2$, $Mg_{0.15}TiO_2$ and $Mg_{0.19}TiO_2$ nanosheets, all clearly depicted mixed phase of disordered and ordered patterns filled with Mg^{2+} inside the zigzag and straight tunnels coinciding to brookite and rutile polymorphs. The degree of disorder in the nanosheets is much greater than that mentioned in the $Mg_{0.19}TiO_2$ of nanoporous architecture. Cooling the nanosheets did not greatly affect the amount of crystalline and non-crystallinity which was also seen after recrystallisation synthesis but rather remained the same which indicates that structural integrity was maintained even when exposed to lower simulated temperatures, which are some of excellent properties for better battery performance.

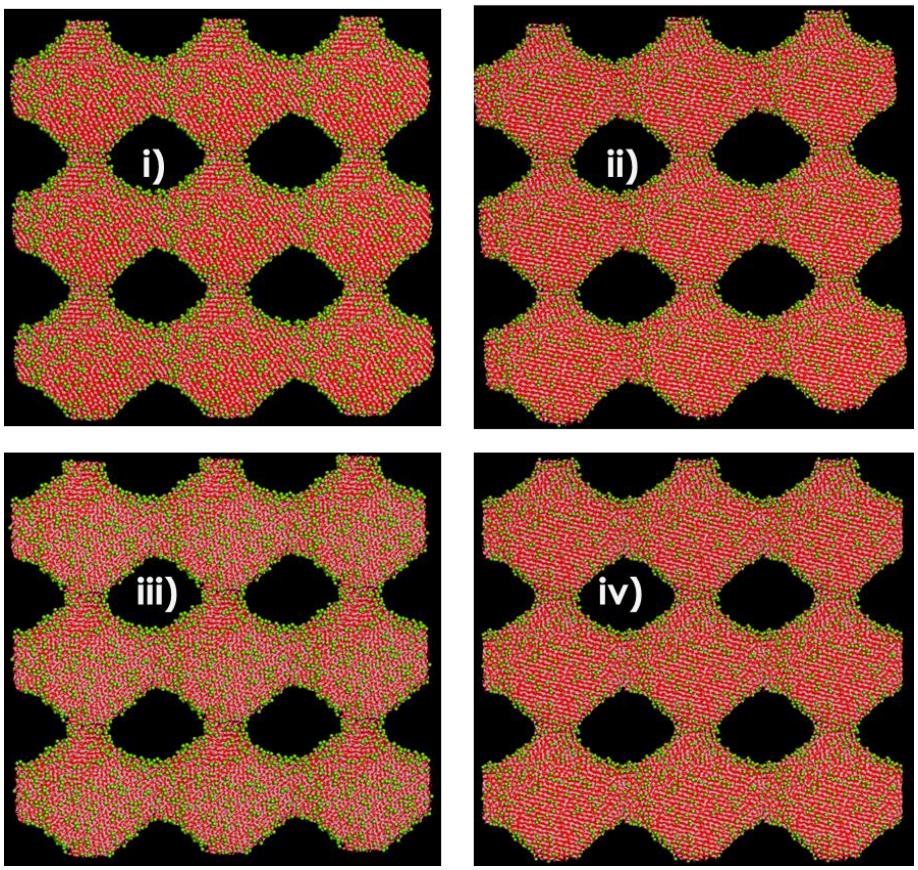

Figure 5.21: Cooled structures of nanosheets $Mg_{0.11}TiO_2$ at i)1500 K, ii) 1000 K, iii) 500 K and iv) 0 K.

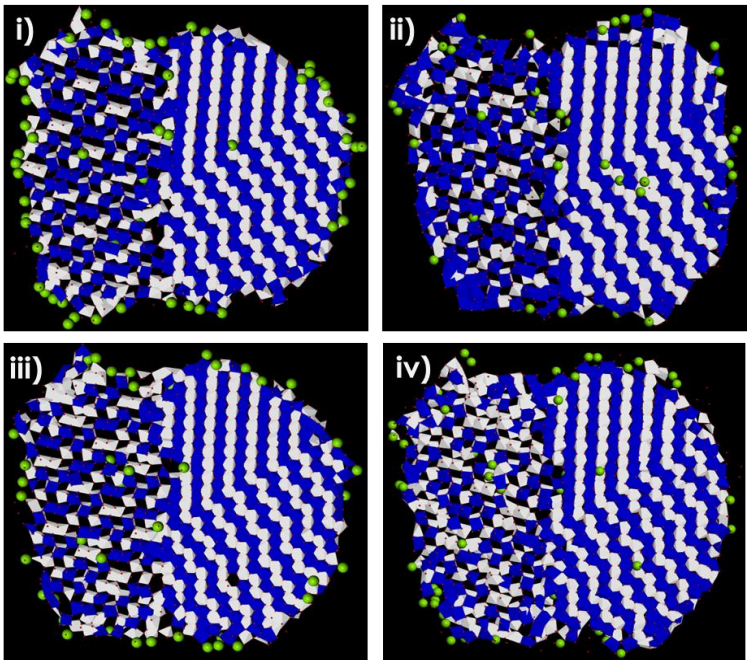

Figure 5.22: Cooled microstructures of $Mg_{0.11}TiO_2$ nanosheets at i) 1500 K, ii) 1000 K, iii) 500 K and iv) 0 K.

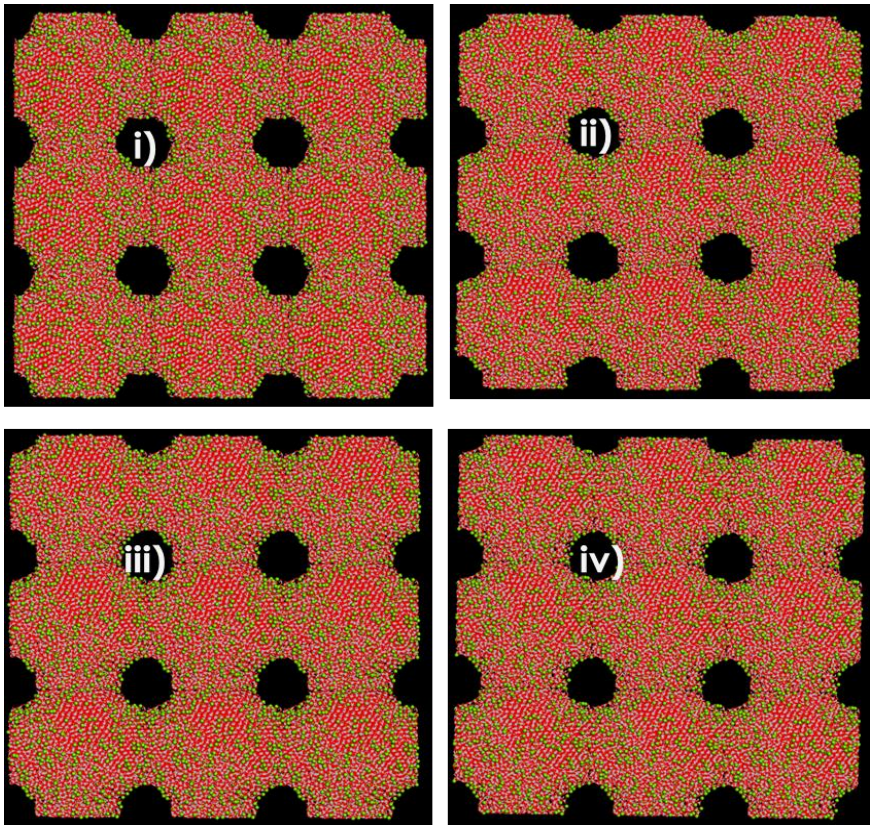

Figure 5.23: Cooled structures of $Mg_{0.15}TiO_2$ nanosheets at i) 1500 K, ii) 1000 K, iii) 500 K and iv) 0 K.

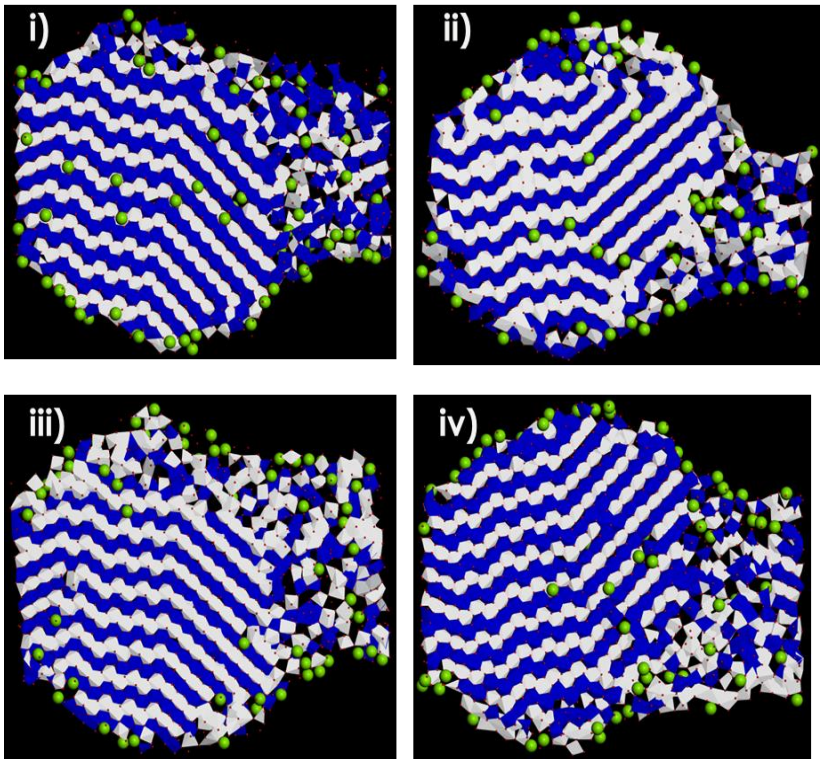

Figure 5.24: Cooled microstructures of $Mg_{0.15}TiO_2$ nanosheets at i) 1500 K, ii) 1000 K, iii) 500 K and iv) 0 K.

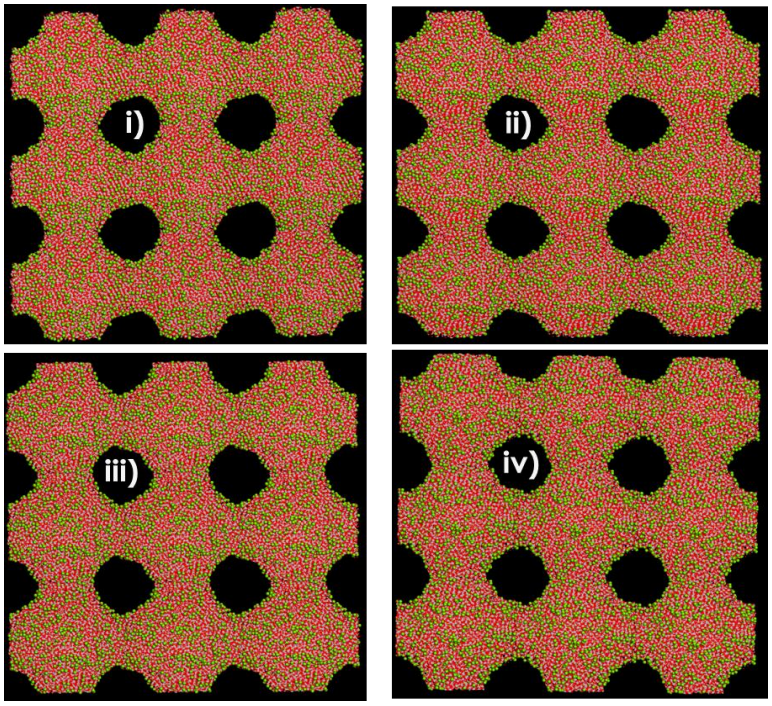

Figure 5.25: Cooled structures of $Mg_{0.19}TiO_2$ nanosheets at i)1500 K, ii) 1000 K, iii) 500 K and iv) 0 K.

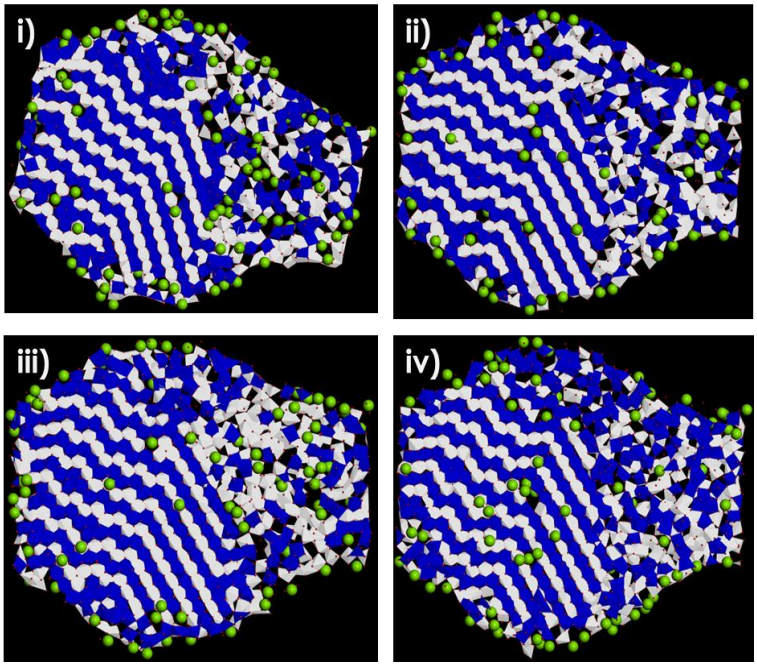

Figure 5.26: Cooled microstructures of $Mg_{0.19}TiO_2$ nanosheets at i) 1500 K, ii) 1000 K, iii) 500 K and iv) 0 K.

5.3. RDFs of $MgxTiO_2$ (x= 0.11, 0.15, 0.18 and 0.23) Nanostructures

The radial distribution function of the Ti-O pair of the Mg_xTiO_2 nanosphere, nanoporous and nanosheets exhibited from 5.27 to Figure 5.38 was analysed to obtain

more insights on the level of crystallinity and amorphous phase present on varied magnesiated TiO_2 systems from high and low temperatures.

5.3.1. Mg_xTiO_2 Nanosphere

The calculated radial distribution functions Ti-O pair in $Mg_{0.11}TiO_2$ $Mg_{0.15}TiO_2$, $Mg_{0.19}TiO_2$ and $Mg_{0.23}TiO_2$ nanosphere were analysed at 1500 K,1000 K,500 K and 0 K and homogeneous peak sharpness and broadness characteristics were observed. Figure 5.27 demonstrates Ti-O pair RDF data in $Mg_{0.11}TiO_2$ nanosphere with maximum g(r) value of 108 at distance 2 Å, the highest sharp peak followed a crystallinity trends of 0 K >500 K>1000 K>1500 K which implies that the $Mg_{0.11}TiO_2$ nanosphere cooled at 0 K was highly crystalline compared to that at 500 K, 1000 K and 1500 K confirmed by its sharp peak while the other three peaks were slightly broader. Therefore, cooling the $Mg_{0.11}TiO_2$ nanosphere has greatly enhanced its crystallinity. Such results were also observed on Ti-O pair RDF peaks in $Mg_{0.15}TiO_2$, $Mg_{0.19}TiO_2$, and $Mg_{0.23}TiO_2$ nanospheres presented in Figures 5.27, 5.28 and 5.29 respectively. However, the only difference observed in the nanosphere RDF is that the crystallinity was increasing with a decrease in temperature and a decrease in Mg^{2+} concentrations since the peaks at 0 K were slightly broader at higher Mg^{2+} concentrations.

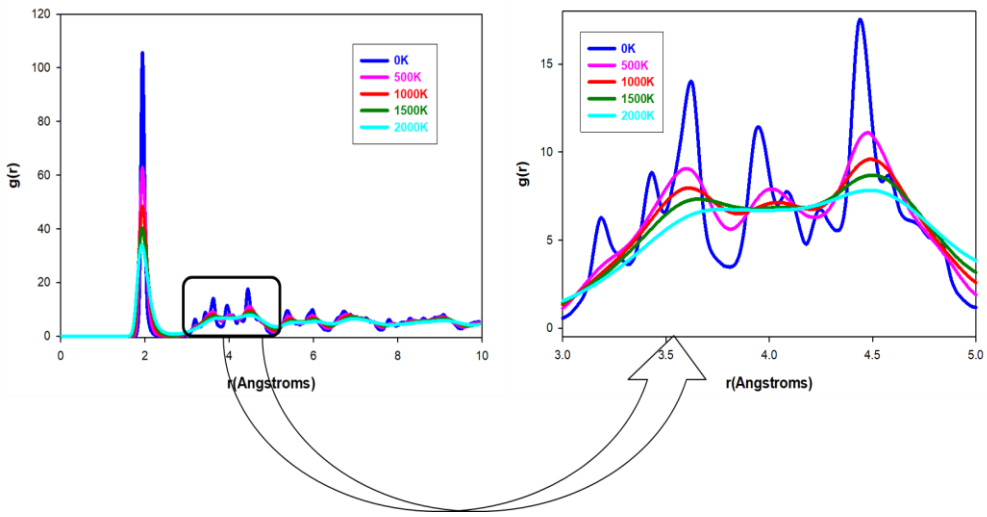

Figure 5.27: Shows simulated RDFs plots for $Mg_{0.11}TiO_2$ nanosphere at cooled and increased temperatures with a magnified RDFs portion between 3 and 5 Å for better visualisation.

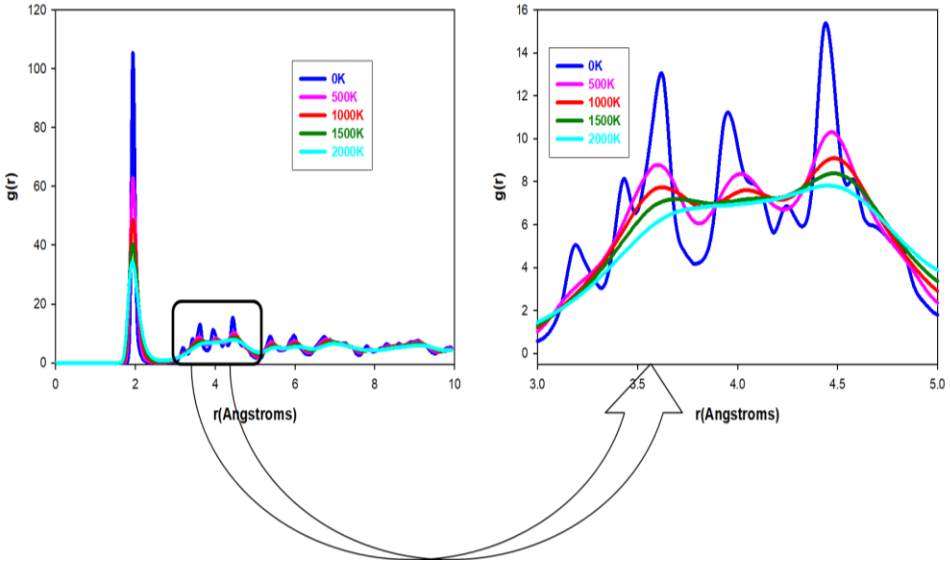

Figure 5.28: Shows simulated RDFs plots for $Mg_{0.15}TiO_2$ nanosphere at cooled and increased temperatures with a magnified RDFs portion between 3 and 5 Å for better visualisation.

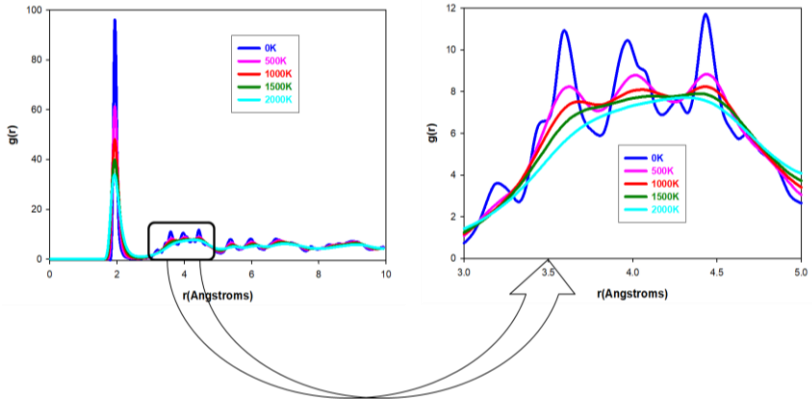

Figure 5.29: Shows simulated RDFs plots for $Mg_{0.19}TiO_2$ nanosphere at cooled and increased temperatures with a magnified RDFs portion between 3 and 5 Å for better visualisation.

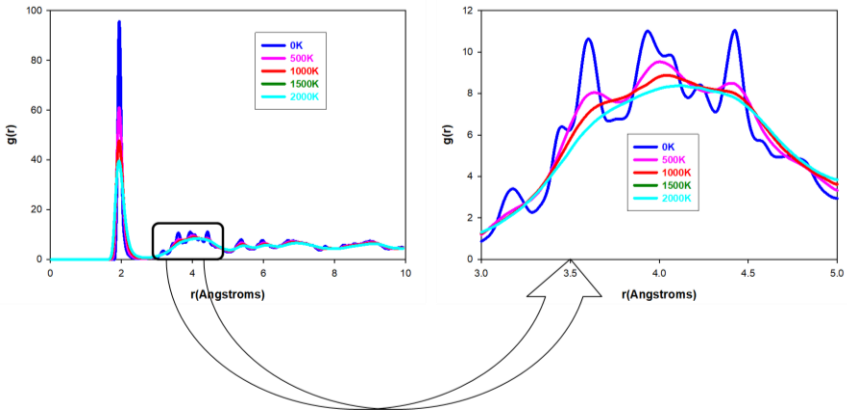

Figure 5.30: Shows simulated RDFs plots for $Mg_{0.23}TiO_2$ nanosphere at cooled and increased temperatures with a magnified RDFs portion between 3 and 5 Å for better visualisation

5.3.2. Mg_xTiO_2 Nanoporous

Structural properties such as the position r(Å) and height g(r) of all the Ti-O bond of RDF peaks obtained at 0K ,500K, 1000K and 1500K in $Mg_{0.11}TiO_2$, $Mg_{0.15}TiO_2$, $Mg_{0.19}TiO_2$ and $Mg_{0.23}TiO_2$ nanoporous structures are presented by Figures 5.31, 5.32, 5.33 and 5.34 respectively. An almost similar peak positions and height are observed in all the Mg_xTiO_2 nanoporous systems illustrated from Figure 5.31 to Figure 5.34 where the maximum peak height at 0 K decreases with an increase in Mg ion concentrations.

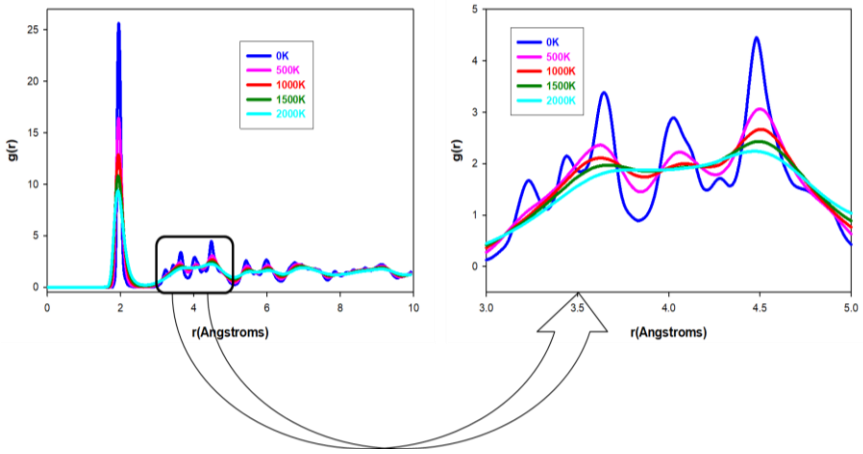

Figure 5.31: Shows simulated RDFs plots for $Mg_{0.11}TiO_2$ nanoporous at cooled and increased temperatures with a magnified RDFs portion between 3 and 5 Å for better visualisation.

However, at 500 K, 1000 K and 1500 K the peak height, located at around 2Å, remains the same on all Mg_xTiO_2 nanoporous systems, suggesting equal coordination's numbers 5-fold of the Ti-O bond lengths. Moreover, the peak height g(r) was decreasing with an increase in temperature in all nanoporous systems of $Mg_{0.11}TiO_2$, $Mg_{0.15}TiO_2$, $Mg_{0.19}TiO_2$ and $Mg_{0.23}TiO_2$ which caused many peak splits especially from 3Å towards 10Å in r position. The only difference was the peak sharpness and peak broadness at all splits which then suggested the presence of crystalline and amorphous phases inside each nanoporous structures at different temperatures while the peaks at 2000 K was in amorphous states, hence the crystallinity phase followed the trend of 0 K>500 K>1000 K>1500 K and the amorphous phase followed the trend of 1500 K>1000 K>500 K>0 K.

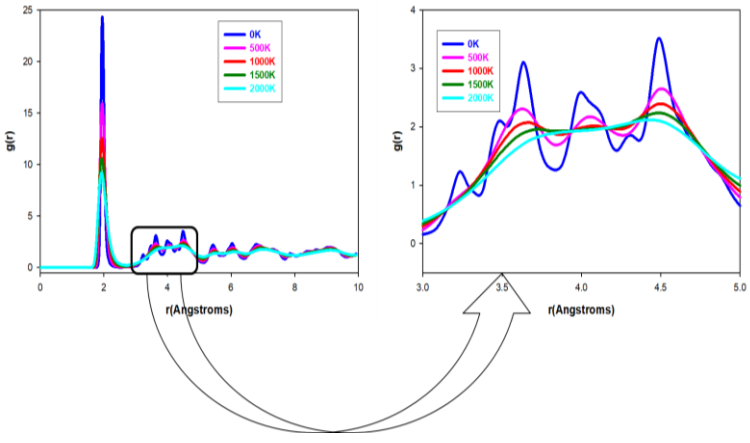

Figure 5.32: Shows simulated RDFs plots for $Mg_{0.15}TiO_2$ nanoporous at cooled and increased temperatures with a magnified RDFs portion between 3 and 5 Å for better visualisation.

So, the peaks at 0 K suggested a highly crystalline systems due to its sharpness and shorter distances while the peaks at 2000 K were amorphous due to its broadness and longer distances and it was observed in all systems of $Mg_{0.11}TiO_2$, $Mg_{01.5}TiO_2$ and $Mg_{0.19}TiO_2$ presented in Figures 5.31, 5.32 and 5.33 respectively. Furthermore, the sharpness decreased with increasing Mg ion concentration hence the peak for $Mg_{0.23}TiO_2$ nanoporous systems was very broad, confirming an amorphous phase at 0 K even at all cooled temperatures of 500 K,1000 K and 1500 K evidenced by their respective highly amorphous structures which were not shown due to its complex molten state. These results suggest that the previously generated TiO_2 nanoporous have the capability of hosting more Mg^{2+} towards $Mg_{0.19}TiO_2$ concentration together with the ability to withstand higher and low temperatures without deforming its original structural frameworks hence structural stability is maintained. However, nanoporous crystallinity could not be maintained at a concentration of $Mg_{0.23}TiO_2$ for all temperatures.

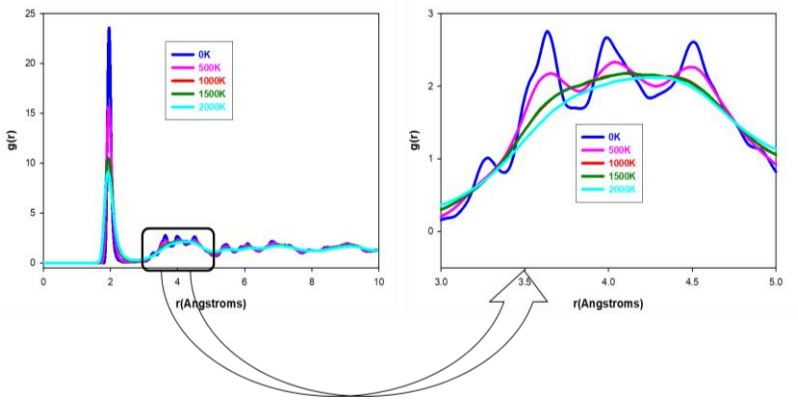

Figure 5.33: Shows simulated RDFs plots for $Mg_{0.19}TiO_2$ nanoporous at cooled and increased temperatures with a magnified RDFs portion between 3 and 5 Å Å for better visualisation.

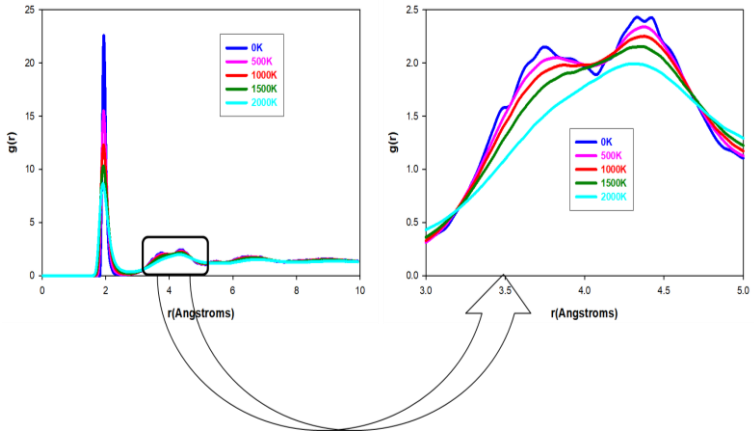

Figure 5.34: Shows simulated RDFs plots for $Mg_{0.23}TiO_2$ nanoporous at cooled and increased temperatures with a magnified RDFs portion between 3 and 5 Å for better visualisation.

5.3.3. Mg_xTiO_2 Nanosheets

The mixed phases in Mg_xTiO_2 nanosheets, observed from their corresponding structures through microstructural snapshots shown in Figures 5.22, 5.24 and 5.26, were characterised by the radial distribution functions (RDF) of Ti-O pairs displayed by Figures 5.35, 5.36 and 5.37 and 5.38 for $Mg_{0.11}TiO_2$, $Mg_{0.15}TiO_2$, $Mg_{0.19}TiO_2$ and $Mg_{0.23}TiO_2$ nanosheets respectively. All RDFs for Mg_xTiO_2 nanosheets had higher and visible peaks splits with equal bond length positioned at 2 Å at all cooling temperatures, the longest and sharpest peaks were those seen at 0 K which determine the maximum g(r)'s of 42 Å , 40 Å, 49 Å and 48 Å in $Mg_{0.11}TiO_2$, $Mg_{0.15}TiO_2$, $Mg_{0.19}TiO_2$ and $Mg_{0.23}TiO_2$ nanosheets systems respectively. Since Mg_xTiO_2 nanosheets contain mixed polymorphic phases of amorphous and crystalline characteristics where the high dominance of crystalline phase was seen more in nanosheet structures with low Mg^{2+} concentration displayed by Figure 5.35 and low temperatures (0 K) in all systems. Hence, $Mg_{0.11}TiO_2$ nanosheets had higher crystalline ordered patterns while the $Mg_{0.23}TiO_2$ nanosheets structure had higher amorphous disordered patterns, which implies that low Mg^{2+} concentration imposed crystallinity upon cooling and more Mg^{2+} concentrations favour amorphisation even upon cooling resulting in a crystalline trend of 0 K>500 K>1000 K>1500 K>2000 K and the reverse is true for amorphous trend. Consequently, the Mg_xTiO_2 nanosheets have the ability of accommodating the Mg^{2+} while maintaining both mixed polymorph's structure up until $Mg_{0.19}TiO_2$ concentration and beyond this they are rendered amorphous.

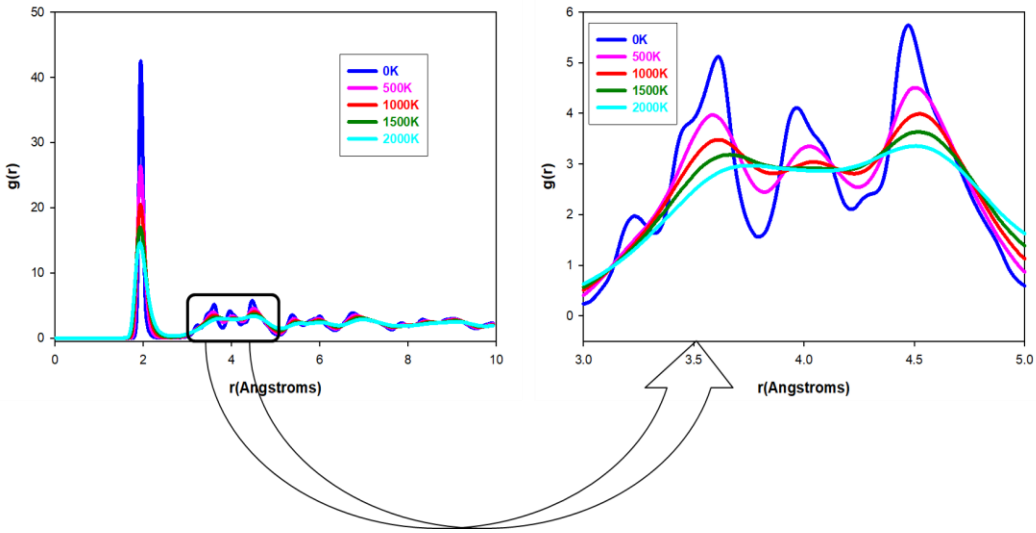

Figure 5.35: Shows simulated RDFs plots for $Mg_{0.11}TiO_2$ nanosheets at cooled and increased temperatures with a magnified RDFs portion between 3 and 5 Å for better visualisation.

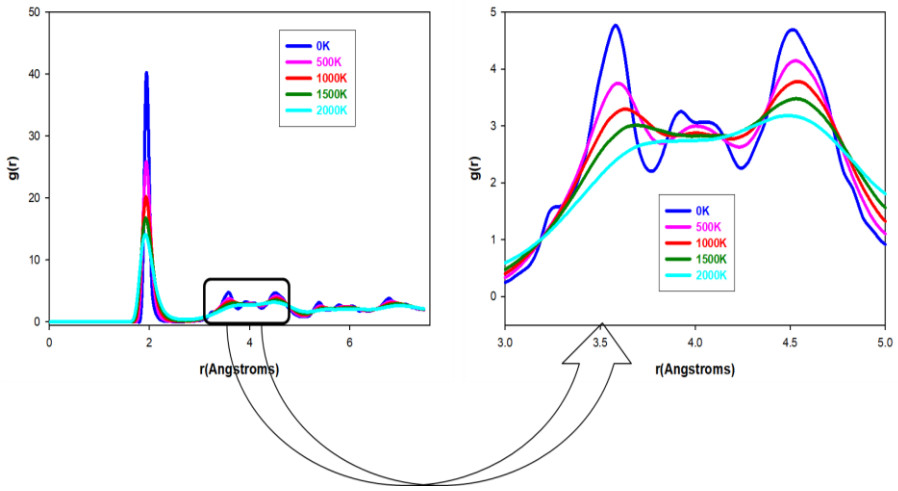

Figure 5.36: Shows simulated RDFs plots for $Mg_{0.15}TiO_2$ nanosheets at cooled and increased temperatures with a magnified RDFs portion between 3 and 5 Å for better visualisation.

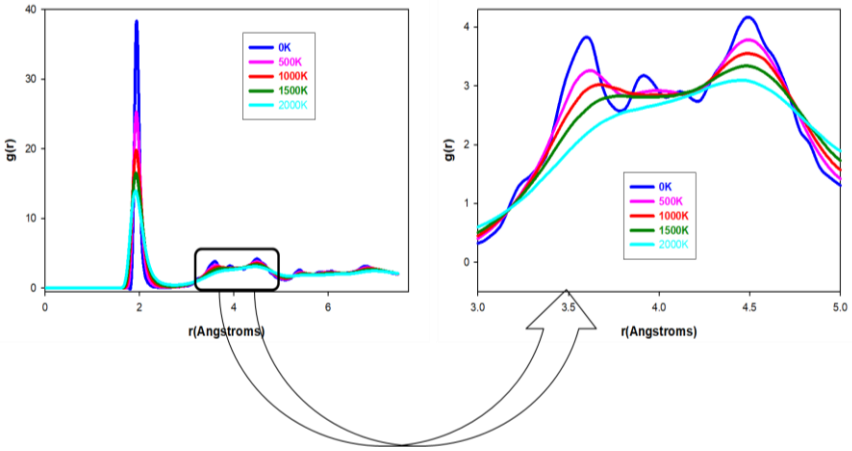

Figure 5.37: Shows simulated RDFs plots for $Mg_{0.18}TiO_2$ nanosheets at cooled and increased temperatures with a magnified RDFs portion between 3 and 5 Å for better visualisation.

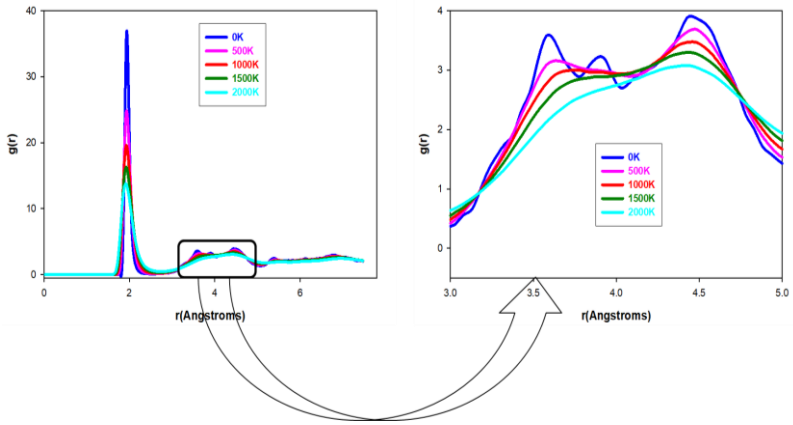

Figure 5.38: Shows simulated RDFs plots for $Mg_{0.23}TiO_2$ nanosheets at cooled and increased temperatures with a magnified RDFs portion between 3 and 5 Å for better visualisation.

5.4. XRDs of Mg_xTiO_2 (x=0.11, 0.15, 0.18 and 0.23) Nanostructure

The X-ray diffraction patterns (XRD) of the Mg_xTiO_2 nanosphere, nanoporous and nanosheets illustrated from Figure 5.39 to Figure 5.50 were analysed to determine the various TiO_2 polymorphic phases under high and low exposed simulated temperatures with various concentrations of Mg^{2+}.

5.4.1. Mg_xTiO_2 Nanosphere

The XRD patterns for the $Mg_{0.11}TiO_2$, $Mg_{0.15}TiO_2$, $Mg_{0.19}TiO_2$ and $Mg_{0.23}TiO_2$ nanospheres analysed at 2000 K and 0 K, depicted in Figures 5.39, 5.40, 5.41 and 5.42 sequentially, were compared to constitute similar peaks positions at 2Θ = 25º, 31º, 35º, 41º, 55º and 56º corresponding to reflections by the planes (111), (101), (120), (121), (012), (210),(211), (131), (610), (002) and (200) in all Mg_xTiO_2 nanosphere structures but different peaks intensities per Mg^{2+} concentration at both temperatures. The intensity of the peaks suggests magnitude and quantity of the presence of anatase, rutile and brookite TiO_2 polymorphs within all the nanospheres. Hence the highly intense peak seen between 20º and 36.2º always appeared in all Mg_xTiO_2 nanospheres systems predicting the dominance of the brookite and rutile phase. The brookite (Zigzag tunnels) and rutile (straight tunnels) phase dominance had appeared more in $Mg_{0.11}TiO_2$ nanospheres at 2000 K and more in $Mg_{0.19}TiO_2$ than $Mg_{0.23}TiO_2$ lastly in $Mg_{0.15}TiO_2$ nanospheres in that sequence at 0 K. The highly intense and sharp peaks clearly confirmed that the Mg_xTiO_2 systems contained highly nanocrystalline mixture of rutile, anatase and brookite polymorphs at both high (2000 K) and low (0 K) simulated temperatures thus also in agreement with their corresponding characterised by viewed structures, microstructures, and Ti-O RDFs plots. Considering the absence of amorphous phase in all Mg_xTiO_2 nanospheres only evince no structural transformation but only influenced structural integrity at all simulated temperature after recrystallisation and cooling synthesis.

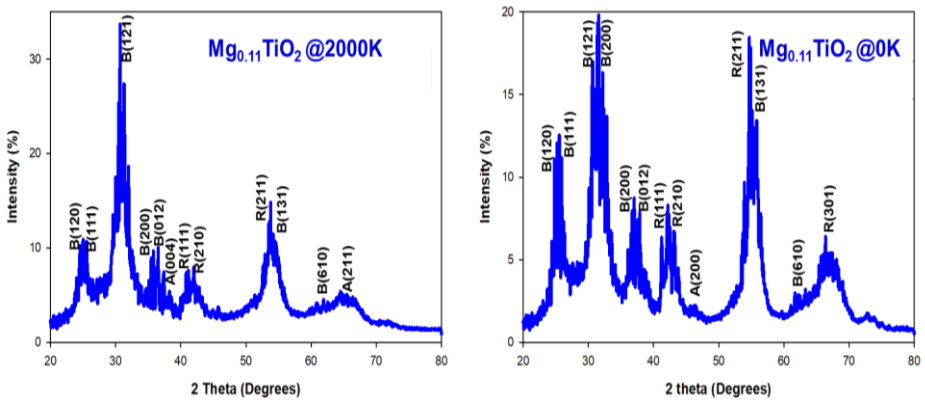

Figure 5.39: Illustrates simulated XRDs plots of $Mg_{0.11}TiO_2$ nanosphere at recrystalised (2000 K) and cooled (0 K) temperatures conditions for structural characterisations.

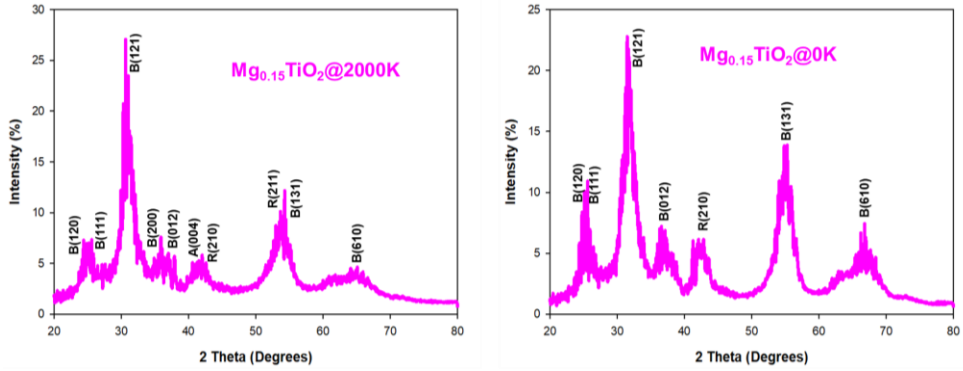

Figure 5.40: Illustrates simulated XRDs plots of $Mg_{0.15}TiO_2$ nanosphere at recrystallized (2000 K) and cooled (0 K) temperatures conditions for structural characterisations.

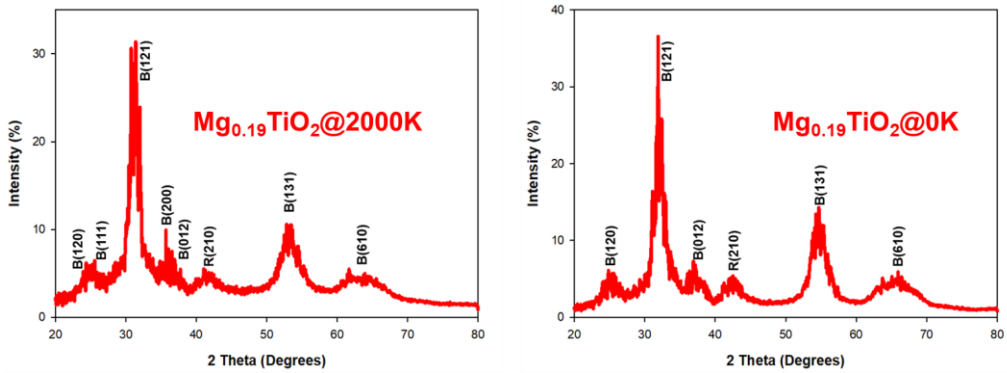

Figure 5.41: Illustrates simulated XRDs plots of $Mg_{0.19}TiO_2$ nanosphere at recrystalised (2000 K) and cooled (0 K) temperatures conditions for structural characterisations.

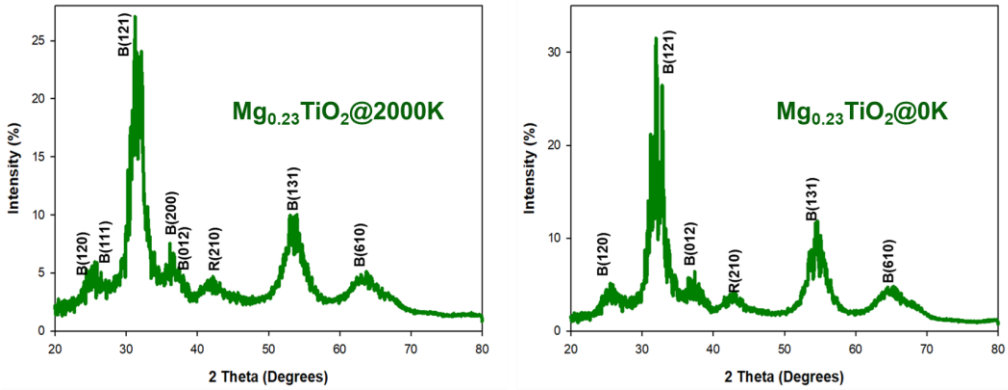

Figure 5.42: Illustrates simulated XRDs plots of $Mg_{0.23}TiO_2$ nanosphere at recrystallized (2000 K) and cooled (0 K) temperatures conditions for structural characterisations.

5.4.2. Mg_xTiO_2 Nanoporous

The quality and quantity of ordered (crystalline) and disordered (non-crystalline) patterns present inside the $Mg_{0.11}TiO_2$, $Mg_{0.15}TiO_2$, $Mg_{0.19}TiO_2$ and $Mg_{0.23}TiO_2$ nanoporous systems depicted by Figures 5.43, 5.44, 5.45 and 5.46 respectively were characterised through by their respective X-ray Diffraction study patterns after heated

to 2000 K and cooled at 0 K. The XRD data for Mg_xTiO_2 nanoporous contained highly intense noisy peaks at both simulated temperatures indicating a very crystalline systems comprising a mixture of brookite, rutile, and anatase polymorphs, these mixture of these three polymorphs were exceedingly observed on Figure 5.43 inside $Mg_{0.11}TiO_2$ nanoporous systems, then the peaks intensities on Figure 5.44 for $Mg_{0.15}TiO_2$ nanoporous systems were reduced with only a mixture of rutile and brookite polymorphs with slight of ramsdellite phase mostly on the edges of the structures confirmed by their respective microstructural snapshots in Figure 5.18 were the highly dominant.

However, the peak intensities mostly at 2Ɵ value of 30º got increased while the peaks intensity at other 2Ɵ values got reduced then disappeared, suggesting an increased in presence of brookite and rutile polymorphs with some nearing disordered systems of the ramsdellite phase at both heated (2000 K) and cooled (0 K) temperatures as shown in Figure 5.45 for the $Mg_{0.19}TiO_2$ nanoporous system hence the complete transformed amorphous molten phase in $Mg_{0.23}TiO_2$ nanoporous systems was obtained confirmed by stretched broader peaks at 2Ɵ value of 30º and up until towards 80º on its XRD patterns in Figure 5.46 whose recrystallised microstructures and cooled structures along with their respective microstructures were not shown due to their molten phase of a highly disordered nanoporous system where two crystalline layers could not be sliced. Consequently, this analysis proves and confirms that crystalline patterns decrease with an increase in Mg^{2+} intercalation in TiO_2 highly influenced by recrystallisation and cooling simulation temperatures. The highly intense peaks at 2Ɵ values of 25º,32º,35º,42º,55º and 65º corresponding to reflections by (111), (101), (120), (121), (012), (210),(211),(131),(610),(002) and (200) planes for crystalline Mg_xTiO_2 polymorphs had only appeared in $Mg_{0.11}TiO_2$,$Mg_{0.15}TiO_2$ and $Mg_{0.19}TiO_2$ nanoporous structures illustrated as seen in Figures 5.43, 5.44 and 5.45 respectively, and therefore not in $Mg_{0.23}TiO_2$ nanoporous systems.

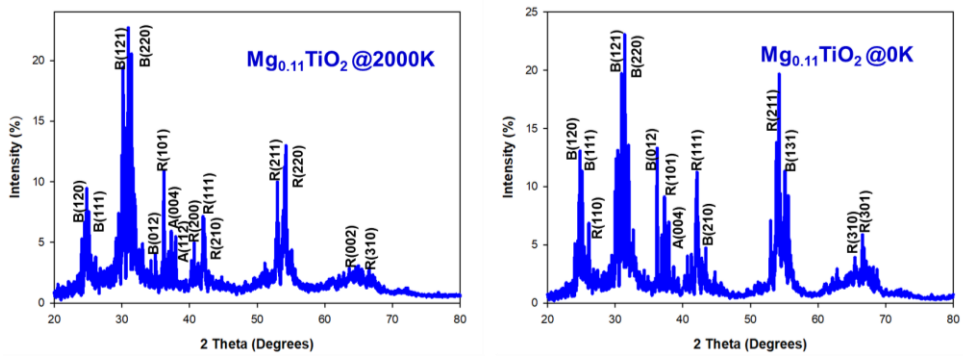

Figure 5.43: Illustrates simulated XRDs plots of $Mg_{0.11}TiO_2$ nanoporous at recrystalised (2000 K) and cooled (0 K) temperatures.

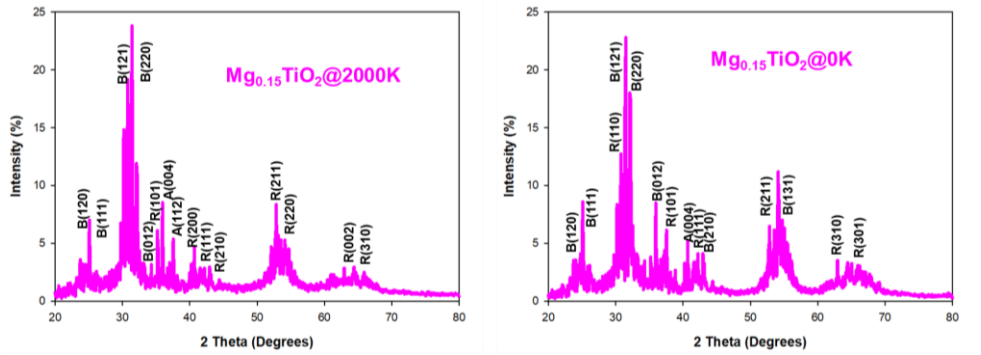

Figure 5.44: Illustrates simulated XRDs plots of $Mg_{0.15}TiO_2$ nanoporous at recrystalised (2000 K) and cooled (0 K) temperatures.

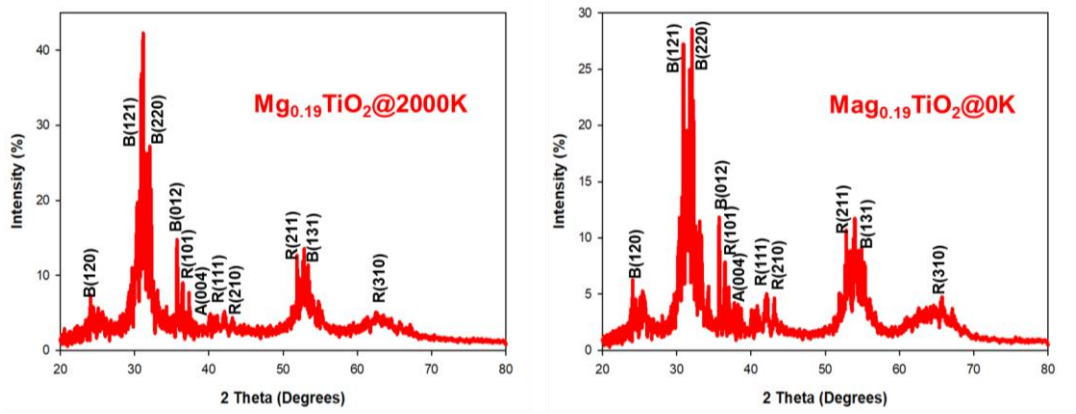

Figure 5.45: Illustrates simulated XRDs plots of $Mg_{0.19}TiO_2$ nanoporous at recrystalised (2000 K) and cooled (0 K) temperatures.

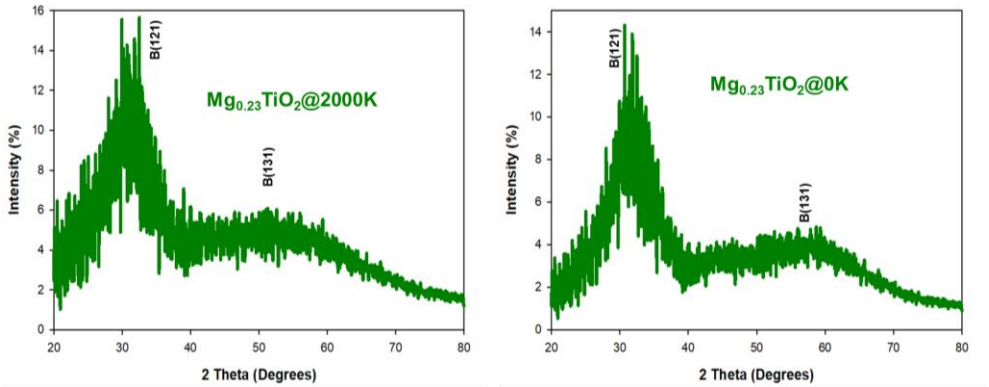

Figure 5.46: Illustrates simulated XRDs plots of $Mg_{0.23}TiO_2$ nanoporous at recrystalised (2000 K) and cooled (0 K) temperatures.

5.4.3. Mg_xTiO_2 Nanosheets

X-ray diffraction patterns in Figures 5.47, 5.48, 5.49 and 5.50 are for $Mg_{0.11}TiO_2$, $Mg_{0.15}TiO_2$, $Mg_{0.19}TiO_2$ and $Mg_{0.23}TiO_2$ nanosheets recrystallised at 2000 K (high) and cooled at 0 K (Low), all Mg_xTiO_2 nanosheets have similar broad peak positions which then depreciate at increased Mg^{2+} insertions/concentrations but contained different peak intensities at all Mg^{2+} concentrations. All XRD patterns for Mg_xTiO_2 had the rutile and brookite polymorphs dominance confirmed by the more intense peaks indexed at

2Θ values of about 31º and 55º respectively while other peaks were more broader. The $Mg_{0.15}TiO_2$ nanosheets system represented in Figure 5.48 had the highest peaks intensities at both high (2000 K) and low (0 K) temperatures which suggest that these systems contained more crystalline patterns than the amorphous patterns when compared to the remaining three Mg_xTiO_2 nanosheets, which then concluded this crystallinity trend i.e., $Mg_{0.15}TiO_2$>$Mg_{0.11}TiO_2$>$Mg_{0.19}TiO_2$>$Mg_{0.23}TiO_2$ where its reverse coincided for highest amorphous patterns in the system. It appears that higher Mg^{2+} intercalation had influenced more disordered patterns than crystalline patterns within nanosheets systems proven by their respective XRD patterns peaks in Figure 5.50 and Figure 5.49 which corresponded to the $Mg_{0.23}TiO_2$ and $Mg_{0.19}TiO_2$ nanosheet structures. Since the Mg_xTiO_2 nanosheet structure is quite a unique system which contains both crystalline and amorphous patterns concurrently show to be more reliable and dependable anode electrode due to its ability to accommodate more magnesium ions while preserving structural framework when exposed to higher (2000 K) and to lower (0 K) temperature conditions, hence being concluded as an excellent nano-architectured materials for future magnesium ion rechargeable battery materials.

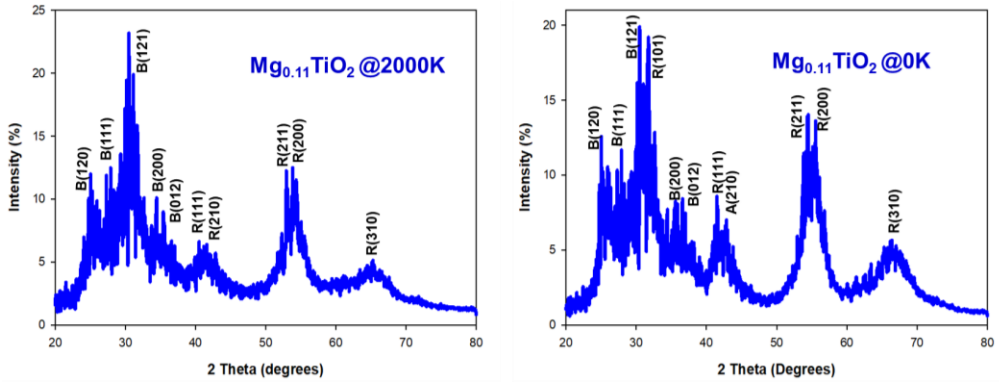

Figure 5.47: Illustrates simulated XRDs plots of $Mg_{0.11}TiO_2$ nanosheets at recrystalised (2000 K) and cooled (0 K) temperatures.

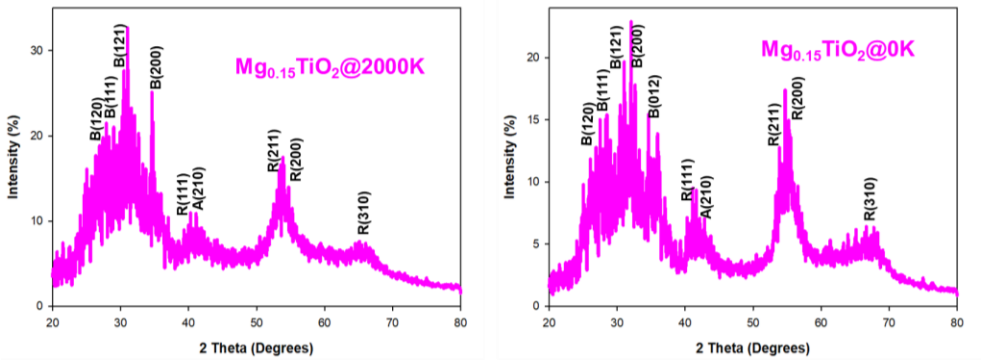

Figure 5.48: Illustrates simulated XRDs plots of $Mg_{0.15}TiO_2$ nanosheets at recrystalised (2000 K) and cooled (0 K) temperatures.

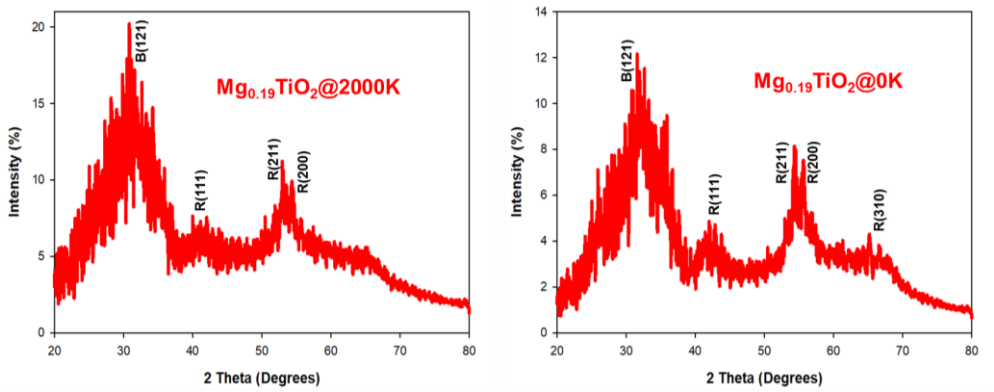

Figure 5.49: Illustrates simulated XRDs plots of $Mg_{0.19}TiO_2$ nanosheets at recrystalised (2000 K) and cooled (0 K) temperatures.

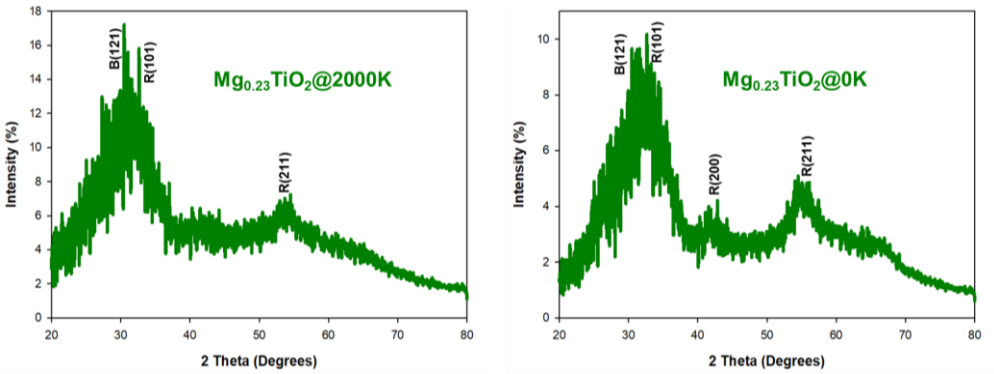

Figure 5.50: Illustrates simulated XRDs plots of $Mg_{0.23}TiO_2$ nanosheets at recrystalised (2000 K) and cooled (0 K) temperatures.

5.5. Diffusion Coefficients of Mg_xTiO_2 (x=0.11, 0.15, 0.18 and 0.23) nanostructures.

5.5.1. Mg_xTiO_2 Nanosphere

Diffusion Coefficient (DC) of Mg^{2+} inside $Mg_{0.11}TiO_2$, $Mg_{0.15}TiO_2$, $Mg_{0.19}TiO_2$ and $Mg_{0.23}TiO_2$ nanospheres had shown to be increasing with an increase in temperature from 100 K up until to 2000 K. Also DC decreased when more Mg^{2+} was intercalated into Mg_xTiO_2 nanospheres as illustrated in Figure 5.51. However, there appears to be significant overlap in Mg^{2+} diffusivity between the $Mg_{0.19}TiO_2$ and $Mg_{0.23}TiO_2$ nanospheres starting at 100 K until 1200 K and the Mg^{2+} diffusivity splitting occurred from 1200 to 2000 K where that of the $Mg_{0.23}TiO_2$ nanosphere exceeded that of $Mg_{0.19}TiO_2$. The highest DC in all Mg_xTiO_2 nanospheres followed the trend, $Mg_{0.11}TiO_2$ > $Mg_{0.15}TiO_2$ > $Mg_{0.23}TiO_2$ > $Mg_{0.19}TiO_2$ with maximum DC values of 7.9×10^{-9} m^2s^{-1} > 6.2×10^{-9} m^2s^{-1} > 3.9×10^{-9} m^2s^{-1} > 2.2×10^{-9} m^2s^{-1} respectively. The jump in DC at 1200 K as clearly noted for $Mg_{0.11}TiO_2$ nanospheres suggests an onset of structural transformation it is also a temperature where DC splitting appeared in $Mg_{0.23}TiO_2$ and $Mg_{0.19}TiO_2$ nanospheres. Such observations support our microstructural snapshots, RDFs, and XRD patterns that TiO_2 nanosphere had wide open tunnels and vacancies which influenced fast Mg^{2+} transportations at high temperatures.

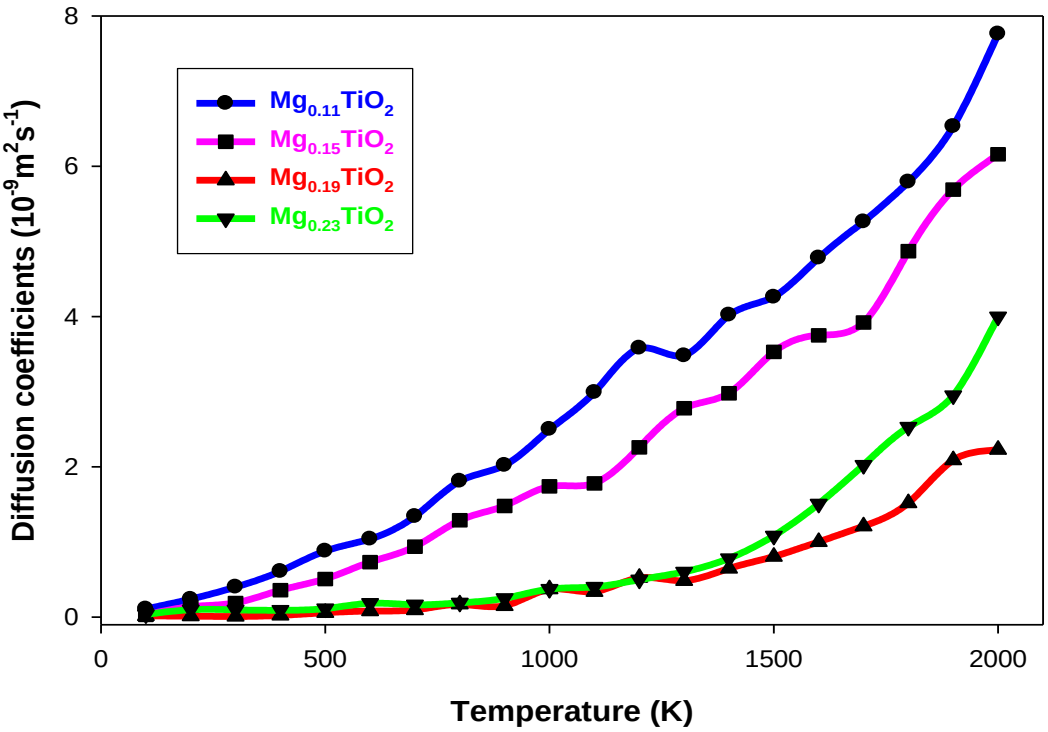

Figure 5.51: Represents graph of Mg^{2+} diffusion coefficients at varied temperatures inside Mg_xTiO_2 nanosphere with x = 0.11, 0.15, 0.19 and 0.23.

5.5.2. Mg_xTiO_2 Nanoporous

Figure 5.52 shows the diffusion coefficients of Mg^{2+} in nanoporous structures of $Mg_{0.11}TiO_2$, $Mg_{0.15}TiO_2$, $Mg_{0.19}TiO_2$ and $Mg_{0.23}TiO_2$ when heated from 100 to 2000 K. Mg^{2+} appears almost immobile between 100 K and 1200 K owing to zero Mg^{2+} DC at all concentrations. However, an abrupt onset of diffusion is observed above this temperature where the splitting of Mg^{2+} DC is also observed in $Mg_{0.11}TiO_2$, $Mg_{0.15}TiO_2$, $Mg_{0.19}TiO_2$ and $Mg_{0.23}TiO_2$ nanoporous systems. $Mg_{0.23}TiO_2$ depicted the highest DC right up to 2000 K and this concentration could not crystallise and remained amorphous. The variations in DC with temperature for Mg_xTiO_2 nanoporous architectures with x<0.23 were relatively lower and closer to each other, with that of $Mg_{0.19}TiO_2$ slightly enhanced. The microstructure of the latter included limited disorder that could improve DC compared to that of $Mg_{0.11}TiO_2$ and $Mg_{0.15}TiO_2$ concentrations.

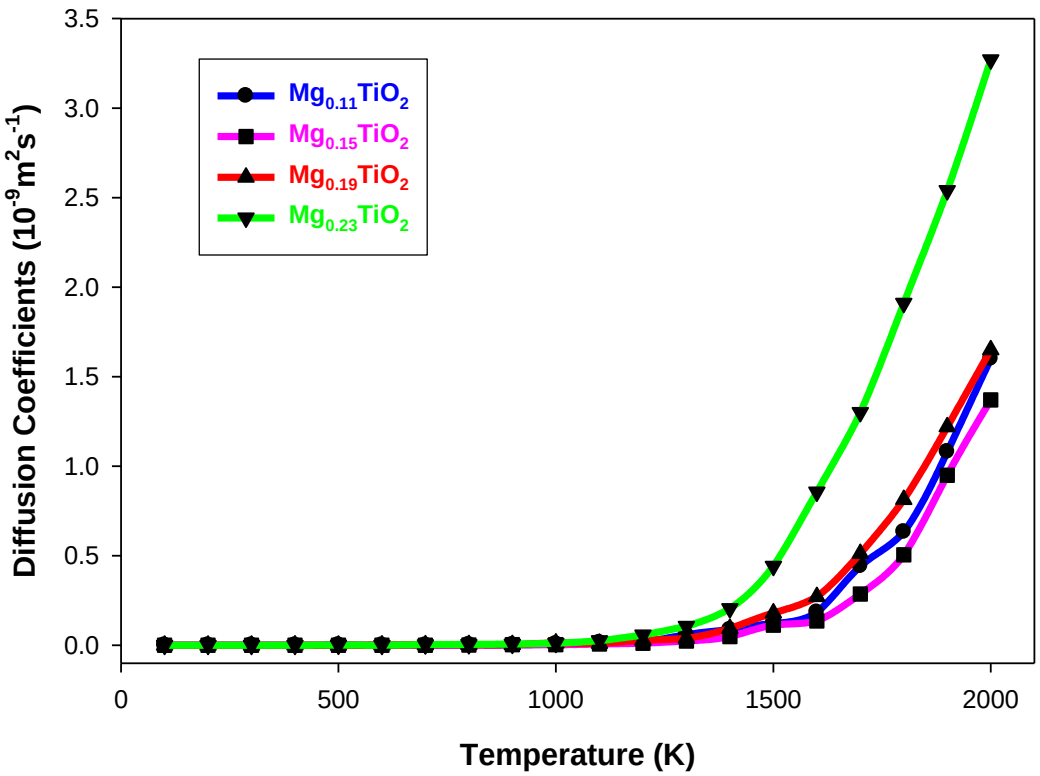

Figure 5.52: Represents Mg^{2+} diffusion coefficients at various temperatures in Mg_xTiO_2 nanoporous architecture with x = 0.11, 0.15, 0.19 and 0.23.

5.5.3. Mg_xTiO_2 Nanosheets

The mobility of Mg^{2+} in $Mg_{0.11}TiO_2$, $Mg_{0.15}TiO_2$, $Mg_{0.19}TiO_2$ and $Mg_{0.23}TiO_2$ nanosheets were also determined from the variation of its diffusion coefficient as function of temperature (Figure 5.53). As noted, Mg^{2+} in $Mg_{0.11}TiO_2$, $Mg_{0.15}TiO_2$, $Mg_{0.19}TiO_2$ and $Mg_{0.23}TiO_2$ nanosheets appears immobile at temperatures between 100 K and 1200 K. Above 1200 K the DC plots for all Mg_xTiO_2 nanosheets began splitting; for $Mg_{0.23}TiO_2$ and $Mg_{0.19}TiO_2$ nanosheets from 1200 K to 1300 K and the visibility of the $Mg_{0.11}TiO_2$ and $Mg_{0.15}TiO_2$ structures above 1400 K then towards 2000 K. The DC of Mg^{2+} in the nanosheets $Mg_{0.11}TiO_2$, $Mg_{0.15}TiO_2$, $Mg_{0.19}TiO_2$ and $Mg_{0.23}TiO_2$ started increasing with increasing temperatures starting from 1200 K towards 2000 K. The trend of DC of Mg^{2+} in various nanosheets were as follows; $Mg_{0.23}TiO_2 > Mg_{0.19}TiO_2 > Mg_{0.15}TiO_2 > Mg_{0.11}TiO_2$. Similarly, to nanoporous systems, the $Mg_{0.23}TiO_2$ nanosheets could not crystallise and remains amorphous. Those of lower Mg^{2+} content recrystallized, however, their microstructures depicted extended disorder or multigrain than the nanoporous systems, in addition to brookite and rutile tunnels. It can be surmised that Mg_xTiO_2 nanosheets have the capability of transporting more Mg^{2+} faster while maintaining structural integrity at high temperatures during charging and discharging.

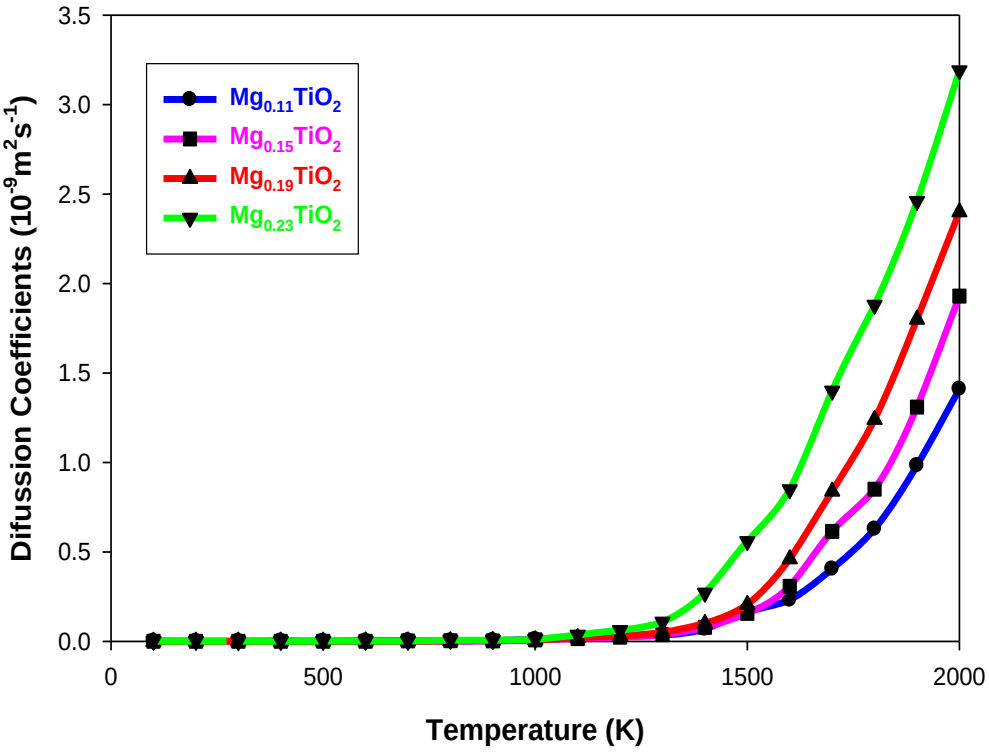

Figure 5.53: Represents Mg^{2+} diffusion coefficients at various temperatures in Mg_xTiO_2 nanosheets, with x = 0.11, 0.15, 0.19 and 0.23.

5.6. Activation Energies of Mg_xTiO_2 (x = 0.11, 0.15, 0.18 and 0.23) Nanoarchitectures.

Figures 5.54, 5.55 and 5.56 show the logarithm of diffusion coefficients vs. the inverse temperatures between 1000 and 2000 K in $Mg_{0.11}TiO_2$, $Mg_{0.15}TiO_2$, $Mg_{0.19}TiO_2$ and $Mg_{0.23}TiO_2$ nanosphere, nanoporous and nanosheets architectures, respectively.

5.6.1. Mg_xTiO_2 Nanosphere

The calculated activation energy in $Mg_{0.11}TiO_2$, $Mg_{0.15}TiO_2$, $Mg_{01.9}TiO_2$ and $Mg_{0.23}TiO_2$ nanospheres structures between 1000 K and 2000 K were determined to be 0.111eV, 0.08eV, 0.166 eV and 0.214eV respectively as shown in Figure 5.54. Hence, lnD was decreasing with an increase in inverse temperatures inside all four Mg_xTiO_2 nanosphere structures. The trend of activation energies in all Mg_xTiO_2 nanospheres is as follows; $Mg_{0.23}TiO_2$ > $Mg_{0.19}TiO_2$ > $Mg_{0.11}TiO_2$ > $Mg_{0.15}TiO_2$ so higher magnesiated TiO_2 nanospheres required more energy for Mg^{2+} to be activated and the $Mg_{0.15}TiO_2$ nanosphere required the least activation energy in the range 1.0 K^{-1} to 2.0 K^{-1}.

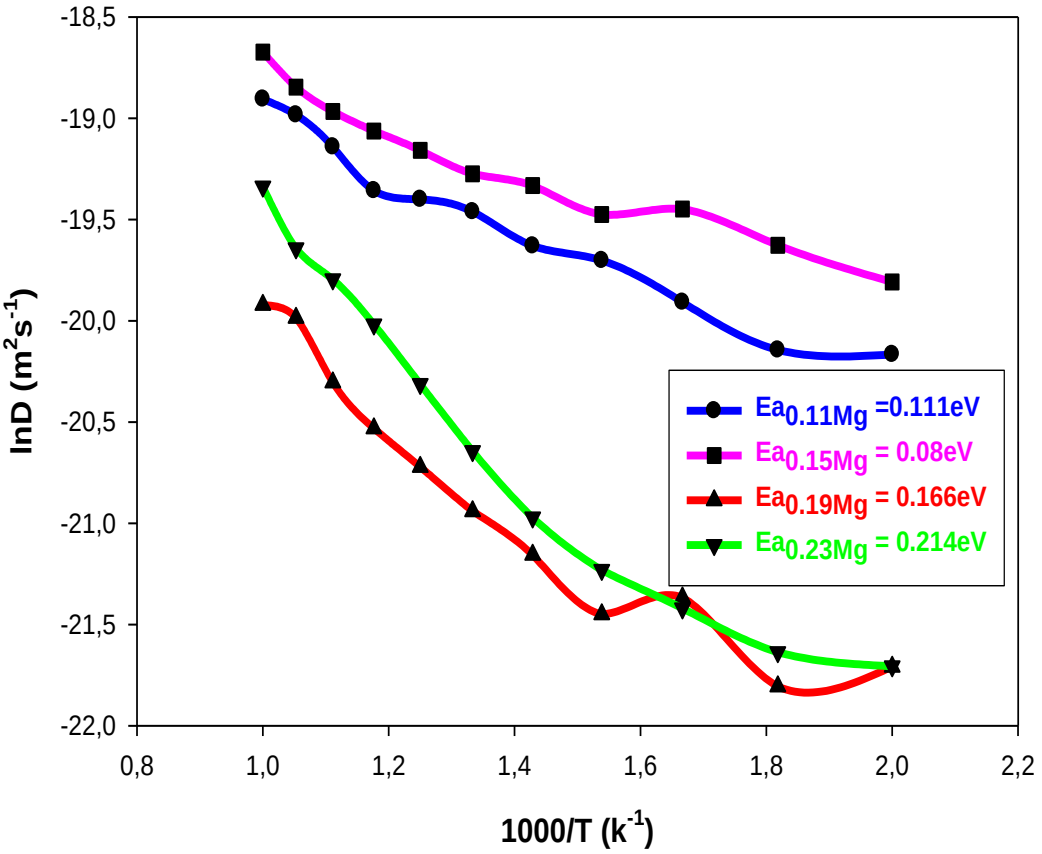

Figure 5.54: Yields activation energies of Mg^{2+} in Mg_xTiO_2 nanosphere with 0.11, 0.15, 0.19 and 0.23 Mg^{2+} concentrations on the same axis.

5.6.2. Mg_xTiO_2 Nanoporous

Figure 5.55 shows the calculated activation energies for Mg^{2+} in nanoporous structures of $Mg_{0.11}TiO_2$, $Mg_{0.15}TiO_2$, $Mg_{0.19}TiO_2$ and $Mg_{0.23}TiO_2$ reported as 0.468 eV, 0.531 eV, 0.468 eV and 0.509 eV respectively. Most lnD values in $Mg_{0.11}TiO_2$, $Mg_{0.15}TiO_2$, $Mg_{0.19}TiO_2$ nanoporous systems were equal and some almost close hence much overlapping of plots was observed between 1.0 and 1.4 K^{-1} this is where the lnD values of $Mg_{0.15}TiO_2$ got detached from the lnD values of $Mg_{0.11}TiO_2$ nanoporous graphs hence resulted in higher activation energies value of 0.53eV. The overlapping of graphs of $Mg_{0.11}TiO_2$ and $Mg_{0.19}TiO_2$ nanoporous systems between 1.0 and 2.0 contributed to an almost equal activation energy value of 0.467eV and 0.468eV, respectively. The trend of activation energies in all Mg_xTiO_2 nanoporous systems of Mg_xTiO_2 was found to be i.e., $Mg_{0.15}TiO_2$>$Mg_{0.23}TiO_2$>$Mg_{0.19}TiO_2$>$Mg_{0.11}TiO_2$ which then demonstrated that Mg^{2+} insertion and high temperatures did not really influence the activation energies but rather how well the porous channels were readily available for the fast Mg^{2+} diffusivity. Moreover, it seems that Mg_xTiO_2 nanoporous structures had similar and equal pathways of highly crystalline interstitial defects.

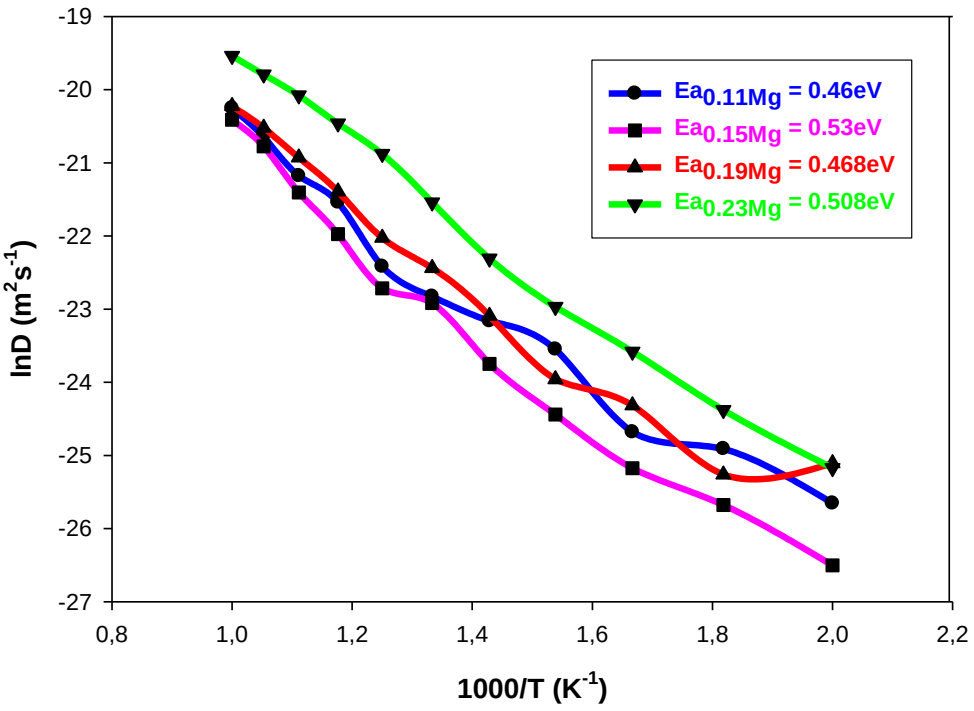

Figure 5.55: Represents graph yielding activation energies of Mg^{2+} inside nanoporous structure with 0.11, 0.15, 0.19 and 0.23 Mg^{2+} concentrations.

5.6.3. Mg_xTiO_2 Nanosheets

The Mg^{2+} in the $Mg_{0.11}TiO_2$, $Mg_{0.15}TiO_2$, $Mg_{0.19}TiO_2$ and $Mg_{0.23}TiO_2$ nanosheets required 0.438 eV, 0.490 eV, 0.515 eV and 0.496 eV respectively, to be fully activated as illustrated in Figure 5.56. The lnD values at 1.3,1.4 and 1.5 K^{-1} were almost equal in $Mg_{0.11}TiO_2$ and $Mg_{0.15}TiO_2$ nanosheets architectured structures hence they overlapped with activation energies of 0.438 eV and 0.490 eV. Moreover, the lowest lnD value of Mg^{2+} in $Mg_{0.19}TiO_2$ at 1.2 K^{-1} have influenced higher activation energy value more than that in $Mg_{0.11}TiO_2$, $Mg_{0.15}TiO_2$ and $Mg_{0.23}TiO_2$ nanosheets structures. The highest activation energies trend in all Mg_xTiO_2 nanosheet systems were found to be i.e., $Mg_{0.19}TiO_2$>$Mg_{0.23}TiO_2$>$Mg_{0.15}TiO_2$>$Mg_{0.11}TiO_2$ which confirms that $Mg_{0.19}TiO_2$ was indeed amorphous confirmed by their respective RDF and XRD patterns in Figure 5.38 and Figure 5.50 respectively. These almost equal values in activation energies clearly proves that the Mg_xTiO_2 nanosheets contained equal patterns of amorphous and crystalline polymorphs heated from 1.0 to 2.0 K^{-1} on each system.

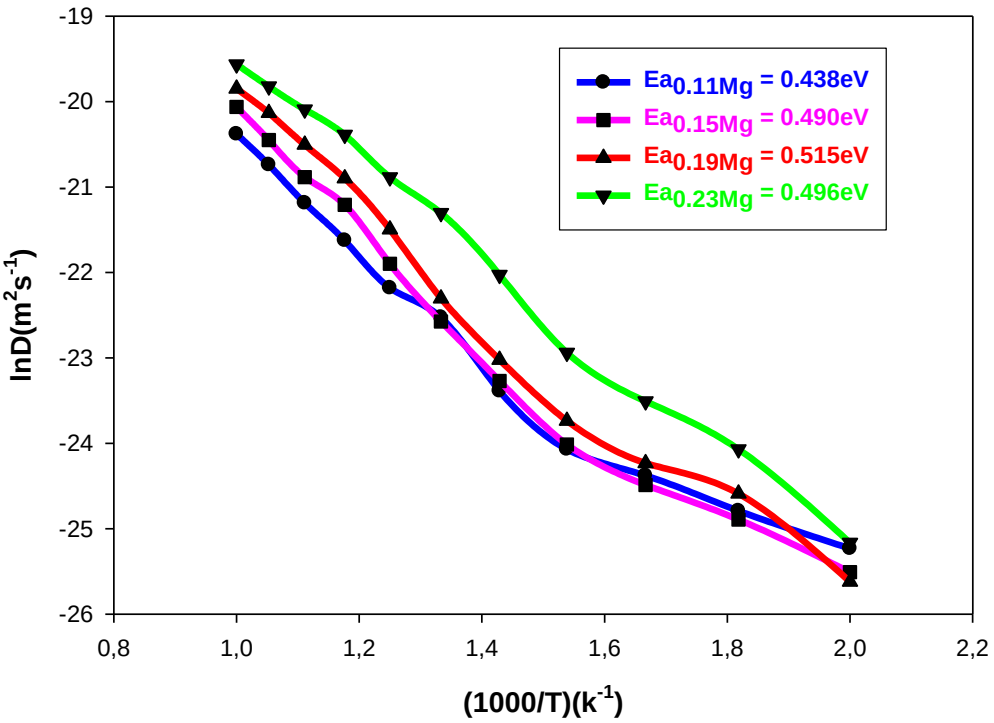

Figure 5.56: Represents graph yielding activation energies of Mg^{2+} inside nanosheets with 0.11, 0.15, 0.19 and 0.23 Mg^{2+} concentrations.

5.7. Summary

The magnesium ion was randomly inserted into amorphous TiO_2 nanosphere, nanoporous and nanosheets architectures with 0.11, 0.15, 0.19 and 0.23 Mg^{2+} concentrations that allowed recrystallisation at 2000 K and were then cooled from 1500 to 0 K at 500 K intervals and finally heated from 100 to 2000 K at 100 K intervals. The $Mg_{0.11}TiO_2$, $Mg_{0.15}TiO_2$, $Mg_{0.19}TiO_2$ $Mg_{0.23}TiO_2$ nanosphere, $Mg_{0.11}TiO_2$, $Mg_{0.15}TiO_2$, $Mg_{0.19}TiO_2$ nanoporous and $Mg_{0.11}TiO_2$, $Mg_{0.15}TiO_2$, $Mg_{0.19}TiO_2$ nanosheets successfully recrystallised which was confirmed by sharp peaks on their respective RDFs and XRDs patterns, while in $Mg_{0.23}TiO_2$ nanoporous and nanosheets nano-architectures no crystallisation occurred but rather complex disordered systems were observed. The microstructures of all crystallised nano-architectures have zigzag and straight tunnels reflecting brookite and rutile polymorphs and this was confirmed by XRD patterns. Nanoporous architectures also showed limited multigrain at higher Mg^{2+} concentrations, whilst those of nanosheets had complex defect arrangements in addition to brookite and rutile tunnels. On the whole, Mg^{2+} ions are well located within tunnels and distorted and defective portions of microstructures for all nano-architectures. Diffusion coefficients of Mg^{2+} commenced at lower temperatures in nanospheres, especially those with lower Mg concentrations. Related activation energies were also relatively low and increased with Mg^{2+} concentrations. However, in the nanoporous and nanosheet architectures, the Mg^{2+} DCs were almost zero below 1000 K and increased significantly above 1200 K with DC being highest in the heavily intercalated nanostructures. The activation energies for the latter two nano-architectures were in the range of 0.400 EV which is higher than in nanospheres, but comparable to those of the nanoporous Li-MnO_2 [Sayle 2016].

Chapter 6

Conclusions and Future Work

6.1 Conclusions

The evolution of lithium-ion batteries towards low-cost solutions for large-scale energy storage has influenced the prediction of complex alternative battery storage systems to those of Li^+ with other abundant elements on earth, with computational modeling methods guiding and complementing experimental studies. Sodium and magnesium batteries are among the most compelling alternatives to Li-ion batteries. Both have advantages in safety and resource abundance. Efforts to develop NIBs are aimed at lowering costs compared to Li-ion batteries, while magnesium can offer higher capacities due to its divalent ion. Both are far less explored than the technologically mature lithium-ion battery, but are attracting considerable interest as we approach the energy density limits of LIB. Sodium benefits from known electrochemical properties, and Na-containing analogs to LIB electrolytes and insertion hosts generally exhibit similar behavior. The major difference, however, is the size of the ions. The larger Na^+ ion puts more strain on the host lattice, leading to pulverization during cycling. Techniques to mitigate this effect are critical for long-term performance. On the other hand, the electrochemistry of magnesium is drastically different from that of lithium. The divalent atom exerts greater electrostatic forces, which generally slows the diffusion of Mg in the solid state, and the search for suitable Mg-compatible electrolytes has been more arduous. The rapidly growing field of research in MIBs has made considerable progress in the last 15 years since the first work on Chevrel by Aurbach [56]. However, other materials such as TiO_2, MnO_2, and $MgFeSiO_4$ are good candidates for future generations of magnesium batteries. In the current study a comparison on performance of lithiated, sodiated and magnesiated TiO_2 nano-architectures, i.e. nanosphere, nanoporous and nanosheet will be considered.

Since rechargeable battery performance involving TiO_2 anode strongly depends on its structural, transport and electrochemical properties, different TiO_2 nano-architectures were studied to explore its ability of hosting mono and multivalent intercalants. Consequently, the current study involved synthesizing M_xTiO_2 ($M = Li^+$, Na^+, and Mg^{2+}) ($x= 0.11, 0.15, 0.19$ and 0.23) nanospheres, nanoporous and nanosheets using the molecular dynamics based amorphization and recrystallization technique. Li^+, Na^+ and Mg^{2+} were inserted into the amorphous TiO_2 nanosphere, nanoporous and nanosheet architectures in order to produce Li_xTiO_2, Na_xTiO_2 and Mg_xTiO_2 ($x= 0.11, 0.15, 0.19$ and 0.23) for each nano-architecture. The amorphous nano-architectures were recrystallized by simulations at 2000 K and resultant structures were cooled from 1500 K to 0 K at intervals of 500 K. Finally all cooled nano-architectures at 0 K were analysed and subsequently heated to 2000 K at 100 K intervals. Amorphization and crystallisation simulation of Na_xTiO_2 and Mg_xTiO_2 nano-architectures were rather challenging and complex since their potentials were fitted for the first time in this study to allow nucleation growth formation from amorphous to crystalline phases to evolve unlike those of Li_xTiO_2 nano-architectures since their potentials were adopted from our previous study [151]. The TiO_2 nanospheres with 0.11, 0.15, 0.23 Li^+ and Na^+ concentrations had similar microstructural defects, present in pure TiO_2 and before Li insertion, characterised by dominant zigzag (brookite) and straight (rutile) tunnels

with empty vacancies and Li^+ and Na^+ filled vacancies with few Li^+ and Na^+ located on the surface. On the other hand, the TiO_2 nanospheres with 0.19 Li^+ and Na^+ concentrations remained amorphous after recrystallization. Surprisingly, the $Mg_{0.19}TiO_2$ nanosphere recrystallised successfully together with those of 0.11, 0.15 and 0.23 Mg^{2+} concentrations and their microstructures had zigzag (brookite), straight (rutile), tunnels with empty vacancies, Mg^{2+} filled vacancies and few Mg^{2+} were situated on the surfaces. The microstructures of the TiO_2 nanoporous structures, with 0.11, 0.15, 0.19 and 0.23 Li^+, Na^+ and Mg^{2+} concentrations, showed crystalline patterns of zigzag tunnels (brookite), straight (rutile) tunnels with empty vacancies and Li^+, Na^+ and Mg^{2+} filled vacancies after being recrystallised and cooled, except for the 0.23 Mg^{2+} concentration which showed highly disordered patterns.

The microstructures of TiO_2 nanosheets, with 0.11, 0.15, 0.19 and 0.23 Li^+, Na^+ and Mg^{2+} concentrations, had a mixture of disordered and crystalline (ordered) patterns of zigzag (brookite) and straight (rutile) tunnels with few empty vacancies, and some were filled with Li^+, Na^+ and Mg^{2+} where most Li^+ and Na^+ ions were situated around the surface of the microstructure except for TiO_2 nanosheets with 0.23 Mg^{2+} concentration which was amorphous, similar to that of $Mg_{0.23}TiO_2$ nanoporous architecture.

Ccomposites of this nature were previously synthesised by simulations for binary MnO_2 [176] and TiO_2 [151], ternary Li_xTiO_2 [24] and Li-Mn-O [163,182] and have also been reported in several experimental studies, such as interconnected anode electrode structures for α-TiO_2/β-$Li_{0.5}TiO_2$ and nano-sized α-TiO_2/ɣ-$LiTiO_2$ and were believed to exhibit high reversibility of lithium and promised better cycling performance compared to conventional pristine α-TiO_2/ conventional ɣ-$LiTiO_2$ [15, 34, 46, 68, 74 and 183] while not much work was reported on the intercalation of sodium and magnesium in nanosized TiO_2 experimentally. Consequently, simulated synthesis of Na_xTiO_2 and Mg_xTiO_2 nanosphere, nanoporous and nanosheets structures in this thesis, has laid a foundation in exploring new alternative materials to those of lithium for optimising performance on TiO_2 nano architecture, based on other earth abundant mobile ions, at extreme temperatures in the future.

All resulting TiO_2 nanostructures were further characterised and analyzed by their respective radial distribution functions (RDFs), simulated X-ray diffraction (XRD) patterns, diffusion coefficients and activation energies to study the effects of increased lithiation, sodiation, and magnesiation at various temperatures. The simulated Ti-O radial distribution functions were utilised to confirm the extent of crystallinity of nano-architectures after recrystallisation, cooling, and heating. In addition, simulated X-ray diffraction (XRD) patterns were employed to determine and compare crystallinity at low and elevated temperatures. Furthermore, they depicted rutile and brookite polymorphs in Li_xTiO_2, Na_xTiO_2 and Mg_xTiO_2, shown by our simulated microstructures and observed in previous experimental and simulated studies of Li_xTiO_2; which suggests possibility of easy and fast Li^+, Na^+ and Mg^{2+} ion passage in the current study. The verification of Li_xTiO_2 polymorphs noted from snapshots of microstructures by XRD methods, were previously reported [151] and is being extended to Na_xTiO_2 and Mg_xTiO_2 in the current study. The invocation of the amorphization and recrystallization method on all lithiated, sodiated, and magnesiated TiO_2

nanomaterials at various temperatures produced interconnected layered composites. Microstructural visuals of Li_xTiO_2 and Na_xTiO_2 nanosphere structures with x = 0.11, 0.15 and 0.23, illustrated similar storage properties of crystalline TiO_6 octahedral layers, with most lithium and sodium ions located within tunnels and channels, while other lithium and sodium ions were thrown to the outer surfaces and away from the structure. Furthermore, the visuals of the $Li_{0.19}TiO_2$ and $Na_{0.19}TiO_2$ nanospheres remained amorphous, after crystallisation attempts, mainly due to frustrated coordination of the TiO_2 frameworks; hence no well tunnelled microstructures were formed. Visuals of the Mg_xTiO_2 nanosphere with x= 0.11, 0.15, 0.19 and 0.23 indicated high storage properties better than those intercalated with high Li and Na concentrations, because all Mg atoms in the TiO_2 nanosphere were retained within octahedral tunnels, illustrating that it has excellent cycle and recharge capabilities.

These observations were also confirmed by McCoil et al. who intercalated Mg^{2+} in anatase TiO_2 through a DFT study [22]. Conversely, in $Mg_{0.23}TiO_2$ nanoporous and nanosheet architectures remained amorphous after crystallisation attempts, influenced by frustrated coordination of Mg, Ti, and O atoms due to high Mg concentrations inside whereas the nanoporous and nanosheets of Mg_xTiO_2 with x = 0.11 ,0.15 and 0.19 systems crystallised well. This observation shows that insertion of Mg^{2+} below 0.23 retains crystalline patterns while insertion of Mg^{2+} above 0.23 caused frustration in the T-O arrangements, which led to structural deformation. Hence the TiO_2 nanosphere indicated great structural stability for storing more Mg ions better than storing more Li and Na ions. Furthermore, TiO_2 nanoporous and nanosheets indicated great structural stability for storing more Li and Na ions better than Mg atoms. So, Li^+ and Na^+ created unstable coordination inside the TiO_2 nanosphere structures because of the closeness of the O^{2-} anions hence that is why Mg^{2+} did not penalise the TiO_2 nanosphere [48].

In the case of Li transport, for different nano-architectures, diffusion coefficients (DCs) for most Li concentrations were predominantly near zero at low temperatures and increased gradually above 500 K and significantly at higher temperatures beyond 1000 K. DCs of higher Li concentration nano-architectures tend to be highest. On the contrary, the diffusion coefficient of the amorphous $Li_{0.19}TiO_2$ nanosphere is elevated at low temperatures, however, it is exceeded by those of other concentrations at higher temperatures. On the whole the activation energies (shown in Table 6.1) of Li in TiO_2 nanosphere, nanoporous and nanosheet structures, in appropriate temperature range, were consistent with observed transport properties. In particular, the lowest activation energy for the amorphous $Li_{0.19}TiO_2$ nanosphere concurs with non-zero DC at lower temperatures. On Na transport in various TiO_2 nano-architectures, diffusion coefficients for most Na concentrations were predominantly near zero at low temperatures, except for the $Na_{0.23}TiO_2$ (associated explanation for such deviant behaviour is not yet available). Diffusion coefficients subsequently increased gradually above 500 K to substantial at higher temperatures, with DCs of higher Na concentrations in different nano-architectures tending to be highest; in particular the DC of the amorphous $Na_{0.19}TiO_2$ which was slightly higher than other crystalline $Na_{0x}TiO_2$. The activation energy of the nanosphere with the highest Na concentration ($Na_{0.23}TiO_2$) was low, consistent with the trend of non-zero diffusion coefficients at low

temperatures. The AEs of nanoporous structures at different Na contents were equivalent and related DCs almost overlap in the 500 to 1000 K range. In the case of nanosheets AEs are also almost equal for all Na_xTiO_2 with that of the $Na_{0.23}TiO_2$ (highest Na concentration) being highest resulting in a slightly lower diffusivity, except at very high temperatures.

These results provide insights and an understanding on how much such TiO_2 nano-architectures can enable operations of sodium ion batteries. Non-zero diffusion coefficients of Mg^{2+} commenced at lower temperatures in nanospheres, especially those with lower Mg concentrations. Related activation energies were also relatively low and increased with Mg^{2+} concentrations. However, in the nanoporous and nanosheet architectures, the Mg^{2+} DCs were almost zero below 1000 K and increased significantly above 1200 K with DC being highest in the heavily intercalated nanostructures. The activation energies for the latter two nano-architectures were in the range of 0.40 eV which is higher than in nanospheres, but comparable to those of the nanoporous Li-MnO_2 reported by Sayle et al [182].

Table 5: Calculated activation energies (AE) of M_xTiO_2 (M = Li, Na and Mg) nano-architectures at different ion concentrations (x = 0.11, 0.15, 0.19 and 0.23)

AE for Nanosphere

Ions	0.11	0.15	0.19	0.23
Li^+	0.25eV	0.29eV	0.18eV	0.37eV
Na^+	0.25eV	0.209eV	0.248eV	0.190eV
Mg^{2+}	0.111eV	0.08eV	0.166eV	0.214eV

AE for Nanoporous

Ions	0.11	0.15	0.19	0.23
Li^+	0.16eV	0.20eV	0.18eV	0.18eV
Na^+	0.19ev	0.215ev	0.222eV	0.224eV
Mg^{2+}	0.46eV	0.53eV	0.468eV	0.508eV

AE for Nanosheets

Ions	0.11	0.15	0.19	0.23
Li^+	0.20eV	0.19eV	0.22eV	0.23eV
Na^+	0.22eV	0.217eV	0.23eV	0.28eV
Mg^{2+}	0.438eV	0.490eV	0.515eV	0.496eV

AE for Nanoporous Li-MnO_2 ~ 0.40 eV: Sayle et al. [182]

Generally calculated maximum diffusion coefficients in the current study extend from 3.5 x 10^{-9} to 250 x10^{-9} m^2s^{-1} in the temperature range 100 – 2000 K. On matching maximum diffusion coefficients of Li, Na and Mg in TiO_2 nano-architectures, it is apparent that they are all highest in nanospheres with DC_{Li} > DC_{Na} > DC_{Mg}. On comparing magnitudes of DCs in different nano-architectures the following trend

emerges; for the monovalent Li and Na mobile ions $DC_{Sphere} \sim 5DC_{Porous} \sim 3DC_{Sheet}$ and for the divalent Mg mobile ion $DC_{Sphere} \sim 2.5DC_{Porous} \sim 2.5DC_{Sheet}$. On the other hand, activation energies for Li^+, Na^+, and Mg^{2+} in TiO_2 nano-architectures range from 0.080 to 0.53 eV between 1.0 K^{-1} and 2.0 K^{-1}.; consistent with those found by Yuwono et al [186] and Olson et al [187]. All calculated activation energies (AE) of Li^+, Na^+ and Mg^{2+} in the TiO_2 nanoarchitectures, at all ion concentrations, were determined in the range of inverse temperatures comparable to those calculated by Sayle et al for Li-MnO_2 [182] which served as a guideline of obtaining reliable AE values.

In conclusion, the objective of the study was achieved and has provided valuable insights on simulated synthesis and characterisation of complex ternary Li-TiO_2, Na-TiO_2 and Mg-TiO_2 composite nano-architectures, the impact of their lithiation, sodiation and magnesiation (charging) on structural aspects, details on ion transport and potential barriers. Consequently, the findings can be used to produce reliable future battery materials as alternate to the current utilised batteries, since the nature of microstructures, diffusion coefficients and activation energies contribute significantly to operations of lithium, sodium, and magnesium-ion batteries. More importantly, the electrochemical performance of Li_xTiO_2, Na_xTiO_2 and Mg_xTiO_2 nanosphere, nanoporous and nanosheets materials are strongly influenced by the thermodynamics, crystallographic, chemistries, phase stability and ion concentrations (intercalant orderings) storage properties in the battery environment hence the necessity to properly understand atomic activity and arrangement in the active sites of the electrode materials [185]

6.2. Future Work

1. Further studies on the factors that contributed towards the non-crystalline structures of $Li_{0.19}TiO_2$ nanosphere, $Na_{0.23}TiO_2$ nanoporous and the transformed $Mg_{0.23}TiO_2$ nanoporous and nanosheet structures to try an improve crystals formation using a different available computational approach of atomistic scale simulations will be explored.
2. Since molecular modelling curve paths for materials prediction, experimental research could be performed on all simulated systems in a chemical laboratory to complement all insights and findings for practical implementation towards commercialisation for future purposes.

6.2. References

[1] M. Armand and J.M Tarascon., Building better batteries., 2008, Nature., **451**, 651-657.

[2] J. B. Goodenough., Electrochemical energy storage in a sustainable modern society., Energy Environ. Sci., 2014, **7,** 141- 8.

[3] M. M. Thackeray, C. Wolverton and E.D. Isaacs., Electrical energy storage for transportation-approaching the limits of and going beyond lithium-ion batteries., 2012, Energy Environ. Sci., **5**, 7854-7863.

[4] H. B. Scrosati. K.M. Abraham,W.A van Schalkwijk, and J. Hassoun., Lithium Batteries: Advanced Technologies and Applications., 2013.,Hoboken, New Jersey : John Wiley & Sons, Inc.

[5] C. Jia, F. Pan, Y. G. Zhu, Q. Huang, L. Lu, and Q. Wang, High–energy density nonaqueous all redox flow lithium battery enabled with a polymeric membrane, 2015, Scie. Adv., **1**, 1-7.

[6] J. M. Tarascon and M. Armand., Issues and challenges facing rechargeable lithium batteries, 2011, Nat., **414**, 359-367.

[7] Z. Yang, J. Zhang, M. C. W. Kintner-Meyer, X. Lu, D. Choi, J. P. Lemmon and J. Liu., Electrochemical Energy Storage for Green Grid., 2011, Chem. Rev., **111**, 3577-3613.

[8] C. Zhang, H. B. Wu, C. Yuan, Z. Guo and X. W. Lou., Confining sulfur in double-shelled hollow carbon spheres for lithium-sulfur batteries., 2012, Angew. Chem. Int. Ed., **51 ,** 9592 - 9595.

[9] W. Tang, Y. Zhu, Y. Hou, L. Liu, Y. Wu, K. P. Loh, H. Zhang and K. Zhu., Aqueous rechargeable lithium batteries as an energy storage system of superfast charging., 2013, Energy Environ. Sci., **6** , 2093-2104.

[10] H. Wang, Y. Yang, Y. Liang, L.-F. Cui, H. Sanchez Casalongue, Y. Li, G. Hong, Y. Cui and H. Dai., Accurate surface control of core-shell structured $LiMn_{0.5}Fe_{0.5}PO_4$@C for improved battery perfomance., 2011, Angew. Chem., **123**, 7502-7506.

[11] Y. Wang, Y. Wang, E. Hosono, K. Wang, H. Zhou, The Design of a $LiFePO_4$/Carbon Nanocomposite With a Core–Shell Structure and Its Synthesis by an In Situ Polymerization Restriction Method., 2008, Angew. Chem. Int. Ed.,**47**, 7461-7465.

[12] W. Tang, Y. Hou, F. Wang, L. Liu, Y. Wu and K. Zhu, $LiMn_2O_4$ Nanotube as Cathode Material of Second-Level Charge Capability for Aqueous Rechargeable Batteries,2013, Nano. Lett, **13**, 2036 - 2040.

[13] C. Jiang and J. Zhang., Nanoengineering Titania for High Rate Lithium Storage: A Review., 2013, J. Mater. Sci.Technol., **29**, 97-122.

[14] M. Fehse and E. Ventosa, Is TiO_2(B) the Future of Titanium-Based Battery Materials.,2015, Chem.Plus.Chem., **80**. 785–795.

[15] R. J. Cava, D. W. Murphy, S. Zahurak, A. Santoro and R. S. Roth., The crystal structures of the lithium-inserted metal oxides $Li_{0.5}TiO_2$ anatase, $LiTi_2O_4$ spinel, and $Li_2Ti_2O_4$., 1984, J. Solid. State. Chem., **53**, 64–75.

[16] R. van de Krol., In Situ X-Ray Diffraction of Lithium Intercalation in Nanostructured., 1999, J. Electrochem. Soc., **146**, 3150 - 3154.

[17] H. Pan, Y.-S. Hu and L. Chen., Room-temperature stationary sodium-ion batteries for large-scale electric energy storage.,2013, Energy Environ. Sci., **6**, 2338-2360.

[18] S. Wang, P. Zhan, Y. Yuan, K. Jiao, H. Jiao and S. Jiao., Update on anode materials for Na-ion batteries., 2015, J. Mater. Chem. A., **3**, 16528-16534.

[19] V. Palomares, P. Serras, I. Villaluenga, K. B. Hueso, J. Carretero-Gonz´alez and T. Rojo., Na-ion batteries, recent advances and present challenges to become low cost energy storage systems.,2012, Energy Environ. Sci., **5**, 5884-5901.

[20] H. Xiong, M. D. Slater, M. Balasubramanian, C. S. Johnson and T. Rajh., Amorphous TiO_2 Nanotube Anode for Rechargeable Sodium Ion Batteries., 2011, J. Phys. Chem. Lett., **2**, 2560-2565.

[21] Y. Xu, E. M. Lotfabad, H. Wang, B. Farbod, Z. Xu, A. Kohandehghan and D. Mitlin., Nanocrystalline anatase TiO_2: a new anode material for rechargeable sodium ion batteries., 2013, Chem. Commun., **49**, 8973-8975.

[22] K. Mccoll and F. Cora., Mg^{2+} storage and mobility in anatase TiO_2: the role of frustrated coordination., 2019, J. Mater. Chem. A, **7**, 3704-3713.

[23] B. Zhao, B. Lin, S. Zhang and C. Deng, Self-assembled wafer-like porous $NaTi_2(PO_4)_3$ decorated with hierarchical carbon as a high-rate anode for aqueous rechargeable sodium batteries., 2015, J. Mater. Chem. A, **3**, 12089-12096.

[24] B.N. Rikhotso, M.G. Matshaba.D.C. Sayle and P.E. Ngoepe.,Simulated synthesis and structure of Li_xTiO_2 nanosheets as anode material., 2020, Opt. Mat., **102**, 109831-109835.

[25] Q. F. Zhang, E. Uchaker, S. L. Candelaria and G. Z. Cao., Nanomaterials for energy conversion and storage., 2013, Chem. Soc. Rev., **42**, 3127-3171.

[26] J. Tian, Z. H. Zhao, A. Kumar, R. I. Boughton and H. Liu., Recent progress in design, synthesis, and applications of one-dimensional TiO_2 nanostructured surface heterostructures: a review., 2014, Chem. Soc. Rev., **43**, 6920-6937.

[27] P. Bottke,Y.Ren,I Hanzu,P.G Bruce, M. Wilkening., Li ion dynamics in TiO_2 anode materials with an ordered hierarchical pore structure - insights from ex situ NMR," Phys. Chem. Chem. Phys., **16**, 1894-1901.

[28] D. Deng, M. G. Kim, J. Y. Lee and J. Cho., Green energy storage materials: Nanostructured TiO_2 and Sn-based anodes for lithium-ion batteries. 2009. Energy and Environmental Science., Energy Environ. Sci., **2**. 818-837.

[29] Y. Li, E.J. Fuller, S. Asapu, S. Argawal, T. Kurita, J.J. Yang and A.A Talin Low-Voltage, CMOS-Free Synaptic Memory Based on Li_XTiO_2 Redox Transistors, 2019, ACS Appl. Mater. Interfaces., **11**, 38982-38992.

[30] U. Farooq, F. Ahmed, S. A. Pervez, S. Rehman, M. A. Pope, M. Fichtner, E.P. L. Roberts, A stable TiO_2–graphene nanocomposite anode with high rate capability for lithium-ion batteries, 2020, RSC Adv., **10**, 29975-29982.

[31] J. A. Yuwono, P. Burr, C. Galvin and A. Linnon, Atomistic Insights into Lithium Storage Mechanisms in Anatase, Rutile, and Amorphous TiO_2 Electrodes, 2021, ACS. Appl. Mater. Interfaces., **13**, 1791-1806.

[32] H. Lindstr¨om, S. S¨odergren, A. Solbrand, H. Rensmo, J. Hjelm, A. Hagfeldt and S.-E. Lindquist., Li^+ Ion Insertion in TiO_2 (Anatase). 2. Voltammetry on Nanoporous Films., 1997, J. Phys. Chem. B.,**101**, 7717-7722.

[33] Z. Y. Weng, H. Guo, X. M. Liu, S. L. Wu, K. W. K. Yeung and P. K. Chu., Nanostructured TiO_2 for energy conversion and storage., 2013, RSC Adv., **3**, 24758-24775.

[34] N. D. Petkovich, S. G. Rudisill, B. E. Wilson, A. Mukherjee and A. Stein., Control of TiO_2 grain size and positioning in three-dimensionally ordered macroporous TiO_2/C composite anodes for lithium ion batteries., 2014, Inorg. Chem., **53**,1100-1112.

[35] W. Li, Z. X. Wu, J. X. Wang, A. A. Elzatahry and D. Y. Zhao., A Perspective on Mesoporous TiO_2 Materials, 2014, Chem. Mater., **26**, 287-298.

[36] J. F. Peters, C. Peña, W. M Alexandra., Exploring the Economic Potential of Sodium-Ion Batteries., 2019, Batteries., **5**, 1-15.

[37] K.M Abraham., How Comparable are Sodium-Ion Batteries to Lithium-Ion Counterparts., 2020, ACS. Ener. Letters., **5**, 3544-3547.

[38] S.-W. Kim, D.-H. Seo, X. Ma, G. Ceder and K. Kang., Electrode Materials for Rechargeable Sodium-Ion Batteries: Potential Alternatives to Current Lithium-Ion Batteries., 2012, Adv.Energy Mater, **2**, 710-721.

[39] H. Pan, Y.-S. Hu and L. Chen., Room-temperature stationary sodium-ion batteries for large-scale electric energy storage., 2013, Energy Environ. Sci., **6**, 2338-2360.

[40] M. Dahbi, N. Yabuuchi, K. Kubota, K. Tokiwa and S. Komaba, Negative electrodes for Na-ion batteries., 2014, Phys. Chem. Chem. Phys.,**16**,15007-15028.

[41] S. P. Ong, V. L. Chevrier, G. Hautier, A. Jain, C. Moore,S, Kim, X. Ma and G. Ceder., Voltage, stability and diffusion barrier differences between sodium-ion and lithium-ion intercalation materials., 2011, Energy Environ. Sci., **4**, 3680-3688.

[42] S. Komaba, W. Murata, T. Ishikawa, N. Yabuuchi, T. Ozeki,T. Nakayama, A. Ogata, K. Gotoh and K. Fujiwara., Electrochemical Na Insertion and Solid Electrolyte Interphase for Hard-Carbon Electrodes and Application to Na-Ion Batteries, 2011, Adv.Funct. Mater., **21**, 3859-3867.

[43] A. Darwiche, C. Marino, M. T. Sougrati, B. Fraisse, L. Stievano and L. Monconduit, Redox reaction of Sn-polyacrylate electrodes in aprotic Na cell., J. Am. Chem. Soc.,**134**, 20805-20811.

[44] Y. Xu, E. Memarzadeh Lotfabad, H. Wang, B. Farbod, Z. Xu, A. Kohandehghan and D. Mitlin., Nanocrystalline anatase TiO_2: a new anode material for rechargeable sodium ion batteries., 2013, Chem. Commun., **49**, 8973 - 8975.

[45] A. Rudola, K. Saravanan, C. W. Mason and P. Balaya, $Na_2Ti_3O_7$: an intercalation based anode for sodium-ion battery applications, 2013, J. Mater. Chem. A, **1**, 2653-2662, 2013.

[46] P. Senguttuvan and M. R. Palac´ın, $Na_2Ti_3O_7$: Lowest Voltage Ever Reported Oxide Insertion Electrode for Sodium Ion Batteries, 2011, Chem. Mater,, **23**, 4109 - 4111.

[47] Y. Sun, L. Zhao, H. Pan, X. Lu, L. Gu, Y.-S. Hu, H. Li, M. Armand, Y. Ikuhara, L. Chen and X. Huang., Direct atomic-scale confirmation of three-phase storage mechanism in $Li_4Ti_5O_{12}$ anodes for room-temperature sodium-ion batteries, 2013,Nat. Commun., **4**,1870-1880.

[48] Y. Wang, X. Yu, S. Xu, J. Bai, R. Xiao, Y.-S. Hu, H. Li, X.-Q. Yang, L. Chen and X. Huang, A zero-strain layered metal oxide as the negative electrode for long-life sodium-ion batteries,2013, Nat. Commun., **4**, 2365 - 2373.

[49] A. Mazzaz, C. Delmas and P. Hagenmuller., A study of the Na_xTiO_2 system by electrochemical deintercalation, 1983, J. lncl. Phen., 1, 45-51.

[50] X. Ma, H. Chen and G. Ceder, Electrochemical Properties of Monoclinic $NaMnO_2$, 2011, J. Electrochem. Soc., **158**, A1307-A1312.

[51] P. Vassilaras, X. Ma, X. Li and G. Ceder., Electrochemical Properties of Monoclinic $NaNiO_2$., 2012, J. Electrochem. Soc.,**160**, A207-A211.

[52] J.-J. Braconnier, C. Delmas and P. Hagenmuller., Etude par desintercalation electrochimique des systemes Na_xCrO_2 et Na_xNiO_2., 1982, Mater. Res. Bull., **17**, 993-1000.

[53] A. Mendiboure, C. Delmas and P. Hagenmuller., Electrochemical intercalation and deintercalation of NaxMnO2 bronzes, 1985, J. Solid Statem.Chem., **57**, 323-331.

[54] U.S. Department of Energy., Battery Storage in the United States: An Update on Market Trends.,U.S. Energy Information Administration., USA, 2021.

[55] M. Walter, M. V. Kovalenko, K. V. Kravchyk., Challenges and benefits of post-lithium-ion batteries., 2020, New J. Chem., **44**, 1677-1683.

[56] H. D. Yoo, I. Shterenberg, Y. Gofer, G. Gershinsky, N. Pour and D. Aurbach, Mg rechargeable batteries: an on-going challenge., 2013, Energy Environ. Sci., **6**, 2265-2279.

[57] P. Canepa, G. S. Gautam, D. C. Hannah, R. Malik, M. Liu, K. G. Gallagher, K. A. Persson and G. Ceder., Odyssey of Multivalent Cathode Materials: Open Questions and Future Challenges.,2017, Chem. Rev., **117**, 4287-4341.

[58] J. Muldoon, C. B. Bucur and T. Gregory., ervent Hype behind Magnesium Batteries: An Open Call to Synthetic Chemists—Electrolytes and Cathodes Needed., Angew. Chem. Int. Ed., 2017, **56**,12064-12084.

[59] W. Xu, J. Wang, F. Ding, X. Chen, E. Nasybulin, Y. Zhang and J.-G. Zhang., Liithium metal anodes for rechargeable batteries, 2014, Energy Environ. Sci., **7**,513–537.

[60] J. O. Besenhard and M. Winter., Advances in battery technology:Rechargeable magnesium batteries and Novel Negative-electrode materials for Lithium ion batteries,, 2002, Chem.Phys.Chem., **3**, 155-159.

[61] H. wang, P. Senguttuvan, D. L. Proffit, B. Pan, C. Liao, A. K. Bureell, J.T. Vaughey and B. Key., Formation of MgO during chemical magnesiation of Mg-Ion Battery Mateerials.,2015, ECS Elect.Lett., **4**, A90-A93.

[62] Z. Rong, R. Malik, P. Canepa, G. S. Gautam, M. Liu, A. Jain, K. Persson and G. Ceder., Materials Design rules for Multivalent Ion Mobility in intercaltion structures.,2015, Chem. Mater., **27**, 6016-6021.

[63] D. Aurbach, Z. Lu, A. Schechter, Y. Gofer, H. Gizbar, R. Turgeman, Y. Cohen, M. Moshkovich and E. Levi., Prototype systems for rechargeable magnesium batteries., 2000, Nat., **407**, 724-727.

[64] V. Aravindan, Y. S. Lee, R. Yazami and S. Madhavi., TiO_2 polymorphs in rocking chair Li-ion batteries., 2015, Mater.Today., **18**, 345-351.

[65] Y. Liu and Y. Yang., Resent Progress of TiO_2-Based Anodes for Li-ion Batteries., 2016, J. Nanomater., **2016**, 1-15.

[66] Y. Zhang, Y. Tang, W. Li and X. Chen., Nanostructured TiO2-Based Anode Materials for high-performance rechargeable lithium ion Batteries., 2016, Chem.Nano.Mat,, **2**, 764-775.

[67] L. Kavan, M. Kalb´aˇc, M. Zukalov´a, I. Exnar, V. Lorenzen, R. Nesper and M. Graetzel., Lithium storage in nanostructured TiO2 made by hydrothermal growth., 2004, Chem. Mater., **16**, 477-485.

[68] Y. Ren, Z. Liu, F. Pourpoint, A. R. Armstrong, C. P. Grey, and P. G. Bruce., Nanoparticulate TiO_2(B): An anode for Lithium -ion Batteries., 2012, Angew. Chem., Int. Ed., **51**, 2164-2167.

[69] D. Su, S. Dou and G. Wang., Anatase TiO_2: Better Anode Material Than Amorphous and Rutile Phases of TiO_2 for Na-Ion Batteries., 2015, Chem. Mater., **27**, 6022-6029.

[70] L.F. Nazar, G. Goward, F. Leroux, M. Duncan, H. Huang, T. Kerr, J. Gaubicher., Nanostructured materials for energy storage., 2001, Inter. J. of Inor. Mater., **3**,191-200.

[71] T. Djenizian, I. Hanzu and P. Knauth., Nanostructured negative electrodes based on titania for Li-ion microbatteries., 2011, J. Mater. Chem., **21**, 9925-9937.

[72] P. Poizot,S. Laruelle,S. Grugeon,L. Dupont and J-M. Tarascon., Searching for new anode materials for the Li-ion technology: time to deviate from the usual path.,2001, J.of Power. Sous., **97-98**, 235-239.

[73] Y.-S. Hu, L, Kienle, Y.-G. Guo and J. Maier., High Lithium Electroactivity of Nanometer-Sized Rutile TiO_2. Advanced Materials., 2006, Adv.Mat.,**18**,1421-1426.

[74] M.A Reddy, M. S. Kishore, V. Pralong and B. Raveau., Room temperature synthesis and Li insertion into nanocrystalline rutile TiO_2., 2006, Electrochem. Commun., **8**,1299-1303.

[75] E. Baudrin, S. Cassaignon, M. Koelsch and J-M. Tarascon., Structural evolution during the reaction of Li with nano-sized rutile type TiO_2 at room temperature., 2007, Electroche. Commun,, **9**, 337-342.

[76] S Bach, J.P. Pereira-Ramos and P. Willman., Investigation of lithium diffusion in nano-sized rutile TiO_2 by impedance spectroscopy, 2010, Electrochimica Acta, Vols., **55**, 4952-4959.

[77] P. G Bruce, B. Scrosati and J.M Tarascon., Nanomaterials for Rechargeable Lithium Batteries., Angew., 2008, Chem. Inte. Ed., **47**, 2930-2946.

[78] S. Panero, B. Scrosati, Mario. Wachtler and F. Croce., Nanotechnology for the progress of lithium batteries R&D.,2004, J. Power. Sources., **129**, 90-95.

[79] M. Wagemaker, W. J. H. Borghols, and F. M. Mulder., Large Impact of Particle Size on Insertion Reactions. A Case for Anatase Li_xTiO_2., 2007, Am. Chem. Soc., **129,** 4323–4327.

[80] N.N. Dinh, N. M. Quyen, D. N. Chung, M. Zikova and V.V. Truong., Highly-efficient electrochromic performance of nanostructured TiO_2 films made by doctor blade technique., 2011, Solar Energy Materials & Solar Cells, **95**, 618-623.

[81] N.N. Dinh, N.T.T. Oanh, P.D. Long, M.C. Bernard and A. H.-L Goff., Electrochromic properties of TiO_2 anatase thin films prepared by a dipping sol–gel method., 2003, Thin. Solid. Films., **423**, 70-76.

[82] C.G. Granqvista, A. Azensb, P. Heszlerc, L.B. Kishd and L. O¨sterlunde., Nanomaterials for benign indoor environments: Electrochromics for ‘‘smart windows’’, sensors for air quality, and photo-catalysts for air cleaning., 2007, Sol Ene. Mat. & Sol. Cel., **91**, 355-365.

[83] C.G. Granqvist., Solar energy materials.,1991, Appl.Phys.A., **52**, 83-93.

[84] A. Ghicov, H. Tsuchiya, R. Hahn, J. M. Macak, A. G. Munoz and P. Schmuki., TiO_2 nanotubes: H^+ insertion and strong electrochromic effects., 2006, Electrochem. Commun, **8** , 528-532.

[85] J. Wang, X. Wei Sun, and Z.Jiao., Application of Nanostructures in Electrochromic Materials and Devices: Recent Progress.,2010, Mat., **3**, 5029-5053.

[86] T. Gaoa, A. Gustavsen, and B. P. Jelle., Nanoelectrochromics with Applied Materials and Methodologies, zero emission buildings - proceedings of Renewable Energy Conference in Trondheim., Norway., Trondheim, 2010.

[87] D. Linden, and T.B. Reddy, Handbook of Batteries 3rd Edition. Chapter 35., New York: McGraw-Hill., (2002).

[88] C. Zhai, D.Hanaor, G.proust,L. Brassart and Y.Gan., Interfacial electro-mechanical behaviour at rough surfaces.,2016, Extre.Mech.Letters., **9**, 422- 429.

[89] H. C. Chung., Charge and discharge profiles of repurposed LiFePO4 batteries based on the UL 1974 standard.,2021, Scie. Dat., **8**, 165-176.

[90] B. Pack., How to rebuild a Li-Ion battery pack., Electronics Lab., Implemented for Fujitsu , 2016.

[91] B. Schweber., Lithium Batteries: The Pros and Cons., Global.Spec., Electronics 360., 2015.

[92] B. S. J.Mayen., Design Review For: Advanced Electric Vehicle Battery Charger, ECE 445 Senior Design Project., TA:Wayne Weaver., 2007.

[93] S. L. (pty)., Lithium Ion Rechargeable Batteries.,Technical Handbook.,sony battery ed website, China, 2009.

[94] L.I.battery pack., Custom Lithium ion Battery Pack Manufacturer.,Large.Power., China., 2015.

[95] S. A. Schaft., CL75 user manual. Siemens AG., 8, Commun., Munich, 2005.

[96] W. machines., Overview of lithium ion Batteries., sanyo., 2016.

[97] W. Machine.,Harding energy specification., Sanyo, 2015.

[98] A. H. Zimmerman., Self-discharge losses in lithium-ion cells., 2004, IEEE Aerospace and Electronic Systems Magazine., J and Mag., **19**,19-24.

[99] P. Weicker., A Systems Approach to Lithium-Ion Battery Management., Norwood: Artech House., 2013.

[100] H. Abe, T. Murai, K. Zaghib., Vapor-grown carbon fiber anode for cylindrical lithium ion rechargeable batteries., 1999, J. of Pow. Sourc., **77**, 110-115.

[101] Encyclopedia., IBattery Performance charactristics: Information on self-discharge characteristics of battery types., M power., UK, 2007.

[102] S. L. M. Vetter., Rechargeable Batteries with Special Reference to Lithium-Ion Batteries., Storing Energy., Germany.,2016, Elsevier.,205-225.

[103] Tektronix., Lithium ion battery materials guidelines.

[104] BU-808., How to Prolong Lithium Based Batteries., Battery University., 2019.

[105] B. Xu, A.Oudalov, A.UIbig, G. Andersson and D.S. Kirshenn., Modeling of Lithium-Ion Battery Degradation for Cell Life Assessment., 2018, IEEE Trans. on Smart. Grid,, 9, 1949-3053.

[106] K.Amine, C.H. Chen, L.Liu, M.Hammond, A.Jansen, D.Dees.I Bloom.D.Vissers and G.Hinriksen Factors Responsible for Impedance Rise in High Power Lithium-Ion Batteries.,2001, Journal of Power Sources., **97-98**, 684-687.

[107] P. Voelker., Trace Degradation Analysis of Lithium-Ion Battery Components., 2014, Resear. & Dev., **408-481-4442**, 1-5.

[108] B. University., Discharging at High and Low Temperatures., Battery University., 2018.

[109] J.R. Choi, Quantization of underdamped, critically damped, and overdamped electric circuits with a power source., 2002, Int. J. of Theo. Phys., 41, 1931-1939..

[110] B. Dunn, H. Kamath, J.M Tarascon., Electrical Energy Storage for the Grid: A Battery of Choices.,2011, Scie., **334**, 928-935.

[111] J.M. Tarascon., Is lithium the new gold?.,2010, Nat. Chem., **2**, 510.

[112] R. S. Carmichael., Practical Handbook of Physcial Properties of Rocks and Minerals., CRC Press., Boca Raton., FL, 1989.

[113] M. D. Slater, D. Kim, E. Lee, C. S. Johnson., Sodium Ion Batteries., 2013, Adv. Funct. Mater., **23**, 947-958.

[114] S. Komaba, W. Murata, T. Ishikawa, N. Yabuuchi, T. Ozeki, T. Nakayama, A. Ogata,K. Gotoh, K. Fujiwara., Electrochemical Na Insertion and Solid Electrolyte Interphase for Hard-Carbon Electrodes and Application to Na-Ion Batteries., 2011, Adv. Funct. Mater.,**21**, 3859-3867.

[115] T. Oshima, M. Kajita, A. Okuno., Development of Sodium-Sulfur Batteries., 2004, Int. J. Appl. Ceram. Technol.,**1**, 269-276.

[116] R. J. Bones, D. A. Teagle, S. D. Brooker, and F. L. Cullen., Development of a Ni,$NiCI_2$ Positive Electrode for a Liquid.,1989, J. Electrochem. Soc., **136**, 1274-1277.

[117] M. Okoshi, Y. Yamada,A. Yamada, H. Nakai., Theoretical Analysis on De-Solvation of Lithium, Sodium,and Magnesium Cations to Organic Electrolyte Solvents.,2013, J. Electrochem. Soc.,**160**, A2160-A2165.

[118] R.D. Shannon.,Revised effective ionic radii and systematic studies of interatomic distances in halides and chalcogenides., 1976, Acta Cryst., **A32**, 751-767.

[119] K. Kuratani, N. Uemura, H. Senoh, H. T. Takeshita, T. Kiyobayashi., Conductivity, viscosity and density of $MClO_4$ (M = Li and Na) dissolved in propylene carbonate and γ-butyrolactone at high concentrations., 2013, J. Power. Sourc., **223**, 175-182.

[120] N.Yabuuchi, Kei. Kubota,M. Dahbi and S. Komaba., Research Development on Sodium-Ion Batteries., 2014, Chem. Rev.,**114**,11636−11682.

[121] F.Parrino,F.R. Pomilla,G.C.Roda, V.Lodolo,L.Palmisano.,Properties of titanium dioxide,Titanium Dioxide (Tio_2) and Its Applications.,2021,UK., Elsevier., 13-66.

[122] X. Wang,Y.Zhao,K.Molhave and H.Sun.,Engineering the Surface/Interface Structures of Titanium Dioxide Micro and Nano Architectures towards Environmental and Electrochemical Applications., 2017, Nano.,**7**, 382-441.

[123] S. Reghunath,D.Pinheiro and S.K.R. Devi., A review of hierarchical nanostructures of TiO_2: Advances and applications., 2021, Appl. Surf. Scien. Adv., **3**, 100063-100096.

[124] M. Manzoli, F.S. Freyria, N.Blangetti and B.Bonelli., Brookite, a sometimes under evaluated TiO_2 polymorph.,2022, RSC Adv.,**12**, 3322-3334.

[125] X. Chen and S.S.Mao.,Titanium dioxide nanomaterials: synthesis,properties, modifications, and applications., 2007, Chem. Rev., **107**,2891-2959.

[126] H. Yildirim., Effect of Concentration on the Energetics and Dynamics of Li IonTransport in Anatase and Amorphous $TiO_{2.}$, 2011, J. Phys. Chem. C., **115**, 15661-15673.

[127] Q. Zhang and C,Li., High Temperature Stable Anatase Phase Titanium Dioxide Films Synthesized by Mist Chemical Vapor Deposition.,2020, Nano.,**10**,, 911-918.

[128] D.H. Lee,B.H.Lee.A.K.Sinha,J.J.Park,M.S.Kim,J.Park,H.shin,K.S.Lee,Y.E.Sung and T.Hyeon.,Engineering Titanium Dioxide Nanostructures for Enhanced Lithium-Ion Storage., 2018, J. Am. Chem. Soc.,**140**, 16676-16684.

[129] G. Schmid., Nanoparticles: From Theory to Application., Chapter 2., Wil. Weinheim., 2005.

[130] E.l. Goresy, A.Chen, M. Gillet, P. Dubrovinsky, L. Graup and G. A. Rajeev., A natural shock-induced dense polymorph of rutile with α-PbO2 structure in the suevite from the Ries crater in Germany., 2001, Earth. Planet. Sci. Lett., **4**, 484 - 485.

[131] R. Marchand, L. Brohan and M. Tournoux., A New Form of Titanium Dioxide and the Potassium Octatitanate $K_2Ti_8O_{17}$.,1980, Mat. Research Bulletin.,**15**,1129 - 1133.

[132] M. Latroche, L. Brohan, R. Marchand, and R. Tournoux., New Hollandite Oxides: TiO_2(H) and $K_{0.06}TiO_2$.,1989, J. of Solid State Chem., **81**, 78 - 82.

[133] J. Akimoto, Y. Gotoh, Y. Oosawa, N. Nonose, T. Kumagai, K. Aoki and H. Takei., Topotactic Oxidation of Ramsdellite-Type $Li_{0.5}TiO_2$, a New Polymorph of Titanium Dioxide: TiO_2(R).,1994, J. Sol. Stat. Chem., **13**, 27 - 36.

[134] P. Y. Simons and F. Dachille., The Structure of TiO_2(II), a High-Pressure Phase of TiO_2.,1967, Acta Crystallogr., Sect. B: Struct. Sci., **23**, 334 - 336.

[135] H. Sato, S. Endo, M. Sugiyama, T. Kikegawa, O. Shimomura and K. Kusaba., Baddeleyite-Type High-Pressure Phase of TiO_2., 1991, Sci., **251**, 786 - 788.

[136] N.A. Dubrovinskaia, L.S. Dubrovinsky, R. Ahuja, V.B. Prokopenko, V. Dmitriev, H.P. Weber, J.M. Osorio-Guillen and B. Johansson.,Experimental and Theoretical Identification of a New High-Pressure TiO_2 Polymorph., 2001, Phys. Rev. Lett., **87**, 275501 - 27550.

[137] M. Mattesini, J.S. de Almeida, L. Dubrovinsky, L. Dubrovinskaia. B. Johansson and R. Ahuja.,High-Pressure and High-Temperature Synthesis of the Cubic TiO_2 polymorph.,2004, Phys. Rev. B., **70**, 212101 - 212102.

[138] L.S. Dubrovinsky, N.A. Dubrovinskaia, V. Swamy, J. Muscat, N.M. Harrison, R. Ahuja, B. Holm and B. Johansson., Materials Science: The hardest known oxide., 2001, Nat., **410**,653 - 654.

[139] G. Zheng, S.W. Lee, Z. Liang, H.W. Lee, K. Yan, H. Yao, H. Wang, W. Li, S. Chu, and Y. Cui., Interconnected Hollow Carbon Nanospheres for Stable Lithium Metal Anodes., 2014, Nat. Nano., **9**, 618 - 623.

[140] D. Howell, T. Duong, J. B. Deppe, Irwin Weinstock, D. Linden and T. B. Reddy., Research for Advanced Lithium Ion Batteries.,2008, Mater. Mat., **100**, 3 - 4.

[141] A.R. Oganov and A.O. Lyakhov., Towards the Theory of Hardness of Materials.,2010, J. Superhard. Mat., **32**, 143 - 147.

[142] D. N. Hamane, A. Shimizu, R. Nakahira, K. Niwa, A. Sano-Furukawa, T. Okada, T. Yagi and T. Kikegawa., The stability and Equation of State for the Cotunnite Phase of TiO_2 up to 70 GPa., 2010, Phys. Chem. Miner., **37**,129 - 136.

[143] E. John., An A–Z Guide to the Elements., 2001, Oxford: Oxford University Press., 451 - 53.

[144] N.N. Greenwood and A. Earnshaw., in Chemistry of the Elements., 1984, Oxford: Pergamon Press., 1117-19.

[145] J.F. Banfield, D.R. Veblen and D.J. Smith., The Identification of Naturally Occurring TiO_2 (B) by Structure Determination Using High-Resolution Electron Microscopy, Image Simulation and Distance–Least–Squares Refinement, 1991, Am. Mineral., **76**, 342 - 343.

[146] A. Kohno, T. Gondo, K. Kogi and T.Tajiri.,Structural and Optical Characterization of TiO_2 nanoparticles-containing mesoporous Silica (SBA-15) thin films., 2011, Mat. Scie. Eng., **24**, 012019 -012028.

[147] K. Amine, Z. H. Chen, Z. Zhang, J. Liu, W. Q. Lu, Y. Qin, J. Lu, L. Curtis and Y. K. Sun., New Class of Nonaqueous Electrolytes for Long-Life and Safe Lithium-Ion Batteries., 2011, J. Mater. Chem., **21**, 17754 -17759.

[148] B. Liu, D. Deng, J. Y. Lee. and E. S. Aydil., Oriented Single-crystalline TiO_2 nanowires on titanium foil for lithium ion batteries.,2010, J. Mater. Res., **25**,1588 -1594.

[149] H. Liu, Z. Bi , X-G. Sun, R. R. Unocic, M. P. Paranthaman, S. Dai and G. M. Brown., Mesoporous TiO_2-B Microspheres with Superior Rate Performance for Lithium Ion Batteries.,2011, Adv. Mater., **23**, 3450-3454.

[150] T.X.T. Sayle, C.R.A. Catlow, D.C. Sayle, S.C Parker and J.H Harding., Computer Simulation of Thin Heteroepitaxial Ceramic Interfaces Using a Near-Coincidence-Site Lattice Theory.,1993, Mag. A., 68, 565 - 573.

[151] M.G. Matshaba, D.C. Sayle, T.X.T. Sayle and P.E. Ngoepe., Structure of Surface Entrance Sites for Li Intercalation Into TiO_2 Nanoparticles, Nanosheets and Mesoporous Architectures with Applications for Li ion Batteries., 2016, J. Phys. Chem. C., **26**, 14001-14008.

[152] P. Pradubkorn, S. Maensiri, E. Swatsitang, P. Laokul., Preparation and characterization of hollow TiO_2 nanospheres: The effect of Fe^{3+} doping on their microstructure and electronic structure.,2020,Curr. Appl. Phys., **20**, 1, 178-185.

[153] S.Hussain, C. Cao,W. S.Khan, G. Nabi, Z. Usman,A. Majid, T. Alharbi, Z. Ali, F. KButt, M. Tahir,M. Tanveer, F. Idress., Cu_2O/TiO_2 nanoporous thin-film heterojunctions: Fabrication and electrical characterization., 2014, Mat. Scie. in Semicon. Proces., **25**,181-185.

[154] S.S. Song, B.-Y. Xia, J. Chen, J. Yang, X. Shen,S.-J. Fan, M.-l. Guo, Y.-M. Sun, and X.-D. Zhang.,Two dimensional TiO_2 nanosheets: in vivo toxicity investigation., 2014, RSC Adv., **4**, 42598-42603.

[155] P.Lian, X.Zhu, S.Liang, Z.Li, W.Yang, H.Wang., Large reversible capacity of high quality graphene sheets as an anode material for lithium-ion batteries., 2010, Electro. chim. Acta., **55**,3909-3914.

[156] P.Poizot, S.Laruelle, S.Grugeon, L.Dupont, J.M.Tarascon., Nano-sized transition-metal oxides as negative-electrode materials for lithium-ion batteries., 2000, Nature., **407**, 496-9.

[157] S. Chu, Y. Cui and N. Liu.,The path towards sustainable energy., 2017, Nat. Mater., **16**,16–22.

[158] S.H. Choe, C.J Yu, K.C Ri,J.S. Kim,U.G Jong,Y.H Kye and S.N Honga.,First Principles study of $NaxTiO_2$ with trigonal Bipyramid Structure: an Insight into Sodium-ion Battery Anode Applications., 2019, Phys.Chem.Chem.Phys., **21,** 8408-8417.

[159] O. Tschauner, C. Ma ,A. Lanzirotti, and M. G. Newville., Riesite, a New High Pressure Polymorph of TiO_2 from the Ries Impact Structure., 2020, Minerals, **10**, 78-95.

[160] I. Tsuyumoto and T. Moriguchi., Synthesis and lithium insertion properties of ramsdellite Li_xTiO_2 anode materials., 2014, Mat. Resea. Bull., **70**, 748-752.

[161] G. Zhu, Y. Wang, Y. Xia.,Ti-based compounds as anode materials for Li-ion batteries., 2012, Energy Environ. Sci., **5**, 6652-6667.

[162] X. Gu and C.Lai., Recent development of metal compound applications in Lithium -Sulphur batteries., 2018, J. Mater. Res., **33**,1-31.

[163] T. X. T. Sayle, C. R. A. Catlow, R. R. Maphanga, P. E. Ngoepe and D. C. Sayle., Generating MnO_2 Nanoparticles Using Simulated Amorphization and Recrystallization., 2005, J. Am. Chem. Soc., **127**,12828-12837.

[164] H.Z. Zhang and J.F. Banfield.,Aggregation, Coarsening and Phase Transformation in ZnS Nanoparticles Studied by Molecular Dynamics Simulations., 2004, Nano Lett., **4**, 713-718.

[165] D. Frenkel and B. Smit., Understanding Molecular Simulations from Algorithms to Applications.,1996, San Diego: Academic Press, 61-62.

[166] W. Smith and I. T. Todorov., A Short Description of DL_POLY.,2006, Mol. Simul, 32, 935-943.

[167] L. Verlet., Computer Experiments on Classical Fluids. I. Thermodynamical Properties of Lennard-Jones molecules.,1967, Phys. Rev., **159**, 98-103.

[168] D.C. Sayle and G.W Watson., Amorphisation and Recrystallisation of an MgO Cluster Supported on BaO(100)., 2002a, J. Phys. Chem. B, 106, 3916-3925.

[169] A. P. Sutton and R.W. Balluffi., Overview no. 61: On Geometric Criteria for Low Interfacial Energy., 1987, Acta. Metal., 35, 2177-2201.

[170] D.C. Sayle and G. W. Watson., Structural Exploration of Thin-Film Oxide Interfaces via Simulated Amorphisation and Recrystallisation., 2001a, Surf. Sci., 437,97-107.

[171] D.C. Sayle and G.W. Watson.,The Atomistic structures of $MgO/SrTiO_3$(001) and BaO/SrTiO3(001) using simulated amorphisation and recrystallisation., 2001b, J. Phys. Chem. B.,**105**, 5506 - 5514.

[172] D.C. Sayle and R.L. Johnston., Evolutionary Techniques in Atomistic Simulation: Thin Films and Nanoparticles., 2003, Curr. Opin. Sol. Stat. Mater. Sci., **7**, 3 - 12.

[173] D.C. Sayle, S.A. Maicaneanu and G.W. Watson.,Atomistic Models for CeO_2 (111), (110) and (100) Nanoparticles, Supported on yttrium stabilised zirconia., 2002c, J. Am. Chem. Soc.,**124**, 11429 - 11439.

[174] T.X.T. Sayle, C.R.A. Catlow, R.R. Maphanga, P.E. Ngoepe and D.C. Sayle., Evolving microstructure in MnO_2 using Amorphisation and recrystallisation., 2006, J.Crys. Growth.,**294**,118 - 129.

[175] T.X.T. Sayle, S.C. Parker and D.C. Sayle., Shape of CeO_2 Nanoparticles using Simulated Amorphisation and Recrystallisation., 2004, Chem.Commun., **21**, 2438 - 2439.

[176] R.R. Maphanga, P.E. Ngoepe, T.X.T. Sayle and D.C. Sayle., Amorphisation and Recrystallisation Study of Sithium Insertion in Manganese Dioxide.,2010, Phys. Chem.Chem. Phys.,**13**,1307 -1313.

[177] M.M. Born and K. Huang.,Dynamic Theory of Crystal Lattices.,1954,Oxford University Press.

[178] M.P. Allen and D.J. Tildesley., Computer Simulation of Liquids.,1987,UK, Oxford Scientific Publishing., **66**.

[179] D.C. Sayle, J.A. Doig, S.A. Maicaneanu and G.W. Watson.,The Atomistic Structure of oxide Nanoparticles Supported on an Oxide Substrate., 2002, Phys. Rev. B. Condens. Matt., **65**, 245413 - 245414.

[180] W. Kob., Computer simulations of Supercooled Liquids and Glasses.,1999, J. Phys. Condens Matt.,**11**, 84 - 85.

[181] W. Smith and T.R. Forester., DL_POLY_2.0: A General-Purpose Parallel Molecular Dynamics Simulation Package.,1996, J. Molec. Graphic., **14**,136-341.

[182] T. X. T. Sayle, K.M Kgatwane, P. E. Ngoepe and D. C. Sayle., 'Breathing-crystals' the origin of electrochemical activity of mesoporous Li–MnO_2., 2016, J. Mater. Chem. A, **4**, 6456–6464.

[183] L.Y.Yang, H.Z.Li, J.Liu, S.S.Tang, Y.K.Lu, S.T.Li, J.Min, N.Yan and M.Lei.,$Li_4Ti_5O_{12}$ nanosheets as high rate and longlife anode materials for sodium ion batteries., 2015, J.Mater.Chem.A, **3**,24446-24452.

[184] L. Xiao, W. Meng, S. Wang, D. Liu, D. Qu, Z. Xie, B. Deng, and J. Liu., The effects of structural properties on the lithium storage behavior of mesoporous TiO_2., 2017, Nanotech.**28** 265401-265411.

[185] J.L. Kaufman, J. Vinckeviciute, S.K. Kolli, J.G. Goiri and A. Van der Ven., Understanding interaction compounds for sodium-ion batteries and beyond.,2019.,Phil.Trans.R.Soc.A.,**377**:2019001-20190020.

[186] J. A. Yuwono, P. Burr, C. Galvin, and A. Lennon., Atomistic Insights into Lithium Storage Mechanisms in Anatase, Rutile, and Amorphous TiO_2 Electrodes., 2021, ACS Appl. Mater. Interfaces., **13**, 1791−1806.

[187] C. L. Olson and J. Nelson., Defect Chemistry, Surface Structures, and Lithium Insertion in Anatase TiO_2., 2006, J. Phys. Chem. B.,**110**, 9995-10001.

[188] H. Yildirim, J. Greeley, and S. K. R. S. Sankaranarayanan., Effect of Concentration on the Energetics and Dynamics of Li Ion Transport in Anatase and Amorphous TiO_2., 2011, J. Phys. Chem. C., **115**, 15661–15673.

[189] G. A. Korablev., Calculation of Activation Energy of Diffusion and Self-Diffusion., 2018, Eur. Chem. Bull., **7**, 23-29.